Spatial and temporal evolution of dynamic nuclear polarization on different scales

Emmanuelle Weber

THÈSE DE DOCTORAT

de l'Université de recherche Paris Sciences et Lettres
PSL Research University

Ecole Normale Supérieure de Paris
UMR 7203 Laboratoire des Biomolécules

Spatial and Temporal Evolution of Dynamic Nuclear Polarization on Different Scales

Evolution spatiale et temporelle de la polarisation dynamique nucléaire à différentes échelles

Ecole doctorale n°388

Chimie Physique et de Chimie Analytique de Paris Centre

Spécialité CHIMIE PHYSIQUE

COMPOSITION DU JURY :

Mme. VAN DOORSLAER Sabine
University of Antwerp - Department of Physics - Biophysics and Biomedical Physics, Rapporteur

M. VEZIN Hervé
Université de Lille1, Laboratoire de Spectrochimie Infrarouge et Raman, Rapporteur

Mme. LESAGE Anne
Université de Lyon 1, Institut des Sciences Analytiques, Membre du jury

Mme. SAGAN Sandrine
Sorbonne Université, Laboratoire des Biomolécules, Présidente du jury

M. KURZBACH Dennis
ENS de Paris, Laboratoire des Biomolécules, Co-superviseur de thèse

M. BODENHAUSEN Geoffrey
ENS de Paris Laboratoire des Biomolécules, Directeur de thèse

Soutenue par
Emmanuelle WEBER
le 18 10 2018

Dirigée par
Geoffrey BODENHAUSEN et
Dennis KURZBACH

ENS | PSL

À Valentin

Acknowledgements

Before everything, it is important to mention that this thesis, financed by the European Research Council (ERC), is the result of the collaboration of many people from the team 3 of the *Laboratoire des Biomolécules* in ENS Paris (France). It relied also a lot on the help from external experts such as EPR spectroscopists from the *LASIR* laboratory in Lille (France), cryo-EM specialists and solid-state NMR scientists from *Sorbonne Université* in Paris (France).

I would like to express my gratitude to my thesis director, Pr. Geoffrey Bodenhausen for having given me the opportunity to join his team at the ENS Laboratory. The environment and intellectual guidance he provided helped me to find my place in the scientific community. Showing me a very human personality, he continuously cared about my well-being and afforded me the freedom to work on the subjects I was the most interested in.

I warmly thank my co-supervisor Dr. Dennis Kurzbach for his constant and tremendous implication during these three years. I feel deeply indebted for his supervision without which this thesis would not have been possible. His advices, encouragements and sense of humor always kept me motivated while his experience, deep knowledge, pedagogy and patience raised me not only in the scientific domain but also philosophically and spiritually. Curious and passionate, working with him every day was very inspiring. It was a real pleasure to share this journey with such a talented scientist and beautiful spirit.

I am beholden to Dr. Daniel Abergel who entirely supervised the radiation damping chapter of this thesis. His impressive knowledge accompanied me all along my

work. Always volunteering to help me, patient and especially understanding, he kept motivating me to hold on and try to understand this very complicated subject. His profound love of science was communicative and I really enjoyed our scientific discussions.

The French network *RENARD* financed the fees relative to the collaboration between the ENS and *LASIR* laboratory. I sincerely enjoyed the time I spent in Lille to perform the EPR measurements with Dr. Giuseppe Sicoli and Dr. Hervé Vezin. Their hardworking, generous and kind personalities made this experience particularly pleasant and rewarding.

I am grateful to Dr. Thierry Azaïs from the *Laboratoire de Chimie de la matière Condensée de Paris* (France) for his implication in the bio-mineralization project sharing with us his knowledge and acquiring the solid-state NMR data.

I also thank Ghislaine Frébourg for the acquisition of the cryo-EM images and Pr. Jacques Dubochet, Dr. Konstantin Ivanov from the *International Tomographic Center* of Novosibirsk (Russia) and Dr. Alberto Rosso from the *Laboratoire de Physique Théorique et Modèles Statistiques* of Paris-Sud (France) for the instructive discussions.

I would like to thank my friends and family for their support. My mother Murielle and my father Pierre who supported me both morally and financially during all these years. Maxence, my brother for his contagious optimism. I would also like to thank Josée and Didier for their help and support during the redaction of the manuscript. Last but not least, Antoine, Florian, Clara, Léo and Victor, who were always present when the need arose (and otherwise). A big thank you to my partner Valentin who supported me for years. His daily humor, reassurance and patience helped tremendously and this thesis certainly would not have been possible without his help.

J'aimerais remercier mes proches que j'ai un peu délaissés ces derniers mois. Ma mère Murielle et mon père Pierre qui m'ont soutenue à la fois financièrement et mentalement pendant toutes ces années. Maxence, mon frère pour son optimisme et sa joie de vivre contagieuse. Merci également à Josée et Didier pour m'avoir supportée, aidée et épaulée lors de la rédaction du manuscrit. Sans oublier Antoine, Florian, Clara, Léo et Victor, toujours présents lorsque j'avais besoin d'eux (et surtout lorsque j'avais un peu moins besoin d'eux). Un grand merci à Valentin, mon partenaire qui me soutient depuis des années. Son humour, son réconfort et sa patience m'accompagnent quotidiennement et cette thèse n'aurait très certainement jamais vu le jour sans son aide.

Contents

List of abreviations

DNP	: dynamic nuclear polarization
D-DNP	: dissolution DNP
NMR	: nuclear magnetic resonance
MRI	: magnetic resonance imaging
EPR	: electron paramagnetic resonance
MAS	: magic angle spinning
cryo-TEM	: transmission electron cryo-microscopy
FID	: free induction decay (observable NMR signal)
CW	: continuous wave
μW	: microwave
CP	: cross-polarization
SNR	: signal over noise ratio
OE	: Overhauser effect
SE	: solid effect
CE	: cross-effect
TM	: thermal mixing
ZQ	: zero quantum
DQ	: double quantum
RD	: radiation damping
RF	: radiofrequency
PA	: paramagnetic agent
eSD	: electron spectral diffusion
NPS	: nanophase separation
BMP	: Bloch-Maxwell-Purcell

CaP	: calcium phosphate
CSA	: chemical shift anisotropy
P_i	: phosphate
PNC	: prenucleation cluster
P_{PNC}	: P_i in PNC

List of symbols

h	: Planck's constant
$\hbar$	: reduced Planck's constant
$\mathrm{k_B}$	: Boltzmann's constant
μ_0	: vacuum permeability
$\hat{\mu}$	: magnetic moment
g	: Landé or g-factor
$\mathbf{S}$	: electron spin angular momentum
ρ	: density operator
γ or γ_I	: nuclear gyromagnetic ratio
γ_n	: gyromagnetic ratio of the proton
γ_e or γ_S	: gyromagnetic ratio of the electron
$\vec{B_0}$	: static magnetic field
$\vec{B}_{eff}$	: effective magnetic field
$\Delta\sigma$	: chemical shift anisotropy
$\mathbf{A}$	: hyperfine tensor
$\mathbf{I}$	: nuclear spin angular momentum
$\vec{M}$	: nuclear magnetization
$\hat{I}_+$, $\hat{I}_-$	: nuclear ladder operators
ΔE	: difference of energy between two energy states
T_1 or T_{1n}	: nuclear spin-lattice relaxation time
T_2	: nuclear spin-spin relaxation time.
T_{1e}	: electronic spin lattice relaxation time
T_{2e}	: electronic spin-spin relaxation time
T_{ripe}	: ripening time of the sample

τ_c	: molecular rotational correlation time
H_{DD}	: hamiltonian associated to the electron dipolar interaction
H_{Ze}	: electron Zeeman hamiltonian
H_{Zn}	: electron non-Zeeman hamiltonian
H_{nZ}	: nuclear Zeeman Hamiltonian
P_I or P_n	: nuclear spin polarization
P_S or P_e	: electron spin polarization
P_{eq}	: nuclear polarization at Boltzmann equilibrium
P_0	: electron polarization at thermal equilibrium
P_{e0}	: polarization of the saturated electronic spin packet
Δ_0	: frequency offset of the microwaves from the electron resonance frequency
Δ_i	: frequency offset of the ith electronic spin packet from the electron resonance frequency
T	: thermodynamical temperature in the NMR tube
T_L	: thermodynamical temperature of the lattice
T_S	: electronic spin temperature
β_I or β_n	: inverse nuclear Zeeman spin temperature. In chapter 5, β_n always refers the inverse spin temperature of the ^{1}H Zeeman reservoir.
β_S or β_e	: inverse spin temperature of the electron Zeeman reservoir
β_{SS} or β_{ee}	: inverse spin temperature of the electron dipolar reservoir
β_d	: inverse spin temperature of the deuterium reservoir
ω_S or ω_e	: electronic Larmor frequency
ω_I or ω_n	: nuclear Larmor frequency
ω_1	: amplitude of the applied RF field
$\omega_{1\,\mu w}$	: amplitude of the microwaves
$\omega_{\mu w}$	: frequency of the microwaves
M^2	: second moment of the EPR line
$\delta\omega$	: width of electronic spectrum
D	: electronic spectral diffusion coefficient

Q : quality factor of the probe

η : chapter 5 - filling factor of the probe

chapter 6 - dynamic viscosity

τ_{rd} : radiation damping characteristic time

C_n : heat capacity of the proton Zeeman reservoir

C_e : heat capacity of the electron dipolar reservoir

C_d : heat capacity of the deuterium Zeeman reservoir

$\tau_{n,ee}$: characteristic time of the transfer of polarization between the electron dipolar and proton Zeeman reservoirs

$\tau_{d,ee}$: characteristic time of the transfer of polarization between the electron dipolar and deuterium Zeeman reservoirs

$\tau_{ee,L}$: characteristic time of the transfer of polarization from the electron dipolar reservoir to the lattice

k_{ex} : exchange rate constant

$\delta(^{31}\mathrm{P})$: ^{31}P isotropic chemical shift

Introduction

The origin of magnetic resonance spectroscopy

In the 1920s, physicists knew that atoms, which are composed of positively charged nuclei surrounded by a cloud of negatively charged electrons, feature a property that could not be described in a classical picture. They hence developed the notion of a quantum mechanical analogue of an angular momentum, which they coined the spin-angular momentum. It describes a sort of spinning of the nuclear and electronic charge (denoted henceforth as "spin"). As any revolving charge, this leads to the creation of a magnetic moment and its associated magnetic field. Moreover, such particles featuring a spin tend to align their magnetic moment with or against any externally applied magnetic field. In 1937, the American physicist Isidor I. Rabi working at Colombia University in New York, followed the idea of the Dutch physicist Cornelius J. Gorter to apply radio waves to atomic nuclei with a spin to manipulate the orientation of their magnetic moment with respect to an external magnetic field. Thus, I. I. Rabi irradiated lithium chloride in a vacuum chamber at different external magnetic fields. He found that by adjusting both the frequency of the radio frequency waves and the external static magnetic field, he could observe an absorption of the irradiated waves, which he associated to a resonance phenomenon between the spin and the radio waves, i.e., magnetic resonance was born.[1] I. I. Rabi was awarded the Nobel Prize in Physics "for his resonance method for recording the magnetic properties of atomic nuclei" in 1944.[2,3] Although his work was crucial for the development of the magnetic resonance method, Rabi focused all his studies on isolated nuclei in vacuum.

Early days of Nuclear Magnetic Resonance (NMR)

Nuclear magnetic resonance (NMR) spectroscopy constitutes a very powerful non-destructive spectroscopic technique. It is widely used in chemistry, biology, medicine and physics to determine the structure and dynamics of small molecules, polymers, nucleic acids or small proteins.

In late 1945, two physicists, Edward Mills Purcell at the Massachusetts Institute of Technology (MIT) and Felix Bloch working in Stanford simultaneously extended Rabi's work to an ensemble of molecules in solid and liquid samples.[4] Hence, at the Radiation Laboratory of MIT, Purcell, Torrey and Pound acquired proton signal of 1 L of solid paraffin in a resonant cavity tuned at 30 MHz. By sweeping the external magnetic field, they observed a change of 0.4 % in the applied radiofrequency (RF) field amplitude that they attributed to energy dissipation through relaxation of ^{1}H nuclei.[5] While the MIT team was working on solid paraffin, the Stanford one which was composed of Bloch, Hansen and Packard measured a proton signal of 1.5 cm^3 in bulk water at 7.7 MHz at room temperature. In their experiment, they used two orthogonal RF coils: one for the excitation of the protons (transmitter coil), the other for the detection of the signal through the de-excitation of the ^{1}H spin of the water molecules (receiver coil).[6,7] Complementary studies have been performed in 1949 by Henry C. Torrey who was working at Rutgers University in the New Jersey and by Erwin L. Hahn in 1950 at the University of Illinois who developed the principle of pulsed NMR inspired by Bloch's 1946 suggestions[8] and measured the Larmor precession frequency of protons in glycerine and water solutions.[9,10].

At this early age of NMR, the nuclear frequency shift generated by the shielding of the magnetic field through the electron clouds was considered as an artifact by particle physicists. In 1951, the scientists Arnold, Dharmatti and Packard working in Purcell's group demonstrated the potential of this phenomenon in chemistry by observing three independent lines at different frequencies corresponding to the resonances of protons belonging to OH, CH_2 and CH_3 groups of ethyl alcohol[11]. This frequency difference, which is characteristic of the direct environment of a nucleus, was coined "chemical shift". Many scientists started to work on applications of this

phenomenon to characterize a large variety of small systems in chemistry and biology such as bovine pancreatic ribonuclease[12], cytochrome c, myoglobin. Furthermore, physical properties of water were examined such as relaxation and diffusion in living human subjects and animals.[13,14] However, hardware problems at this time led to many artifacts as consequences of static magnetic field inhomogeneities.[15]

In 1966, the Swiss Richard R. Ernst, together with the American Weston A. Anderson, found a way to considerably decrease the experimental time by using short radiofrequency pulses to excite nuclei instead of irradiation by long frequency sweeps. A decaying temporal signal is acquired during the acquisition containing all the system information: the free induction decay (FID). A frequency analysis is possible by a Fourier transform (FT) of the FID.[16] Decreasing the experimental time enables the repetition of an experiment and the rapid averaging of the signals; this has considerably increased the signal-to-noise ratio in NMR. Ernst received the Nobel prize in chemistry in 1991 "for his contributions to the development of the methodology of high resolution nuclear magnetic resonance (NMR) spectroscopy".

In 1976, two-dimensional FT applied to NMR spectroscopy by Ernst constituted a major breakthrough in biochemistry, though the original idea stemmed from the Belgian physicist Jean Jeener. This development gave birth to correlation maps between spins[17] opening a lot of new perspectives for structural and dynamical biology.

NMR applications have continued to evolve and constitute nowadays an indispensable tool in chemical and biological research fields. NMR also offers great perspectives for investigating in-cell metabolisms as proteins in bacterial and human cells could be differentiated from the cellular background either by over-expression[18] of isotopic-labeled proteins or by injecting them into the cellular cytoplasm.[19–21] Additionally, NMR is nowadays indispensable in medical diagnosis through magnetic resonance imaging (MRI).

Electron Paramagnetic Resonance (EPR)

In electron paramagnetic resonance (EPR) spectroscopy the signal of unpaired electrons is studied. Many molecules such as free radicals or metallic ions can thus be detected by this technique. The EPR phenomenon has been simultaneously discovered in 1944 by Zavoisky,[22,23] a Soviet physicist from Kazan State University in Russia, and Bleaney from the University of Oxford. Even if Zavoisky never received any Nobel Prize for his discovery, he is nowadays considered as the father of the EPR spectroscopy for his experiments in manganese salts. Aqueous and non-aqueous samples have been irradiated by constant radio-frequency waves, while the magnetic field was swept. He demonstrated that the ratio between the irradiation frequency that corresponds to the maximum absorption coefficient and the magnetic field induction is constant and corresponds to the value predicted by the theory. Zavoisky gave its name to an important distinction in the EPR community, the Zavoisky prize,[24] and might even have observed NMR phenomenon before Bloch and Purcell in one of his unpublished works.[25] Zavoisky's experiment was the first continuous-wave electron spectrum to be acquired.

In 1958, a major breakthrough in EPR occured: Blume measured the first electron spin echo from a solution of sodium ammonia at -33.8 °C at 0.62 mT with a microwave irradiation at 17.4 MHz.[26] The same year, the first microwave electron spin echoes were reported in doped silicon.[27] These events gave birth to pulsed EPR spectroscopy. This technique is however quite demanding and the lack of available technology such as very high power microwave generators and fast digital electronics at that time discouraged many research groups. Since then, the technology has greatly evolved and EPR is widely used today to study properties of metals or radicals.[28]

NMR and EPR are very closely related techniques as they both rely on the same theory. But one main difference between them is the considered energy involved in all processes. The absolute value of the electronic gyromagnetic ratio is ca. 660 times larger than the proton one leading to a stronger response to magnetic stimulation and stronger interactions. The electron is consequently much more sensitive than

nuclei.[29,30] There is however one main drawback of EPR as electrons in many natural materials tend not to stay unpaired in external orbitals. Paramagnetic agents have thus to be artificially added either by covalent attachment to the target (spin label)[31–33] or by the addition of tracer molecules to the chemical system under study without any chemical linkage (spin probe).[34] Spin labelling in EPR spectroscopy is not limited by the size of the protein and gives access to interactions on time scales that are different to the NMR ones,[35–37] which makes NMR and EPR two complementary methods to study structural and dynamical properties of molecules.

Overview of different hyperpolarization methods that boost nuclear signals

Considering the low sensitivity of NMR, new approaches have been developed to boost the signal to noise ratio. A whole field of research is dedicated to find means to enhance the nuclear polarization beyond Boltzmann's predictions in thermal equilibrium. Such a particular spin state is called a hyperpolarized state. Many different approaches exist to achieve this specific nuclear spin configuration such as chemical reactions in specific systems or optical pumping that leads to hyperpolarized noble gases.

Hyperpolarization of nuclei by chemical reactions

Some efficient techniques using chemical reactions can efficiently increase the polarization of nuclei. The main advantage of these methods is their low cost and their rapidity. The most famous ones imply the use of a generator of para-dihydrogen (p-H_2). The production of para-hydrogen relies on the fact that the singlet (para) and triplet (ortho) states in H_2 systems are dynamically separated due to symmetry properties. This means that conversion from p-H_2 to ortho-H_2 (o-H_2) is symmetrycally forbidden to first order. Overpopulations of p-H_2 will therefore persist despite the fact that the population ratio between ortho- and para-states is 1:3 at equilibrium.

The non-magnetic singlet state is well protected from relaxation mechanisms as no direct transitions connect it to the ortho states and it does not interact with the external magnetic field. Its lifetime is on the order of hours whereas the spin-lattice relaxation of triplet states is on the order of seconds.[38–40] A flow of population from o-H_2 to p-H_2 can be triggered by breaking the magnetic symmetry of H_2 or by lowering the temperature of the system. The latter is a very efficient method which consists in slowly lowering the temperature of hydrogen gas over active charcoal down to a ca. 25 K, close to the boiling point of H_2 (20 K). Thus it allows for a p-H_2 enrichment between 93 % to 97 %.[41–44]

Parahydrogen-Induced Polarization (PHIP) The para-H_2 gas can be used to hyperpolarize unsaturated organic molecules by a hydrogenation reaction. This hyperpolarization method is called parahydrogen-induced polarization (PHIP). The transfer of p-H_2 polarization to a neighboring ^{13}C attached to an unsaturated molecule does require a catalyst. The latter assures the simultaneous fast exchange between the substrate and both hydrogens of p-H_2 without breaking their relative spin orientation. Polarization that has been created in p-H_2 is hence transferred to the carbon. This transfer of polarization depends on the coupling between the two H, relatively to the external magnetic field. In the case of a weak coupling (i.e., at high magnetic fields), the hydrogenation is called PASADENA (Parahydrogen and Synthesis Allow Dramatic Enhancement of Nuclear Alignment). In this case, the hydrogenation of the substrate occurs directly in the sample tube inside the spectrometer. The para-state of the dihydrogen is magnetically inert and does not interact with the $\vec{B}_0$ field nor create any field inhomogeneities or spurious signals. Another method consists in transferring the polarization at low field outside the spectrometer and then acquiring the NMR signal at high field. This is known as ALTADENA (Adiabatic Longitudinal Transport After Dissociation Engenders Nuclear Alignment). The PHIP techniques can lead to an increase the carbon hyperpolarization up to 4 orders of magnitude.

Signal Amplification by Reversible Exchange (SABRE) Unlike PHIP, SABRE[45] does not require an unsaturated molecule but it involves a metal complex catalyst,

which typically contains an iridium center.[46] Despite their great efficiency in the case of *in vitro* NMR or MRI experiments, these techniques are not suitable for *in vivo* cases because of the toxicity of the agents and the short lifetimes of hyperpolarized molecules due to their strong paramagnetic relaxation. However, some developments that tend to decrease the relaxation of substrate are in progress.[47] One successful approach, which is inspired by the Dynamic Nuclear Polarization (DNP), consists in the use of deuterated agents and substrates. This method aims at reducing the relaxation of the hyperpolarized substrate through dipolar interactions. 50% ^{1}H polarization with a lifetime of 100 s has been reached in the case of ^{2}H-labelled nicotinate with SABRE in 2017, which constitutes an encouraging result toward *in vivo* applications.

Hyperpolarization by spin-exchange optical pumping (SEOP)

A second way to hyperpolarize nuclei consists in transferring the polarization from polarized light to noble gases. This method exploits the quantum mechanical selection rule of angular momentum to increase the electron's polarization and therefore the interacting nuclei polarization by three to four orders of magnitude.[48] Irradiating vapor of alkali metals in a weak magnetic field with circularly polarized light results in the excitation of the electrons following the selection rule: $\Delta m_S = +1$ or $\Delta m_S = -1$ depending on the direction of the magnetic field compared to the direction of the polarization of the light. The interaction of the circularly polarized light with the electrons of a metal gas, which eventually leads to non-equilibrium distributions of the electronic spin populations, has first been observed by Kastler in 1949. This work earned him the Nobel Prize.[49,50] Nowadays, the technique has been developed to hyperpolarize noble gases through collision and or spin-exchange of gaseous alkali metal that has been excited by optical pumping.[51,52] Hence, enriched ^{3}He, ^{21}Ne, ^{83}Kr and ^{129}Xe can be hyperpolarized when they are in contact with optically pumped gaseous ^{97}Rb.

Xenon is the most widely used nucleus among the noble gases for optical pumping experiments because its good storability in comparison to other nobles gases, and en-

ables one to perform experiments both in liquid and gaseous phases. Moreover, ^{129}Xe is highly soluble in aqueous solvents and tissues[53,54] with a T_1, long enough to acquire hyperpolarized *in vivo* images of the thorax and heads of humans and rodents.[55] These particularities make it particularly efficient for diffusion experiments.[56] Chemical shift windows of ^{129}Xe are larger than 200 ppm when this nucleus is dissolved in different solvents. It therefore can give access to a lot of different dynamical and structural information by exchanging with surrounding molecules. Finally, its polarization can even be transferred to nearby protons by cross-relaxation.[57] Even with the previously mentioned advantages, Xenon is quite difficult to hyperpolarize compared to lighter noble gases. Hence, scientists working with Xenon that has a polarization of ca. 50% cannot perform real-time experiments. in comparison, ^{3}He can reach much higher polarization through optical pumping but, on the other hand, its thermodynamical properties are much more difficult to handle. That is why hyperpolarized helium is mainly used in hyperpolarized gas-phase magnetic resonance experiments. Note that ^{3}He has been combined with MRI for clinical applications where *in vivo* hyperpolarized ^{3}He images of lungs of humans and small animals have been acquired.[55]

Dynamic Nuclear Polarization (DNP)

DNP is a hyperpolarization method that allows an increasing of NMR signals. It consists in hyperpolarizing the nuclei using the magnetic properties of electrons and therefore, this technique combines NMR and EPR features. The saturation of a transition of unpaired electron spins carried by paramagnetic agents through microwave irradiation leads to a transfer of their polarization to neighboring hyperfine-coupled nuclei. This process can occur through four different mechanisms, depending on the experimental conditions.[58–63]

DNP is almost as old as NMR. Indeed, in 1953, Albert Overhauser predicted this phenomenon by theory.[64] His work has been at first strongly rejected by the scientific community. Its apparent transgression of thermodynamical laws strongly bothered physicists such as the famous Felix Bloch or Norman Ramsey. However, Thomas.

R. Carver and Charles P. Slichter validated this theory by testing it on metallic lithium and sodium.[65] They thus observed this phenomenon, which has been coined as the Overhauser Effect, on several nuclei: ^{7}Li, ^{23}Na and ^{1}H in liquid ammonia. After the experimental validation of this theory, Ramsay sent a letter of apology to Overhauser. The name "Dynamic Nuclear Polarization" was first introduced by Abragam to describe the phenomenon observed in diamagnetic insulators that are doped with paramagnetic species.[66,67] The observation of a DNP mechanism which is called solid effect has been done independently and simultaneously by Jeffries.[59] Nowadays, the term DNP concerns all mechanisms that enable to boost nuclear spin polarization using electrons and microwave irradiation.

Since its discovery in late 1950's, this method has greatly evolved to reach higher and higher nuclear polarizations by developing powerful setups to study systems at cryogenic temperatures or using gyrotrons to irradiate the electrons with more selective and powerful microwaves. In 1985, the combination of a gyrotron with the 'magic-angle'-spining (MAS) technique used in solid-state NMR enabled to hyperpolarize the ^{13}C in solid-state samples.[68] In this experiment, the hyperpolarization of highly concentrated proton nuclei has been transferred to carbon nuclei by cross-polarization (CP).

In 2003, another major development concerning the DNP method has been made. Ardenkjær-Larsen et al. working at Amersham Health Research and Development AB in Sweden developed a technique that enables to achieve strong hyperpolarized nuclear spins in solution: dissolution-DNP (D-DNP). In this apparatus, a solid sample is hyperpolarized at liquid helium temperatures and high magnetic fields (5 to 10 T). Once the nuclei are fully polarized, ca. 7 mL of hot pressurized water are injected into the solid sample to dissolve it. Then, the dissolved sample is transferred to an NMR spectrometer where the signal of the hyperpolarized nuclei can be detected at high field and room temperature. They tested this system on hyperpolarized ^{13}C in labeled Urea using 15-20 mM trityl radicals (Tris8-carboxyl-2,2,6,6-tetra[2-(1-hydroxyethyl)]-benzo(1,2-d:4,5-d)bis(1,3)dithiole-4-ylmethyl sodium salt). Thanks to this method, ^{13}C signals can be enhanced by up to four orders of magnitude. This discovery opened new perspectives for DNP such as the possibility to combine

it with MRI[69,70].

Nowadays, DNP is widely used in solid-state NMR (ssNMR)[71,72], liquid state NMR and MRI, to increase the polarization of nuclei of diverse chemical and biological systems. MAS-DNP (the combination of the MAS solid-state technique with the DNP) is particularly efficient to get information on polymers,[73,74] amyloid fibrils[75], membrane proteins[76,77] and surfaces.[72,78] D-DNP is particularly interesting to study real-time chemical reactions using small hyperpolarized molecules[79–81] or to get information on nuclei that have a low natural abundance in non-labeled samples.[82] Finally, clinical applications of the combination of MRI with D-DNP are in development. Indeed, until recently, MRI was mostly limited to proton signals due to its intrinsic low sensitivity. However, the enhancement of nuclear signals can permit observations of nuclei with low gyromagnetic ratio such as ^{13}C at physiological concentrations. This development allows MRI monitoring of reactions of small hyperpolarized metabolites in cells. Thus, the injection of hyperpolarized labeled 1-^{13}C-pyruvate into human bodies can help the preclinical diagnosis of cancer because cancer tissues demonstrate abnormally high enzymatic activity resulting in an increased rate of degradation of pyruvate into lactate. It has been shown that one can detect cancerous prostate tissues by DNP-enhanced MRI thanks to their higher concentration of lactate.[83,84]

EPR and DNP

The transfer of polarization from electrons to nuclei in DNP relies on a compromise between electronic and nuclear properties. It thus becomes important to investigate both the nuclear dynamics and the electronic characteristics of our samples in order to understand the hyperpolarization mechanisms. This opens new fields of research that focus on boosting the efficiency of this process by finding the right balance between paramagnetic species and nuclear properties of DNP samples.[85,86] In this regard, DNP is at the intersection of NMR and electron paramagnetic resonance (EPR). While some research groups actively work on investigating new polarizing agents whose electronic properties enable one to increase the efficiency of DNP,[87–93]

others decided to focus their attention on the electron spin irradiation and new facilities to get ever-higher enhancements of nuclear signals. Although most DNP experiments use a continuous microwave irradiation, observations prove that this does not generate the optimum final nuclear polarization. Modulations of the microwave field[94] or new set-ups composed of pulsed EPR spectrometers coupled to high field ssNMR spectrometers have been developed to boost experimental enhancements. These new facilities also help to obtain a better understanding of the complex theory that describes the transfer of polarization from electrons to nuclei.[95,96]

Structure of this thesis

This thesis describes my contributions to three different projects during my PhD at ENS Paris. Even though all of them gravitate around dissolution dynamic nuclear polarization (D-DNP), these projects cover different aspects of the technique. First, chapters 1 and 2 introduce the basis of D-DNP and gives an overview about this hyperpolarization method. A very brief description of the EPR experiments that have been used is also given. Chapters 3 and 4 concern the study at 4 K of the properties (dynamical and morphological) of the typical samples that are used in D-DNP. These studies use EPR to 1) give a better prediction of the nuclear polarization using existing models by considering electron dynamical properties and 2) understand how time-dependent morphological variations that occur in the samples can impact the ^{1}H polarization in DNP experiments. A second project that consists in studying non-linear dynamics of ^{1}H signals at temperature as low as 1.2 K is then developed in the chapter 5. Finally, the last chapter in this thesis shows an example of an application of D-DNP: kinetic information about the pre-nucleation process of calcium phosphate clusters could have been extracted.

Bibliography

[1] I. Rabi, J. Zacharias, S. Millman, and P. Kusch. A new method of measuring magnetic moment. *Phys. Rev.*, 53:353, 1938.

[2] I. I. Rabi. Space quantization in a gyrating magnetic field. *Phys. Rev.*, 51:652–654, Apr 1937.

[3] J. M. B. Kellog, I. I. Rabi, N. F. Jr Ramsey, and J. R. Zacharias. The magnetic moments of the proton and the deuteron, the radiofrequency spectrum of h_2 in various magnetic fields. *Phys. Rev.*, 56:728–743, oct 1939.

[4] M. E. Hayden, P.-J. Nacher, and Luca Saba. *Magnetic Resonance Imaging Handbook*.

[5] E. Purcell, H Torrey, and R. Pound. Resonance absorption by nuclear magnetic moments in a solid. *Phys. Rev.*, 69:37–38, 1946.

[6] F Bloch, W Hansen, and M Packard. Nuclear induction. *Phys. Rev.*, 69:127, 1946.

[7] F Bloch, W Hansen, and M Packard. The nuclear induction experiment. *Phys. Rev.*, 70:474–485, 1946.

[8] F. Bloch. Nuclear induction. *Phys. Rev.*, 70:460–474, Oct 1946.

[9] H. C. Torrey. Transient nutations in nuclear magnetic resonance. *Phys. Rev.*, 76:1059–1068, Oct 1949.

[10] E. L. Hahn. Nuclear induction due to free larmor precession. *Phys. Rev.*, 77:297–298, Jan 1950.

[11] J. T. Arnold, S. S. Dharmatti, and M. E. Packard. Chemical effects on nuclear induction signals from organic compounds. *J. Chem. Phys.*, 19:507, 1951.

[12] M. Saunders and J. G. Kirkwook. The nuclear magnetic resonance spectrum of ribonucleases. *J. Am. Chem. Soc.*, 79:3289–3290, 1957.

[13] J. Singer. Blood flow rates by nuclear magnetic resonance measurement. *Science*, 130:1652–1653, 1959.

[14] J. Jackson and W. Langhman. Whole body NMR spectrometer. *Rev. Sci. Instrum.*, 39:510–&.

[15] D. Marion. An introduction to biological NMR spectroscopy. *Molecular & Cellular Proteomics*, 12:3006–3025, 2013.

[16] R. Ernst and W Anderson. Application of fourier transform spectroscopy to magnetic resonance. *Rev. Sci. Instrum.*, 37:93, 1966.

[17] W. p. Aue, E. Bartholdi, and R. R. Ernst. Two-dimensional spectroscopy. application to nuclear magnetic resonance. *J. Chem. Phys.*, 64:2229–2246, 1976.

[18] A. R. Aricescu, W. Lu, and E. Y. Jones. A time- and cost-efficient system for high-level protein production in mammalian cells. *Acta Cryst. Sec. D*, 62(10):1243–1250, 2006.

[19] K. Inomata, A. Ohno, H. Tochio, S. Isogai, T. Tenno, I. Nakase, T. Takeuchi, S. Futaki, Y. Ito, H. Hiroaki, and M. Shirakawa. High-resolution milti-dimensional NMR spectroscopy of proteins in human cells. *Nature*, 458:106–105, 2009.

[20] E. Luchinat and L. anci. In-cell NMR: a topical review. *IUCr J.*, 4:108–118, 2017.

[21] F.-X. Theillet, A. Binolfi, B. Bekei, A. Martorana, H. M. Rose, M. Stuiver, S. Verzini, D. Lorenz, M. van Rossum, D. Goldfarb, and P. Selenko. Structural disorder of monomeric α-synuclein persists in mammalian cells. *Nature*, 530:45–50, 2016.

[22] E. Zavoisky. Paramagnetic absorption in

perpendicular and parallel fields for salts, solutions and metals., 1944.

[23] E. Zavoisky. Spin-magnetic resonance in paramagnetics. *Fizicheskiĭ Zhurnal*, 9:211–245, 1945.

[24] Kev Salikhov. Modern development of magnetic resonance (zavoisky 100). *App. Magn. Reson.*, 35(3):361–362, 2009.

[25] L. J. Bertliner. The evolution of biomedical EPR. *Biomed. Spectr. Imag.*, 5:5–26, 2016.

[26] R. J. Blume. Electron spin relaxation times in sodium-ammonia solutions. *Phys. Rev.*, 109:1867–1873, 1958.

[27] J. P. Gordon and K. D. Bowers. Microwave spin echoes from donor electrons in silicon. *Phys. Rev. Lett.*, 1:368–370, 1958.

[28] S. Kempe, H. Metz, and M˙ Application of electron paramagnetic resonance (EPR) spectroscopy and imaging in drug delivery research - chances and challenges. *Europ. J. Pharma. and Biopharma.*, 74(1):55 – 66, 2010.

[29] G. Jeschke. *Adv. ESR meth. pol. res.* Schlick S (ed), Wiley, 2006.

[30] D. Hinderberger and G. Jeschke. *Modern magnetic resonance.* Webb G.A., Springer, 2006.

[31] C. S. Klug and J. B. Feix. Methods and applications of site-directed spin labeling EPR spectroscopy. *Methods Cell. Biol.*, 84:617–658, 2008.

[32] C. Altenbach, S. L. Flitsch, H. G. Khorana, and W. L. Hubbell. Structural studies on transmembrane proteins. 2. spin labeling of bacteriorhodopsin mutants at unique cysteines. *Biochemistry*, 28(19):7806–7812, 1989.

[33] C. Altenbach, T. Marti, H. G. Khorana, and W. L. Hubbell. Transmembrane protein structure: spin labeling of bacteriorhodopsin mutants. *Science*, 248(4959):1088–1092, 1990.

[34] G. I. Likhtensheim, J. Yamauchi, S. Nakatsuki, A. I. Smirnov, and R. Tamura. *Nitroxides - applications in chemistry, biomedicine and materials science.* Wiley-VCH, Weinheim, 2008.

[35] Lorigan G. A. Sahu, I. D. Site-directed spin labeling EPR for studying membrane proteins. *Biomed. Res. Int.*, 2018:3248289, 2018.

[36] L. J. Berliner. From spin-labeled proteins to in vivo EPR applications. *Europ. Biophys. J.*, 39(4):579–588, 2010.

[37] E. J. Hustedt and A. H. Beth. Nitroxide spin-spin interactions: applications to protein structure and dynamics. *Ann. Rev. of Biophys.*, 28:129–153, 1999.

[38] C. R. Bowers and D. P. Weitekamp. Parahydrogen and synthesis allow dramatically enhanced nuclear alignment. *J. Am. Chem. Soc.*, 109:5541–5542, 1987.

[39] M. G. Pravica and D. P. Weitekamp. Net NMR alignment by adiabatic transport of parahydrogen addition products to high magnetic field. *Chem. Phys. Lett.*, 145:255–258, 1988.

[40] A. Trabesinger. Nuclear magnetic resonance: Long live the spin. *Nat. Phys.*, 8:781–782, 2012.

[41] B. Feng, A Coffey, R Colon, E.Y. Chekmenev, and K. Waddell. A pulsed injection parahydrogen generator and techniques for quantifying enrichment. *J. Magn. Res.*, 214:258–262, 2012.

[42] H. Gamliel, A.and Allouche-Arnon, R. Nalbandian, C. M. Barzilay, J. M. Gomori, and R. Katz-Brull. An apparatus for pro-

duction of isotopically and spin-enriched hydrogen for induced polarization studies. *Appl Magn Reson*, 39:329–345, 2010.

[43] D. Graafen, S. Rbert, O. Neudert, L. Buljubasich, M. B. Franzoni, J. F. Dechent, and K. Münnemann. *Annual Reports on NMR Spectroscopy*, volume 82. 2014.

[44] Jan-Bernd Hövener, Sébastien Bär, Jochen Leupold, Klaus Jenne, Dieter Leibfritz, Jürgen Hennig, Simon B. Duckett, and Dominik Elverfeldt. A continuous-flow, high-throughput, high-pressure parahydrogen converter for hyperpolarization in a clinical setting. *NMR in Biomedicine*, 26(2):124–131, 2013.

[45] R. W. Adams, J. A. Aguilar, K. D. Atkinson, M. J. Cowley, P. I. P. Elliott, S. B. Duckett, G. G. R. Green, I. G. Khazal, J. López-Serrano, and D. C. Williamson. Reversible interactions with para-hydrogen enhance NMR sensitivity by polarization transfer. *Science*, 323(5922):1708–1711, 2009.

[46] Ralph W. Adams, Simon B. Duckett, Richard A. Green, David C. Williamson, and Gary G. R. Green. A theoretical basis for spontaneous polarization transfer in non-hydrogenative parahydrogen-induced polarization. *J. Chem. Phys.*, 131(19):194505, 2009.

[47] Peter J. Rayner, Michael J. Burns, Alexandra M. Olaru, Philip Norcott, Marianna Fekete, Gary G. R. Green, Louise A. R. Highton, Ryan E. Mewis, and Simon B. Duckett. Delivering strong ^{1}H nuclear hyperpolarization levels and long magnetic lifetimes through signal amplification by reversible exchange. *Proceedings of the National Academy of Sciences*, 114(16):E3188–E3194, 2017.

[48] R. Bernheim. *Optical Pumping*. W. A. Benjamin, inc, The Pennsylvania State University, New York, 1965.

[49] J. Brossel and A. Kastler. La detection de la resonance magnetique des niveaux excites-leffect de depolarisation des radiations de resonance optique et de fluorescence. *Compt. Rend. Hebd. Sean. Acad. Scien.*, 229(23):1213–1215, 1949.

[50] A. Kastler. Optical methods of atomic orientation and of magnetic resonance. *J. Opt. Soc. Am*, 47(6):460–465, 1957.

[51] M. R. Bouchiat, T. R. Carver, and C. M. Varnum. Nuclear polarization in he3 gas induced by optical pumping and dipolar exchange. *Phys. rev. Lett.*, 5:373, 1960.

[52] B. C. Grover. Noble-gas NMR detection through noble-gas-rubidium hyperfine contact interaction. *Phys. Rev. Lett.*, 40:391, 1978.

[53] S. C. Cullen and E. G. Gross. The anesthetic properties of xenon in animals and human beings, with additional observations on krypton. *Science*, 113(2942):580–582, 1951.

[54] R. R. Kennedy, J. W. Stokes, and P. Downing. Anaesthesia and the 'inert' gases with special reference to xenon. *Anaesthesia and Intensive Care*, 20(1):66–70, 1992.

[55] M. S. Albert and D. Balamore. Development of hyperpolarized nocle gas MRI. *Nuc. Instr. Meth. Phys. Resear. A*, 402:441–453, 1998.

[56] R. W. Mair, M. S. Rosen, R. Wang, D. G. Cary, and R. L. Walsworth. Diffusion NMR methods applied to xenon gas for materials study. *Magn. Res. Chem.*, 40:S29–S39,

2002.

[57] B. M. Goodson. Nuclear magnetic resonance of laser polarized noble gases in molecules, materials, and organisms. *J. Magn. Res.*, 155:157–216, 2002.

[58] E. Ravera, C. Luchinat, and G. Parigi. Basic facts and perspectives of Overhauser DNP NMR. *J. Magn. Res.*, 264:78–87, 2016.

[59] C. D. Jeffries. Polarization of nuclei by resonance saturation in paramagnetic crystals. *Phys. Rev.*, 106:164–165, 1957.

[60] C. D. Jeffries. Dynamic orientation of nuclei by forbidden transitions in paramagnetic resonance. *Phys. Rev.*, 117:1056–1069, 1960.

[61] M. Abraham, R. W. Kedzie, and C. D. Jeffries. γ-ray anisotropy of co^{60} nuclei polarized by paramagnetic resonance saturation. *Phys. Rev.*, 106:165–166, Apr 1957.

[62] A. V. Kessenikh, V. I. Lushchikov, A. A. Manenkov, and Y. V. Taran. Proton polarization in irradiated polyethylenes. *Sov. Phys.-Sol. St. (Eng. Transl.)*, 5, 8 1963.

[63] A. Abragam and M. Borghini. *Chapter VIII Dynamic Polarization of Nuclear Targets*, volume 4 of *Progress in Low Temperature Physics*. Elsevier, 1964.

[64] A. W. Overhauser. Polarization of nuclei in metals. *Phys. Rev.*, 92:411 – 415, 1953.

[65] T. R. Carver and C. P. Slichter. Experimental verification of the overhauser nuclear polarization effect. *Phys. Rev.*, 102:975, 1956.

[66] A. Abragam and W. G. Proctor. A novel method of dynamic polarization of atomic nuclei in solids. *C. R. Acad. Sci.*, 246:2253–2256, 1958.

[67] A. Abragam and W. G. Proctor. Spin temperature. *Phys. Rev.*, 109:1441, 1958.

[68] R. A. Wind, M. J. Duijvestijn, C. van der Lugt, A. Manenschijn, and J. Vriend. *Prog. Nucl. Magn. Reson. Spectrosc.*, 55:285–295, 2009.

[69] F.A. Gallagher, M. I. Kettunen, and K. M. Brindle. Biomedical applications of hyperpolarized ^{13}C magnetic resonance imaging. *Prog. Nucl. Magn. Reson. Spectrosc.*, 55:285–295, 2009.

[70] J. G. Krummenacker, V. P. Denysenkov, M. Terekhov, L. Schreiber, and T. F. Prisner. DNP in MRI: An in-bore approach at 1.5 T. *J. of Magn. Res.*, 215:94–99, 2012.

[71] M. L. Mak-Jurkauskas and R. G. Griffin. High-frequency dynamic nuclear polarization. *John Wiley & Sons, Ltd*, 2010.

[72] A. Lesage, M. Lelli, D. Gajan, M. A. Caporini, V. Vitzthum, P. Miéville, J. Alauzun, A. Roussey, C. Thieuleux, A. Mehdi, G. Bodenhausen, C. Copéret, and L. Emsley. Surface enhanced NMR spectroscopy by dynamic nuclear polarization. *J. Am. Chem. Soc.*, 132:15459–15461, 2010.

[73] F. Blanc, S. Y. Chong, T. O. McDonald, D. J. Admas, S. Pawsey, M. A. Caporini, and A. I. Cooper. Dynamic nuclear polarization NMR spectroscopy allows high-throughput characterization of microporous organic polymers. *J. Am. Chem. Soc.*, 135:15290–15293, 2013.

[74] D. Le, G. Casano, T. N. Phan, F. Ziarelli, O. Ouari, F. Aussenax, P. Thureau, G. Mollica, D. Gigmes, P. Tordo, and S. Viel. Optimizing sample preparation methods for dynamic nuclear polarization solid-state NMR of synthetic polymers. *Macromolecules*, 47:3909–3916, 2014.

[75] G. T. Debelouchina, M. J. Bayro, A. W. Fitzpatrick, V. Ladizhansky, M. T. Colvin, M. A. Caporini, C. P. Jaroniec, V. S. Bajaj, M. Rosay, C. E. MacPhee, M. Vendruscolo, W. E. Maas, C. M. Dobson, and R. G. Griffin. Higher order amyloid fibril structure by MAS NMR and DNP spectroscopy. *J. Am. Chem. Soc.*, 135:19237–19247, 2013.

[76] B. J. Wylie, S. Dzikovski, Pawsey, M. Caporini, M. Rosay, J. H. Freed, and A. E. McDermott. Dynamic nuclear polarization of membrane proteins: covalently bound spin-labels at protein-protein interfaces. *J. Biomol. NMR*, 61:361–367, 2015.

[77] S. Y. Liao, M. Lee, T. Wang, I. V. Sergeyev, and M. Hong. Efficient DNP NMR of membrane proteins: sample preparation protocols, sensitivity, and radical location. *J. Biomol. NMR*, 64:223–237, 2016.

[78] F. A. Perras, T. Kobayashi, and M. Pruski. Natural abundance 17o dnp two-dimensional and surface-enhanced nmr spectroscopy. *J. Am. Chem. Soc.*, 137(26):8336–8339, 2015.

[79] Sadet A., Weber E. M. M., Jhajharia A., Kurzbach D., Bodenhausen G., Miclet E., and Abergel D. Rates of chemical reactions embedded in a metabolic network by dissolution dynamic nuclear polarisation NMR. *Chem. – Europ. J.*, 24(21):5456–5461, 2017.

[80] D. Kurzbach, E. Canet, A. G. Flamm, A. Jhajharia, E. M. M. Weber, R. Konrat, and G. Bodenhausen. Investigation of intrinsically disordered proteins through exchange with hyperpolarized water. *Ang. Chem. Inter. Ed.*, 56(1):389–392, 2017.

[81] Q. Chappuis, J. Milani, B. Vuichoud, A. Bornet, A. D. Gossert, G. Bodenhausen, and S. Jannin. Hyperpolarized water to study protein–ligand interactions. *J. Phys. Chem. Lett.*, 6(9):1674–1678, 2015.

[82] J.-N. Dumez, J. Milani, B. Vuichoud, A. Bornet, J. Lalande-Martin, I. Tea, M. Yon, M. Maucourt, C. Deborde, A. Moing, L. Frydman, G. Bodenhausen, S. Jannin, and P. Giraudeau. Hyperpolarized nmr of plant and cancer cell extracts at natural abundance. *Analyst*, 140:5860–5863, 2015.

[83] H. Gutte, A. E. Hansen, H. H. Johannesen, A. E. Clemmensen, J. H. Ardenkjæ-Larsen, C. H. Nielsen, and A. Kjær. The use of dynamic nuclear polarization ^{13}C-pyruvate MRS in cancer. *Am J Nucl Med Mol Imaging*, 5:548–560, 2015.

[84] S. J. Nelson, D. Vigneron, J. Kurhanewicz, A. Chen, R. Bok, and R. Hurd. DNP-hyperpolarized ^{13}C magnetic resonance metabolic imaging for cancer applications. *Appl. Magn. Reson.*, 34:533–544, 2008.

[85] J.H. Ardenkjær-Larsen, I. Laursen, I. Leunbach, G. Ehnholm, L.-G. Wistrand, J. S. Petersson, and K. Golman. EPR and DNP properties of certain novel single electron contrast agents intended for oximetric imaging. *J. Magn. Reson.*, 133(1):1 – 12, 1998.

[86] C. Ysacco, E. Rizzato, M.-A. Virolleaud, H. Karoui, A. Rockenbauer, F. Le Moigne, D. Siri, O. Ouari, R. G. Griffin, and P. Tordo. Properties of dinitroxides for use in dynamic nuclear polarization (DNP). *Phys. Chem. Chem. Phys.*, 12:5841–5845, 2010.

[87] D. Banerjee, J. C. Paniagua, V. Mugnaini, J. Veciana, A. Feintuch, M. Pons, and D. Goldfarb. Correlation of the EPR properties of perchlorotriphenylmethyl rad-

icals and their efficiency as DNP polarizers. *Phys. Chem. Chem. Phys.*, 13:18626–18637, 2011.

[88] B. Corzilius, A. A. Smith, A. B. Barnes, C. Luchinat, I. Bertini, and R. G. Griffin. High-field dynamic nuclear polarization with high-spin transition metal ions. *J. Am. Chem. Soc.*, 133:5648–5651, 2011.

[89] B. Corzilius. Theory of solid effect and cross effect dynamic nuclear polarization with half-integer high-spin metal polarizing agents in rotating solids. *Phys. Chem. Chem. Phys.*, 18:27190–27204, 2016.

[90] C. Song, K.-N. Hu, C.-J. Joo, T.M. Swager, and R. G. Griffin. TOTAPOL: A biradical polarizing agent for dynamic nuclear polarization experiments in aqueous media. *J. Am. Chem. Soc.*, 128:11385–11390, 2006.

[91] O. Haze, B. Corzilius, A. A. Smith, R. G. Griffin, and T. M. Swager. Water-soluble narrow-line radicals for dynamic nuclear polarization. *J. Am. Chem. Soc.*, 134:14287–14290, 2012.

[92] D. Kubichi, G. Casano, M. Schwarzwälder, S. Abel, C. Sauvée, G. Ganesan, M. Yulikov, A. Rossini, G. Jeschke, and C. et al. Copéret. Rational design of dinitroxide biradicals for efficient cross-effect dynamic nuclear polarization. *Phys. Rev. Lett.*, 7:550–558, 2016.

[93] S. Macholl, H. Johannesson, and J. H. Ardenkjær-Larsen. Trityl biradicals and ^{13}C dynamic nuclear polarization. *Phys. Chem. Chem. Phys.*, 12:5804–5817, 2010.

[94] A. Bornet, A. Pinon, Aditya Jhajharia, M. Baudin, X. Ji, L. Emsley, G. Bodenhausen, J. H. Ardenkjær-Larsen, and S. Jannin. Microwave-gated dynamic nuclear polarization. *Phys. Chem. Chem. Phys.*, 18:30530–30535, 2016.

[95] A. Feintuch, D. Shimon, Y. Hovav, D. Banerjee, I. Kaminker, Y. Lipkin, K. Zibzener, B. Epel, S. Vega, and D. Goldfarb. A dynamic nuclear polarization spectrometer at 95GHz/144MHz with EPR and NMR excitation and detection capabilities. *J. Magn. Reson.*, 209(2):136 – 141, 2011.

[96] I. Kaminker and S. Han. Amplification of dynamic nuclear polarization at 200 GHz by arbitrary pulse shaping of the electron spin saturation. *J. Phys. Chem. Lett.*, 2018.

Chapter 1

Dynamic Nuclear Polarization: a combination of NMR and EPR enabling the hyperpolarization of nuclei

1.1 Basic theory of magnetic resonance techniques

1.1.1 The spin

In physics, particles such as protons, electrons or neutrons are assemblies of quarks, which entail intrinsic properties such as their mass and their electric charges leading to the spin. These characteristics enable one to predict many physical properties and interactions, even chemical reactions in many cases, since the mass, the charge or the spin are important properties. The spin[1] is commonly used in the context of quantum mechanical description of particle systems[2], and enable to describe and predict a system's magnetic properties. Mathematically, we describe the spin as an angular momentum operator ($\hat{\mathbf{S}}$) , which can be conveniently described as a vector as it gives rise to three spatial components $\hat{S}_x$, $\hat{S}_y$ and $\hat{S}_z$. The spin angular momentum

is directly related to the magnetic moment $\hat{\mu}$ of a particle:

$$\hat{\mu} = g\frac{q}{2m}\hat{\mathbf{S}} = \gamma\hat{\mathbf{S}} \tag{1.1}$$

In equation 1.1, q and m respectively represent the particle charge and mass and g is a dimensionless coefficient called Landé factor or g-factor. It adopts respectively the values of -2.0023, 5.586 and -3.826 for the free electron, free proton and free neutron. It is important to mention that even though the neutron does not bear any electric charge, its quarks provide nonetheless a non-zero magnetic moment. The eigenvalues of an operator determine the system's possible states. For nuclei or electrons in a quantum state $|\psi\rangle$, only two spin states are possible in each of the three spatial directions of the frame:

$$\hat{S}_i |\psi\rangle = \pm\frac{\hbar}{2} |\psi\rangle \tag{1.2}$$

with i corresponding to x,y or z. More generally, for a system associated with a quantum state $|\psi_m\rangle$ with m an eigenvalue of its spin angular momentum operator the following holds:

$$\hat{S}_i |\psi_m\rangle = \hbar m |\psi_m\rangle \tag{1.3}$$

In this thesis, we will refer to the maximum of m to characterize the total spin $\mathbf{I}$ of any particle. The simplest case is that of a spin $\frac{1}{2}$ particle such as electrons, protons and neutrons, for which m can adopt values $+\frac{1}{2}$ and $-\frac{1}{2}$. As the gyromagnetic ratio γ determines the strength of the magnetic moment of a particle, even though each isolated electron or nucleons have the same spin, the observable associated to their spin angular momentum operator (or their magnetic moments) can be different because (see equation 1.1).

One can also associate a spin to an ensemble of nuclei. By convention, the total spin angular momentum of nuclei is introduced by the operato rÎ which is composed of three spatial operators $\hat{I}_x$, $\hat{I}_y$ and $\hat{I}_z$. The number of protons and neutrons in the nucleus will thus directly characterize its spin. Hence, when the number of protons and neutrons are even the total nucleus spin number is zero as in the case of the ^{12}C or the ^{16}O. Nuclei with odd mass number have a half integer spin number. Thus,

^{1}H, ^{13}C and ^{31}P have a spin $\frac{1}{2}$ whereas ^{7}Li has I= $\frac{3}{2}$ and ^{17}Al has I=$\frac{5}{2}$. Finally, when nuclei have even number of nucleons and odd number of protons, their spin number necessarily belong to the integers. ^{2}H, ^{6}Li and ^{14}N verify I= 1.

1.1.2 The Zeeman interaction

Interactions of nuclei with their surrounding (magnetic field, other atomes etc.) are the keys to information about a system. They enable us to differentiate between different nuclei, allow access to nuclear dynamics on different time scale (depending on their magnitude) or help to describe the structure of molecules. In a more fundamental way, we could not detect any NMR or EPR signal in the absence of any interaction.

The Zeeman interaction is the strongest of the interactions typically encountered in magnetic resonance.[3,4] It corresponds to the interaction between the spin angular momentum and an applied external magnetic field. In a quantum mechanical description, establishing the Hamiltonian operator $\hat{\mathrm{H}}$ for a system enables to determine the different energy levels a spin can adopt. Indeed, the eigenvalues of $\hat{\mathrm{H}}$ are the energy levels of the system in the chosen basis. Equation 1.4, which corresponds to the mathematical expression of this theory, is the quantum mechanical Schrödinger equation where the Hamiltonian is time independent. $|\psi_n\rangle$ and E_n are respectively the eigenvectors and eigenvalues (or energy levels) of $\hat{\mathrm{H}}$.

$$\hat{\mathrm{H}}\,|\psi_n\rangle = E_n\,|\psi_n\rangle \tag{1.4}$$

When a nucleus that possesses a spin angular momentum operator $\hat{\mathbf{I}}$ is placed in a static magnetic field $\vec{B_0}$ with a frequency depending on the fundamental properties of the nucleus it will precess around $\vec{B_0}$. This is denoted the Larmor precession and the corresponding frequency is the ω_0. By convention, the Cartesian frame $(\vec{x}, \vec{y}, \vec{z})$ - also called laboratory frame - is chosen in order to align $\vec{B_0}$ to the $\vec{z}$ axis: $\vec{B_0} = B_0\vec{z}$. The energy of interaction of the spin with the static external magnetic field can be described by the free precession operator $\hat{H_0}$ which is also a time independent

Hamiltonian.

$$\hat{H}_0 = -\gamma B_0 \hat{I}_z = -\omega_0 \hat{I}_z \tag{1.5}$$

where γ is the gyromagnetic ratio and B_0 corresponds to the norm $|\vec{B_0}|$. For spin $\frac{1}{2}$, $\hat{I}_z$ only possess two distinct eigenvalues: $\frac{\hbar}{2}$ and $-\frac{\hbar}{2}$.Hence, the energy of the system will differ by $\frac{\omega_0}{2\pi}$ if spins are parallel or anti parallel to $\vec{B_0}$. This effect which causes a splitting of energy levels is called the Zeeman interaction.

$$\hat{H}_0 \left|\psi_{1/2}\right\rangle = -\omega_0 \frac{\hbar}{2} \left|\psi_{1/2}\right\rangle \qquad \text{and} \qquad \hat{H}_0 \left|\psi_{-1/2}\right\rangle = +\omega_0 \frac{\hbar}{2} \left|\psi_{-1/2}\right\rangle \tag{1.6}$$

Hence, the difference of energy between the two spin states ΔE depends on the Larmor precession frequency $\omega_0 = \gamma B_0$.

$$\Delta E = E_\beta - E_\alpha = \omega_0 \hbar = h\nu \tag{1.7}$$

with h, the Planck constant, $\nu = \frac{\omega_0}{2\pi}$, E_α and E_β, the energy of spin state α and β. In the case of a $\frac{1}{2}$ spin system, the lower energy level is called α whereas the upper one is associated to β. This lifting of degeneration is the key phenomenon that enables a nuclear signal to be acquired by exciting the transition of a spin between both its states .

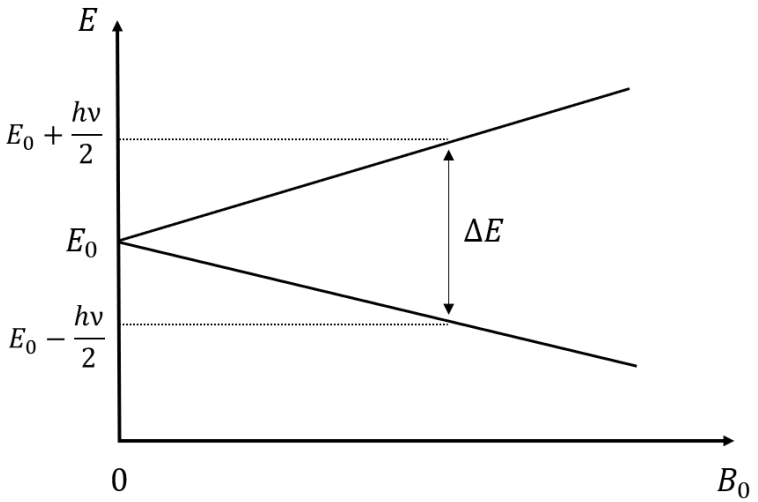

Figure 1.1: Perturbation of $\frac{1}{2}$ spin energy level at zero field E_0 due to the Zeeman interaction between the magnetic moment and an external static magnetic field $\vec{B_0}$.

1.1.3 The dipolar interaction

As explained in the beginning of this thesis, spins are intrinsically linked to magnetic moments through equation 1.1. Hence, each nucleus acts as a magnetic dipole that generates a magnetic field. Naturally, the magnetic field produced by one spin will interact with the field of another neighbouring one and vice versa. This perturbation is called 'dipolar coupling'. The strength of this interaction has a magnitude on the order of one to hundreds of kHz.

We can establish the dipolar Hamiltonian $\hat{H}_{DD}$ of two interacting spins:

$$\hat{H}_{DD} = -\frac{\mu_0 \gamma_1 \gamma_2}{4\pi} \left[\frac{\hat{\mathbf{I}}_1 \cdot \hat{\mathbf{I}}_2}{r^3} - \frac{3(\hat{\mathbf{I}}_1 \cdot \vec{r})(\hat{\mathbf{I}}_2 \cdot \vec{r})}{r^5} \right] \tag{1.8}$$

where γ_1 and γ_2 are respectively the gyromagnetic ratios associated to the spins $\hat{\mathbf{I}}_1$ and $\hat{\mathbf{I}}_2$ and $\vec{r}$ is the vector that connects spin 1 to spin 2 (see Fig. 1.2). Commonly, we use $\hat{H}_{DD}$ expressed in polar coordinates:[5,6] $\vec{r} = (r\sin\theta\cos\phi,\, r\sin\theta\sin\phi,\, r\cos\phi)$

$$\begin{aligned}
\hat{H}_{DD} &= -\frac{\mu_0 \gamma_1 \gamma_2}{4\pi r^3} (A + B + C + D + E + F) \qquad (1.9)\\
A &= \hat{I}_{1z}\hat{I}_{2z}(3\cos^2\theta - 1)\\
B &= -\frac{1}{4}\left(\hat{I}_{1+}\hat{I}_{2-} + \hat{I}_{1-}\hat{I}_{2+}\right)(3\cos^2\theta - 1)\\
C &= -\frac{3}{2}\left(\hat{I}_{1z} + \hat{I}_{2+} + \hat{I}_{1+}\hat{I}_{2z}\right)\sin\theta\cos\theta e^{-i\phi}\\
D &= -\frac{3}{2}\left(\hat{I}_{1z} + \hat{I}_{2-} + \hat{I}_{1-}\hat{I}_{2z}\right)\sin\theta\cos\theta e^{+2i\phi}\\
E &= -\frac{3}{4}\left(\hat{I}_{1+}\hat{I}_{2+}\right)\sin^2\theta e^{-2i\phi}\\
F &= -\frac{3}{4}\left(\hat{I}_{1-}\hat{I}_{2-}\right)\sin^2\theta e^{+2i\phi}
\end{aligned}$$

In the equation 1.9, A is the only term that is static. It defines the splitting of each of the Zeeman energy levels, giving rise to four spin states in the case of two interacting spins $\frac{1}{2}$: $|\alpha\alpha\rangle$, $|\alpha\beta\rangle$, $|\beta\alpha\rangle$ and $|\beta\beta\rangle$ (see Fig. 1.3). The energy that separates each of the dipolar energy levels is given by A. All the other terms are off-diagonal elements of the dipolar matrix $\hat{H}_{DD}$. The ladder operators (see section A.11) describe a dynamical phenomenon. Thus, they correspond to transition probability from one state to another. B is the probability for a zero-quantum transition (or 'flip-flop'

transition), which is a simultaneous 'flip' of one spin ($|\alpha\rangle \rightarrow |\beta\rangle$) and a 'flop' ($|\beta\rangle \rightarrow |\alpha\rangle$) of the other one ($|\alpha\beta\rangle \leftrightarrow |\beta\alpha\rangle$). This process is crucial in magnetic resonance as it describes the complete transmission of information from one spin to another through space without any gain or loss of energy of the total homonuclear system. This diffusion can occur between spins (homo- or heteronuclear) if:

$$A \leq B \tag{1.10}$$

C and D are one-quanta transitions (such as $|\alpha\alpha\rangle \leftrightarrow |\beta\alpha\rangle$) and finally E and F are associated to double-quanta transitions, in other words, the probability for both spins to 'flip' (or flop') simultaneously ($|\alpha\alpha\rangle \leftrightarrow |\beta\beta\rangle$).

The energy E generated by two dipoles in interaction depends thus on two parameters: the distance between the two nuclei and the angle between the internuclear vector $\vec{r}$ and the external magnetic field θ (Eqn. 1.11).

$$E = -\frac{\mu_0}{4\pi}\left[\frac{\vec{\mu_1}\cdot\vec{\mu_2}}{r^3} - \frac{(\vec{\mu_1}\cdot\vec{r})(\vec{\mu_2}\cdot\vec{r})}{r^5}\right] \tag{1.11}$$

where μ_0 is the vacuum permeability constant. As $\vec{\mu_1}$ and $\vec{\mu_2}$ are parallel, we can simplify the equation 1.11 into equation 1.12.

$$E = -\frac{\mu_0}{4\pi}\frac{\vec{\mu_1}\cdot\vec{\mu_2}}{r^3}(1 - 3\cos^2\theta) \tag{1.12}$$

The magnetic dipolar coupling gives plenty of information on a spin system. First of all, it is a through space interaction enabling to have a direct quantification of the internuclear distances. Then, the coupling between two magnetic moments depends on the orientation of their internuclear segment relative to $\vec{B_0}$ which makes the angle accessible. Knowing the angle and the distance between the two dipoles, we can deduce the spatial position of the nuclei, a precious information for the determination of the structure of molecules.

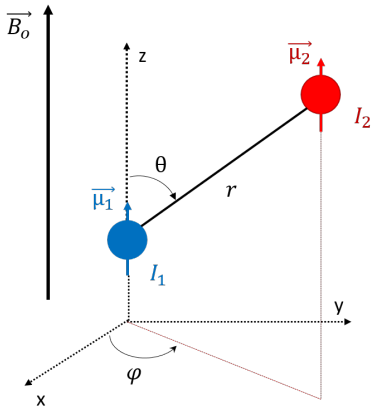

Figure 1.2: Schematic representation of a coupling between two magnetic dipoles in a static magnetic field. The interacting magnetic moments $\vec{\mu_1}$ and $\vec{\mu_2}$ respectively corresponding to $\mathbf{I}_1$ and $\mathbf{I}_2$ spins and separated by a distance r are represented by colored arrows. θ corresponds to the angle between the internuclear segment and $\vec{B_0}$ and ϕ to the angle between the projection of r onto the $(\vec{x}, \vec{y})$ plane.

1.1.4 The chemical shift

Even if the external field is homogeneous for a sample, the electronic cloud surrounding each atom will locally perturb the magnetic field. Thus, nuclei experience an effective magnetic field $\vec{B_{eff}}$ that has been shielded by the neighboring electrons.[7]

$$\vec{B_{eff}} = \vec{B_0}(1 - \sigma) \tag{1.13}$$

with σ, the second-rank shielding tensor (Eqn. 1.14) and 1, the unit matrix.

$$\sigma = \begin{pmatrix} \sigma_{XX} & \sigma_{XY} & \sigma_{XZ} \\ \sigma_{YX} & \sigma_{YY} & \sigma_{YZ} \\ \sigma_{ZX} & \sigma_{ZY} & \sigma_{ZZ} \end{pmatrix} \tag{1.14}$$

This shielding of the static magnetic field influences the nucleus resonance frequency and gives information about the spin environment. To extract these informations and get rid of the tremendous static field contribution, NMR spectroscopists usually compare the shift of resonance frequency relatively to the frequency of nucleus of reference ω_{ref}. They thus consider the isotropic chemical shift δ_{iso} as:

$$\delta_{iso} = \frac{\omega_{ref} - \omega}{\omega_{ref}} \tag{1.15}$$

δ_{iso} is a particularly convenient parameter in NMR as field strength contribution is canceled. This makes the variation of frequency comparable for all the experiments whatever the value of the spectrometer field.

In liquid state, fast rotation of molecules averages out the different elements of the chemical shift tensor to δ_{iso} as they are much faster than the acquisition time. We then only observe the superposition of all possible orientations of molecules relatively to the external magnetic field.[8] The δ_{iso} can be directly measured on the spectra by monitoring the peak position in the spectral window. In solid state, molecular motions are much more limited. Tumbling is not possible, the different components of the shielding are not averaged out any more during the acquisition.

In a powder, all orientations of crystallites are possible. As shielding depends on the geometry of the electron cloud (relatively to the magnetic field), each crystallite possesses its own shielding and thus, its own resonance frequency. This phenomenon leads to strong inhomogeneous broadening of spectra that are typically known as "powder spectra".

According to the quantum mechanical theory, there is a basis (1,2,3) in which the chemical shift tensor matrix (σ) is diagonal. This frame is commonly called the Principal Axis System (PAS).

$$\sigma = \begin{pmatrix} \sigma_{XX} & \sigma_{XY} & \sigma_{XZ} \\ \sigma_{YX} & \sigma_{YY} & \sigma_{YZ} \\ \sigma_{ZX} & \sigma_{ZY} & \sigma_{ZZ} \end{pmatrix} \rightarrow \delta = \begin{pmatrix} \delta_{11} & 0 & 0 \\ 0 & \delta_{22} & 0 \\ 0 & 0 & \delta_{33} \end{pmatrix} \tag{1.16}$$

In this frame, δ_{iso} is defined as:

$$\delta_{iso} = \frac{\delta_{11} + \delta_{22} + \delta_{33}}{3} \tag{1.17}$$

In the case of a perfectly spherical electronic environment of the nucleus, $\delta_{11} = \delta_{22} = \delta_{33} = \delta_{iso}$. On the contrary, when this equality is not respected, the nucleus shielding depends on its orientation relatively to the magnetic field. This phenomenon is called chemical shift anisotropy (CSA). The anisotropy of the chemical shift ($\Delta\sigma$)

is quantified by:[9]

$$\Delta\sigma = |\delta_{33} - \delta_{iso}| \tag{1.18}$$

provided that $|\delta_{33} - \delta_{iso}| > |\delta_{22} - \delta_{iso}| \geq |\delta_{11} - \delta_{iso}|$. All usual nuclei that are used as NMR probes such as ^{13}C, ^{15}N or ^{17}O can be affected by CSA[7,10,11]. Its contribution is particularly important in the case of ^{31}P as it constitutes the main source of relaxation at high field.[12–14]

1.1.5 The Boltzmann theory and polarization

Population and Boltzmann factor

The NMR signal intensity strongly depends on the energy level difference ΔE. The larger the Zeeman splitting (see 1.1.2) , the higher the difference of population at the equilibrium between the low energy state N_α^0 and the high energy one N_β^0. We can determine the populations N_α and N_β for each energy level using the partition function $Z(T)$ for a spin $\frac{1}{2}$ system:

$$Z(T) = \sum_j g_i \exp\left(-\frac{E_j}{k_B T}\right) = \exp\left(-\frac{E_\alpha}{k_B T}\right) + \exp\left(-\frac{E_\beta}{k_B T}\right) \tag{1.19}$$

In equation 1.19, g_j represents the degeneracy of energy level E_j, T is the thermodynamic "spin" temperature and k_B, the Boltzmann constant. The probability to find a spin in one of the two Zeeman states depend on the ratio between the energy of the state and $k_B T$, the thermal energy. We define the probabilities p_α and p_β, which are the probabilities for a spin to be in the α or in the β state as:

$$p_\alpha = \frac{\exp\left(-\frac{E_\alpha}{k_B T}\right)}{Z(T)} \; ; \; p_\beta = \frac{\exp\left(-\frac{E_\beta}{k_B T}\right)}{Z(T)} \tag{1.20}$$

N_α^0 and N_β^0 can be obtained by multiplying the total number of spins N by the probability to be on the different states (Eqn. 1.21).

$$N_\alpha^0 = N \cdot p_\alpha = \frac{N \exp\left(-\frac{E_\alpha}{k_B T}\right)}{Z(T)} \; ; \; N_\beta^0 = N \cdot p_\beta = \frac{N \exp\left(-\frac{E_\beta}{k_B T}\right)}{Z(T)} \tag{1.21}$$

Finally, the relative population of the two energy levels can be expressed by the equation 1.22. It corresponds to a thermodynamical description of the system and resembles a Boltzmann-type distribution.

$$\frac{N_\alpha^0}{N_\beta^0} = \exp\left(-\frac{\Delta E}{k_B T}\right) \tag{1.22}$$

The population difference in a two spin states system depends on the ratio of ΔE to the thermal energy. Hence, the lower is the temperature, the more difficult it is for the nuclei to cross the energetic barrier and thus, the higher is the difference of population between the states α and β.

Spin polarization

The polarization of one spin S, $P_s = (P_x^s, P_y^s, P_z^s)$ quantifies the alignment of the spin angular momentum operator $\hat{S}$ of this spin with a given direction in the chosen frame ($\vec{x}$, $\vec{y}$, $\vec{z}$).

$$P_s = \frac{1}{|\mu_s|}\frac{Tr\left(\rho\mu_s\right)}{Tr\left(\rho\right)} = \frac{\gamma}{|\gamma S_z|}\frac{Tr\left(\rho S_z\right)}{Tr\left(\rho\right)} \tag{1.23}$$

$$\rho = \sum_i p_i \left|\psi_i\right\rangle \left\langle\psi_i\right| \tag{1.24}$$

In the equations 1.23 and 1.24, ρ corresponds to the density matrix of the system, μ_s to the magnetic moment of spin S, p_i to the probability associated to the states described by the hamiltonian of the system ψ_i. Thus, by employing equation 1.24, we can easily determine the density matrix of an isolated spin (electron or nucleus) at thermal equilibrium that experiences a $\vec{B_0}$ field. For the sake of simplicity and to illustrate the advantages of the notion of polarization, we will first focus our study on electrons and then extends it to nuclei. Electrons being in accordance with the Boltzmann theory, the probabilities p_α and p_β for the spins to populate each state α and β are expressed as:

$$p_\alpha = \frac{\exp\left(\frac{1}{2}\frac{\hbar\omega_s}{k_B T_s}\right)}{Z} \quad \text{and} \quad p_\beta = \frac{\exp\left(-\frac{1}{2}\frac{\hbar\omega_s}{k_B T_s}\right)}{Z} \tag{1.25}$$

$$Z = \exp\left(\frac{1}{2}\frac{\hbar\omega_s}{k_B T_s}\right) + \exp\left(-\frac{1}{2}\frac{\hbar\omega_s}{k_B T_s}\right) \tag{1.26}$$

k_B is defined as the Boltzmann constant, T_s represents the thermodynamical temperature associated to the electrons, ω_s corresponds to the Larmor frequency of the electron and finally, Z is the partition function. For the following equations, we will use the scalar β_s instead of the factor $\frac{1}{k_B T_s}$. The system being at equilibrium, we can consider that the off-diagonal terms of the density operator are 0. Hence, the density operator of the electron ρ is represented by a diagonal 2-by-2 matrix (cf Eqn. 1.27).

$$\rho = \begin{pmatrix} \rho_+ & \rho_\perp \\ \rho_\perp * & \rho_- \end{pmatrix} = \begin{pmatrix} \exp\left(\frac{1}{2}\beta_s \hbar \omega_s\right) & 0 \\ 0 & \exp\left(-\frac{1}{2}\beta_s \hbar \omega_s\right) \end{pmatrix} \tag{1.27}$$

With ρ and S_z at hand, we are able to calculate the expectation value of S_z in equilibrium state: $\langle\psi| S_z |\psi\rangle$.

$$\begin{aligned} \langle\psi| S_z |\psi\rangle =< S_z > &= \frac{Tr\left(\rho S_z\right)}{Tr\left(\rho\right)} \\ &= -\frac{1}{2}\frac{\exp\left(+\frac{1}{2}\beta_s \hbar \omega_s\right) - \exp\left(-\frac{1}{2}\beta_s \hbar \omega_s\right)}{\exp\left(+\frac{1}{2}\beta_s \hbar \omega_s\right) + \exp\left(+\frac{1}{2}\beta_s \hbar \omega_s\right)} \\ &= -\frac{1}{2}\tanh\left(\frac{1}{2}\beta_s \hbar \omega_s\right) \end{aligned} \tag{1.28}$$

Thus, we can deduce the polarization of the electrons by combining the equations 1.23 and 1.28:

$$P_s = \tanh\left(\frac{1}{2}\beta_s \hbar \omega_s\right) \tag{1.29}$$

The determination of the polarization P_I of an ensemble of nuclear spins $\mathbf{I} = \frac{1}{2}$ is then straightforward. Indeed, the convention used for the polarization that has been defined in the equation 1.23 drops the sign of the gyromagnetic ratio. Hence, the nuclear polarization has the same form as the electronic one even if the ground and the excited states, defined by the magnetic quantum number m, are inverted (see chapter 1.1.1).

$$P_I = \tanh\left(\frac{1}{2}\beta_I \hbar \omega_I\right) \tag{1.30}$$

In equation 1.30, we have introduced $\beta_I = \frac{1}{k_B T_I}$ with T_I, the nuclei temperature and ω_I, the Larmor frequency of nuclei. Hence, the polarization can only adopt values between -1 and +1. It depends on the gyromagnetic ratio of the spin, the applied

magnetic field $\vec{B_0}$ and the temperature as predicted by the Boltzmann's theory. Vanishing polarization means that the spins equally populate the energy levels: no signal can be detected. The transition that connects the two-equally populated energy levels "saturated". A negative (resp. positive) polarization requires that the upper (resp. lower) energy levels are overpopulated.

1.1.6 The relaxation

The mechanisms of relaxation

Relaxation is a non-radiative phenomenon caused by a time dependent modulation of local a magnetic field experienced by the nucleus. This modulation is induced by molecular motions on the nanosecond timescale, or vibrations that have a contribution in the picosecond time scale. In the liquid state, we thus find a fluctuating local magnetic field $B_{loc}(t)$ experienced by the spins. When the environment of a spin is the same in all x, y and z directions, the strength of interactions do not depend on spatial orientation: they are said to be isotropic. On the contrary, if the local environment changes with respect to a system orientation, the resulting interactions are anisotropic. Their terms in the different directions are not equivalent, which generates variations in the local magnetic field around the spin. Motions tend then to locally change the spin environment and modulate the strength of these interactions causing time dependent local variations of $B_{loc}(t)$ that spins experience.

Spin-lattice relaxation

Spin-lattice relaxation, also called "longitudinal relaxation" is associated to energy dissipation from the spin system to the surrounding or "the lattice". This relaxation process only concerns the projection of the magnetization onto the z axis: $\vec{M}_z$. Through spin-lattice relaxation, an excited spin system is driven back to its thermal equilibrium magnetization $\vec{M}_0$ as described by the Boltzmann theory. We can model the relaxation process in the case of a single spin-$\frac{1}{2}$ system with two energy states: $|\alpha\rangle$ and $|\beta\rangle$. The variation of the populations N_α and N_β can be expressed by

introducing the transition probability W (see Eqn. 1.31 and 1.32) describing a flow of population from the $|\alpha\rangle$ state to the $|\beta\rangle$ state WN_β or vice versa WN_α.

$$\frac{dN_\alpha}{dt} = W\left(N_\beta - N_\beta^0\right) - W\left(N_\alpha - N_\alpha^0\right) \tag{1.31}$$

$$\frac{dN_\beta}{dt} = W\left(N_\alpha - N_\alpha^0\right) - W\left(N_\beta - N_\beta^0\right) \tag{1.32}$$

In equations 1.31 and 1.32, we consider the deviations of populations of $|\alpha\rangle$ and $|\beta\rangle$ from their respective thermal equilibrium values: N_α^0 and N_β^0. As the magnitude of the operator operator $\hat{I}_z(t) = I_z$ is proportional to the difference of population $N_\alpha - N_\beta$, the temporal evolution of I_z also depends on the transition rate W according to the equation 1.33.

$$\begin{aligned}\frac{dI_z}{dt} &= \frac{d\left(N_\alpha - N_\beta\right)}{dt} \\ &= -2W\left(I_z - I_z^0\right) \\ &= -R_1\left(I_z - I_z^0\right)\end{aligned} \tag{1.33}$$

R_1, which is a scalar, represents the relaxation rate of the spin angular momentum towards its equilibrium value I_z^0. The solution of the differential equation 1.33 is in the form:

$$I_z(t) = \left[I_z(0) - I_z^0\right]\exp(-R_1 t) + I_z^0 \tag{1.34}$$

where the operator I_z in the $I_z(0)$ state at $t = 0$ turns back to the equilibrium I_z^0 with a rate R_1.

The transition rate W depends on three factors: A, Y and $J(\omega)$ (see Eqn. 1.35).

$$W = A \times Y \times J(\omega) \tag{1.35}$$

A describes the quantum mechanical properties of spin interactions. These properties define the conditions for a coupled spin system to be excited or to relax through the transition that is characterized by W. The second component that contribute to the transition rate is the size factor Y. The latter includes the geometrical properties of the interactions causing the relaxation. Y is commonly directly connected to the molecular geometry of the system. Finally, $J(\omega)$ is the well-known spectral

density function as widely used in relaxometry by NMR.[15–17] This function constitutes a direct measurement of the molecular motions that can induce relaxation by producing time-dependent variations of the local magnetic field at an appropriate frequency. As W is twice the longitudinal relaxation rate R_1 (cf equation 1.33), R_1 strongly depends on the nature of the nucleus and its environment. In this thesis, we will commonly refer to the spin-lattice relaxation time which corresponds to the inverse of the relaxation rate (see Eqn. 1.36).

$$T_1 = \frac{1}{R_1} \tag{1.36}$$

This longitudinal relaxation time is a key constant in NMR. For example, one important functional implication is the repetition rate of an NMR experiment. To be sure that the system is at equilibrium before the beginning of the pulse sequences, we define the repetition time t_r between each accumulation as: $t_r = 5T_1$. Hence, short T_1 enables rapid repetition time for NMR accumulations and thus faster experiments.

Spin-spin relaxation

Unlike spin-lattice relaxation that is linked to a loss of energy of the spin system, spin-spin (or transverse) relaxation describes the loss of coherence of spins precessing in the xy plane, which is often denoted as the transverse plane. Two different contributions can cause a shrink of the transverse magnetization: a non-secular and a secular ones.[4]

The non-secular contribution to transverse relaxation is caused by the interaction of the x and y components of the spin-angular momentum $\mathbf{I}$ with an oscillating transverse magnetic field at the spin Larmor frequency. This process is the same as the one causing longitudinal relaxation and hence depends on the spectral density function at the Larmor frequency $J(\omega)$ in liquid state. By analogy to the T_1 relaxation, the characteristic time associated to this process is T_2.

The second contribution to the transverse relaxation is secular, which means that it depends on local field along the z axis. A non-uniform field generates variations

of precession frequencies of the different spin-angular momentum with time in the sample. Hence, two spins with different precession frequencies progressively build up a difference in phase. In liquid state, the lower the correlation time of the molecules τ_c is (i.e. the faster molecular motions are), the slower this process is and the lower is the contribution of the secular part of the transverse relaxation. The characteristic time associated to this phenomenon is T_2^*. Unlike the T_2 and T_1, the T_2^* does not depend on the fluctuations at Larmor frequency field $J(\omega)$ but on the spectral density function at 0 frequency $J(0)$. At a larger scale, all the spins in the sample will experience unique time-dependent modifications of their local magnetic field, which will eventually lead to a random distribution of phase angles. After a characteristic time, the phases are randomly spread between 0 and 2π inside the sample and the net transverse magnetization is null.

In practice, both T_2 and T_2^* simultaneously contribute to the decay of the magnetization in the transverse plane. They lead to a exponential decay of the signal with a rate constant $\frac{1}{T_2'} = \frac{1}{T_2} + \frac{1}{T_2^*}$. T_2' corresponds to the time required for the spin system to lose 37% of its signal in the transverse plane. This phenomenon is completely uncorrelated to the loss of energy of the system. In contrast to T_1 that has a major impact on the intensity of the spectrum, T_2^* contributes to the spectral linewidth. T_2^* implies the contribution of different precession frequencies in the sample, obviously leading to a broadening of the spectrum.

Cross-relaxation

Studying the relaxation of spin systems require the use of models due to the complexity of the problem. The most famous ones in NMR are Solomon's equations[18] and the Redfield's theory[19]. Both use a semi-classical approach and consider relaxation as a second order perturbation of the Hamiltonian. This second order approximation accurately describes systems in liquid states but do not fit properly to solid state NMR where the dipolar interaction between coupled spins features much stronger values and molecules do not rotate freely in the sample. The main difference between this two models relies on the fact that Solomon's equations describes the system evolution in term of populations (i.e. energy changes) whereas

Redfield's theory derives the Master equation (also known as Liouville von Neumann equation for the density matrix). In this extend, unlike the Solomon's theory, the Redfield's one describes both: the evolution of the energies and the coherences in a system of spins. However, in this thesis, we will explain the cross-relaxation using the Solomon's description.

The energy levels of a system composed of two spins-$\frac{1}{2}$, **I** and **S** that are not coupled by J-coupling (see section A.1) but that interacts with dipolar coupling, can be described by four energy levels: $|\alpha\alpha\rangle$, $|\alpha\beta\rangle$, $|\beta\alpha\rangle$, $|\beta\beta\rangle$. In the figure 1.3, four transitions are allowed which means that the variation of the total magnetic moment m verifies: $\Delta m = \pm 1$. In other words, W_I^1, W_I^2, W_S^1, W_2^1 involve a change of a unique spin from one energy level to another. These transitions are called: single quantum transitions. By analogy, we can deduce that W_0 and W_2, which respectively involve $\Delta m = 0$ and $\Delta m = \pm 2$, are zero-quantum and double quantum transitions. Although zero and double quanta transitions are forbidden, two spins that are coupled with dipolar interaction can simultaneously change state. Then,

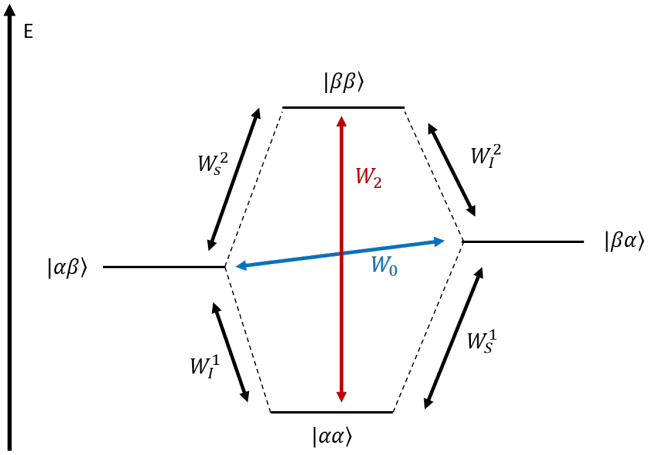

Figure 1.3: Diagram of the four energy levels of a two spin-$\frac{1}{2}$ system and the six corresponding transitions. W_I^i with $i = 1, 2$ corresponds to a change of state of spin I whereas W_S^i is associated to a change of energy of spin S. Colored transitions represent a simultaneous change of energy of the two spins. In red, both I and S "flip" or "flop", which is respectively a gain or a loss of energy. This is a double quantum transition (DQ). In blue, the transition is associated to a gain of energy the energy for one of the spins, whereas it decreases for the other. It corresponds to a spin "flip-flop" or a zero quantum transition (ZQ).

after expressing the evolution of the populations of each energy state as a function

of the transitions rates and the populations of the other energy levels (as it has been done previously for the longitudinal relaxation), we can end up with equations that describe the evolution of each spin angular momentum I_z and S_z (cf. Eqn. 1.37 and 1.38). The system requires the introduction of an additional operator: I_zS_z that depends on the difference of the population difference of transitions W_S^1 and W_S^2 (cf. Eqn. 1.39).

$$\frac{dI_z}{dt} = -R_{1I}\left(I_z - I_z^0\right) - \sigma_{IS}\left(S_z - S_z^0\right) - \Delta_I 2I_zS_z \tag{1.37}$$

$$\frac{dS_z}{dt} = -R_{1S}\left(S_z - S_z^0\right) - \sigma_{IS}\left(I_z - I_z^0\right) - \Delta_S 2I_zS_z \tag{1.38}$$

$$\frac{dI_zS_z}{dt} = -\Delta_I\left(I_z - I_z^0\right) - \Delta_S\left(S_z - S_z^0\right) - R_{1IS}2I_zS_z \tag{1.39}$$

Equations 1.37, 1.38 and 1.39 are the Solomon's equations for the relaxation of a two spin-$\frac{1}{2}$ system. It is now obvious that the angular momentum of the spins **I** and **S** are inter-dependent through dipolar interaction.

$$\begin{aligned} R_{1I} &= W_I^1 + W_I^2 + W_2 + W_0 \\ R_{1S} &= W_S^1 + W_S^2 + W_2 + W_0 \\ \sigma_{IS} &= W_2 - W_0 \\ \Delta_I &= W_I^1 - W_I^2 \\ \Delta_S &= W_S^1 - W_S^2 \end{aligned}$$

The rate σ_{IS} that drives the magnetization from one spin to the other is called "cross-relaxation" and only depends on forbidden transition rates W_0 and W_2. R_{1I} and R_{1S} corresponds to auto-relaxation of spin I and S. Finally, R_{1IS} is associated to the auto-relaxation of the operator $2I_zS_z$. In this section, we use dipolar interaction to derive the equations that leads to CR but other coupling mechanisms (for example J-coupling between nuclei) also induce such a process.

1.1.7 Spectral broadening: homogeneous vs inhomogeneous interactions

Interactions can cause a broadening of the spectra. In liquid state and for spin-$\frac{1}{2}$ in high field approximation, the line broadening essentially comes from the fluctuating components of the dipolar interaction between homonuclear spins.[20,21] It has been shown that when this interaction is strong, the shape of the line can be well approximated by a Lorentzian profile. Interactions that lead to a convolution of the line with a Lorentzian function are said homogeneous. Hamiltonians that describe these interactions $\hat{H}_{homo}$ do not commute with themselves at different times:

$$\forall t \neq t' \qquad [\hat{H}_{homo}(t), \hat{H}_{homo}(t')] \neq 0 \tag{1.40}$$

By contrast, an interaction is said inhomogeneous when its corresponding Hamiltonian $\hat{H}_{inhomo}$ commute with itself at different times:[22,23]

$$\forall t, t' \qquad [\hat{H}_{inhomo}(t), \hat{H}_{inhomo}(t')] = 0 \tag{1.41}$$

This means that the broadening does not come from a temporal modulation of the interaction but is generated by a difference of the spin resonance frequencies in the sample. Inhomogeneous broadening[23] is particularly important in solid state magnetic resonance as molecular tumbling does not average out the anisotropic components of the interactions. Different orientations of the molecules lead therefore to different local fields that are experienced by the spins. In crystal structures where all spins have very close frequency resonance values, the line shape is composed of several unresolved Lorentzian peaks. In such circumstances, the final line shape can be well-approximated by a gaussian profile.[24]

For experiments with nitroxides in glassy matrix at low temperature, electron spectra are characterized by strong inhomogeneous broadening with each resonance being homogeneously broadened.[25,26] The more the paramagnetic agents are concentrated, the more important the contribution of the inhomogeneous broadening becomes.[27]

1.2 Basics of Dynamic Nuclear Polarization

1.2.1 Hyperfine and super-hyperfine interaction

A nucleus with a non-zero spin (**I**) and an electron (**S**) interacts because of their magnetic moments μ_I and μ_S. The electron creates a magnetic field B_S at the nucleus location that modifies its energy levels. The Hamiltonian H_{SI} of this coupling can be expressed as:[28]

$$H_{SI} = -B_S \cdot \mu_I = \hbar \mathbf{S} \cdot \mathbf{A} \cdot \mathbf{I} \tag{1.42}$$

The energy splitting A depends on the distance between the nuclear spin I and the electron spin S represented by the vector $\vec{r}$. It is also directly proportional to the integral of the electron probability of presence $|\psi(\vec{r_S})|^2$ according to the equation 1.43.

$$\mathbf{A} = \frac{\mu_0}{4\pi} \hbar \gamma_I \gamma_S \int_\infty |\psi(\vec{r_S})|^2 dr_S \left(\frac{1}{r^3} - 3\frac{\vec{r} \cdot \vec{r}}{r^5} \right) \tag{1.43}$$

The hyperfine tensor has two properties: it is symmetric and the value of its trace is 0 ($A_{xx} + A_{yy} + A_{zz} = 0$). In the PAS frame defined by the axis x, y and z, the hyperfine tensor matrix is diagonal.

$$\mathbf{A} = \begin{pmatrix} A_{xx} & A_{xy} & A_{xz} \\ A_{yx} & A_{yy} & A_{yz} \\ A_{zx} & A_{zy} & A_{zz} \end{pmatrix} = \begin{pmatrix} A_{xx} & 0 & 0 \\ 0 & A_{yy} & 0 \\ 0 & 0 & A_{zz} \end{pmatrix} \tag{1.44}$$

When the probability to find the electron at nucleus location ($\vec{r_S} = \vec{0}$) is non-zero, which can only be achieved for s orbitals, the hyperfine interaction possesses an additional isotropic contribution: the *Fermi contact interaction*.

$$\begin{aligned} \mathbf{A} &= A_{Fermi} + A_{dipolar} \\ A_{Fermi} &\propto |\psi(0)|^2 \end{aligned} \tag{1.45}$$

In equation 1.45, A_{Fermi} represents a discontinuity in the equation 1.43 that occurs when $r_S = 0$ and $A_{dipolar}$ is the contribution of electron-nucleus dipolar interaction

to the hyperfine interaction.

In the case where the coupled electron and nucleus are located in the same molecule, A corresponds to the *hyperfine coupling* otherwise, it is associated to the *super-hyperfine interaction*. Purely dipolar, the super-hyperfine interaction enables to transfer the polarization from electrons to the surrounding nuclei that are located in neighboring molecules in DNP experiments. Its strength being much lower than the nuclear Zeeman interaction, the influence of the super-hyperfine interaction can be neglected in the nuclear energy levels. The truncated super-hyperfine interaction $\hat{H}_{super-hyper}$ between an electron spin $\mathbf{S}$ and N_I nuclear spins I^k is defined as in the equation 1.46.

$$\hat{H}_{super-hyper} = \hbar \sum_{k=1}^{N_I} \left(A_{zx} S_z I_x^k + A_{zy} S_z I_y^k + A_{zz} S_z I_z^k \right) \tag{1.46}$$

In this equation, only the secular and the pseudo-secular terms have been considered. Secular operators commute with I_z and S_z whereas pseudo-secular operators only commute with S_z. Even though it has no visible impact on the nuclear states, the intermolecular hyperfine interaction generates an homogeneous broadening of the electron spectrum.[21]

1.2.2 Adaptation of the energy diagram to coupled electron spin-$\frac{1}{2}$ nucleus

In order to properly understand the DNP different mechanisms, we can use the same description as the one developed in section 1.1.6. The figure 1.3, which describes a general case of two spins I and S in interaction, can then be applied to a system composed of an electron interacting with a spin-$\frac{1}{2}$ nucleus. Note that the opposite sign of electron and nucleus gyromagnetic ratios induces an inversion of $|\alpha\rangle$ and $|\beta\rangle$ energy states. By convention, we will refer to electron spin as S and to the nuclear spin as I. We arbitrarily associate $|\alpha\rangle$ to the magnetic moment $m_k = -\frac{1}{2}$ with $k = S, I$ and $|\beta\rangle$ to $m_k = +\frac{1}{2}$. In figure 1.4, purple and blue transitions are allowed whereas the red ones that refer to zero-quantum (W_n^2) and double-quantum (W_{ne}^1)

transitions are forbidden. It is important to note that a forbidden transition does exist but the probability of a system to change energy through it is very low. The energy difference between the spin states $|\beta\beta\rangle$ and $|\alpha\alpha\rangle$ is $\hbar\,(\omega_e - \omega_n)$ and the states $|\beta\alpha\rangle$ and $|\alpha\beta\rangle$ are separated by an energy of $\hbar\,(\omega_e + \omega_n)$ with ω_e and ω_n respectively the resonance frequencies of nucleus and electron.

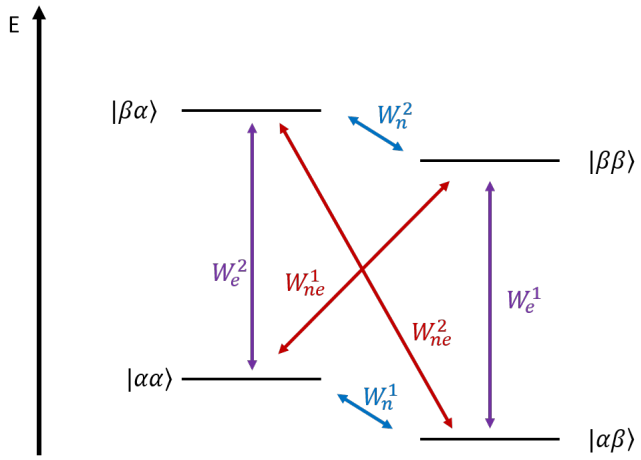

Figure 1.4: Energy diagram of an interacting electron-nucleus system. Purple arrows refer to the ESR transitions, blue ones are associated to NMR transitions and red ones indicate the ZQ and DQ transitions.

1.2.3 The DNP mechanisms that involve two interacting spins: Overhauser and Solid Effect

All DNP mechanisms are mediated through the hyperfine coupling that connects nuclei with electrons in presence of microwave irradiation. Depending on the polarizing agent that we chose, its concentration and external parameters such as the temperature or the microwave frequency, one of four mechanisms may dominate: the Overhauser Effect (OE), the Solid effect (SE), the Cross-Effect (CE) or the Thermal Mixing process (TM).

The Overhauser Effect (OE)

The Overhauser Effect (OE) was the first mechanism to be discovered.[29,30] It has been demonstrated at first that irradiating electrons at their Larmor frequency ω_e with microwaves generates an increase of the nuclear signal of alkali metals in solution at low magnetic field. If we refer to figure 1.4, only one of the allowed transitions W_e^2 or W_e^1 is saturated. The modulation of the hyperfine coupling leads to cross-relaxation that transfers energy from the electrons to the interacting nuclei. When the transition W_e^2 is saturated, the populations in the energy levels $|\beta\alpha\rangle$ and $|\alpha\alpha\rangle$ are the same. The hyperfine coupling enables then the spins to relax through the nuclear transition W_{ne}^2 to drive the nuclear population back to the corresponding Boltzmann factor. Using this method, the difference of population between the two states $|\alpha\beta\rangle$ and $|\alpha\alpha\rangle$ is increased, which generates a more intense NMR signal compared to the one associated to the same system without microwave irradiation.

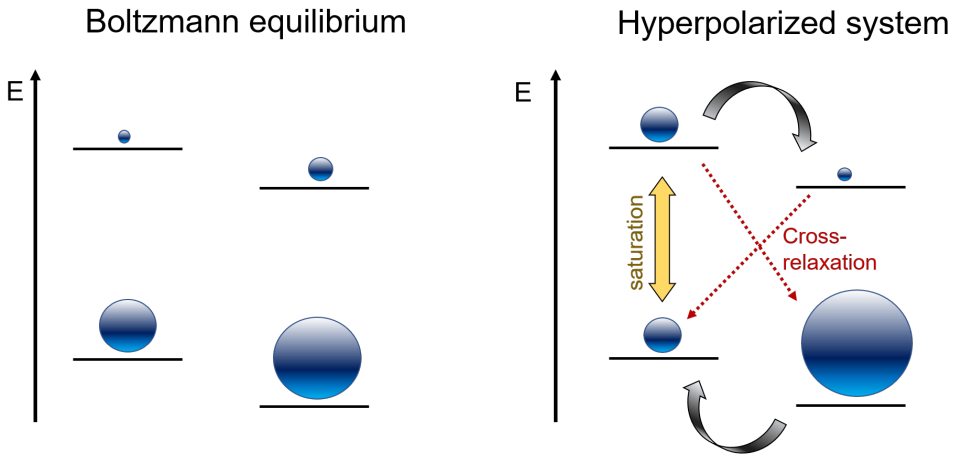

Figure 1.5: Summary of the different steps that compose the OE. The qualitative population of each energy level (see fig. 1.3) is represented by the blue spheres. At the equilibrium, the population of each energy level follows the Boltzmann factor. The MW saturates EPR allowed transitions. The saturated electrons transfer then their polarization to coupled nuclei through temporal modulation of the hyperfine coupling (cross-relaxation). The relaxation to the Boltzmann equilibrium is illustrated by the two black arrows.

The maximum enhancement in NMR signals ϵ that can be achieved by solution DNP can be expressed as:[31]

$$\epsilon = \frac{P_n}{P_{eq}} = 1 - \xi f s \frac{|\gamma_S|}{\gamma_I} \tag{1.47}$$

In equation 1.47, P_n corresponds to the polarization of the nucleus and P_{eq}, its polarization at Boltzmann equilibrium. The highest enhancement that one can reach is defined by $\left|\frac{\gamma_S}{\gamma_I}\right| \sim 660$. ϵ also depends on experimental factors: the leakage f, the saturation s and the coupling ξ. Even if the enhancements achieved by solution-DNP at high field are not as high as in DNP at low temperature, the hyperpolarization build-up time is much shorter and experiments do not require heavy additional facilities to transfer samples.[32–35] (The reader is referred to chapter 2.1.1 for a description of the ENS facilities for the transfer of hyperpolarized samples in dissolution-DNP.)

As explained in this subsection, the OE dominates at low field in microwave irradiated solutions that has been doped with polarizing agents or in metallic environments. The experimental conditions relevant for this thesis (see chapter 2.1) yet allow us to neglect its contribution in the results that are presented.

The Solid Effect (SE)

In late 50's, the Solid Effect (SE) mechanism has been described in insulating solids.[36–40] SE is employed in MAS-DNP where gains of signal intensity up to 144 at 5 T have been observed, but also in static solids at low tempreatures.[41]

The SE is induced by saturation of forbidden transitions. The pseudo-secular part of the hyperfine coupling mixes the spin states, which partly allows the formerly forbidden DQ and ZQ transitions (for more details, see appendix B.2). Two peaks with opposite phase are generated when the electrons are irradiated at the frequencies $\hbar\left(\omega_e - \omega_n\right)$ or $\hbar\left(\omega_e + \omega_n\right)$. The two resonance peaks are separated by twice the nuclear Larmor frequency. The enhancement of the signal ϵ is governed by the nuclear polarization of the system P_n compared to the same polarization at Boltzmann equilibrium P_{eq}.

$$\epsilon = \frac{P_n}{P_{eq}} \tag{1.48}$$

If we consider the definition of the nuclear signal enhancement (eqn. 1.48), microwave irradiation of the ZQ transition generates negative hyperpolarization of the system whereas saturating the DQ transition leads to a positive ϵ.[42] The SE dom-

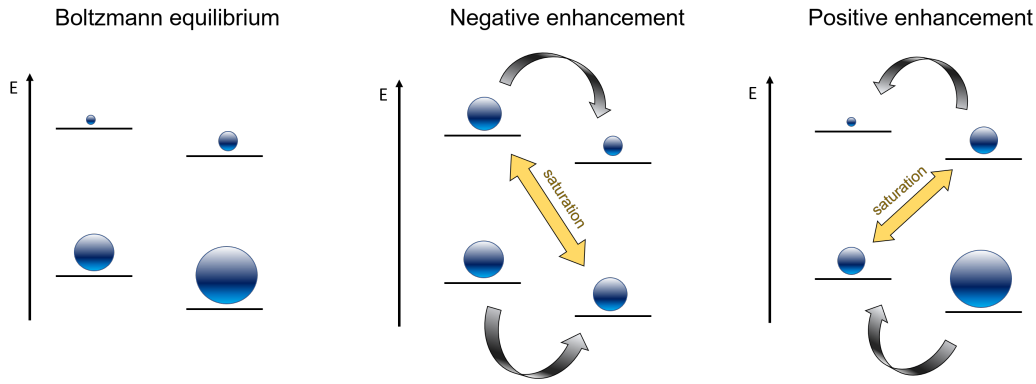

Figure 1.6: Summary of the SE mechanism. A continuous wave microwave irradiation at the frequency $(\omega_e + \omega_n)$ (respectively $(\omega_e - \omega_n)$) leads to a saturation of the ZQ transition (resp. DQ) ending up with a positive (resp. negative) ϵ. Black arrows indicate the flow of population generated by the saturation of DQ or ZQ transition.

inates when the homogeneous linewidth Δ and the inhomogenous breadth δ of the electron spectrum of the paramagnetic species is smaller than the Larmor frequency:

$$(\delta, \Delta) \ll \omega_n \tag{1.49}$$

As the concentration of the polarizing agent directly impacts this linewidth through the electron-electron dipolar interaction, the dominant mechanism depends not only on the chosen polarizing agent but also in its concentration as well as on the gyromagnetic ratio of the nuclues. Thus, the SE is the dominant mechanism for low concentrated paramagnetic agent with thin electron resonance spectrum.[43,44] Polarizing agents with high symmetry property, quasi-isotropic g factor and weak hyperfine coupling such as BDPA[45] or Trityl(oxo63)[46] are the most likely to satisfy these conditions. On another hand, the stronger the external magnetic field, the lower is the mixing factor q. The SE enhancement in continuous wave irradiation for solid insulators decreases with the square of the external magnetic field: $\epsilon \propto \omega_e^{-2}$. This gives rise to very low spin hyperpolarization when the field is above 3 T using common SE paramagnetic agents. Several ways to circumvent this issue are possible such as the use of strong microwave power to excite a larger bandwidth into the EPR line or using polarizing agents whose linewidth diminish with the magnetic field as it is the case for some metal-based polarizing agents.[47]

1.2.4 The triple spin flip process

Both, the theories of the OE and SE describe polarization mechanisms based on two coupled spins. This matches systems with low concentratations of monoradicals as paramagnetic agents. Electron-electron dipolar interaction can be neglected in the description of hyperpolarization processes for such systems. However, in many cases, such descriptions are not valid, e.g., in MAS-DNP, biradicals, molecules that house two unpaired electrons are commonly used. Even though the intramolecular dipolar interaction between the two unpaired electrons is too strong to impact DNP based on the SE, these radicals lead to very high enhancements and frequently offer better DNP efficiencies at high magnetic fields.[48–51]. Another examples that demands for another thepry beyond OE and SE are mixtures that contain high concentration of nitroxide monoradicals as these are very efficient to hyperpolarize nuclei with high gyromagnetic ratio at cryogenic temperatures.[52–55]

The mechanism behing process that leads to high efficiencies of DNP in the absence of SE or OE DNP involves two interacting electrons and one nucleus.[56] To transfer the polarization from the electrons to the nucleus, the system must fulfill two requirements. Firstly, one of the two electrons must interact with the nucleus. Secondly, the two electrons have to resonate at frequencies ω_{e1} and ω_{e2} that are approximately separated by the Larmor frequency of the nucleus ω_n.

$$|\omega_{e1} - \omega_{e2}| \approx \omega_n \tag{1.50}$$

In systems that possess such properties, microwave irradiation can induce flip-flop processes of the two electron spins and a simultaneous flip of the nucleus due to the degeneracy of the energy levels dipolar and nuclear energy levels (see figure 1.7).[57,58] This three spin flip process is the basis of the two fundamental DNP mechanisms: the Cross-Effect and Thermal Mixing.

1.2.5 The Cross-Effect (CE)

The Cross-Effect (CE) has been discovered in 1964.[59–61] It is generally boosted when the inhomogeneous δ and the homogeneous linewidth Δ satisfy the equation 1.51.

$$\Delta < \omega_n < \delta \tag{1.51}$$

This process relies on triple spin flips and consequently involves two electrons and one nucleus. As mentioned in the previous section, the two electronic frequencies must be separated by the Larmor frequency of the coupled nucleus. If this condition is validated, the previously forbidden electron-electron flip-flop transition is replaced by the allowed electron-electron-nucleus flip-flop-flip. Saturating one of

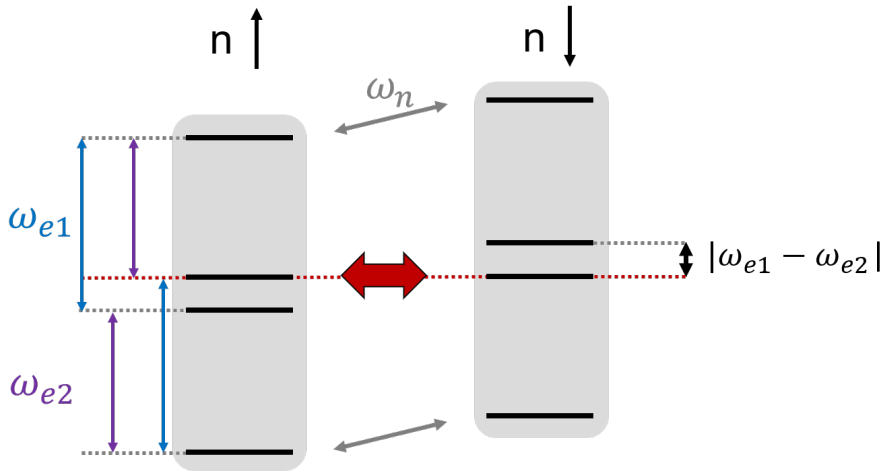

Figure 1.7: Energy diagram of three interacting spins: two electrons and a spin-$\frac{1}{2}$ nucleus. ω_{e1} and ω_{e2} are the Larmor frequencies of the two electrons and ω_n, the resonance frequency of the interacting nucleus. If the dipolar coupling between the two electrons matches ω_n, a degeneracy of the energy levels is created. The previously forbidden electronic flip-flop transition becomes then allowed (red arrow). Irradiating the spin system at the allowed transition ω_{e1} (resp. ω_{e2}) leads therefore to a flip of the electron at the resonance ω_{e2} (resp. ω_{e1}) and of the nuclear spin.

the two electronic transitions ω_{e1} or ω_{e2} leads to a transfer of polarization from the electrons to the coupled nucleus.[57] The CE mechanism dominates in most appliactions of MAS-DNP experiments as they are typically performed at high field (ca between 5 and 10 T) and low temperature ($\sim$ 100 K).[62,63] At the point of writing of this thesis, dinitroxides such as AMUPol and TOTAPOL demonstrate the best efficiency to hyperpolarize nuclei under such experimental conditions. They lead to enhancements of the proton polarization of $\epsilon \sim 60$ for AMUPol and up to more than

200 for TOTAPOL under MAS.

A lot of studies are focused in the design of new polarizing agents that leads to the better nuclear polarization levels.[64–67] Controlling electron-electron distance in order to match the dipolar interaction strength between the two electrons to the Larmor frequency of nuclei as well as the rigidity of the polarizing agent or the longitudinal electron spin relaxation can significantly improve the efficiency of the CE mechanism.[68–71] Another approach that consists in attaching a TEMPO monoradical with broad EPR line to a trityl radical with a thin resonance line has recently been developed.[72,73] Such systems have the advantage of not creating a depolarizing field under MAS as it is the case for AMUPol and TOTAPOL. This effect is one of the main drawback of the MAS-DNP as it considerably reduces the nuclear polarization that can be achieved. It can lead to a loss of Boltzmann polarization of the protons up to $\sim 60\%$ (AMUPol) and $\sim 20\%$ (TOTAPOL) at 110 K under a 10 kHz rotation of the sample compared to a static sample.[73] The impact of the depolarization field increases as the temperature decreases.[74]

1.2.6 Spin temperature

Another way of describing a spin system has been intensively studied in the middle of the 20$^{\text{th}}$ century. The goal was to find a way to unite thermodynamics and the quantum mechanistic descriptions to predict the behavior of systems with high concentrations of interacting spins. Thus, the concept of the spin temperature was developed for the description of NMR, DNP and EPR.[75,76] In this approach, all interactions that have an impact on the spin states and/or transitions rate can be assigned to thermodynamic reservoirs. Each reservoir possesses its own intrinsic polarization and consequently its own spin temperature. As an example, let's consider a system composed of non interacting spin-$\frac{1}{2}$ in a static external magnetic field. The Zeeman interaction splits the energy levels of each spin, which induces a Boltzmann distribution of the population, even in thermal equilibrium (cf Fig. 1.8). One may hence assign a temperature reservoir to the Zeeman interaction. This "spin temperature" will depend on the difference in populations between the two non-degenerate

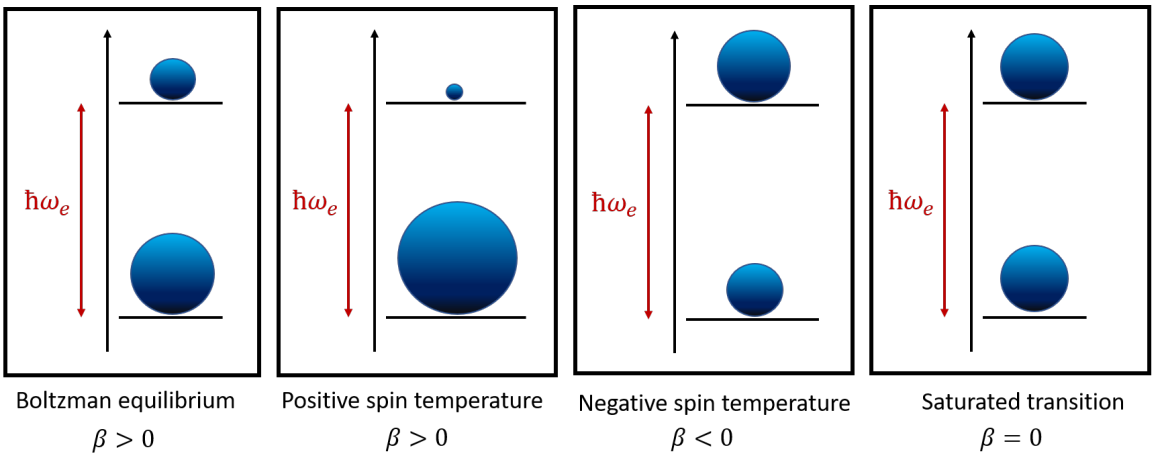

Figure 1.8: Population of an electron spin system in a static magnetic field for different spin temperatures. ω_e represents the Larmor frequency of the electron spins. The inverse spin temperature $\beta = \frac{1}{k_B T_S}$, with k_B the Boltzmann constant and T_S the spin temperature, describes the population difference between the two energy levels. A positive (resp. negative) spin temperature means that the lower (resp. excited) state is overpopulated. Therefore, β is always positive at Boltzmann equilibrium in such conditions. Finally, when a transition is saturated, the population is the same in the two energy levels. This leads to $\beta = 0$.

energy levels. The higher (resp. the lower) the polarization is, the higher (resp. the lower) is the reciprocal spin temperature. An inverse spin temperature of zero means that energy levels have the same population or that the transition is saturated. An infinite inverse spin temperature is associated to systems where all spins are in the same energy level and the others are completely depleted.

In a next step, we add interactions, dipolar coupling between the spins. This corresponds to system where radicals are highly concentrated and strong intermolecular electron dipolar interactions broaden the EPR spectrum. Thus, energy levels are again split and the energy of the dipolar reservoir that emerges from the splitting is $\hbar\omega_e$. This situation is schematically depicted in Figure 1.9. We represent the dipolar coupling that splits each Zeeman state into 2n+1 substates (n being the number of coupled electrons) by discrete energy levels within each Zeeman

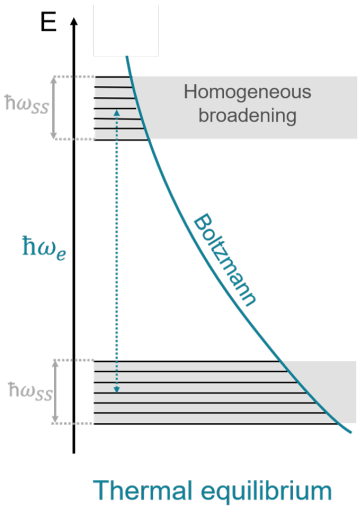

Figure 1.9: Schematic representation of the equilibrium electronic spin temperature in the case of strong electron-electron dipolar coupling.

manifold despite the fact that dipolar coupling is typically considered as homogenous. Hence, within each Zeeman manifold we find a distribution of energy levels with an intrinsic polarization that corresponds to the spin temperature of the dipolar energy reservoir. Summing up, typically the dipolar and Zeeman spin temperatures (T_S and T_{SS}) are employed to describe the thermodynamics of spin systems under DNP conditions. The density matrix ρ of the electronic spin system can hence be described as Eqn. 1.52 considering all involved electrons.[77]

$$\rho = \frac{\exp(-\alpha\omega_e S_z - \beta H_{DD})}{\mathrm{Tr}\{\exp(-\alpha\omega_e S_z - \beta H_{DD})\}} \tag{1.52}$$

where $\alpha = \frac{1}{\mathrm{k_B} T_S}$ and $\beta = \frac{1}{\mathrm{k_B} T_{SS}}$ with $\mathrm{k_B}$. $\omega_e S_z$ and H_{DD} respectively are the Zeeman and dipolar Hamiltonians.

1.2.7 Thermal Mixing (TM)

In 1964, Borghini and Abragam used Solomon, Redfield and Provotorov's theories[75,76,78] as a basis to develop the Thermal Mixing (TM) theory.[79,80] The phenomenon was however only observed nine years later, by Cox[81] in solid samples of lithium fluoride at very low temperature ($g\beta_e H > k_B T$ with g, the g-factor, β_e, the Bohr magneton and H the inductance of the magnetic field). Cox and coworkers demonstrated a connection between the ^{19}F and ^{7}Li nuclear baths mediated via the electronic dipolar reservoir by following the temporal evolution of their hyperpolarized signal in absence of microwave irradiation. As soon as the microwave is turned off, mixing of the two nuclear reservoirs, i.e., an equilibration of their spin temperatures, on the time scale of the minute can be detected by a process of repolarization of the ^{7}Li. At longer time scale (several minutes), it has been shown that the signal ^{7}Li and ^{19}F intensities decay with a common rate to their respective thermal equilibrium values.

Strong electron-electron dipolar coupling is required for TM. The basic phenomenon behind the transfer of polarization from electrons to nuclei is depicted in figure 1.10. Irradiating the system with a microwave at a frequency $\omega = \omega_e \pm \omega_{SS}$, which is slightly different from the electron Larmor frequency ω_e, would burn a hole in the

EPR spectrum,[28,82] creating a rearrangement of population among the electron dipolar energy sublevels if electronic spectral diffusion (eSD) would be slow.[83]. However, if it is fast, as Provotorov assumed, the saturation is distributed among the different spin packages that constitute a heterogeneously broadened line. If the nuclear Larmor frequency ω_n is smaller than the range of the EPR line covered by eSD (or smaller than the homogenous broadening of the line in case of slow eSD), some electron spins transfer their energy to nuclei via triple spin flips. Hence, this process is dominant when the homogeneous linewidth (either intrinsic or through eSD) of the paramagnetic species becomes larger than the Larmor frequency of the nuclei:

$$\Delta \gg \omega_n \tag{1.53}$$

As the homogeneous linewidth depends on the mutual interactions between electrons, a higher concentration of polarizing agents in the sample often leads to stronger TM effect.[84,85]

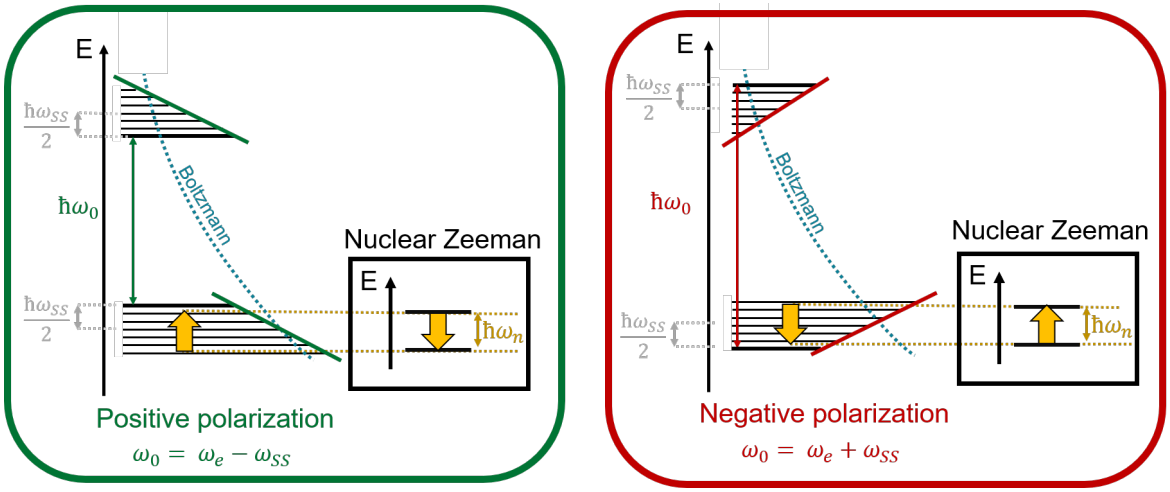

Figure 1.10: Schematic representation the thermal mixing mechanism. A saturation of the transition ω_0 leads to a rearrangement of the spin populations among the dipolar sublevels (yellow arrow). Bold energy levels are equally populated. If $\omega_n < \omega_{SS}$, the electrons transfer their energy to the nuclei as they relax in the energy levels of the dipolar manifolds.

Provotorov's intial theory relies on the high temperature approximation: $\beta\omega_e \ll 1$. It can be extended to systems with inhomogeneously broadened spectra submitted to very fast spectral diffusion.[28,82] Borghini demonstrated that this model could partially be generalized to low temperatures and high magnetic fields by splitting the inhomogeneously broadened EPR line into spin packets[86] and assuming an electron

spin lattice relaxation much slower than the eSD. Some mathematical details of the Abragam and Borghini's model are discussed in the chapters 3 and 5. This introduction consequently just gives an overview of this theory. The Hamiltonian $\hat{H}$ of a system that is composed of a bath of electrons interacting with a reservoir of nuclei by three interactions: the electron Zeeman $\hat{H}_{Ze}$, the nuclear Zeeman $\hat{H}_{Zn}$ and the electron non Zeeman (or dipolar) $\hat{H}_{nZ}$ can be expressed as:

$$\hat{H} = \hat{H}_{Ze} + \hat{H}_{Zn} + \hat{H}_{nZ} \tag{1.54}$$

Borghini assumed that the energy involved in the electron Zeeman interaction ($\langle \hat{H}_{Ze} \rangle$) is much higher than the energy associated to the electron dipolar and nulear Zeeman interactions ($\langle \hat{H}_{nZ} + \hat{H}_{Zn} \rangle$). Hence, the temporal evolution of the energy wihtin the system is approximately equivalent to the evolution of $\langle \hat{H}_{Ze} \rangle$ and $\langle \hat{H}_{nZ} + \hat{H}_{Zn} \rangle$.[87] In other words, as the energies of the nuclear Zeeman and the electron dipolar baths are comparable the electrons and nuclei can efficiently interact by hyperfine coupling. Therefore, a thermal contact is estabiushed between the electronic and nuclear reservoirs. Each reservoir is additionally in contact with the lattice that acts as a thermostat (possess a stables temperature). The equilibrium temperature of all reservoirs becomes by definition the lattice temperature. To hyperpolarize a sample, continuous microwave irradiation can be applied to i) bring the Zeeman and dipolar reservoirs into contact by reducing the effective magnetic field and ii) to cool down both thermodynamic reservoirs. Due to the triple spin flips connecting electrons and nuclei, this process induces a cool down of the nuclear Zeeman reservoir or in other words, hyperpolarization of the nuclei. Finally, to fully polarize a sample the electron spin-lattice relaxation is needed.[88] Electron spins polarize nuclei once one of their transition is saturated. Their relaxation through spin-lattice coupling repolarizes them and allows them to transfer another time their polarization under constant microwave irradiation.[28]

Even though all mechanisms treated here are well established, experiments show that the limit between the different mechanisms is often not that well-defined. Indeed, in most of cases, the experimental conditions enable the simultaneous contribution of more than one mechanism.[89,90] Moreover, the slight variation of parameters such

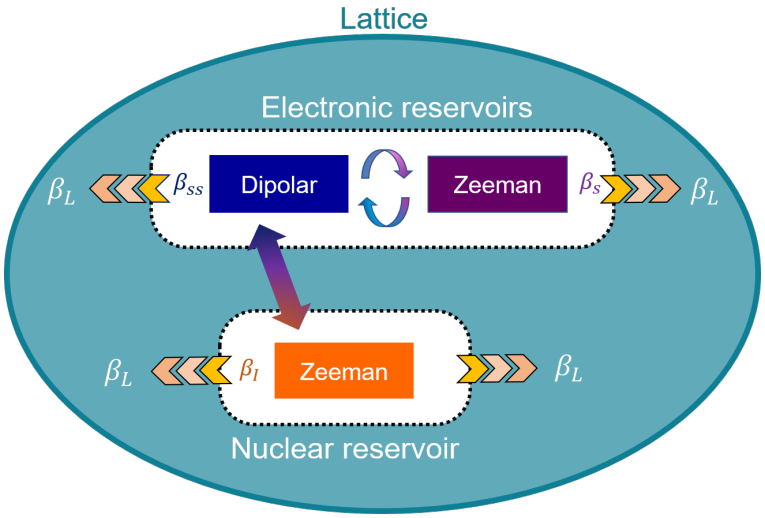

Figure 1.11: Schematic representation of the DNP system as described in the TM theory. Each interaction can be represented by a reservoir that has its own spin temperature. β_k with $k = L, S, SS$ and I respectively represent the inverse spin temperatures of the lattice, the electron Zeeman, the electron dipolar and the nucleus Zeeman reservoirs. The hyperfine coupling induces a thermal contact between the electronic and nuclear manifolds. The lattice can be compared to the thermostat in thermodynamics: it has a stable temperature and set the spin temperature of all reservoirs at equilibrium.

as the polarizing agent concentration, the magnetic field or the temperature usually leads to a change of the dominant mechanism in the DNP process.[91,92]

1.2.8 Hyperpolarization of the nuclei that are located far from the polarizing agent

As we typically produce samples with low polarizing agent concentration to reduce paramagnetic relaxation enhancements (PREs) that nuclear spins experience, most target nuclei are too far away from electrons to be directly polarized. These nuclei can nonetheless be hyperpolarized through nuclear spin diffusion processes.[93] Once a nucleus has successfully been polarized, its polarization can be transported to other nuclei via flip-flop processes. If the longitudinal nuclear relaxation is slow, this process of spin diffusion can distribute hyperpolarization throughout an entire sample. This is, e.g., the case at low temperatures where nuclear T_1 times can be-

come several tens of minutes. For nuclei with high gyromagnetic ratio, this process is especially effective. For nuclei with low gyromagnetic ratio, the presence of a minor concentration of protons can assist spin diffusion through multi-spin flip-flop processes comparable to the triple spin flips introduced above (so-called proton assisted spin diffusion).

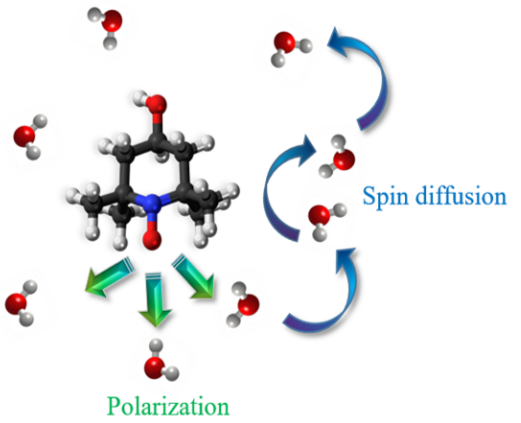

To summarize the different steps to reach the maximum of nuclear polarization in the DNP samples:[94]

1. Electron spin-relaxation polarizes electrons
2. Microwave irradiation transfer the polarization from electrons to nuclei through intermolecular hyperfine interaction. This is achieved by one of the four DNP mechanisms.
3. Diffusion of the polarization among the dipolarly coupled nuclei polarizes further spins[95,96]

Bibliography

[1] Walther Gerlach and Otto Stern. Der experimentelle nachweis der richtungsquantelung im magnetfeld. *Zeitschrift für Physik*, 9(1):349–352, Dec 1922.

[2] C. Cohen-Tannoudji, B. Diu, and B. Laloë. *Mécanique quantique*. Hermann, Paris, 1973.

[3] J. A. Weil and J. R. Bolton. *Electron Paramagnetic Resonance: Elementary Theory and Practical Applications - Second Edition*. John Wiley & Sons, Inc, 2006.

[4] J. Keeler. *Understanding NMR Spectroscopy - Second Edition*. 2010.

[5] J. H. van Vleck. On the role of dipole-dipole coupling in dielectric media. *J. Chem. Phys.*, 5:556, 1937.

[6] J. H. van Vleck. On the anisotropy of cubic ferromagnetic crystals. *Phys. Rev.*, 52:1178–1198, 1937.

[7] H. Saitô, I. Ando, and A. Ramamoorthy. Chemical shift tensor - the heart of NMR: Insights into biological aspects of proteins. 57:181–228, 2010.

[8] K. Malinakova. Solution and solid-state NMR paramaters: Applications in structural chemistry, 2010.

[9] A. Abragam. *The Principles of Nuclear Magnetism*. Clarendon Press, Oxford, UK, 1961.

[10] D. Sitkoff and D. A. Case. Theories of chemical shift anisotropies in proteins and nucleic acids. *Prog. Nuc. Magn. Reson. Spec.*, 32(2):165 – 190, 1998.

[11] R. Harris, E. Becker, S. Cabral de Menezes, P. Granger, R. E. Hoffman, and K. W. Zilm. Further conventions for NMR shielding and chemical shifts. *Pure Appl. Chem.*, 80(1):59–84, 2009.

[12] S. Heisaburo. NMR relaxation processes of ^{31}P in macromolecules. *Biopolymers*, 19(3):509–522, 1980.

[13] M. F. Roberts and A. G. Redfield. High-resolution ^{31}P field cycling NMR as a probe of phospholipid dynamics. *J. Am. Chem. Soc.*, 126(42):13765–13777, 2004.

[14] M. J. Forster and A. N. Lane. ^{31}P NMR relaxation measurements of the phosphate backbone of a double stranded hexadeoxynucleotide in solution: determination of the chemical shift anisotropy. *Europ. Biophys. Jour.*, 18(6):347–355, 1990.

[15] J. W. Peng and G. Wagner. Mapping of spectral density functions using heteronuclear NMR relaxation measurements. *J. of Magn. Reson. (1969)*, 98(2):308 – 332, 1992.

[16] N.A. Farrow, O. Zhang, A. Szabo, D. A. TorchiaLewis, and L. E. E. Kay. Spectral density function mapping using ^{15}N relaxation data exclusively. *J. Biomol. NMR*, 6:153 – 162, 1995.

[17] C. Charlier, S. N. Khan, T. Marquardsen, P. Pelupessy, V. Reiss, D. Sakellariou, G. Bodenhausen, F. Engelke, and F. Ferrage. Nanosecond time scale motions in proteins revealed by high-resolution NMR relaxometry. *J. Am. Chem. Soc.*, 135(49):18665–18672, 2013.

[18] I. Solomon. Relaxation processes in a system of two spins. *Phys. Rev.*, 99:559–565, 1955.

[19] A. G. Redfield. On the theory of relaxation processes. *IBM J. Res. Dev.*, 1(1):19–31, 1957.

[20] J.-H. Chem and S. Singer. High-resolution magic angle spinning spectroscopy. In J. C.

Lindon, J. K. Nicholson, and E. Holmes, editors, *The Handbook of Metabonomics and Matebolomics*, chapter 4, pages 113–147. Elsevier B. V., 2007.

[21] Stanislav Sýkora. Linewidths in high-resolution NMR spectra. homogeneous broadening due to intermolecular relaxation. *J. Chem. Phys.*, 52(11):5949–5951, 1970.

[22] M. M. Maricq and J. S. Waugh. Nmr in rotating solids. *J. Chem. Phys.*, 70(7):3300–3316, 1979.

[23] F. K. Kneubühl. Line shapes of electron paramagnetic resonance signals produced by powders, glasses, and viscous liquids. *The Journal of Chemical Physics*, 33(4):1074–1078, 1960.

[24] J. H. Van Vleck. The dipolar broadening of magnetic resonance lines in crystals. *Phys. Rev.*, 74:1168–1183, 1948.

[25] B. Berner and D. Kivelson. The electron spin resonance line width method for measuring diffusion. a critique. *J. Phys. Chem.*, 83:1406–1412, 1979.

[26] Ho. Elgabarty, M. Wolff, A. Glaubitz, D. Hinderberger, and D. Sebastiani. First principles calculation of inhomogeneous broadening in solid-state cw-EPR spectroscopy. *Phys. Chem. Chem. Phys.*, 15:16082–16089, 2013.

[27] G. I. Likhtenshtein, J. Yamauchi, S.'i. Nakatsuji, A. I. Smirnov, and R. Tamura. *Nitroxides: Applications in Chemistry, Biomedicine, and Materials Science*. Wiley-CH, 2008.

[28] T. Wenckebach. *Essentials of Dynamic Nuclear Polarization*. Sprindrift Publications, 2016.

[29] A. W. Overhauser. Polarization of nuclei in metals. *Phys. Rev.*, 92:411 – 415, 1953.

[30] T. R. Carver and C. P. Slichter. Experimental verification of the overhauser nuclear polarization effect. *Phys. Rev.*, 102:975, 1956.

[31] K. H. Hausser and D. Stehlik. Dynamic nuclear polarization in liquids. *Adv. Magn. Res.*, 3:79–139, 1968.

[32] J. A. Villanueva-Garibay, G. Annino, G. J. M. van Bentum, and A. P. M. Kentgens. Pushing the limit of liquid-state dynamic nuclear polarization at high field. *Phys. Chem. Chem. Phys*, 12:5846–5849, 2010.

[33] P. Höfer, G. Parigi, P. Carl, G. Guthausen, M. Reese, T. Carlomagno, C. Griesinger, and M. Bennati. Field dependent dynamic nuclear polarization with radicals in aqueous solution. *J. Am. Chem. Soc.*, 130:3254–3255, 2008.

[34] M.-T. Türke, I. Tkach, M. Reese, P. Höfer, and M. Benatti. Optimization of dynamic nuclear polarization experiments in aqueous solution at 15 MHz/9.5 GHz: a comparative study with DNP at 140 MHz/94 GHz. *Phys. Chem. Chem. Phys.*, 12:589–5901, 2010.

[35] V. Denysenkov, M. J. Prandolini, M. Gafurov, D. Sezer, B. Endeward, and T. F. Prisner. Liquid state DNP using a 260 GHz high power gyrotron. *Phys. Chem. Chem. Phys.*, 12:5786–5790, 2010.

[36] M. Abraham, R. W. Kedzie, and C. D. Jeffries. γ-ray anisotropy of co^{60} nuclei polarized by paramagnetic resonance saturation. *Phys. Rev.*, 106:165–166, Apr 1957.

[37] C. D. Jeffries. Polarization of nuclei by resonance saturation in paramagnetic crystals. *Phys. Rev.*, 106:164–165, 1957.

[38] C. D. Jeffries. Dynamic orientation of nuclei by forbidden transitions in paramagnetic resonance. *Phys. Rev.*, 117:1056–1069, 1960.

[39] A. Abragam and W. G. Proctor. A novel method of dynamic polarization of atomic nuclei in solids. *C. R. Acad. Sci.*, 246:2253–2256, 1958.

[40] E. Erb, J. L. Motchane, and J. Uebersfeld. *C. R. Acad. Sci.*, 246:2121, 1958.

[41] A. A. Smith, B. Corzilius, J. A. Bryant, R. DeRocher, P. P. Woskov, R. J. Temkin, and R. G. Griffin. A 140 GHz pulsed EPR/212 MHz NMR spectrometer for DNP studies. *J. Magn. Res.*, 223:170–179, 2013.

[42] Q. Z. Ni, E. Daviso, T. V. Can, E. Markhasin, S. K. Jawla, T. M. Swager, R. J. Temkin, J. Herzfeld, and R. G. Griffin. High frequency dynamic nuclear polarization. *Acc. Chem. Res.*, 46:1933–1941, 2013.

[43] Y. Hovav, A. Feintuch, and S. Vega. Theoretical aspects of dynamic nuclear polarization in the solid state – the solid effect. *J. Magn. Res.*, 207:176–189, 2010.

[44] C. F. Hwang and D. A. Holl. Phenomenological model for the new effect in dynamic polarization. *Phys. Rev. Lett.*, 19:1011–1013, 1967.

[45] O. Haze, B. Corzilius, A. A. Smith, R. G. Griffin, and T. M. Swager. Water-soluble narrow-line radicals for dynamic nuclear polarization. *J. Am. Chem. Soc.*, 134:14287–14290, 2012.

[46] J.H. Ardenkjær-Larsen, I. Laursen, I. Leunbach, G. Ehnholm, L.-G. Wistrand, J.S. Petersson, and K. Golman. EPR and DNP properties of certain novel single electron contrast agents intended for oximetric imaging. *Journal of Magnetic Resonance*, 133(1):1 – 12, 1998.

[47] B. Corzilius, A. A. Smith, A. B. Barnes, C. Luchinat, I. Bertini, and R. G. Griffin. High-field dynamic nuclear polarization with high-spin transition metal ions. *J. Am. Chem. Soc.*, 133:5648–5651, 2011.

[48] K.-N. Hu, H.-h. Yu, T. M. Swager, and R. G. Griffin. Dynamic nuclear polarization with biradicals. *J. Am. Chem. Soc.*, 126:10844–10845, 2004.

[49] S. Lange, A. Linden, Ü. Akbey, W. Franks, N. M Loening, B.-J. Rossum, and H. Oschkinat. The effect of biradical concentration on the performance of DNP-MAS-NMR. *J. Magn. Res.*, 216:209–12, 01 2012.

[50] Ümit Akbey, W. Trent Franks, Arne Linden, Marcella Orwick-Rydmark, Sascha Lange, and Hartmut Oschkinat. *Dynamic Nuclear Polarization Enhanced NMR in the Solid-State*, pages 181–228. Springer Berlin Heidelberg, Berlin, Heidelberg, 2013.

[51] S. Y. Liao, M. Lee, T. Wang, I. V. Sergeyev, and M. Hong. Efficient DNP NMR of membrane proteins: sample preparation, protocols, sensitivity, and radical location. *J. Biomol. NMR*, 64:223–237, 2016.

[52] T. Harris, O. Szekely, and L. Frydman. On the potential of hyperpolarized water in biomolecular NMR studies. *J. Phys. Chem. B*, 118(12):3281–3290, 2014.

[53] B. Vuichoud, J. Milani, Q. Chappuis, A. Bornet, G. Bodenhausen, and S. Jannin. Measuring absolute spin polarization in dissolution-DNP by spin PolarimetrY Magnetic Resonance (SPY-MR). *Journal of Magnetic Resonance*, 260:127 – 135, 2015.

[54] A. Bornet, R. Melzi, S. Jannin, and G. Bodenhausen. Cross polarization for dissolution dynamic nuclear polarization experiments at readily accessible temperatures 1.2 K < T < 4.2 K. *App. Magn. Reson.*, 43:107–117, 2012.

[55] D. Kurzbach, E. Canet, A. G. Flamm, A. Jhajharia, E. M. M. Weber, R. Konrat, and G. Bodenhausen. Investigation of intrinsically disordered proteins through exchange with hyperpolarized water. *Ang. Chem. Inter. Ed.*, 56(1):389–392, 2017.

[56] O. S. Leifson and Eric Vogel. Observation of the influence of electron-pair spin flips on nuclear thermal relaxation. *Phys. Rev. B*, 2:4626–4631, 1970.

[57] K. Thurber and R. Tycko. Theory for cross effect dynamic nuclear polarization under magic-angle spinning in solid state nuclear magnetic resonance: The importance of level crossings. *J. Chem. Phys*, 137:084508, 08 2012.

[58] T. V. Can, Q. Z. Ni, and R. G. Griffin. Mechanisms of dynamic nuclear polarization in insulating solids. *J. Magn. Res.*, 253:23–35, 2015.

[59] A. V. Kessenikh, V. I. Lushchikov, A. A. Manenkov, and Y. V. Taran. Proton polarization in irradiated polyethylenes. *Sov. Phys.-Sol. St. (Eng. Transl.)*, 5, 8 1963.

[60] A. V. Kessenikh, A. A. Manenkov, and G. I. Pyatnitskii. On explanation of experimental data on dynamic polarization of protons in irradiated polyethylenes. *Soviet Phys.-Solid State (English Transl.)*, 6, 9 1964.

[61] C. F. Hwang and D. A. Hill. Phenomenological model for the new effect in dynamic polarization. *Phys. Rev. Lett.*, 18:110–112, 1967.

[62] A. B. Barnes, G. De Paëpe, P. C. A. van der Wel, K.-N. Hu, C.-G. Joo, V. S. Bajaj, M. L. Mak-Jurkauskas, J. R. Sirigiri, J. Herzfeld, R. J. Temkin, and R. G. Griffin. High-field dynamic nuclear polarization for solid and solution biological NMR. *App. Magn. Reson.*, 34(3):237–263, 2008.

[63] A. J. Rossini, J. Schlagnitweit, A. Lesage, and L. Emsley. High-resolution NMR of hydrogen in organic solids by DNP enhanced natural abundance deuterium spectroscopy. *J. Magn. Reson.*, 259:192–198, 2015.

[64] A. Zagdoun, G. Casano, O. ouari, M. Scwarzwälder, A. J. Rossini, F. Aussenac, M. Yulikov, G. Jeschke, C. Copéret, A. Lesage, P. Tordo, and L. Emsley. Large molecular weight nitroxide biradicals providing efficient dynamic nuclear polarization at temperatures up to 200 K. *J. Am. Chem. Soc.*, 135:12790–12797, 2013.

[65] Y. Matsuki, T. Maly, O. Ouari, H. Karoui, F. Le Moigne, E. Rizzato, S. Lyubenova, J. Herzfeld, T. Prisner, P. Tordo, and R. G. Griffin. Dynamic nuclear polarization with a rigid biradical. *Angew. Chem. Int. Ed.*, 48(27):4996–5000.

[66] A. Zagdoun, G. Casano, O. Ouari, G. Lapadula, A. J. Rossini, M. Lelli, M. Baffert, D. Gajan, L. Veyre, W. E. Maas, M. Rosay, R. T. Weber, C. Thieuleux, C. Coperet, A. Lesage, P. Tordo, and L. Emsley. A slowly relaxing rigid biradical for efficient dynamic nuclear polarization surface-enhanced NMR spectroscopy: Expeditious characterization of functional group manipulation in hybrid materials. *J. Am. Chem. Soc.*, 134(4):2284–2291, 2012.

[67] C. Ysacco, H. Kaoui, G. Casano,

F. Le moigne, S. Combes, A. Rockenbauer, M. Rosay, W. Maas, O. Ouari, and P. Tordo. Dinitroxides for solid state dynamic nuclear polarization. *App. Magn. Reson.*, 43:251–261, 2012.

[68] F. A. Perras and M. Priski. In silico design of DNP polarizing agents: Can current dinitroxides be improved? *Chem. Phys. Chem.*, 18:2279–2287, 2017.

[69] L. F. Pinto, I. Marin-Montesinos, V. Lloveras, J. L. Munoz-Gomez, M. Pons, J. Veciana, and J. Vidal-Gancedo. NMR signal enhancement of ¿50 000 times in fast dissolution dynamic nuclear polarization. *Chem. Commun.*, 53:3757–3760, 2017.

[70] C. Ysacco, E. Rizzato, M.-A. Virolleaud, H. Karoui, A. Rockenbauer, F. Le Moigne, D. Siri, O. Ouari, R. G. Griffin, and P. Tordo. Properties of dinitroxides for use in dynamic nuclear polarization (DNP). *Phys. Chem. Chem. Phys.*, 12:5841–5845, 2010.

[71] E. L. Dane, B. Corzilius, E. Rizzato, P. Stocker, T. Maly, A. A. Smith, R. G. Griffin, O. Ouari, P. Tordo, and T. M. Swager. Rigid orthogonal bis-tempo biradicals with improved solubility for dynamic nuclear polarization. *J. Org. Chem.*, 77:1789–1797, 2012.

[72] G. Mentink-Vigier, F.and Mathies, Y. Liu, A.-L. Barra, M. A. Caporini, D. Lee, S. Hediger, R. G. Griffin, and G. De Paëpe.

[73] F. Mentink-Vigier, S. Paul, D. Lee, A. Feintuch, S. Hediger, S. Vega, and G. De Paëpe. Nuclear depolarization and absolute sensitivity in magic-angle spinning cross effect dynamic nuclear polarization. *Phys. Chem. Chem. Phys.*, 17(1):21824–21836, 2015.

[74] K. R. Thurber and R. Tycko. Perturbation of nuclear spin polarizations in solid state NMR of nitroxide-doped samples by magic-angle spinning without microwaves. *J. Chem. Phys.*, 140(18):184201, 2014.

[75] B. N. Provotorov. *Soviet Phys. JEPT*, 14:1126, 1962.

[76] A. G. Redfield. Nuclear magnetic resonance saturation and rotary saturation in solids. *Phys. Rev.*, 98:1787–1809, 1955.

[77] A. Abragam and M. Goldman. Principles of dynamic nuclear polarisation. *Rep. Prog. Phys.*, 41:397 – 467, 1978.

[78] Solomon. *Magnetic and Electric Resonance and Relaxation*. North-Holland, 1963.

[79] A. Abragam and W. G. Proctor. Spin temperature. *Phys. Rev.*, 109:1441–1458, Mar 1958.

[80] A. Abragam and M. Borghini. *Chapter VIII Dynamic Polarization of Nuclear Targets*, volume 4 of *Progress in Low Temperature Physics*. Elsevier, 1964.

[81] S. F. J. Cox, V. Bouffard, and M. Goldman. The coupling of two nuclear zeeman reservoirs by the electronic spin-spin reservoir. *J. Phys. C: Sol. St. Phys.*, 6(5):L100, 1973.

[82] S. A. Dzuba and A. Kawamori. Selective hole burning in EPR: Spectral diffusion and dipolar broadening. *Concepts Magn. Reson.*, 8(1):49–61, 1996.

[83] V. A. Atsarkin and A. V. Kessenikh. Dynamic nuclear polarization in solids: The birth and development of the many-particle concept. *App. Magn. Reson.*, 43:7–19, 2012.

[84] D. Guarin, S. Marhabaie, A. Rosso, D. Abergel, G. Bodenhausen, K. L. Ivanov, and D. Kurzbach. Characterizing thermal mixing dynamic nuclear polarization via cross-talk between spin reservoirs. *J. Phys.*

Chem. Lett., 8(22):5531–5536, 2017.

[85] M. Filibian, E. Elisei, S. Colombo Serra, A. Rosso, F. Tedoldi, A. CesÃro, and P. Carretta. Nuclear magnetic resonance studies of dnp-ready trehalose obtained by solid state mechanochemical amorphization. *Phys. Chem. Chem. Phys.*, 18:16912–16920, 2016.

[86] M. Borghini. Spin-temperature model of nuclear dynamic polarization using free radicals. *Phys. Rev. Lett.*, 20:419–421, 1968.

[87] W. T. Wenckebach, T. J. B. Swanenburg, and N. J. Poulis. Thermodynamics of spin systems in paramagnetic crystals. *Phys. Rep.*, 14(5):181 – 255, 1974.

[88] C. Sauvée, G. Casano, S. Abel, A. Rockenbauer, D. Akhmetzyanov, H. Karoui, D. Siri, F. Aussenac, W. Maas, R. T. Weber, T. Prisner, M. Rosay, P. Tordo, and O. Ouari. Tailoring of polarizing agents in the bturea series for cross-effect dynamic nuclear polarization in aqueous media. *Chem. Europ. J.*, 22(16):5598–5606.

[89] C. T. Farrar, D. A. Hall, G. J. Gerfen, S. J. Inati, and R. G. Griffin. Mechanism of dynamic nuclear polarization in high magnetic fields. *J. Chem. Phys.*, 114(11):4922–4933, 2001.

[90] Y. Hovav, A. Feintuch, and S. Vega. Theoretical aspects of dynamic nuclear polarization in the solid state - the cross effect. *J. Magn. Res.*, 214(1):29–41, 2012.

[91] D. Banerjee, D. Shimon, A. Feintuch, S. Vega, and D. Goldfarb. The interplay between the solid effect and the cross effect mechanisms in solid state ^{13}C DNP at 95GHz using trityl radicals. *J. Magn. Reson.*, 230:212 – 219, 2013.

[92] D. Shimon, Y. Hovav, A. Feintuch, D. Goldfarb, and S. Vega. Dynamic nuclear polarization in the solid state: a transition between the cross effect and the solid effect. *Phys. Chem. Chem. Phys.*, 14:5729–5743, 2012.

[93] G. R. Khutsishvili. Spin diffusion and nuclear magnetic relaxation in a crystal containing a magnetic impurity. *Sov. Phys. Uspekhi*, 11(6):802, 1969.

[94] W. T. Wenckebach. The solid effect. *Applied Magnetic Resonance*, 34(3):227, 2008.

[95] C. Ramanathan. Dynamic nuclear polarization and spin-diffusion in non-conducting solids. *Appl. Magn. Reson.*, 34:409–421, 2007.

[96] S. Pylaeva, K. L. Ivanov, D. Sebastiani, and H. Elgabarthy. Dynamic nuclear polarization and spin-diffusion in non-conducting solids. *J. Phys. Chem. Lett.*, 8(10):2137–2142, 2017.

Chapter 2

Experimental set up

2.1 D-DNP system and polarizer

2.1.1 The dissolution system

Dissolution DNP (D-DNP) enables to obtain enhancements up to 10^4 of NMR signals in liquid state. The principle of this technique relies on 1) cooling down the sample to a cryogenic temperature, 2) a transfer of polarization from electrons to surrounding nuclei which is driven by a microwave irradiation and 3) a detection at high field and room temperature of the nuclear signal. Two different apparatuses are consequently required: the first one enables to perform DNP at low temperature whereas the second is used for detection.[1] To bring a sample from its solid state inside the polarizer to liquid state in another NMR spectrometer for detection at room temperature, hot D_2O at 10 to 10.5 bar pressure is released inside the probe through a "dissolution" stick that is inserted inside the sample stick and connected to a pressure vessel. Typically, 5 mL of heavy water are injected. After dissolution of the sample it is propelled with approximately 7 bar gaseous He via a "magnetic tunnel" towards the detection NMR spectrometer (cf Fig. 2.1).

The magnetic tunnel is composed of an assembly of small magnets and has been especially designed to prevent the hyperpolarized nuclei from experiencing passages

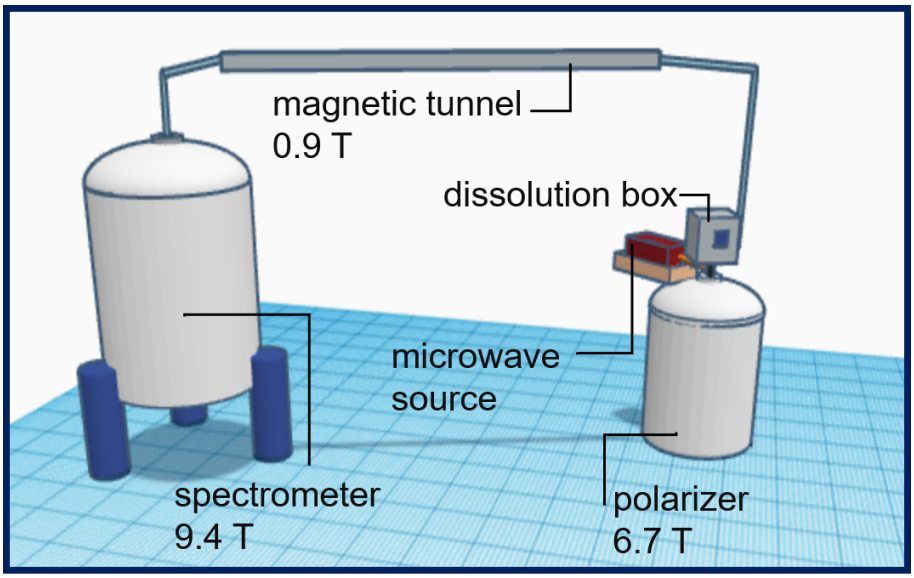

Figure 2.1: Dissolution DNP set up. A 9.4 T magnet for liquid state NMR is connected to a DNP apparatus in which the sample is hyperpolarized. Approximately 5 mL of D_2O is heated and pressurized in the "dissolution box" and released inside the probe to dissolve the frozen hyperpolarized sample. Once it has been dissolved, the sample is propelled by 7 bar gaseous He through a magnetic tunnel. The liquid sample typically reaches the high field NMR magnet 1.3 to 4 s after the beginning of the dissolution.

through zero field that would lead to fast relaxation and loss of NMR signals during the sample transfer.[2] The transfer typically takes between 1.3 and 4 s depending on the desired final volume of the sample in the NMR tube for detection.

2.1.2 The polarizer

The DNP apparatus (commonly called a "polarizer") is a 6.7 T NMR spectrometer that has been specifically modified to enable very low temperature experiments. Its consists of a variable temperature insert (VTI) embedded in its central bore, which can be filled with liquid helium (lHe). lHe is provided via a connected external Dewar. A membrane pump is used to pump lHe from the Dewar to a phase separator compartment (PS) where gaseous helium is separated from the lHe. Two further vacuum pumps enable one to control the pressure within the VTI. To operate the machine around 4 K, atmospheric pressure is sufficient and the use one of these two pumps (the so-called fore-vacuum pump) is sufficient to stabilize the inner volume at a slightly-below-atmospheric pressure around 900 mbar. The second pump (called root pump) enables to cool the system to VTI temperatures down to 1.2 K. With this

system, approximately 100 L of lHe are consumed per week for daily use. The NMR

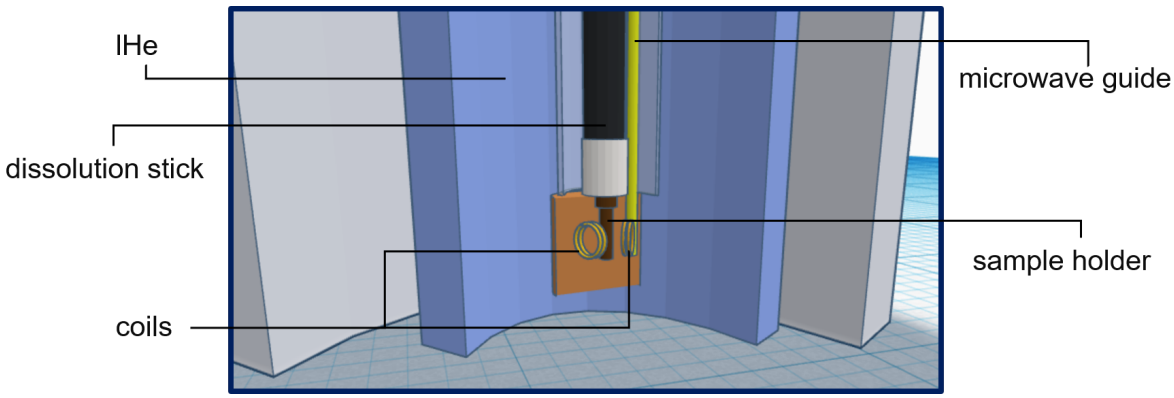

Figure 2.2: Schematic inner volume of the polarizer. The probe contains two different coils that enable one to irradiate the proton and a heteronucleus transitions. It is also equipped with a microwave guide for saturating the spins of the unpaired electrons of the sample. The latter is located inside the sample holder. Liquid He cools down all of these components between 4 and 1.2 K. Once the sample is fully hyperpolarized, the dissolution stick is directly inserted into the probe and guides the hot pressurized D_2O to melt the solid sample.

probe is immersed in the lHe bath in the polarizer. Its design allows it to withstand strong temperature gradients, which is required during dissolution. (cf section 2.1.1) Two radiofrequency coils, one for protons and another for heteronuclei (^{13}C, ^{2}H or ^{31}P) enable one to perform cross-polarization (see section 2.2.4) experiments. Samples are introduced in a PTFE samples holder, which can be screwed onto ca. 1.5 m long graphene stick that can be inserted from the top of the polarizer to guide the sample to its destination. Graphene has been chosen due to its robustness as "sample stick" material. Finally, a microwave guide has been built directly into the probe. It irradiates the central part of the sample by guiding the microwaves from an ELVA-1 source located outside the spectrometer to the sample. The former sends microwaves at 94 GHz, which does not allow one to excite the electron spins in an external magnetic field of 6.7 T. Under these conditions, the frequency must be doubled to ca. 188.2 GHz. The microwave frequency is therefore led through a Virginia Diodes frequency doubler, which is located between the generator and the probe. Microwaves are finally modulated by a 1 kHz saw-tooth signal over a 10 to 100 MHz bandwidth.[3] Microwave modulation enables to saturate a larger fraction of the EPR spectrum, which results in higher polarizations.

2.1.3 NMR spectrometers

Two high field Bruker spectrometers are connected to the polarizer and can be used for detection in D-DNP experiments that are performed at the ENS laboratory. They enable one to acquire spectra of dissolved samples at two different magnetic fields: 18.8 T and 9.4 T (corresponding to 800 and 400 MHz proton Larmor frequencies). The field and magnet is chosen depending on the characteristics of the chemicals and the properties that we want to investigate. For example, phosphorus nuclei are commonly featuring strong chemical shift anisotropy inducing fast relaxation at high field[4]. If we want to monitor the temporal evolution of a phosphorus signal, it is therefore advantageous to transfer the hyperpolarized sample from the polarizer to the lower field magnet. In chapter 6, we apply the D-DNP technique to detect hyperpolarized ^{31}P signals at 162 MHz using a Bruker BroadBand Observe (BBO) probe. Such probes contain two independent detection circuits: an inner one, close to the sample and an outer one which is optimized for the excitation of ^{1}H spins at 400 MHz. The first coil is equipped with a tuning system to vary its resonance frequency to match the Larmor frequency of the heteronucleus of interest. Their wide excitation windows enable one to choose the heteronuclear spin for NMR experiments. The inner diameter of the BBO probe enables to insert 10 mm NMR tubes.

2.2 D-DNP samples

2.2.1 Commonly used paramagnetic agents

Even if some high-spin transition metal ions such as Mn^{2+} or some ions from the lanthanide series such as Gd^{3+}[5] have proven to be effective and cheap polarizing agents (PAs) in MAS-DNP[6] and even if a lot of research groups focus their work on the development of new radicals for optimized DNP , TEMPOL (4-hydroxy-1-oxyl-2,2,6,6 -tetramethylpiperidine), TOTAPOL (1-(TEMPO-4-oxy)-3-(TEMPO-4-amino)propan-2-ol)[7], AMUPol[8,9] and trityl[10] (Finland and ox063) remain the most

commonly used PAs in DNP. Biradicals such as TOTAPOL[11] and AMUPol that favor the CE mechanisms are often used in LT-MAS DNP applications. Contrary, the narrow EPR lines of trityl and BDPA[12] enable one to hyperpolarize nuclei through the SE, which is often used in direct DNP of heteronuclei in static samples at low temperatures. Monoradicals such as TEMPOL are commonly used in DNP of protons. Due to their good solubility in aqueous media, they are often used for dissolution DNP experiments. These PAs are also particularly persistent allowing for efficient storage. However, mono-nitroxides such as TEMPOL and TEMPO are not very efficient in DNP of heteronuclei as their electron spin linewidths are quite large favoring TM DNP, which is not very efficient for nuclei with low gyromagnetic ratio.[13]

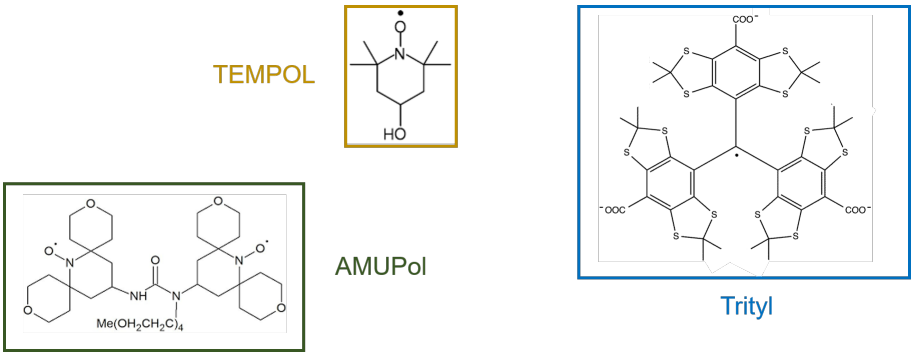

Figure 2.3: Schematic representation of the paramagnetic agents TEMPOL, AMUPol and Trityl (Finland).

2.2.2 Sample preparation

Typical D-DNP experiments require specific samples to boost the efficiency of the polarization. These samples correspond to a mixture of a vitrification agent, water and PAs as wvell as a target molecule of interest. The vitrification agent prevents samples from crystallizing during their fast freezing, which entails a rather homogeneous sample topology and consequently a maximum achievable polarization achievable. In our laboratory, samples composed of 50% of glycerol-d_8, 40% D_2O and 10% H_2O have proven to be widely applicable and efficient for hyperpolarization. In our DNP experiments, we use samples with TEMPOL as PA at concentrations between 30 and 50 mM. Typical sample volumes are 50 to 200 μL.

2.2.3 Heteronuclear DNP

Heteronuclei can be polarized in two different ways: either by a direct DNP process, i.e., SE, CE, TM or OE, or by using cross-polarization (CP) pulse sequences to transfer polarization from 1H to the heteronucleus of choice. This strategy is often used in our laboratory for nuclei with low gyromagnetic ratios such as ^{13}C whose direct build-up times are very long. CP is a very useful technique in NMR that consists in transferring the polarization of a nucleus to another one that possesses a different gyromagnetic ratio. This is method commonly used in MAS ssNMR experiments to obtain information on low gamma nuclei (typically carbon-13, phosphorus-31 or nitrogen-15) while exploiting the polarization of nuclei possessing a high gyromagnetic ratio.[14–16] Combining DNP with CP can significantly reduce the build-up times at cryogenic temperature: in experiments on hyperpolarized glucose, ^{13}C polarization through ^{1}H $\rightarrow$ ^{13}C CP at 1.2 K took less than 45 min to reach 49% polarization, whereas in a direct polarization experiment, this would have taken hours.[17,18]

2.2.4 Detection of the polarization build up

However, as this thesis is mostly focused on ^{1}H polarization, a detailed description of CP-based DNP is beyond the scope of this introduction. The reader is referred to references[19–24].

The sequence used in the DNP experiments to monitor the build-up of the ^{1}H polarization as a function of time is depicted in figure 2.4. During our experiments,

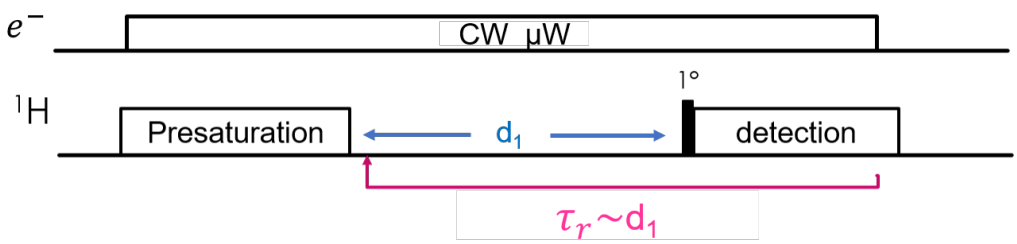

Figure 2.4: Pulse sequence used to monitor the build-up of the polarization of a nucleus. d_1 corresponds to the time between the presaturation block and the detection whereas τ_r is the repetition time of the delay and the acquisition blocks.

the sample is continuously irradiated with microwaves. The experiment thus begins with saturating the appropriate transitions in the EPR spectrum to induce the transfer of polarization from electrons to nuclei. On the proton channel, a presaturation block, which is composed of a train of $\frac{\pi}{2}$ pulses with pseudo-random phases, initiates the sequence by removing all nuclear spin coherences and saturating the nuclear Boltzmann polarization. Subsequently, a delay d_1 separates RF pulses with small flip angels (typically 1° for protons) applied in order to detect a small fraction of the total nuclear polarization while avoiding saturation. After each pulse an FID is detected and stored. These steps are repeated until the polarization is high enough. To quantify the build-up, we perform a Fourier transformation (FT) of the temporal signal for each time point and integrate the resonance signal. As the nuclear polarization is proportional to the integral, one can thus monitor the build-up of the polarization (see Fig. 3.1 a). The typical proton build-up time at 4 K is rather short ($\sim 5 - 15$ min in a sample containing 50 mM TEMPOL). This build-up time increases as the temperature decreases and can take 45 to 90 min at 1.2 K. The ^{1}H polarizations that can be obtained at 4 K and 1.2 K are ca. 60% and 95% respectively.

2.3 Electron Paramagnetic Resonance (EPR)

2.3.1 Basic instrumentation

Unlike NMR spectrometers that are characterized according to their static magnetic field, EPR spectrometers are classified according to the frequency of the applied microwaves. Common spectrometers are classified as: X-band (9.5 GHz), Q-band (35 GHz) and W-band (95 GHz). An EPR spectrometer is composed of three main components: a magnet, a cavity and a microwave bridge. Two types of magnets are used in the EPR community depending on the frequency of the microwaves: electromagnets for X and Q band spectrometers and superconducting magnets for W-band or higher frequencies. An important aspect for this thesis, which mostly focuses on nitroxide radicals, is that the inhomogeneous line broadening of electrons

increases with the magnetic field while the intramolecular hyperfine couplings do not depend on the strength of the external magnetic field. Hence, hyperfine splittings dominate the broadening of EPR lines of nitroxides in X-band spectra whereas the g-anisotropy gives rise to the dominant contribution to line broadening in W-band spectra. In the magnet, a cavity creates a steady-state wave at the sample location that has the property of amplifying weak signals.[25] The higher the quality factor of the cavity, the more sensitive the spectrometer. The microwave bridge contains both the microwave source and the detector. It generates a continuous wave at constant power that is guided by the microwave guide to the cavity. The reflected microwaves that come from the sample into the bridge is converted into an electrical current by the detector diode.

2.3.2 Continuous wave EPR

In typical CW EPR experiments, continuous low power microwave irradiation (μW-mW) is applied to a sample, while the magnetic field is swept over the EPR line of the PA. The field is modulated by an oscillating magnetic field with a typical frequency of 1kHz.[26] As a result, CW acquired spectra are the first derivative of the absorption spectra. If necessary, the absorption spectrum can be recovered by line integration. From a mathematical viewpoint, one could say that this method increases the sensitivity of CW EPR as integration of a spectrum increases the apparent SNR, but the SNR is not changed due to microwave modulation. CW EPR is particularly useful to get information on paramagnetic proteins.[27] A broadening of the spectra of a pair of nitroxides that are specifically attached to a biological macromolecule can be detected when the distance between the two interacting unpaired electron spins is between 8 and 25 Å.[28] As the dipolar interaction strength d depends on the spin-spin distance r ($d \propto \frac{1}{r^3}$), the closer the spins, the broader the corresponding spectra. A convolution of the spectrum of a non-interacting spin with a broadening function thus enables one to extract the electron spin-spin distance, which gives information on the structure of the protein target.[29–32] This method is accurate in cases where electron spin labels are immobilized. Such a condition is rarely fulfilled in liquid state[33] but freezing the sample generally solves the prob-

lem.[34,35] In addition to structural information, SDSL also gives access to dynamic properties of labeled proteins.[36,37] The broadening of nitroxide spectra is affected by molecular motions. Some complex computationnal models have been developed to estimate the mobility of nitroxides,[38] characteristic times of molecular diffusion[39] and local motions[40] if the protein crystal structure is known. In this thesis, we use the CW technique for two different purposes: 1) simulating the X-band spectrum enables us to extract parameters such as the g values (g_{xx}, g_{yy}, g_{zz}) with x, y and z axis that have been defined in the molecular frame (see figure 3.2 c) and the intramolecular hyperfine coupling constants (A_{xx}, A_{yy}, A_{zz}) of CW spectra of the "DNP-juice" provide us with information on the solvent polarity in the vicinity of the unpaired electron[41,42] (see chapters 3 and 4) as it has been shown that the isotropic g (g_{iso}), the isotropic hyperfine coupling (A_{iso}), and the z component of the hyperfine coupling A_{zz} are all affected by solvent properties.

2.3.3 Pulsed EPR

In addition to CW experiments, pulsed EPR experiments can give access to dynamic properties of a sample and to electron spin-spin distances.[43,44] The technique, which has been developed in 1958,[45] is very similar to NMR spectroscopy: while electron spins are polarized in an external magnetic field at low temperature, a short pulse of an oscillating magnetic field (microwave pulse) perturbs the system. The detector acquires the microwaves that are emitted by the electron spins as they relax back to thermal equilibrium. Contrary to CW EPR, pulsed EPR experiments are almost exclusively carried out at low temperatures in the solid state due to fast relaxation of the signals in the liquid state.[46]

The Hahn echo

Even though NMR and pulsed EPR techniques are very similar, their detection processes differ. Contrary to NMR, pulsed EPR spectroscopy does not detect a decaying temporal signal right after a $\frac{\pi}{2}$ pulse. As the receiver is very sensitive, it cannot bear the strong power generated by the pulses. A dead time between the

last pulse of the sequence and the opening of the receiver for the detection is thus necessary to protect the apparatus. Moreover, the electron line is very broad for most of the paramagnetic agents at low temperatures. This generates a fast signal decay, which complicates the extraction of the informations contained in the signal. To protect the spectrometer and to limit the contribution of the inhomogeneous linewidth to the signal decay, a Hahn echo sequence[47] is often preferred as detection scheme (cf Fig. 2.5).

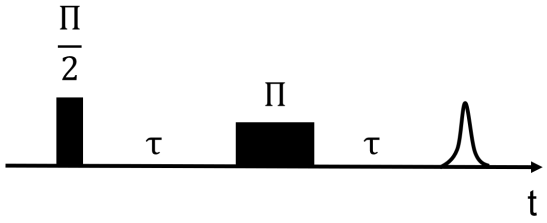

Figure 2.5: Hahn echo detection pulse sequence. The black squares schematically represent the pulses that are applied to the spin system. A $\frac{\pi}{2}$ pulse followed by a π pulse after a delay τ generates an echo signal (white) that is due to the spin rephasing. The receiver is opened to detect the echo.

A classical description of this pulse sequence starts with a first $\frac{\pi}{2}$ pulse that brings the magnetization into the transverse plane, then the dephasing of the different isochromats of the EPR line occurs during a time τ. A π pulse is subsequently applied to invert all spins. This leads to rephasing of all spins after a time τ. This creates a recovery of the electron spin signals and a so-called echo is detected. The Hahn echo block is used in most of the pulsed EPR sequences.

Echo detected inversion recovery

The inversion recovery experiment[48] enables one to measure the electron spin-lattice relaxation time. The sequence consists of a Hahn echo detection block that is preceded by a π pulse. This π pulse is called "inversion pulse" as it drives the electron magnetization from its Boltzmann equilibrium (aligned with the +z axis) to the -z direction. A delay t_1 during which the magnetization partly returns to its equilibrium value follows this pulse. The sequence $\pi - t_1 - \frac{\pi}{2} - \tau - \pi - \tau$ is repeated while incrementing t_1. Thus, each point measures the signal after a different relaxation delay. In a case where all electron spins in a non-interacting spin system experience

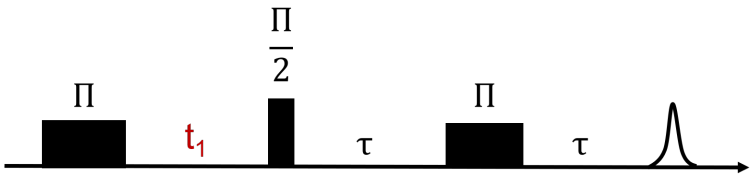

Figure 2.6: Inversion recovery pulse sequence. An inversion pulse π pulse is applied before the Hahn echo block. t_1 is incremented for each acquisition.

the same interaction strength, the evolution of the signal intensity versus the delay t_1 can be fitted using a mono-exponential function.[49] However, when nitroxides are frozen in a glassy matrix, the radicals are randomly oriented in the sample which leads to a distribution of spin-lattice relaxation times.[50] A mono-exponential fit becomes therefore inadequate. Under such conditions, it is often more accurate to model the relaxation of the longitudinal magnetization by a stretched exponential function. The average experimental electronic spin-lattice relaxation time (T_{1e}) can be approximated by the time required for the magnetization to reach 63% of its equilibrium value (cf Fig. 2.7).

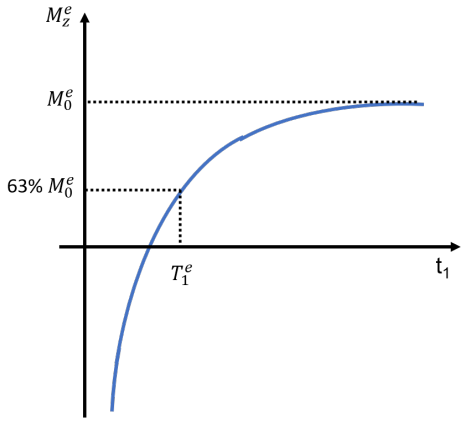

Figure 2.7: Schematic representation of the data acquired during an inversion recovery experiment. At $t_1 = 0$, the electron magnetization M^e has just been inverted by the π pulse. Then, it relaxes back to the magnetization in the Boltzmann equilibrium M_0^e.

Pulsed Electron-Electron Double Resonance

Double Electron-Electron Resonance (DEER) experiments, also known as pulsed electron double resonance (PELDOR) spectroscopy, corresponds to a method that gives access to inter-electronic distances between ca. 1.5 to 10 nm.[51] The basic idea of this sequence is to modulate the amplitude of the echoes by the electron-electron

dipolar couplings. This is realized with the pulse sequence defined in figure 2.8. The different channels in figure 2.8 refer to different microwave frequencies of the

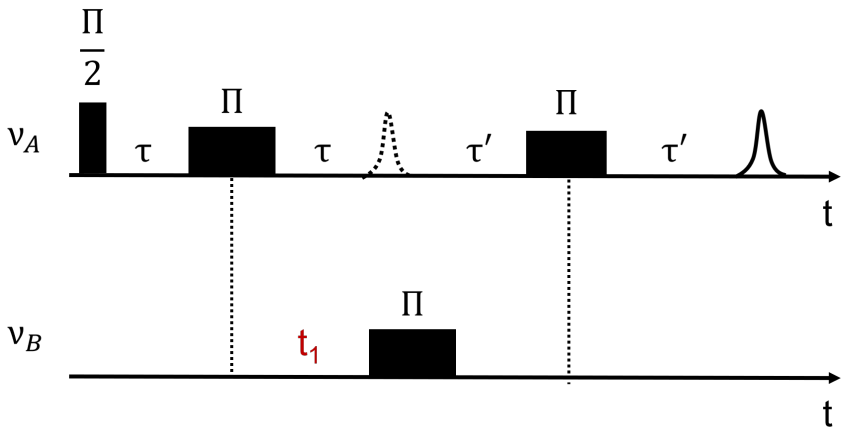

Figure 2.8: : DEER pulse sequence. Selective pulses enable to excite different spin packets (A and B with respective Larmor frequencies ν_A and ν_B) within the EPR line. A refocusing pulse at a frequency ν_A excites and generate a first Hahn echo (dashed line). It is immediately followed by another refocusing pulse ($\tau' - \pi - \tau'$) at the same frequency. A π pulse inverts electron spins at the frequency ν_B between the first and the second π pulse that excites spin packet A. Only t_1 is incremented in this sequence.

pulses. In the case of selective pulses that do not excite the entire width of the EPR spectrum, excitation at the frequency ν_A does not affect the spin packet B with a Larmor frequency ν_B. The DEER sequence is composed of three steps. First, a refocusing pulse excites the electron spin packet A. This creates a first Hahn echo that is not detected (cf dashed echo in figure 2.8). Next, a π pulse inverts spin packet B and finally, an additional π pulse at the frequency ν_A generates a second echo, which is detected. If A and B do not interact, changing the state of spin B has no impact on the detected signal. However, if A and B are coupled through a dipolar interaction, inverting spin packet B modifies the amplitude of the echo signal. Hence, one can modulate the amplitude of the detected echo by incrementing the t_1 delay and get access to the dipolar interaction strength.

Bibliography

[1] J. H. Ardenkjær-Larsen, B. Fridlund, A. Gram, G. Hansson, L. Hansson, M. H. Lerche, R. Servin, M. Thaning, and K. Golman. Increase in signal-to-noise ratio of > 10,000 times in liquid-state NMR. *Proceed. Nat. Acad. Sc.*, 100(18):10158–10163, 2003.

[2] J. Milani, A. Bornet, P. Miéville, R. Mottier, S. Jannin, and G. Bodenhausen. A magnetic tunnel to shelter hyperpolaryzed fluids. *Rev. Sc. Inst.*, 86:024101–1–8, 2015.

[3] A. Bornet, J. Milani, B. Vuichoud, A. J. P. Linde, G. Bodenhausen, and S. Jannin. Microwave frequency modulation to enhance dissolution dynamic nuclear polarization. *Chem. Phys. Lett.*, 602:63–67, 2014.

[4] S. Schott, J. Hahn, Kurbacher C., and Moka D. ^{31}P and ^{1}H nuclear magnetic resonance spectroscopy of blood plasma in female patients with preeclampsia. *IJBS*, 8:258–263, 2012.

[5] J. W. Gordon, S. B. Fain, and I. J. Rowland. Effect of lanthanide ions on dynamic nuclear polarization enhancement and liquid-state T_1 relaxation. *Magn. Reson. Med.*, 68(2):1949–1954, 2012.

[6] B. Corzilius, A. A. Smith, A. B. Barnes, C. Luchinat, I. Bertini, and R. G. Griffin. High-field dynamic nuclear polarization with high-spin transition metal ions. *J. Am. Chem. Soc.*, 133:5648–5651, 2011.

[7] M. J. Prandolini, V. P. Denysenkov, M. Gafurov, S. Lyubenova, B. Endeward, M. ennati, and T. F. Prisner. First DNP results from a liquid water-TEMPOL sample at 400 MHz and 260 GHz. *Appl. Magn. Reson.*, 34:399–407, 2007.

[8] F. Mentink-Vigier, S. Paul, D. Lee, A. Feintuch, S. Hediger, S. Vega, and G. De Paepe. Nuclear depolarization and absolute sensitivity in mafic-angle spinninng croos effect dynamic nulear polarization. *Phys. Chem. Chem. Phys.*, 17(34):21824–21836, 2015.

[9] S. R. Chaudhari, D. Wisser, A. C. Pinon, P. Berruyer, D. Gajan, P. Tordo, O. Ouari, C. Reiter, F. Engelke, C. Coperet, M. Lelli, A. Lesage, and L. Emsley. Dynamic nuclear polarization efficiency increased by very fast magis angle spinning. *J. Am. Chem. Soc.*, 139:10609–10612, 2017.

[10] Juan Carlos Paniagua, Veronica Mugnaini, Cristina Gabellieri, Miguel Feliz, Nans Roques, Jaume Veciana, and Miquel Pons. Polychlorinated trityl radicals for dynamic nuclear polarization: the role of chlorine nuclei. *Phys. Chem. Chem. Phys.*, 12:5824–5829, 2010.

[11] C. Song, K.-N. Hu, C.-J. Joo, T.M. Swager, and R. G. Griffin. TOTAPOL: A biradical polarizing agent for dynamic nuclear polarization experiments in aqueous media. *J. Am. Chem. Soc.*, 128:11385–11390, 2006.

[12] O. Haze, B. Corzilius, A. A. Smith, R. G. Griffin, and T. M. Swager. Water-soluble narrow-line radicals for dynamic nuclear polarization. *J. Am. Chem. Soc.*, 134:14287–14290, 2012.

[13] B. Vuichoud. Novel sample formulations for pure and persistent hyperpolarized solutions via dissolution dynamic nuclear polarization, 2017.

[14] A. Pines, M. G. Gibby, and J. S. Waugh. Proton-enhanced nuclear induction spectroscopy. a method for high resolution nmr of dilute spins in solids. *J. Chem. Phys.*, 56(4):1776–1777, 1972.

[15] M. G. Gibby, A. Pines, and S. Waugh.

Proton-enhanced NMR of dilute spins in solids. *J. Chem. Phys.*, 59:569–590, 1973.

[16] D. Marks and S. Vega. A theory for cross-polarization NMR of nonspinning and spinning samples. *J. Magn. Res. A*, 118(2):157 – 172, 1996.

[17] Sadet A., Weber E. M. M., Jhajharia A., Kurzbach D., Bodenhausen G., Miclet E., and Abergel D. Rates of chemical reactions embedded in a metabolic network by dissolution dynamic nuclear polarisation NMR. *Chem. – Europ. J.*, 24(21):5456–5461, 2017.

[18] A. Bornet, R. Melzi, A. J. P. Linde, P. Haulte, B. van den Brandt, S. Jannin, and G. Bodenhausen. Boosting dissolution dynamic nuclear polarization by cross polarization. *J. Phys. Chem. Lett.*, 4:111–114, 2013.

[19] S. Jannin, A. Bornet, S. Colombo, and G. Bodenhausen. Low-temperature cross polarization in view of enhancing dissolution dynamic nuclear polarization in NMR. *Chem. Phys. Lett.*, 517(4):234 – 236, 2011.

[20] M. Batel, A. Dapp, A. Hunkeler, B. H. Meier, S. Kozerke, and M. Ernst. Cross-polarization for dissolution dynamic nuclear polarization. *Phys. Chem. Chem. Phys.*, 16:21407–21416, 2014.

[21] P. Linde. Application of cross-polarisation techniques to dynamic nuclear polarisation dissolution experiments., 2010.

[22] A. Bornet and S. Jannin. Optimizing dissolution dynamic nuclear polarization. *J. Magn. Res.*, 264:13–21, 2016.

[23] D. Kurzbach, E. M. M. Weber, A. Jhajharia, S. F. Cousin, A. Sadet, S. Marhabaie, E. Canet, N. Birlirakis, J. Milani, S. Jannin, D. Eshchenko, A. Hassan, R. Melzi, S. Luetolf, M. Sacher, M. Rossire, J. Kempf, J. A. B. Lohman, M. Weller, G. Bodenhausen, and D. Abergel. Dissolution dynamic nuclear polarization of deuterated molecules enhanced by cross-polarization. *J. Chem. Phys.*, 145(19):194203, 2016.

[24] A. Bornet, R. Melzi, S. Jannin, and G. Bodenhausen. Cross polarization for dissolution dynamic nuclear polarization experiments at readily accessible temperatures 1.2 K $<$ T $<$ 4.2 K. *App. Magn. Reson.*, 43:107–117, 2012.

[25] G. E. Eaton, S. Eaton, D. P. Barr, and R. T. Weber. *Quantitative EPR*. Springer Science & Business Media Publications, 2010.

[26] V. Chechik, E. Carter, and D. Murphy. *Electron Paramagnetic Resonance*. Oxford Chemistry Primers, New York, 2016.

[27] M. D. Rabenstein and Y. K. Shin. Determination of the distance between two spin labels attached to a macromolecule. *Proc. Nation. Acad. Sc.*, 92(18):8239–8243, 1995.

[28] J. Cooke and L. J. Brown. *Distance measurements by continuous wave EPR spectroscopy to monitor protein folding*, volume 752 of *Methods in Molecular Biology*, pages 73–96. Humana Press Inc., 2011.

[29] F. Zhang, Y. Chen, D.-H. Kweon, C. S. Kim, and Y.-K. Shin. The four-helix bundle of the neuronal target membrane snare complex is neither disordered in the middle nor uncoiled at the c-terminal region. *J. Bio. Chem.*, 277:24294–24298, 2002.

[30] L. J. Brown, K. L. Sale, R. Hills, C. Rouviere, L. Song, X. Zhang, and P. G. Fajer. Structure of the inhibitory region of troponin by site directed spin labeling elec-

tron paramagnetic resonance. *Proc. Nation. Acad. Sc.*, 99(20):12765–12770, 2002.

[31] E. Perozo, D. M. Cortes, and L. G. Cuello. Three-dimensional architecture and gating mechanism of K^+ channel studied by EPR spectroscopy. *Nat. Struc. Bio.*, 5:459–469, 1998.

[32] E. J. Hustedt and A. H. Beth. *Bio. Magn. Res.*, volume 19. Springer, Boston, 2002.

[33] M. Persson, J. R. Harbridge, P. Hammarstrom, R. Mitri, L.-G. Martensson, U. Carlsson, G. R. Eaton, and S. S. Eaton. Comparison of electron paramagnetic resonance methods to determine distances between spin labels on human carbonic anhydrase ii. *Biophys. Journ.*, 80(6):2886 – 2897, 2001.

[34] N.-K. Kim, A. Murali, and V. J. DeRose. A distance ruler for RNA using EPR and site-directed spin labeling. *Chem. Bio.*, 11(7):939 – 948, 2004.

[35] Leigh Jr. J.S. ESR rigid-lattice line shape in a system of two interacting spins. 52:2608–2612, 03 1970.

[36] K. Schorn and D. Marsh. Lipid chain dynamics in diacylglycerol-phosphatidylcholine mixtures studied by slow-motional simulations of spin label ESR spectra. *Chem. Phys. Lip.*, 82(1):7 – 14, 1996.

[37] V. A. Livshits, D. Kurad, and D. Marsh. Simulation studies on high-field EPR spectra of lipid spin labels in cholesterol-containing membranes. *J. Phys. Chem. B*, 108(27):9403–9411, 2004.

[38] K. Sale, C. Sár, K. A. Sharp, K. Hideg, and P. G. Fajer. Structural determination of spin label immobilization and orientation: A monte carlo minimization approach. *Journal of Magnetic Resonance*, 156(1):104 – 112, 2002.

[39] D. E. Budil, K. L. Sale, K. A. Khairy, and P. G. Fajer. Calculating slow-motional electron paramagnetic resonance spectra from molecular dynamics using a diffusion operator approach. *J. Phys. Chem.*, 110:3703–3713, 2006.

[40] S. C. DeSensi, D. P. Rangel, A. H. Beth, T. P. Lybrand, and E. J. Hustedt. Simulation of nitroxide electron paramagnetic resonance spectra from brownian trajectories and molecular dynamics simulations. *Biophys. Journ.*, 94(10):3798 – 3809, 2008.

[41] R. Owenius, M. Engstrom, M. Lindgren, and M. Huber. Influence of solvent polarity and hydrogen bonding on the EPR parameters of a nitroxide spin label studied by 9-GHz and 95-GHz EPR spectroscopy and DFT calculations. *J. Phys. Chem. A*, 105(49):10967–10977, 2001.

[42] T. Kawamura, S. Matsunami, and T. Yonezawa. Solvent effects on the g-value of di-t-butyl nitric oxide. *Bull. Chem. Soc. Japn.*, 40:1111–1115, 1967.

[43] O. Schiemann and T. F. Prisner. Long-range distance determinations in biomacromolecules by EPR spectroscopy. *Quater. Rev. Biophys.*, 40:1–53, 2007.

[44] T. F. Prisner, M. Rohrer, and F. Macmillan. Pulsed EPR spectroscopy: biological applications. *Ann. Rev. Phys. Chem.*, 52:279–313, 2001.

[45] R. J. Blume. Electron spin relaxation times in sodium-ammonia solutions. *Phys. Rev.*, 109:1867–1873, 1958.

[46] D. R. Vij. *Handbook of Applied Solid State Spectroscopy*. Springer, Boston, Massachusetts, 2006.

[47] E. L. Hahn. Spin echoes. *Phys. Rev.*, 80:580–594, 1950.

[48] E. Hoffman and A. Shweiger. Inversion-recovery detected EPR. *App. Magn. Res.*, 9:1–22, 1995.

[49] S. Eaton and Eaton G. R. Multifrequency pulsed EPR and the characterization of molecular dynamics. *Meth. Enzymol.*, 563:37–58, 2015.

[50] J.L. Du, G.R. Eaton, and S.S. Eaton. Temperature, orientation, and solvent dependence of electron spin-lattice relaxation rates for nitroxyl radicals in glassy solvents and doped solids. *Journal of Magnetic Resonance, Series A*, 115(2):213 – 221, 1995.

[51] G. Jeschke. DEER distance measurements on proteins. *An. Rev. Phys. Chem.*, 63(1):419–446, 2012.

Chapter 3

Anisotropic longitudinal electronic relaxation affects DNP at cryogenic temperatures

3.1 Introduction

As previously explained in this thesis, the main purpose of Dynamic nuclear polarization (DNP) is to overcome one of the major limitations of NMR, namely the intrinsically low sensitivity by obtaining high polarization levels of nuclear spins.[1–3] DNP requires the presence of paramagnetic agents and combines electron paramagnetic resonance (EPR) with nuclear magnetic resonance (NMR). The irradiation of unpaired electron spins by microwaves eventually leads to the enhancement of the nuclear polarization, most efficiently for protons (for a review see Abragam and Goldman[1]). Polarization levels $P(^1\mathrm{H}) > 90\%$ can be achieved at cryogenic temperatures between 1.2 and 4.2 K.[4–6] The mechanisms that are responsible for the transfer of polarization from electrons to protons are complex and depend on many factors, including the type and concentration of mono- or bi-radicals used for DNP, the field strength, temperature, solvent, and sample heterogeneity. Typically, one distinguishes between different models to describe DNP in the solid state under varying conditions. The most prominent examples are the solid effect (SE), the

cross effect (CE), and thermal mixing (TM) (see section 1.2).[1,5]

TM-based hyperpolarization processes can occur when the EPR linewidth of the radical exceeds the nuclear Larmor frequency. In this case, electronic and nuclear spins are associated with distinct heat reservoirs that are characterized by distinct spin temperatures. Due to the presence of dipole– dipole couplings between the electrons, one should distinguish Zeeman and non-Zeeman electron reservoirs. Only the latter is coupled to the nuclear Zeeman bath via hyperfine interactions. Microwave irradiation induces a coupling and dynamic cooling of the two electron baths, which eventually leads to a cooling of the nuclear Zeeman bath in cases where electronic spectral diffusion is fast (cf section 1.2.7).

The CE mechanism that underlies TM-based DNP is most efficient if two distinct EPR transitions feature a difference in resonance frequencies that matches the NMR transition. It is therefore frequently observed in the presence of bi-radicals but (in contrast to TM) does not require fast spectral diffusion. The SE requires EPR linewidths that are narrow with respect to the NMR Larmor frequency. This condition enables a flow of polarization from the electron spins to the nuclei via forbidden flip-flop transitions driven by the pseudo-secular part of the electron–nuclear hyperfine interaction (section 1.2.3).[7] In this contribution, we investigate the role of the electronic longitudinal relaxation time $T_{1e}(\omega)$, which is an important parameter for almost all DNP models. We investigate this parameter for TEMPOL (4-hydroxy-2,2,6,6-tetramethylpiperidin-1- oxyl) nitroxide radicals, which feature very broad EPR spectra, where, in addition to anisotropic g-tensors that describe the resonance frequencies of the different spectral components, the linewidth is partly due to hyperfine interactions involving the ^{14}N nuclei of the NO moiety. Despite recent developments of sophisticated models and extensive experimental studies of nitroxide-based DNP[8–14], the anisotropy of electronic longitudinal relaxation has so far been neglected, because it was assumed that fast electronic spectral diffusion (eSD) effectively averages $T_{1e}(\omega)$ across the entire EPR spectrum. However, under our experimental conditions we predict an incomplete averaging and show the impact of experimentally measured $T_{1e}(\omega)$ variations across the EPR spectrum. We demonstrate how anisotropic $T_{1e}(\omega)$ can be incorporated into simple models

for DNP.[15] Moreover, $T_{1e}(\omega)$ critically depends on the solvents used to form the glassy DNP matrix at low temperatures. Understanding these effects allows one to optimize DNP protocols and to shed new light on the connections between DNP enhancements and properties of EPR spectra.

3.2 Material and methods

3.2.1 DNP

DNP data were acquired on a Bruker prototype system operating at 6.7 T (ca. 285 MHz Larmor frequency for protons and 188.2 GHz for electrons) equipped with doubly tuned radio frequency (RF) coils immersed in liquid helium. All experiments were performed at 4.2 K. To saturate the EPR transitions, continuous microwave irradiation was applied between 187.6 and 188.5 GHz, with a transmitted power of about 12 mW at the position of the sample, generated by a 94.1 GHz ELVA-1 source combined with a Virginia Diodes frequency doubler. The microwave frequency was modulated by a 2 kHz saw-tooth signal over a range of 10 MHz.[16,17]

3.2.2 EPR

X-band CW EPR measurements at 6 K were performed in Lille on a Bruker ElexSys 580 spectrometer equipped with a Bruker Flexline split ring (9.4–9.7 GHz near 0.335 T). Field-swept continuous-wave spectra were obtained by modulating the B_1 field at 100 kHz in combination with phase-sensitive detection. The resulting spectra thus appear as first derivatives of the absorption line, not to be confused with dispersion spectra. The field-dependence of the longitudinal electron relaxation times $T_{1e}(\omega)$ was measured at 6 K at Lille on the same X-band spectrometer and at ETH on a Bruker W-band ElexSys E680 EPR spectrometer (ca. 94 GHz at ca. 3.3 T). Echo-detected inversion recovery experiments were performed with 200 or 400 ns echo delays, recovery delays of 0–0.5 s and a recycling delay of 0.51 s at X-band and 0–1 s and 1.12 s at W-band, respectively. Selective inversion pulses between

16 and 20 ns length (depending on the radical concentration) length were used to excite only a narrow frequency band within the EPR spectrum, covering a width of approximately 1.8–2.3 mT.

3.2.3 Sample preparation

For DNP experiments, the samples were loaded in cylindrical cups made of polytetrafluoroethylene (PTFE), a material that does not contain any protons and therefore does not contribute to background signals. Sample A consisted of a 25 mM solution of paramagnetic 4-hydroxy-2,2,6,6-tetramethylpiperidine-1-oxyl (TEMPOL) in a mixture of glycerol-d_8 (50%), D_2O (40%) and H_2O (10%). The glass-forming agent glycerol prevents crystallization at low temperatures. Sample B consisted of a 25 mM TEMPOL solution in 90% ethanol-d_6 and 10% non-deuterated ethanol. For EPR experiments, samples A and B were loaded in quartz tubes with 4 and 1 mm inner diameters for X-band and W-band experiments, respectively. The concentration was varied between 1 and 50 mM for $T_{1e}(\omega)$ measurements (indicated in the text), for CW EPR at X-band concentrations of 1 mM were used.

3.2.4 Data analysis

All NMR data were processed with NMRPipe.[18] The free induction decay signals were zero-filled, but not apodized to retain the natural line shapes. After Fourier transformation, the spectra were fitted to theoretical models with home-written scripts using MATLAB. CW and absorption-mode EPR spectra were simulated using the well-known EasySpin package.[19,20]

3.2.5 Experimental design

One of our objectives was to rationalize "proton DNP profiles", i.e., the dependence of the proton polarization $P(^1\mathrm{H})$ on the microwave irradiation frequency. The microwave frequency was incremented in steps of 20 MHz between 187.580 and 188.460

GHz over a range of 880 MHz, limited by the sweep width of our microwave source. The full EPR spectrum extends over ca. 1000 MHz approximately from 187.6 GHz to 188.6 GHz. At each applied microwave frequency, a spin packet with a width of ca. 20 MHz was saturated using microwave frequency modulation. Spectral diffusion causes this saturation to propagate partly to neighbouring spin packets, as discussed below. For each microwave frequency, the build-up of the proton signal, which is proportional to the proton polarization $P(^1\mathrm{H})$, was detected every 5 s using 1° flip angle RF pulses. Typically, the build-up of the proton polarization occurs within a few minutes when saturating near the centre of the EPR spectrum, but can be much slower (hours) near the edges of the EPR spectrum, where the populations of the irradiated spin packets are small. It is therefore cumbersome to follow the complete build-up of the proton polarization all the way up to its steady-state at every microwave frequency. However, to a good approximation, the polarization build-up is monoexponential at all microwave frequencies. Hence, we monitored each build-up curve over a sufficiently long period (up to $\sim 50\%$ of its plateau) to allow extrapolation to the steady-state. This is illustrated in Fig. 3.1 a for sample A at 4

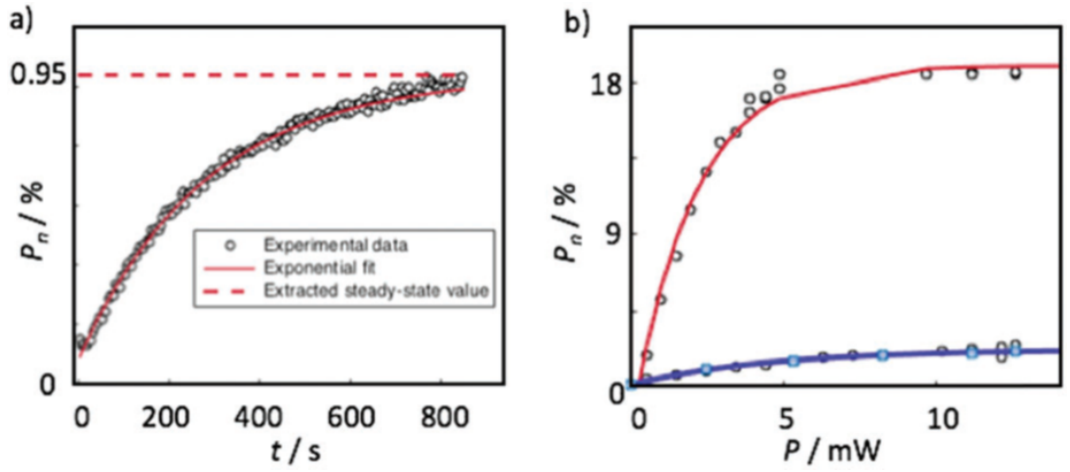

Figure 3.1: (a) Initial build-up of nuclear polarization as a function of time when saturating the low-field edge of the EPR spectrum (near 187.6 GHz). The experimental data has been fitted to a mono-exponential function (red). The dashed line indicates the steady-state nuclear polarization estimated by extrapolation. (b) ^{1}H nuclear polarization as a function of microwave power applied at the centre of the EPR spectrum (red, 187.9) or at its outermost low-field edge (blue, 187.6 GHz). Above 12 mW of transmitted power no significant change can be observed, indicating that the corresponding bands in the EPR spectrum are fully saturated.

K near the low-field (187.6 GHz) edge of the EPR spectrum. Fig. 3.1 b shows that the measured proton polarization, does not change when the transmitted microwave

power is increased beyond 12 mW. This is observed both in the centre and at an edge of the EPR line, indicating that the irradiated spin packets are always fully saturated in our experiments. Hence, slow build-ups near the edges do most-likely not stem from incomplete saturation.

3.3 Results and discussion

To predict the nuclear polarization with various DNP models one needs to record the EPR spectrum, which was not possible with our apparatus at 4 K and 6.7 T (central frequency: 188.2 GHz). For the case at hand, we therefore simulated the relevant EPR line shape, using parameters determined at 6 K and 9.4 GHz (X-band, central field: 0.335 T). Our simulations led to the following EPR parameters for sample A (water–glycerol matrix): A_{xx} = 19.8 MHz, A_{yy} = 22.1 MHz, A_{zz} = 108 MHz, g_{xx} = 2.00908, g_{yy} = 2.00554, g_{zz} = 2.00233. For sample B (90% ethanol-d6 and 10% protonated ethanol), we found A_{xx} = 19.9 MHz, A_{yy} = 25.2 MHz, A_{zz} = 98.1 MHz, g_{xx} = 2.01090, g_{yy} = 2.00676, g_{zz} = 2.00330. These parameters determined at a concentration of 1 mM TEMPOL allowed us to simulate EPR spectra that are relevant for our DNP experiments at 4 K and 6.7 T (central frequency: 188.2 GHz), as shown in Fig. 3.2 b. This absorption-mode spectrum corresponds to the integral of the derivative spectrum in Fig. 3.2 a. Fig. 3.2 c illustrates how different directions (x, y, z) of the principal axis system (PAS) correspond to the molecular frame of TEMPOL. The values obtained by spectral simulations match published data.[21]

Simulations of the EPR spectra take into account both the anisotropic g-, and **A**-tensors of TEMPOL radicals, determined with the EasySpin routines developed by Stoll et al.[19,20] The homogeneous linewidth as well as weak hyperfine and dipolar couplings were accounted for by a mixed Voigtian convolution.

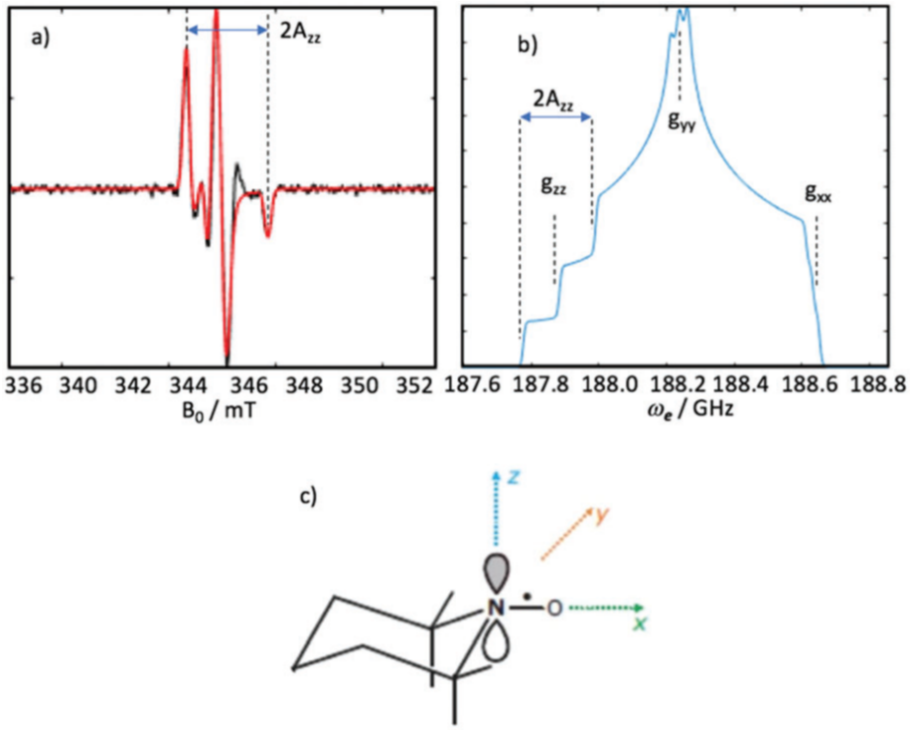

Figure 3.2: (a) Experimental (black) field-swept derivative EPR spectrum of 1 mM TEMPOL in a water/glycerol mixture at 6 K and 9.6 GHz (X-band). The simulated spectrum is superimposed and depicted in red. (b) Simulated absorption line shapes at 6.7 T where the DNP experiments were carried out, using parameters obtained from the fit in (a). (c) Molecular frame and principal axis system for nitroxides.

Table 3.1: Left: $T_{1e}(\Delta_i)$ values found for the five positions indicated in Fig. 3.3 for sample A. Right: $T_{1e}(\Delta_i)$ values found at six field positions indicated in Fig. 3.3 for sample B. All values were determined at W-band (94.1 GHz, central field 3.35 T, 1 mM TEMPOL)

Sample A		Sample B	
B_0 / mT	$T_{1e}(\omega)$ / ms	B_0 / mT	$T_{1e}(\omega)$ / ms
3344.3	124	3341.7	5
3348.0	30	3345.0	11
3351.7	46	3348.2	6
3355.4	127	3351.5	13
3359.1	272	3354.8	30
		3358.1	79

3.3.1 Electron spin relaxation times

For both samples A and B, field-dependent electron relaxation times $T_{1e}(\omega)$ have been determined at 6 K at W-band (94.1 GHz, central field 3.35 T, 1 mM TEMPOL) at selected field positions corresponding to different spin packets, as indicated in Fig. 3.3 together with the measured relaxation times $T_{1e}(\omega)$. The latter are also

listed in Table 3.1. Clearly, the relaxation times $T_{1e}(\omega)$ vary significantly across the EPR line shape, by more than an order of magnitude. The value of $T_{1e}(\omega)$ generally depends on the coupling of the electrons to the phonons in the solid matrix in which the radicals are dispersed. For nitroxides, this coupling is generally mediated via the spin–orbit coupling of the unpaired electrons.[7] The origin of the non-uniformity of the $T_{1e}(\omega)$ relaxation times of the electrons can thus be ascribed to the electronic orbitals of the electrons (the singly occupied π^* molecular orbital (SOMO) in NO moieties) which are intrinsically anisotropic, leading to orientation-dependent couplings of the SOMO to the phonons. Additionally, orientation-dependent dipolar couplings can also play a minor role. We will refer in the following to this nonuniform relaxation as "anisotropic" $T_{1e}(\omega)$. The values in Fig. 3.3 have been determined at a TEMPOL concentration of 1 mM. With respect to DNP where we use much higher concentrations it is important to note that we observed an anisotropic behaviour of $T_{1e}(\omega)$ at 6 K up to TEMPOL concentrations of 50 mM at W-band of 94.1 GHz (for the principle components of the g-tensor we found, g_{xx}: $T_{1e}(\omega) =$ 52.17 ms, g_{yy}: $T_{1e}(\omega) = 14.99$ ms, g_{zz}: $T_{1e}(\omega) = 63.01$ ms). We observed comparable, anisotropic relaxation times of $T_{1e}(\omega) = 70$, 39 and 31 ms for $M_I(^{14}\mathrm{N}) = +1$, 0 and -1, respectively, at X band (9.4 GHz, central field 0.335 T, 50 mM TEMPOL), indicating that the relaxation times do not strongly depend on the field. We shall assume that this also holds for our DNP experiments that have been performed at approximately twice the field used in W-band EPR studies. Furthermore, similar anisotropic behaviour was observed at higher temperatures of 100 K. Our results are in agreement with the observations of Eaton, Eaton and co-workers who reported similar anisotropic relaxation for nitroxides between 20 and 150 K.[22]

3.3.2 Electronic spectral diffusion

The mechanisms of nitroxide-based DNP have been investigated in detail by Griffin, Wenckebach, Vega and their co-workers[8,13,23–27] who discussed in some detail the influence of electronic spectral diffusion (eSD) on nitroxide DNP, which spreads the polarization of a spin packet across the EPR spectrum via flip-flops of dipolarcoupled electrons, thereby averaging relaxation times. If eSD were infinitely fast, we

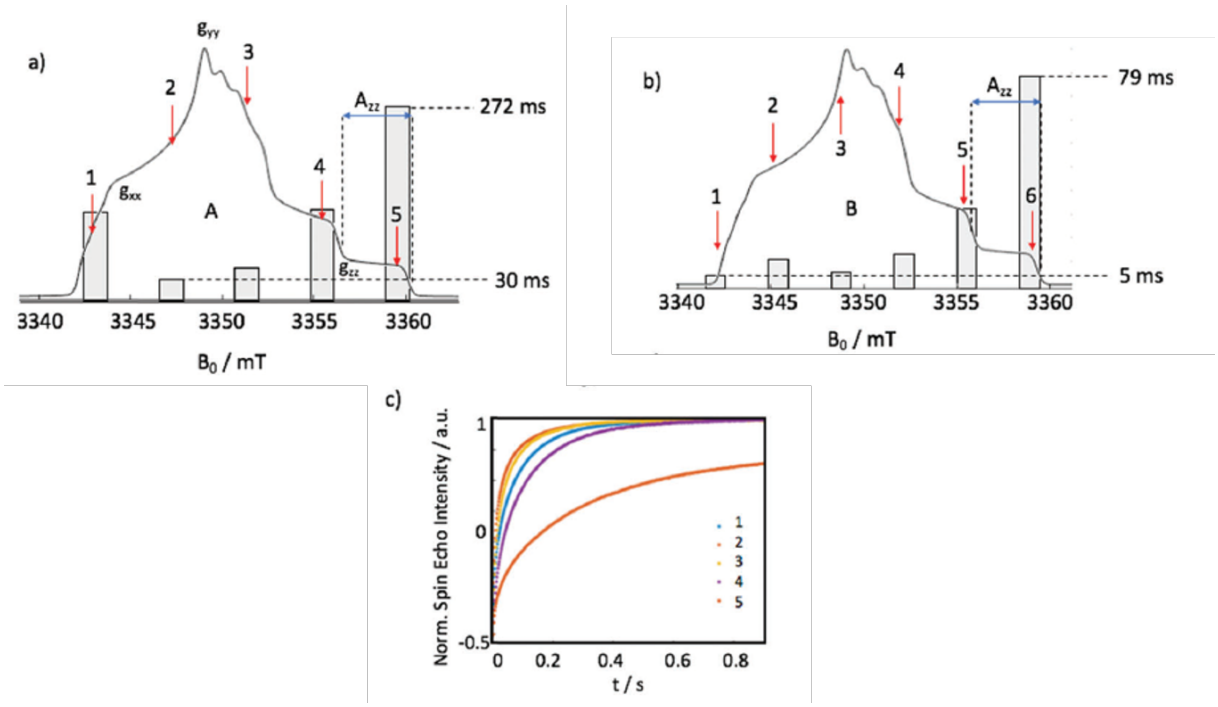

Figure 3.3: (a and b) Simulated field-swept spin-echo W-band absorption mode EPR spectrum for sample A and B highlighting the positions for which the longitudinal electron relaxation times $T_{1e}(\omega)$ were determined as indicated by red arrows. The heights of the grey bars in (a and b) are proportional to the $T_{1e}(\omega)$, values listed in Table 3.1. (c) Electron inversion recovery experiment recorded at 94.1 GHz using electron spin echoes for sample A for the five different field positions indicated in (a). The anisotropic behaviour is clearly observable. Note that nitroxides typically feature a stretched exponential decay functions. $T_{1e}(\omega)$ values were determined by fitting to a stretched exponential function and determining the average decay rate by assuming $s(T_{1e}(\omega))/s(0) = e^{-1}$.

would thus observe a single isotropic $T_{1e}(\omega)$ value regardless of the saturated spin packet. However, for moderate eSD coefficients, variations in anisotropic longitudinal relaxation times $T_{1e}(\omega)$ are not completely averaged out. Thus, the interplay between eSD and the intrinsic electron longitudinal relaxation times (i.e., $T_{1e}(\omega)$ at infinite dilution) determines the spectral window that is effectively averaged, while infinitely long relaxation times would be averaged over the entire spectrum. Yet, for our samples, we experimentally determined anisotropic $T_{1e}(\omega)$ values even for 50 mM TEMPOL at W-band at 6 K (94.1 GHz; central field 3.35 T; vide supra) showing that the polarization is not completely averaged by eSD across the entire EPR linewidth in the absence of continuous microwave irradiation. This is in agreement with earlier findings by Farrar et al.[13]

It has been pointed out by Wenckebach[7] that eSD is strongly temperature and field dependent, so that it is difficult to make any reasonable assumptions for 6.7 T and

4 K. Yet, using eSD coefficients recently estimated by Siaw et al.[28] and the $T_{1e}(\omega)$ values reported in Table 3.1, we can approximate the fractions of the EPR spectrum that are averaged by eSD via the formalism described in Wenckebach's monograph (chapter 5.3).[7] We assume a frequency ω_0, with an offset to the centre of gravity ω_e of the EPR line is $\Delta_0 = \omega_0 - \omega_e$. In the case of DNP, when a spin packet at an offset Δ_0 is saturated, the microwave field also disturbs the i$^{\text{th}}$ electron spin packet at an offset $\Delta_i = \omega_i - \omega_e$. Accordingly, we determined the contribution of a spin packet i to the electronic relaxation $T_{1e}(\omega)$ measured at an offset Δ_0 by

$$c(\Delta_i) = f(\Delta_i) \exp\left(\frac{\Delta_i - \Delta_0}{\sqrt{D T_{1e}(\Delta_i)}}\right) \tag{3.1}$$

where D denotes the spectral diffusion coefficient and where the frequency ω has been replaced by the offset Δ_i to yield $T_{1e}(\Delta_i)$. We denote the normalized amplitude of the absorption EPR spectrum by $f(\Delta_i)$. If the width of the EPR spectrum is M^2, the spectral diffusion coefficient is

$$D = \frac{M^2}{4 t_{SD}} \tag{3.2}$$

Since t_{SD} can be estimated to be 10 ms,[28] only part of the EPR spectrum is effectively smoothed by eSD at the concentrations used in our DNP experiments.

The spin packets of the EPR spectrum that are graphically depicted in Fig. 3.4 represent contributions to the detected $T_{1e}(\Delta_i)$ values. Note that significant parts of the spin packets in the spectrum are averaged, though not across the entire spectrum, thus making it possible for $T_{1e}(\Delta_i)$ to remain anisotropic. In the presence of a CW microwave field, it has further to be considered that eSD coefficients change as the polarization of the individual spin packets varies and $D \propto (1 - P_e^2)$. Yet, recent double-electron resonance experiments,[14] show that even under such conditions the EPR line is not entirely averaged via eSD for our experimental setup (6.7 T, 4 K, 25 mM TEMPOL). Furthermore, the spectral diffusion rate might also depend on the amplitude of the EPR spectrum at a particular field or frequency, a fact that also affects the anisotropy of $T_{1e}(\Delta_i)$ relaxation, since eSD-induced averaging is much stronger near the centre of gravity of the spectrum than at its extremities. Indeed,

the observed relaxation time $T_{1e}(\Delta_i)$ is a weighted average across the spectral range covered by eSD, as demonstrated in Fig. 3.4. Hence, the faster eSD, the more packets will contribute to each $T_{1e}(\Delta_i)$ value, so that these will appear more isotropic if spectral diffusion is fast. On the contrary, for slow eSD, the anisotropy of $T_{1e}(\Delta_i)$ can be more pronounced. Thus, $T_{1e}(\Delta_i)$ values detected near the centre of the EPR spectrum can be less anisotropic then those observed near the edges of the spectrum. Such a behaviour can be observed in Fig. 3.3, where the strongest deviations from the average relaxation time can be observed near the edges of the EPR spectrum.

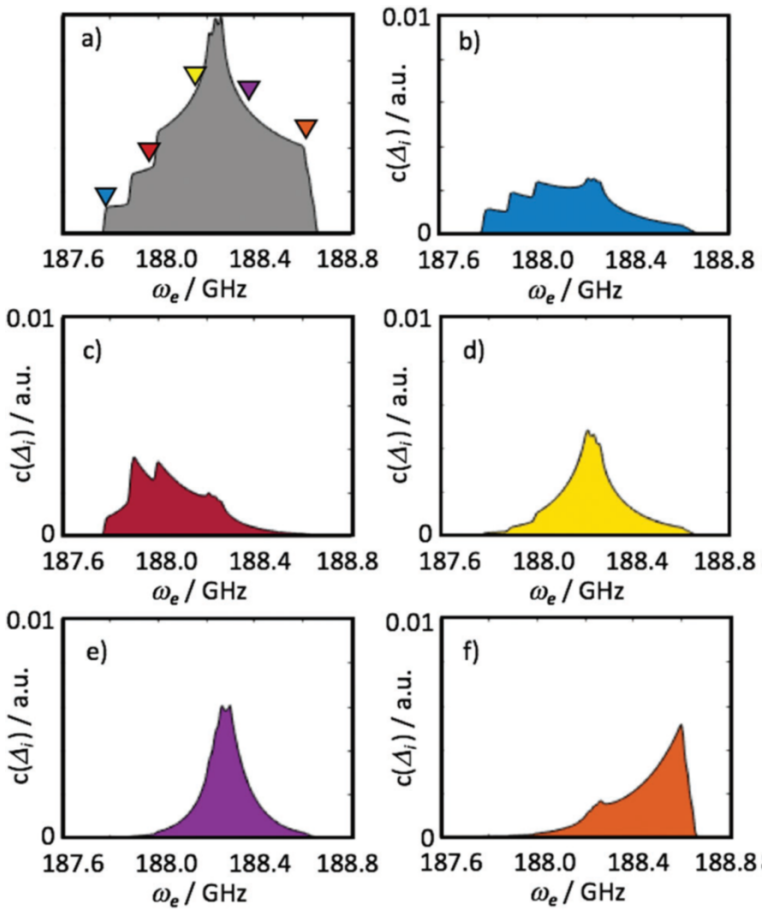

Figure 3.4: (a) Simulated EPR spectrum at 6.7 T with $N = 5$ different $T_{1e}(\Delta_i)$ measured at the frequencies indicated by color codes. Note that the eSD rates could not be determined experimentally. (b–f) Simulated contributions $c(\Delta_i)$ of different spin packets to the apparent $T_{1e}(\Delta_i)$ measured at five different positions. The coefficients are normalized so that $\sum_i c(\Delta_i) = 1$.

3.3.3 Dynamic nuclear polarization

For the case at hand, we consider a mono-radical with a broad EPR spectrum at low temperatures, with a width that is comparable to the proton nuclear Larmor frequency, which is near 285 MHz in our experiments. To demonstrate how anisotropic $T_{1e}(\Delta_i)$ can be incorporated into a model describing DNP at low temperatures, we chose Borghini's theory for the sake of simplicity. Based on strong assumptions, i.e., a single spin temperature and a strong contact between the nuclear Zeeman and electronic dipolar bath, this model yields simple predictions, which can easily be adapted to anisotropic $T_{1e}(\Delta_i)$ although the model assumes fast eSD to justify the use of a single spin temperature. Borghini's model has been reviewed in depth by Abragam and Goldman[1] using a thermodynamic description. Jannin et al. pointed out that Borghini's approach corresponds to a Redfield model with a single spin temperature in the rotating frame.[29] It can be regarded as an extension of Provotorov's theory to low temperatures, since one can predict the temperature of the non-Zeeman reservoir for off-centre saturation of the EPR line by dissecting the latter into several spin packets. We briefly outline Borghini's theory.[15] At equilibrium, the polarization P_0 of the electrons is given by a Boltzmann distribution:

$$|P_0| = \tanh\left(\frac{1}{2}\beta_L\omega_e\hbar\right) \tag{3.3}$$

$$\beta_L = \frac{1}{k_B T_L} \tag{3.4}$$

where ω_e, T_L, k_B are the electron Larmor frequency, the lattice temperature and the Boltzmann constant, whilst β_L the inverse temperature coefficient of the lattice.

For the case at hand, the linewidth of the EPR spectrum is dominated by a spread (anisotropy) of the electronic g factor at the magnetic field of 6.7 T. It is possible to relate the nuclear polarization to the EPR line shape if we consider electrons at frequency Δ_0 to be fully saturated (cf. Fig. 3.1 b). Under these conditions, $P_e(\Delta_0) = 0$, while the polarization $P_e(\Delta_i)$ of a spin packet at an offset Δ_i is $P_e(\Delta_i) = -\tanh[\frac{1}{2}\beta\,(\Delta_0 - \Delta_i)\,\hbar]$, where β is the electron dipolar (non-Zeeman) inverse temperature coefficient, so that spin packets located at a frequency offset Δ_i are partially saturated and contribute to DNP. If the electronic g anisotropy

dominates the spread of the electron frequencies, the electron polarization affects the steady-state nuclear polarization P_n according to Borghini:[1]

$$P_n = \frac{T_{1n}C}{\omega_n T_{1e}} \left(\sum_i f(\Delta_i) \left[(\Delta_0 - \Delta_i) P_e(\Delta_i) + \Delta_0 P_0 \right] \right) \tag{3.5}$$

Here ω_n is the nuclear Larmor frequency and $C = N_e/N_n$ denotes the ratio of the number of electron spins to the number of nuclear spins. T_{1e} and T_{1n} are the longitudinal electron and nuclear relaxation times, respectively, both of which are considered to be isotropic in Borghini's original model. The steady-state value of the inverse dipolar (non-Zeeman) temperature coefficient of the electrons β_0 under microwave irradiation at the offset Δ_0 can be expressed by Eqn. 3.6 and 3.7:

$$\beta_0 = \frac{2\Delta_0 |P_0|}{(\Delta_0^2 + D^2)} = \frac{1}{k_B T_S} \tag{3.6}$$

$$M^2 = \int_{-\infty}^{+\infty} \Delta^2 f(\Delta) d\Delta \tag{3.7}$$

Here M^2 is the second moment of the EPR line, P_0 the thermal electronic polarization and T_s is the spin temperature. To account for the anisotropy of the longitudinal electronic relaxation times that vary across the EPR line, we introduce an offset-dependent $T_{1e}(\Delta_i)$. To this end, we adapt the following rate equations derived by Abragam and Goldman:[1]

$$\frac{d}{dt}\langle H_{Ze} \rangle = -\frac{N_e \omega_e}{2\mathrm{T}_{1e}} \left(\sum_i f(\Delta_i) \left[P_e(\Delta_i) - P_0 \right] + U f_0 P_{e0} \right) \tag{3.8}$$

and

$$\frac{d}{dt}\langle H_{Zn} + H_{nZ} \rangle = -\frac{N_e P_n \omega_n}{\mathrm{T}_{1n} 2C} + \frac{N_e}{2} \left(\frac{1}{\mathrm{T}_{1e}} \sum_i f(\Delta_i) P_{ei} + U \Delta_0 f_0 P_{e0} \right) \tag{3.9}$$

where H_{Ze}, H_{Zn} and H_{nZ} denote the electron-Zeeman, nuclear- Zeeman and non-Zeeman Hamiltonians. P_{e0} is the polarization of the saturated packet Δ_0. Ne is the number of electron spins. Replacing T_{1e} by $T_{1e}(\Delta_i)$ and setting the derivatives to zero to describe the steady state, we can derive a modified Borghini equation where

$T_{1e}(\Delta_i)$ terms remain within the summation. Combining Eqn. 3.8 and 3.9 leads to:

$$P_n = \frac{\mathrm{T}_{1n} C}{\omega_n} \left(\sum_i \frac{f(\Delta_i)(\Delta_0 - \Delta_i)}{T_{1e}(\Delta_i)} [P_e(\Delta_i) - P_0] \right) \tag{3.10}$$

Note that for nitroxides in partially deuterated glassymatrices, the width of EPR spectra at 6.7 T is primarily determined by the g-anisotropy and by intramolecular hyperfine couplings. However, the presence of additional contributions to homogeneous and heterogeneous line broadening cannot be entirely excluded a priori. Indeed, intermolecular dipolar electron–electron couplings can contribute to the width of the EPR spectra, especially at the high nitroxide concentrations that are typically used for DNP.

In conclusion, since the nuclear polarization P_n in Eqn. 3.10 depends on the various $T_{1e}(\Delta_i)$ contributions, which can vary significantly even after averaging through eSD, the observed proton signal intensity will also vary across the microwave profile. The incorporation of an offset-dependent $T_{1e}(\Delta_i)$ for different spin packets is of

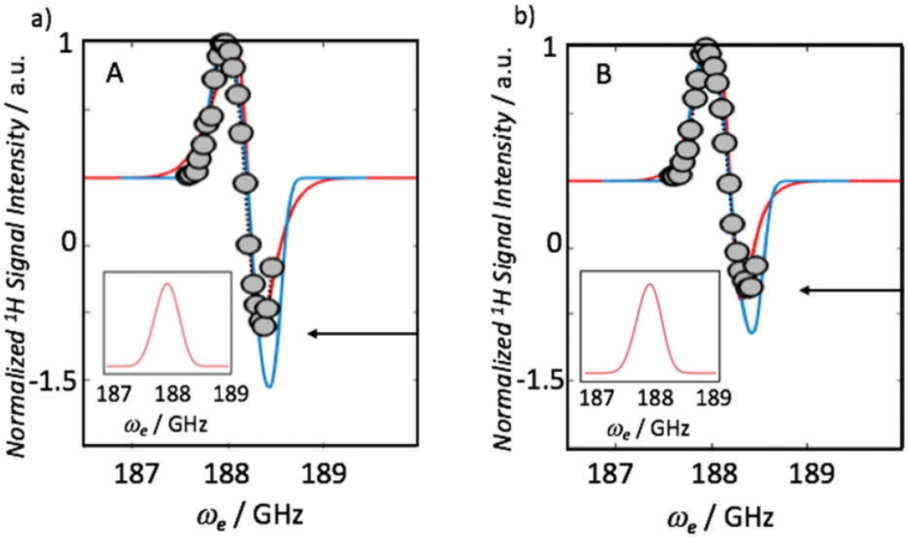

Figure 3.5: (a) Normalized steady-state proton signal intensity as a function of the microwave frequency ω_e ("DNP enhancement profile" or simply "DNP profile") for 25 mM TEMPO at 4.2 K: (a) in glycerol-d_8/D_2O/H_2O (5:4:1); (b) in ethanol-d_6/ ethanol (9:1). Circles indicate experimentally determined steady-state polarizations, solid red lines the calculated responses. The inserts display the simulated EPR spectra underlying the calculations. Pronounced differences in the negative lobes are emphasized by arrows. The blue lines indicate DNP profiles based on Eqn. 3.5 obtained for a single isotropic relaxation time T_{1e} that does not depend on Δ_i.

importance as the bottleneck of the spin dynamics is influenced by $T_{1e}(\Delta_i)$. In other

words, the nuclear polarization that can be reached in each spin packet is directly related to $T_{1e}(\Delta_i)$ as pointed out by Serra et al.[12] Hence, the dependence of P_n on $T_{1e}(\Delta_i)$ must be considered to predict the shape of a DNP profile if eSD is sufficiently slow such that $T_{1e}(\Delta_i)$ varies with the orientations of the g-tensors for different spin packets. As the Borghini model neglects the anisotropy of $T_{1e}(\Delta_i)$, since it assumes fast eSD underlying TM this leads to a bias in the frequency dependence of the predicted nuclear polarization.

More generally, any model that takes into account the whole EPR line profile must also address the frequency dependence of the electron spin–lattice relaxation times $T_{1e}(\Delta_i)$ within that line adequately.

Borghini's model does not describe all details of nitroxide based DNP. In particular, absolute polarization levels cannot be predicted correctly, as the requirement of a single spin temperature is often not fulfilled under practical conditions. Nonetheless, the match between theory and experiment can be significantly improved by incorporating anisotropic relaxation properties. More sophisticated models such as those presented by Vega and co-workers,[8–11,13,17,24–27,30] which account for subtle aspects of DNP (e.g., temperature- and concentration-dependence, absolute polarization), could presumably be improved by taking into account the anisotropy of electronic relaxation. Fig. 3.5 displays "DNP enhancement profiles", i.e., the normalized steady-state integrated proton signal intensity observed at 4.2 K (after complete build-up or extrapolated to the steady-state; cf. Fig. 3.1) as a function of the microwave frequency in our DNP apparatus. After normalization, the ^{1}H signal intensity corresponds to P_n in Eqn. 3.10. The data shown in Fig. 3.5 a and b were obtained for samples A and B, both of which contain 25 mM TEMPOL but in different solvents (cf. Experimental). Calculated enhancement profiles based on Eqn. 3.10 are superimposed as solid lines, assuming that the simulated EPR spectra (based on experimentally determined g- and $\mathbf{A}$-tensors plus an additional linewidth; see insets) are broadened in accordance with the influence of eSD.

If the polarity of the solvent is modified, changes in the DNP enhancement profiles are observed. For TEMPOL dissolved in ethanol (sample B in Fig. 3.5 b), the observed changes with respect to the more polar environment of sample A can be

modelled by variations of the anisotropic $T_{1e}(\Delta_i)$ (recalling that the g- and **A**-tensors were determined experimentally, vide supra). When switching from sample A to B, the DNP efficiency of the highfield lobe is significantly reduced. The shape of the DNP profile can be modelled by Eqn. 3.10, if one considers the anisotropy of $T_{1e}(\omega)$ documented in Table 3.1. Although variations in solvent polarity can lead to variations in local microscopic environments and hence to variations of nitroxide g- and **A**-tensors, we find that the calculations of Fig. 3.5 need not to invoke such effects, which can be neglected here due to the strong line broadening at high TEMPOL concentrations.[31]

The solid blue lines in Fig. 3.5 clearly show that the shapes and relative magnitudes of the lobes of the experimental DNP profiles cannot be reproduced if only a single frequency-independent relaxation time T_{1e} is considered. Changing the EPR linewidth (which is the only adaptable parameter) cannot account for the discrepancies. Obviously, the match between the experimental data and theoretical prediction is significantly improved by considering anisotropic relaxation times $T_{1e}(\Delta_i)$.

3.3.4 Methodological considerations

Several points must be critically considered when using Eqn. 3.10: (i) $T_{1e}(\Delta_i)$ varies significantly with the microwave offset as indicated in Fig. 3.3 and Table 3.1. To obtain a continuous fit (Fig. 3.5), we measured $T_{1e}(\Delta_i)$ at low concentrations and hence slow eSD with selective pulses to obtain values that reflect the $T_{1e}(\Delta_i)$ of a narrow spin packet of the EPR spectrum and interpolated $T_{1e}(\Delta_i)$ between the observed data points using 4th and 5th-order polynomials for samples A and B respectively (cf. Fig. 3.5) to account for the averaging through eSD. Because of the sparse $T_{1e}(\Delta_i)$ measurements, abrupt changes in $T_{1e}(\Delta_i)$ might have been overlooked. Nevertheless, the match is improved between the experimental DNP profiles and those predicted via this approach. It was further assumed that changes of $T_{1e}(\Delta_i)$ between 6 K (where $T_{1e}(\Delta_i)$ was measured) and 4.2 K (where the DNP enhancement profiles were obtained) are uniform across the spectrum and do not depend on the offset Δ_0, so that normalization of the DNP profiles compensates for

a possible temperature dependence (we excluded the field dependence, vide supra). (ii) The solution of Eqn. 3.10 and the fits of the enhancement profiles in Fig. 3.5 require prior knowledge of the EPR spectra $f(\Delta_i)$. These spectra were obtained via simulation as illustrated in Fig. 3.2. (Note, however, that the EPR spectrum was determined at a TEMPOL concentration of 1 mM, whereas DNP was performed at 25 mM. The spectra should thus not be compared directly.) After normalization, the only freely adjustable parameter in Eqn. 3.10 is the EPR line width (since the g- and **A**-tensors of the EPR spectrum have been determined experimentally, vide supra). The EPR line width cannot account for the discrepancy between experimental data and the theoretical predictions obtained via Eqn. 3.5, i.e., for the case of isotropic relaxation times T_{1e} that do not depend on Δ_0. Further, spectral diffusion mixes the on-resonance spin packet saturated by microwave irradiation at the frequency ω_0 with spin packets at other frequencies. Thus, DNP-determined spectra at 6 K and 25 mM typically appear strongly broadened[32] since at each EPR frequency the intensity is averaged by spectral diffusion. This is taken into account by superimposing an additional linewidth on the spectrum shown in Fig. 3.2 b. (iii) Borghini's model does not consider possible effects of non-uniform spectral diffusion coefficients on the EPR line shape. Spectral diffusion is only accounted for by assuming a rapid equilibration over the entire EPR spectrum.

One might therefore speculate that anisotropic spectral diffusion and line broadening could likewise account for discrepancies between the model and the experiments, and should therefore also be incorporated into more sophisticated models. For the case at hand we did not include such eSD effects or line width parameters in the Borghini model, which was in this work mainly used to emphasize the importance of $T_{1e}(\Delta_i)$ anisotropy. Note, however, that the simulated EPR spectrum is in agreement with spectra obtained under comparable conditions[32] and was kept constant in all our calculations. (iv) Borghini's TM model is only valid when the on-resonance spin packet is fully saturated and when the thermal contact between the electronic dipolar and nuclear Zeeman reservoirs is strong. Although we verified that the on-resonance electrons were fully saturated (see Fig. 3.1), the Borghini model (even after incorporating anisotropic electronic relaxation) still overestimates P_n at the extremities of the profile, as the irradiated spin packet is only a small fraction of the

ensemble and the contact with the nuclear bath is therefore weaker than assumed in the model.[33] Other more sophisticated models might be capable of compensating for such flaws. Especially, recent work by Wenckebach[34] extends the theoretical description of TM DNP to low temperatures, overcoming limitations of Borghini's model by predicting the polarization of off-resonance electron spins. However, the focus of this work is not to propose a new model to describe DNP, but to draw attention to the importance of anisotropic electronic relaxation. Its incorporation into virtually any physical model should improve the agreement between predicted and experimental DNP profiles if spectral diffusion is slow.

3.4 Conclusions

Our data suggest that DNP models should be refined by incorporating the anisotropy of electronic longitudinal relaxation times, since at low temperatures and high magnetic fields $T_{1e}(\Delta_i)$ significantly depends on the molecular orientation if the electronic spectral diffusion does not lead to full averaging of the polarization across the entire EPR spectrum.[35] This amendment seems quite reasonable in view of our measurements of the frequency-dependence of $T_{1e}(\Delta_i)$, corresponding to a dependence on the molecular orientation. The variations of $T_{1e}(\Delta_i)$ can be neglected at lower fields (e.g., at X-band at 0.3 T), but at W-band (94.1 GHz, central field 3.5 T), and a fortiori at 6.7 T (central frequency 188.2 GHz) where our DNP experiments have been carried out, the anisotropy of $T_{1e}(\Delta_i)$ cannot be neglected. While the extension of Borghini's model introduced here can reproduce the main features of our DNP profiles it will certainly not adequately describe all the subtleties of DNP at cryogenic temperatures. Yet, we show that even the rather rudimentary Borghini model can be amended to take our observations into account. Clearly, anisotropic electronic relaxation should be included in all models describing nitroxide-based DNP. Indeed, to the best of our knowledge, all known models indicate that the proton polarization depends on the $T_{1e}(\Delta_i)$.

Bibliography

[1] A. Abragam and M. Goldman. Principles of dynamic nuclear polarisation. *Rep. Prog. Phys.*, 41:397 – 467, 1978.

[2] D. Kurzbach, E. M. M. Weber, A. Jhajharia, S. F. Cousin, A. Sadet, S. Marhabaie, E. Canet, N. Birlirakis, J. Milani, S. Jannin, D. Eshchenko, A. Hassan, R. Melzi, S. Luetolf, M. Sacher, M. Rossire, J. Kempf, J. A. B. Lohman, M. Weller, G. Bodenhausen, and D. Abergel. Dissolution dynamic nuclear polarization of deuterated molecules enhanced by cross-polarization. *J. Chem. Phys.*, 145(19):194203, 2016.

[3] Min H., Sekar G., and Hilty C. Polarization transfer from ligands hyperpolarized by dissolution dynamic nuclear polarization for screening in drug discovery. *ChemMedChem*, 10(9):1559–1563, 2015.

[4] S. Jannin, A. Bornet, S. Colombo, and G. Bodenhausen. Low-temperature cross polarization in view of enhancing dissolution dynamic nuclear polarization in NMR. *Chem. Phys. Lett.*, 517(4):234 – 236, 2011.

[5] J. H. Ardenkjær-Larsen, B. Fridlund, A. Gram, G. Hansson, L. Hansson, M. H. Lerche, R. Servin, M. Thaning, and K. Golman. Increase in signal-to-noise ratio of > 10,000 times in liquid-state NMR. *Proceed. Nat. Acad. Sc.*, 100(18):10158–10163, 2003.

[6] D. Kurzbach, E. Canet, A. G. Flamm, A. Jhajharia, E. M. M. Weber, R. Konrat, and G. Bodenhausen. Investigation of intrinsically disordered proteins through exchange with hyperpolarized water. *Ang. Chem. Inter. Ed.*, 56(1):389–392, 2017.

[7] T. Wenckebach. *Essentials of Dynamic Nuclear Polarization*. Sprindrift Publications, 2016.

[8] Y. Hovav, A. Feintuch, and S. Vega. Theoretical aspects of dynamic nuclear polarization in the solid state – the solid effect. *J. Magn. Res.*, 207:176–189, 2010.

[9] Y. Hovav, O. Levinkron, A. Feintuch, and S. Vega. Theoretical aspects of dynamic nuclear polarization in the solid state: The influence of high radical concentrations on the solid effect and cross effect mechanisms. *Appl. Magn. Reson.*, 43(1-2):29–41, 2012.

[10] Y. Hovav, A. Feintuch, and S. Vega. Theoretical aspects of dynamic nuclear polarization in the solid state - the cross effect. *J. Magn. Res.*, 214(1):29–41, 2012.

[11] Y. Hovav, A. Feintuch, and S. Vega. Theoretical aspects of dynamic nuclear polarization in the solid state - spin temperature and thermal mixing. *Phys. Chem. Chem. Phys.*, 15:188 – 203, 2013.

[12] S. C. Serra, A. Rosso, and F. Tedoldi. Electron and nuclear spin dynamics in the thermal mixing model of dynamic nuclear polarization. *Phys. Chem. Chem. Phys.*, 14:13299–13308, 2012.

[13] C. T. Farrar, D. A. Hall, G. J. Gerfen, S. J. Inati, and R. G. Griffin. Mechanism of dynamic nuclear polarization in high magnetic fields. *J. Chem. Phys.*, 114(11):4922–4933, 2001.

[14] A. Leavesley, D. Shimon, T. A. Siaw, A. Feintuch, D. Goldfarb, S. Vega, I. Kaminker, and S. Han. Effect of electron spectral diffusion on static dynamic nuclear polarization at 7 tesla. *Phys. Chem. Chem. Phys.*, 19:3596–3605, 2017.

[15] M. Borghini. Spin-temperature model of nuclear dynamic polarization using free

radicals. *Phys. Rev. Lett.*, 20:419–421, 1968.

[16] A. Bornet, J. Milani, B. Vuichoud, A. J. P. Linde, G. Bodenhausen, and S. Jannin. Microwave frequency modulation to enhance dissolution dynamic nuclear polarization. *Chem. Phys. Lett.*, 602:63–67, 2014.

[17] Y. Hovav, A. Feintuch, S. Vega, and D. Goldfarb. Dynamic nuclear polarization using frequency modulation at 3.34t. *J. Magn. Res.*, 238:94 – 105, 2014.

[18] F. Delaglio, S. Grzesiek, G. W. Vuister, G. Zhu, J. Pfeifer, and A. Bax. NMRPipe: a multidimensional spectral processing system based on UNIX pipes. *J. Biomol. NMR.*, 6:277–293, 1995.

[19] S. Stoll and A. Schweiger. EasySpin, a comprehensive software package for spectral simulation and analysis in EPR. *J. Magn. Reson.*, 178(1):42–55, 2006.

[20] S. Stoll and A. Schweiger. EasySpin: Simulating cw ESR spectra. *Biol. Magn. Reson.*, 27:299–321, 2007.

[21] M. F. Ottaviani, M. Garcia-Garibay, and N. J. Turro. TEMPO radicals as EPR probes to monitor the adsorption of different species into X zeolite. *Coll. Surf. A: Phys. Engin. Asp.*, 72:321 – 332, 1993.

[22] J. L. Du, G. R. Eaton, and S. S. Eaton. Temperature, orientation, and solvent dependence of electron spin-lattice relaxation rates for nitroxyl radicals in glassy solvents and doped solids. *J. Magn. Reson. A*, 115(2):213 – 221, 1995.

[23] V.A. Atsarkin, A.E. Mefeod, and M.I. Rodak. Electron cross relaxation and nuclear polarization in ruby. *Phys. Lett. A*, 27(1):57 – 58, 1968.

[24] Y. Hovav, D. Shimon, I. Kaminker, A. Feintuch, D. Goldfarb, and S. Vega. Effects of the electron polarization on dynamic nuclear polarization in solids. *Phys. Chem. Chem. Phys.*, 17:6053–6065, 2015.

[25] Y. Hovav, I. Kaminker, D. Shimon, A. Feintuch, D. Goldfarb, and S. Vega. The electron depolarization during dynamic nuclear polarization: measurements and simulations. *Phys. Chem. Chem. Phys.*, 17:226–244, 2015.

[26] D. Shimon, Y. Hovav, A. Feintuch, D. Goldfarb, and S. Vega. Dynamic nuclear polarization in the solid state: a transition between the cross effect and the solid effect. *Phys. Chem. Chem. Phys.*, 14:5729–5743, 2012.

[27] A. Feintuch, D. Shimon, Y. Hovav, D. Banerjee, I. Kaminker, Y. Lipkin, K. Zibzener, B. Epel, S. Vega, and D. Goldfarb. A dynamic nuclear polarization spectrometer at 95GHz/144MHz with EPR and NMR excitation and detection capabilities. *J. Magn. Reson.*, 209(2):136 – 141, 2011.

[28] T. A. Siaw, M. Fehr, A. Lund, A. Latimer, S. A. Walker, D. T. Edwards, and S.-I Han. Effect of electron spin dynamics on solid-state dynamic nuclear polarization performance. *Phys. Chem. Chem. Phys.*, 16:18694–18706, 2014.

[29] S. Jannin, A. Comment, F. Kurdzesau, J. A. Konter, P. Hautle, B. van den Brandt, and J. J. van der Klink. A 140 GHz prepolarizer for dissolution dynamic nuclear polarization. *J. Chem. Phys.*, 128(24):241102, 2008.

[30] D. Shimon, A. Feintuch, D. Goldfarb, and S. Vega. Static ^{1}H dynamic nuclear polarization with the biradical TOTAPOL: a transition between the solid effect and the

cross effect. *Phys. Chem. Chem. Phys.*, 16:6687–6699, 2014.

[31] D. Kurzbach, M. J. N. Junk, and D. Hinderberger. Nanoscale inhomogeneities in thermoresponsive polymers. *Macromol. Rap. Comm.*, 34(2):119–134, 2013.

[32] P. Niedbalski, C. Parish, A. Kiswandhi, and L. Lumata. ^{13}C dynamic nuclear polarization using isotopically enriched 4-oxo-TEMPO free radicals. *Magn. Reson. Chem.*, 54(12):962–967, 2016.

[33] S. C. Serra, A. Rosso, and F. Tedoldi. On the role of electron-nucleus contact and microwave saturation in thermal mixing DNP. *Phys. Chem. Chem. Phys.*, 15:8416–8428, 2013.

[34] W. T. Wenckebach. Dynamic nuclear polarization via thermal mixing: Beyond the high temperature approximation. *Journal of Magnetic Resonance*, 277:68 – 78, 2017.

[35] A. Leavesley, D. Shimon, T. A. Siaw, A. Feintuch, D. Goldfarb, S. Vega, I. Kaminker, and S. Han. Effect of electron spectral diffusion on static dynamic nuclear polarization at 7 tesla. *Phys. Chem. Chem. Phys.*, 19:3596–3605, 2017.

Chapter 4

Sample ripening through nanophase separation influences the performance of DNP

The polarization that one can achieve by DNP is very sensitive to experimental conditions. It is known that mixtures of water and organic solvents may feature unusual physicochemical events like spontaneous nanophase separations (NPS)[1–3] that occur in solutions despite their homogenous appearance on a macroscopic scale.[4] Such NPS describe rather counterintuitive phenomena, where the two components of a binary solvent mixture spontaneously form coexisting metastable transient nanophases. The intriguing nature of NPS recently stimulated much academic interest.[5–8] In this chapter, we show how such phenomena can impact the performance of DNP,which has recently undergone significant developments, allowing one to achieve ever-higher levels of polarization due to (1) instrumental developments and (2) novel polarization agents (PAs) such as bi-nitroxides or tri-aryl-methyl radicals, also known as "Trityls". These developments provide access to systems that could not be studied before by NMR due to poor sensitivity.

Water/glycerol mixtures that contain concentrations of PAs[9–11] of 10 – 80 mM are frequently used as low-temperature DNP matrices. We here show that such sample preparations can feature distributions of radicals that are heterogeneous on

nanometric length scales as a consequence of "ripening" effects that lead to the emergence of two co-existing phases that may have different local PA concentrations. We find that water/glycerol mixtures can indeed lead to the formation of nanoscopic water vesicles dispersed in a glycerol-rich matrix, which can be trapped during the vitrification step that precedes low-temperature DNP. As a result, the local PA concentration in water- and proton-rich phases varies, which impacts DNP performances. Such behavior can be of importance in many fields of research, such as dissolution DNP of biomolecules,[12] drug screening,[13–15] in-vivo imaging[16] and cancer monitoring,[17] since many of these studies employ water-glycerol mixtures.[18] The transient accumulation of various molecular agents in an environment that is confined on a nanometric scale may not only improve DNP, but may also serve other technologies that employ transiently formed nanostructures,[19] shelters[20] or reactors[21] by increasing the selectivity and specificity of chemical reactions under investigation.

The DNP samples studied here consisted of a mixture of 50% v/v glycerol-d8 and 50% v/v of a solution of one of the following PAs in 80% D_2O and 20% H_2O: **I**) 100 mM TEMPOL (4-hydroxy- 2,2,6,6-tetramethylpiperidin-1-oxyl), **II**) 40 mM AMUPol (15-[(7- oxyl-3,11-dioxa-7-azadispiro[5.1.5.3]hexadec-15- yl)carbamoyl][2-(2,5,8,11-tetraoxatridecan-13-ylamino)-[3,11- dioxa-7-azadispiro[5.1.5.3]hexadec-7-yl]) oxidanyl) and **III**) 30 mM Trityl (Finland) (see Fig. 2.3). The solutions were stirred during ca. 60 s at 22.5 °C until they appeared macroscopically homogeneous. To study the influence of ripening on the preparations, the samples were allowed to rest at 22.5 °C for a suitable "ripening interval" T_{ripe}, which can be on the order of minutes to hours. Subsequently, they were "flash vitrified" in liquid helium at 4.2 K prior to DNP.

The duration of the "ripening interval" T_{ripe} has important effects on the proton polarization level in DNP experiments as shown in Fig. 4.1 a for sample **I**, containing 50 mM TEMPOL, where we find more efficient DNP for $T_{ripe} = 45$ min in comparison to $T_{ripe} < 1$ min. Fig. 4.1 b displays the dependence of the proton polarization $|P(^1\mathrm{H})^s|$ on the ripening interval. The highest polarization is achieved for 40 min $< T_{ripe} < 60$ min. In comparison to polarization levels obtained for $T_{ripe} < 1$ min or

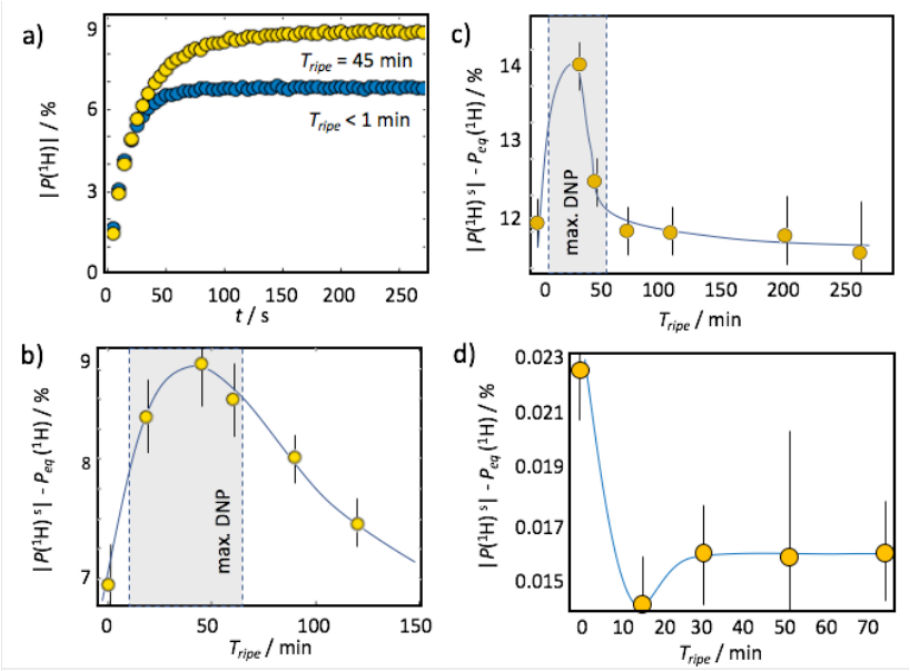

Figure 4.1: Build-up curves of the proton polarization $|P(^1\mathrm{H})^s|$ induced by microwave saturation (187.9 GHz with a 2 kHz frequency modulation over a bandwidth of 100 MHz) of the EPR transitions of 50 mM TEMPOL at 4.2 K and 6.7 T. Blue: Sample vitrified immediately after preparation ($T_{ripe} < 1$ min). Yellow: Sample vitrified after a ripening interval $T_{ripe} = 45$ min following sample preparation. b) Difference $|P(^1\mathrm{H})^s| - P_{eq}(^1\mathrm{H})$ between absolute steady-state proton polarization $|P(^1\mathrm{H})^s|$ and thermal equilibrium polarization P_{eq} at 4.2 K as a function of the interval T_{ripe} between preparation and vitrification of the water glycerol/mixtures. The solid line serves to guide the eye. Similar results have been reproduced in three independent experiments (see appendix C). c) Difference $|P(^1\mathrm{H})^s| - P_{eq}(^1\mathrm{H})$ versus T_{ripe} for 20 mM AMUPol at 4.2 K. d) Difference $|P(^1\mathrm{H})^s| - P_{eq}(^1\mathrm{H})$ versus T_{ripe} for 15 mM trityl at 4.2 K. In this case, one observes a drop of ca. 43% for $T_{ripe} = 15$ min.

for $T_{ripe} > 4$ h, gains in $|P(^1\mathrm{H})^s|$ from 7 to 9% at 4.2 K and 6.7 T translate into a gain of more than 20% in the NMR signal enhancement factor ϵ.(see appendix C)

Fig. 4.1 c displays a similar profile for sample **II** containing 20 mM AMUPol. Here, we observe a maximum DNP performance after a ripening interval $30 < T_{ripe} < 50$ min. The enhancement factor ϵ is improved by ca. 17% when $|P(^1\mathrm{H})^s|$ increases from 12% to 14%. In stark contrast, for sample **III** (Fig. 4.1d) containing 15 mM Trityl, we observed a 40% decrease of $|P(^1\mathrm{H})^s|$ for $T_{ripe} = 15$ min.

Unlike for TEMPOL and AMUPol, the EPR line of Trityl is narrower than the proton Larmor frequency. Hence, the solid effect (SE) is dominant for Trityl, while thermal mixing (TM) dominates for nitroxides under our experimental conditions. This has two consequences: (1) the SE is less effective than TM because the build-

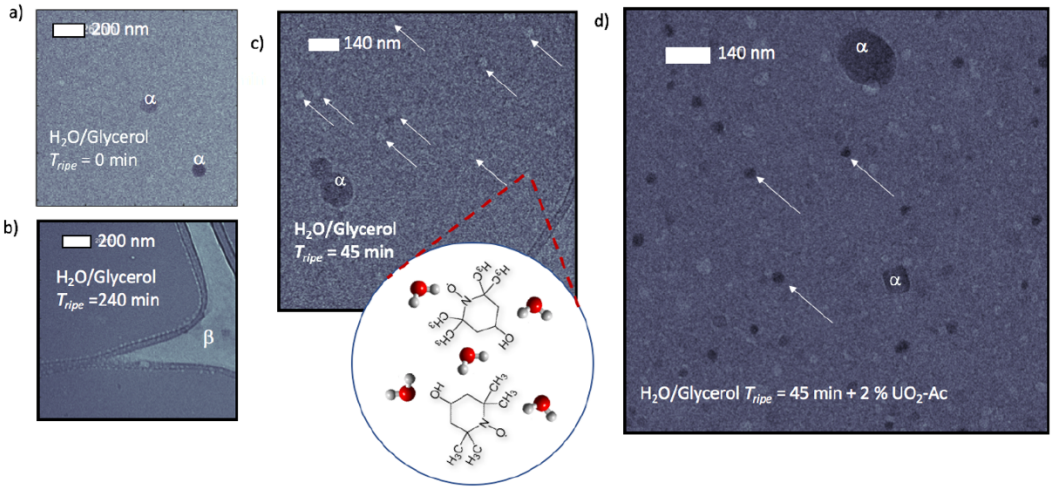

Figure 4.2: Cryo-TEM pictures of morphological changes due to nanophase separation (NPS) resulting from ripening during an interval T_{ripe} between mixing at room temperature and rapid vitrification by plunging the samples into liquid ethane at 90 K. For T_{ripe} = 0 min (a) or 240 min (b), no NPS could be observed. The letter a on the figure indicates ethane droplets on the vitrified film. The letter b indicates the carbon support grid. c) Water-rich phases (in which the TEMPOL radicals are confined) appear as light vesicles at T_{ripe} = 45 min, indicated by white arrows. d) Addition of 2% uranyl acetate stains the water-rich vesicles by a dark contrast as indicated by the white arrows.

up rate of $|P(^1\mathrm{H})^s|$ is on the same order as the proton relaxation rate $\mathrm{R}_1(^1\mathrm{H})$ and (2) the dependence of the DNP efficiency on the local PA concentration is not the same for SE and TM mechanisms. Indeed, contrary to samples **I** and **II** the difference $|P(^1\mathrm{H})^s| - P_{eq}(^1\mathrm{H})$ drops from only 0.023% at $T_{ripe} = 0$ to 0.013% at $T_{ripe} = 15$ min before stabilizing around 0.016% after $T_{ripe} = 30$ min. Despite the obvious differences between Trityl and the two nitroxides under investigation, we again observe a ripening process on a time scale of 30 - 60 min. (Note that we observed ripening also at lower global radical concentrations; see appendix C). This fact should henceforth be considered in DNP optimization studies. To cast light on the processes underlying our observations, we studied the time evolution of the nanoscopic morphology of the DNP samples by cryo-transmission electron microscopy (cryo-TEM). We prepared similar samples and vitrified them at 90 K in liquid ethane after different intervals T_{ripe}. For $T_{ripe} = 0$ or 240 min (Fig. 4.2 a and b) we observed a homogeneous morphology of the water/glycerol mixture by cryo-TEM. However, the DNP samples undergo morphological transitions during ripening leading to the spontaneous formation of spherical water vesicles of ca. 10-50 nm diameter (Fig. 4.2 c). A similar phenomenon of de-mixing and subsequent

re-mixing, was reported by Murata and Tanaka.[4] For $20 < T_{ripe} < 45$ min, we clearly observed the nanoscopic separation of a water-rich phase (vesicles) and a glycerol-rich phase (matrix, Fig. 4.2 c). We only observed such a formation of vesicles for glycerol contents of 40-50% v/v, since cryo-TEM is not possible at 60% v/v since the glass transition temperatures becomes too low. To confirm the formation of water-rich phases, we employed negative staining techniques using the hydrophilic uranyl ion (UO_2^{2+}), which preferentially accumulates in water-rich environments. In Fig. 4.2 d, the water vesicles are stained in a darker shade due to the presence of the heavy ions, thereby corroborating the observation of NPS in the DNP samples. Note that the hyperpolarization build-up time in Fig. 4.1 a appears longer for T_{ripe} = 45 min than for $T_{ripe} = 0$. This is likely a consequence of NPS, as shown by Ji et al.[22] for heterogeneous samples, where PA-depleted phases feature slow build-up processes when they are spatially separated from PA-rich phases that feature faster build-up processes.

Fig. 4.3 a and b show that the longitudinal proton relaxation rate $R_1(^1H)$ at 4 K and 6.7 T increases due to NPS for samples **I** and **II** containing TEMPOL and AMUPol. This occurs between T_{ripe} = 20 and T_{ripe} = 60 min for sample **I** and between T_{ripe} = 40 and T_{ripe} = 100 min for sample **II**. This finding indicates a local increase in PA concentration (depending on the ripening interval) in proton-rich environment, i.e., in the water vesicles, based on the fact that for the mono-radical TEMPOL, the proton relaxation rate at 4.2 K is predominantly determined by electron-proton flip-flop transitions.[18] Therefore, since the relaxation rates increase by ca. 20% due to ripening of sample **I**, the PA concentration must increase in the water vesicles during NPS, since all other parameters (temperature, overall concentrations, etc.) remain unchanged. For sample **II**, the presence of two coupled radicals in the PA complicates the relaxation behavior as three-spin processes are facilitated; yet a qualitatively similar concentration dependence can be expected. In contrast, for sample **III** (Trityl, Fig. 4.3 c) we find a decrease of $R_1(^1H)$ from 10 to ca. $7.5 \cdot 10^{-3}$ s^{-1} between $T_{ripe} = 0$ and T_{ripe} = 40 min. As the DNP performance also decreases for Trityl (Fig. 4.1)[23,24] between $T_{ripe} = 0$ and T_{ripe} = 30 min, in contrast to samples **I** and **II**, it is likely that the Trityl radicals are accumulated in the glycerol-rich phase and, hence, separated from the protons in the water-rich phase that we observe by

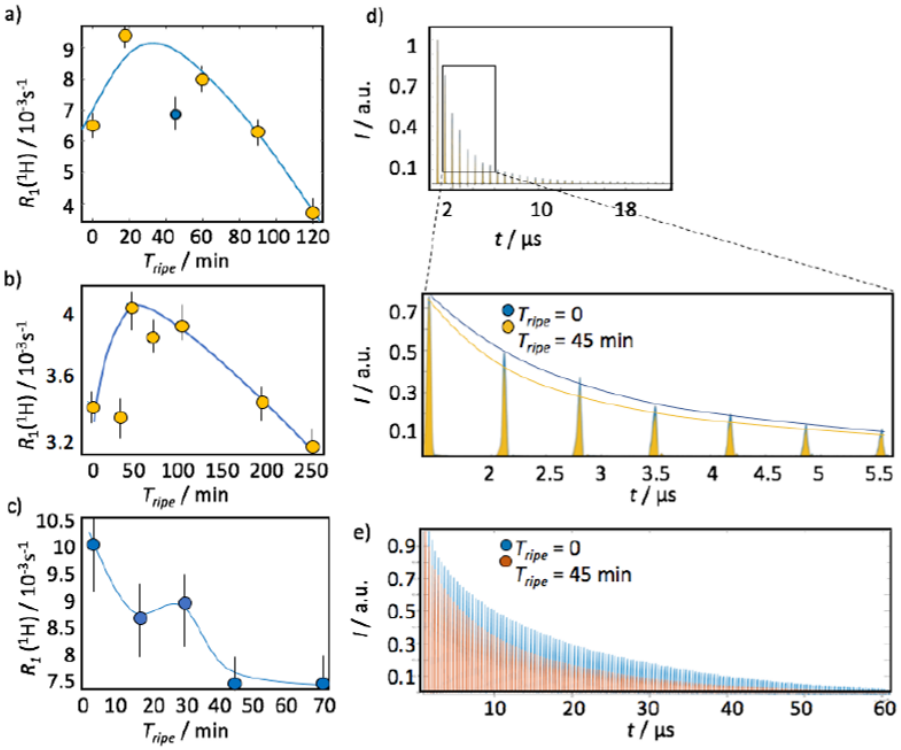

Figure 4.3: Local PA distribution. a) $R_1(^1H)$ as a function of the ripening interval for sample **I**. Between T_{ripe} = 20 min and 60 min, increased relaxation rates for protons can be observed, confirming that the local PA concentration is increased due to NPS. At T_{ripe} = 45 min the decay showed a bi-exponential behavior (blue point indicates the fast component; the slow component was $8.4 \cdot 10^{-4}$ s^{-1}; not shown for the sake of visibility; see appendix C). The blue line serves to guide the eye. b) The longitudinal relaxation rate $R_1(^1H)$ as a function of the ripening interval for sample **II**. An increase can be observed for 30 min < T_{ripe} < 100 min. The blue line guides the eye. c) $R_1(^1H)$ as a function of the ripening interval for sample **III**. The blue line is again to guide the eye. d) Transverse electron spin relaxation rates $R_{2e} = 1/T_{2e}$ of 10 mM TEMPOL measured at 77 K using a CPMG pulse sequence after T_{ripe} = 0 (blue dots) and T_{ripe} = 45 min (yellow dots). The black box indicates the enlarged region shown below. The solid blue and yellow lines indicate the signal envelopes to which R_{2e} was fitted. R_{2e} raises for T_{ripe} = 45 min, indicating increased local radical concentrations. e) Same as in d), but for sample **III**. Again, ripening effects are clearly observed and relaxation is faster for T_{ripe} = 45 min.

NMR, so that proton relaxation decelerates upon NPS.

Note that, also from the viewpoint of relaxation, all three samples again show ripening in water/glycerol mixtures with distinct features for 15 < T_{ripe} < 60 min. Interestingly, we find bi-exponential relaxation behavior for sample **I** when $|P(^1H)^s|$ reaches a maximum at T_{ripe} = 45 (see blue data point in Fig. 4.3 a and appendix C) indicating that spin diffusion cannot cover the entire sample due to NPS. Assuming a perfect phase separation and an even distribution of all labile protons and deuterons in the sample - which might be an oversimplification, since the water-

glycerol proton/deuterium exchange (H/D exchange) might proceed on a similar or longer timescale as the NPS reported here - the proton concentration in the water-rich phase would be 5 times higher than in the glycerol-rich phase. Slow H/D exchange would further boost the local ^{1}H concentration, since all samples were prepared with fully deuterated glycerol and partly deuterated water so that slow exchange would further increase the local ^{1}H concentration in the water vesicles. Hence, not only PAs but also protons become enriched in the water-rich phases due to NPS. In a next step, we measured the transverse electronic relaxation rates R_{2e} of the PAs as a function of T_{ripe} by means of pulsed electron paramagnetic resonance (EPR) experiments, for which the samples were prepared with the same protocol as for DNP, but vitrified in liquid nitrogen. Fig. 4.3 d shows that R_{2e} increases for sample **I** from $4.9 \cdot 10^5$ to $5.8 \cdot 10^5$ s^{-1} when going from $T_{ripe} = 0$ to 45 min. Thus, in comparison to samples with $T_{ripe} < 1$ min, the transverse electronic relaxation rates R_{2e} of the radicals becomes faster. As the rates R_{2e} primarily depend on the local radical concentration and their mutual dipolar couplings (ceteris paribus), increased R_{2e} rates indicate stronger couplings corresponding to locally increased concentrations of TEMPOL in the aqueous phase. For sample **II** we determined that the relaxation rates are independent of T_{ripe} as the electronic relaxation is likely to be dominated by concentration-independent intramolecular dipolar couplings. For 5 mM AMUPol R_{2e} barely varied, from $2.6 \cdot 10^5$ s^{-1} to $2.5 \cdot 10^5$ s^{-1} between $T_{ripe} < 1$ min and 45 min, respectively. For the Trityl, sample **III**, we again observed ripening via electronic relaxation as displayed in Fig. 4.3 e. For 5 mM Trityl the R_{2e} rate increased from $8.3 \cdot 10^4$ s^{-1} to $1.3 \cdot 10^5$ s^{-1} between $T_{ripe} = 0$ and 45 min. Hence, sample ripening influences the electronic relaxation rates of both monoradicals indicating clustering and increased local PA concentrations due to NPS.

To corroborate these findings, we systematically varied the water-glycerol ratio. The effect on continuous-wave EPR spectra recorded at 120 K after $T_{ripe} = 45$ min confirm a preferential accumulation of TEMPOL and AMUPol in the water-rich phase, while Trityl accumulates in the water-depleted phase (see appendix C.)

Finally, we ran preliminary studies on sample **I** based on double electron-electron resonance (DEER) (see appendix C)[25] which allows one to measure distance-dependent

dipolar couplings between electrons. After sample ripening, a non-homogeneous distribution of short distances was observed for TEMPOL, while for $T_{ripe} < 1$ min the distribution was found to be more homogeneous, again highlighting the local accumulation of PAs during the NPS.

Bibliography

[1] D. A. Jahn, J. Wong, J. Bachler, T. Loerting, and N. Giovambattista. Glass polymorphism in glycerol-water mixtures: I. a. computer simulation study. *Phys. Chem. Chem. Phys.*, 18:11042–11057, 2016.

[2] J. Bachler, V. Fuentes-Landete, D. A. Jahn, J. Wong, N. Giovambattista, and T. Loerting. Glass polymorphism in glycerol-water mixtures: Ii. experimental studies. *Phys. Chem. Chem. Phys.*, 18:11058–11068, 2013.

[3] K.-I. Murata and H. Tanaka. Liquid–liquid transition without macroscopic phase separation in a water–glycerol mixture. *Nat. Mat.*, 11:436–443, 2012.

[4] K.-I. Murata and H. Tanaka. General nature of liquid-liquid transition in aqueous organic solutions. *Nat. Commun.*, 4:2844, 2013.

[5] N. Severin, J. Gienger, V. Scenev, P. Lange, I. M. Sokolov, and J. P. Rabe. Nanophase separation in monomolecularly thin water–ethanol films controlled by graphene. *Nano Lett.*, 15(2):1171–1176, 2015.

[6] Z. Zuofeng and A. C. Austen. Apparent first-order liquid–liquid transition with pre-transition density anomaly, in water-rich ideal solutions. *Ang. Chem. Inter. Ed.*, 128(7):2520–2523, 2016.

[7] D. Kurzbach, W. Hassouneh, J. R. McDaniel, E. A. Jaumann, A. Chilkoti, and D. Hinderberger. Hydration layer coupling and cooperativity in phase behavior of stimulus responsive peptide polymers. *J. Am. Chem. Soc.*, 135(30):11299–11308, 2013.

[8] S. E. Reichheld, L. D. Muiznieks, F. W. Keeley, and S. Sharpe. Direct observation of structure and dynamics during phase separation of an elastomeric protein. *Proc. Nat. Ac. Sc.*, 2017.

[9] A. Leavesley, D. Shimon, T. A. Siaw, A. Feintuch, D. Goldfarb, S. Vega, I. Kaminker, and S. Han. Effect of electron spectral diffusion on static dynamic nuclear polarization at 7 tesla. *Phys. Chem. Chem. Phys.*, 19:3596–3605, 2017.

[10] M. Kaushik, T. Bahrenberg, T. V. Can, M. A. Caporini, R. Silvers, J. Heiliger, A. A. Smith, H. Schwalbe, R. G. Griffin, and B. Corzilius. Gd(III) and Mn(II) complexes for dynamic nuclear polarization: small molecular chelate polarizing agents and applications with site-directed spin labeling of proteins. *Phys. Chem. Chem. Phys.*, 18:27205–27218, 2016.

[11] G. Mathies, S. Jain, M. Reese, and R. G. Griffin. Pulsed dynamic nuclear polarization with trityl radicals. *J. Phys. Chem. Lett.*, 7(1):111–116, 2016.

[12] E. Miclet, D. Abergel, A. Bornet, J. Milani, S. Jannin, and G. Bodenhausen. Toward quantitative measurements of enzyme kinetics by dissolution dynamic nuclear polarization. *J. Phys. Chem. Lett.*, 5(19):3290–3295, 2014.

[13] R. Buratto, A. Bornet, J. Milani, D. Mammoli, B. Vuichoud, N. Salvi, M. Singh, A. Laguerre, S. Passemard, S.and Gerber-Lemaire, S. Jannin, and G. Bodenhausen. Drug screening boosted by hyperpolarized long-lived states in NMR. *Chem. Med. Chem.*, 9:2509–2515, 2014.

[14] N. Salvi, R. Buratto, A. Bornet, S. Ulzega, I. Rentero Rebollo, A. Angelini, C. Heinis, and G. Bodenhausen. Boosting the sensitivity of ligand–protein screening by NMR of long-lived states. *J. Am. Chem. Soc.*, 134(27):11076–11079, 2012.

[15] Q. Chappuis, J. Milani, B. Vuichoud, A. Bornet, A. D. Gossert, G. Bodenhausen, and S. Jannin. Hyperpolarized water to study protein–ligand interactions. *J. Phys. Chem. Lett.*, 6(9):1674–1678, 2015.

[16] S. Ito and F. Hyodo. Dynamic nuclear polarization-magnetic resonance imaging at low ESR irradiation frequency for ascorbyl free radicals. *Sc. Rep.*, 6:21407, 2016.

[17] D. M. Wilson and J. Kurhanewicz. Hyperpolarized ^{13}C MR for molecular imaging of prostate cancer. *J. Nucl. Med.*, 55(10):1567–1572, 2014.

[18] T. Wenckebach. *Essentials of Dynamic Nuclear Polarization*. Spindrift Publications, 2016.

[19] D. Kurzbach, M. J. N. Junk, and D. Hinderberger. Nanoscale inhomogeneities in thermoresponsive polymers. *Macromol. Rap. Comm.*, 34(2):119–134, 2013.

[20] M. J. N. Junk, U. Jonas, and D. Hinderberger. EPR spectroscopy reveals nanoinhomogeneities in the structure and reactivity of thermoresponsive hydrogels. *Small*, 4(9):1485–1493, 2008.

[21] S. H. Petrosko, R. Johnson, H. White, and C. A. Mirkin. Nanoreactors: Small spaces, big implications in chemistry. *J. Am. Chem. Soc.*, 138(24):7443–7445, 2016.

[22] X. JI, A. Bornet, B. Vuichoud, J. Milani, D. Gajan, A. J. Rossini, L. Emsley, G. Bodenhausen, and S. Jannin. Transportable hyperpolarized metabolites. *Nat. Comm.*, 8:13975, 2017.

[23] I. Marin-Montesinos, J. C. Paniagua, A. Peman, M. Vilaseca, F. Luis, S. Van Doorslaer, and M. Pons. Paramagnetic spherical nanoparticles by the self-assembly of persistent trityl radicals. *Phys. Chem. Chem. Phys.*, 18:3151–3158, 2016.

[24] I. Marin-Montesinos, J. C. Paniagua, M. Vilaseca, A. Urtizberea, F. Luis, M. Feliz, F. Lin, S. Van Doorslaer, and M. Pons. Paramagnetic spherical nanoparticles by the self-assembly of persistent trityl radicals. *Phys. Chem. Chem. Phys.*, 18:3151–3158, 2016.

[25] D. Kurzbach, D. R. Kattnig, N. Pfaffenberger, W. Schärtl, and D. Hinderberger. Highly defined, colloid-like ionic clusters in solution. *ChemistryOpen*, 1(5):211–214, 2012.

Chapter 5

Observation of a DNP-hyperpolarized solid-state water NMR MASER phenomenon

5.1 Introduction

It is well known that, under conditions of strong coupling with the detecting circuit, a large magnetization originating from an ensemble of isolated nuclear spins may exhibit unconventional behavior that departs from the Bloch equations. This mechanism, designated as "radiation damping" was observed in the early days of NMR[1] and is well understood. It can be described in classical terms by coupling the evolution of the magnetization as given by the Bloch equations, to the Kirchoff equations describing the evolution of the electrical detection circuit, through a set of Bloch-Maxwell equations.[2–4] The presence of radiation damping gives rise to various unexpected features, such as spurious harmonic peaks in two-dimensional liquid state NMR spectra.[5–8] Some characteristic features of the magnetization dynamics are related to the nonlinearity of the evolution equations, and have been investigated by several authors.[6,9–12] Radiation damping is a phenomenon that is typically

observed in case of a large solvent magnetization, usually water, in the context of liquid state NMR. Water NMR masers, with the presence of multiple magnetization bursts, have been previously observed artificially by the addition of an electronic feedback, or in the case of system with very large magnetization such as hyperpolarized spin states.[12] Alternatively, such unconventional magnetization dynamics has been achieved through DNP on a ruby crystal[13,14] In this study, we present observations of an NMR maser in a sample of (vitrified) water at 1.2 K, generated by DNP polarized ^{1}H magnetization in a 6.7 T magnet. This is particularly striking, due to the presence of a large, dipolar-broadened, resonance line. Moreover, the recorded induction signal could be observed for several tens of seconds, even in the absence of microwave irradiation. Our observations are described in terms of a model involving a large magnetization generated through DNP hyperpolarization of water protons through thermal mixing, and rationalized through the Maxwell-Bloch-Provotorov equations. This, surprisingly, shows that the collective behavior of an ensemble of dipolar coupled nuclear spins can be qualitatively taken into account by a simple vector model.

5.2 Radiation Damping: the modified Bloch equations

5.2.1 Radiation Damping (RD) in the liquid state

Radiation damping is a cooperative phenomenon. In the presence of a large magnetization, the precession of the transverse component of the latter creates an electromotive force (e.m.f.) in the detection circuit that is large enough to generate a current and a RF field in the sample. The latter is strong enough so as to drive the magnetization to the +z direction, and to coherently align the spins with the magnetic field.[8]

In 1957, S. Bloom combined the Bloch equations with the ones that describe the probe reaction field, previously developed by Bloembergen and Pound,[2,3] to obtain

a description of the dynamics of the magnetization ($\vec{M}$) in this situation. $\vec{M}$ obeys the following equations, in a frame rotating around the z axis at the frequency ω:[4]

$$\begin{cases} \dot{M}_x = \delta M_y - \gamma G M_z M_x - \frac{M_x}{T_2} \\ \dot{M}_y = -\delta M_x - \omega_1 M_z - \gamma G M_z M_y - \frac{M_y}{T_2} \\ \dot{M}_z = \omega_1 M_y + \gamma G (M_x^2 + M_y^2) - \frac{(M_z - M_0)}{T_1} \end{cases} \tag{5.1}$$

with $G = \frac{\mu_0}{2}\eta Q$ where μ_0 is the vacuum permeability. The radiofrequency field (RF) aligned along x is ω_1 and $\delta = \omega - \omega_0$ is the offset frequency with respect to the Larmor frequency ω_0. The description of the coupling between the nuclear magnetization and an RF coil is very similar to the laser phenomenon in optics where the polarization is coupled to a cavity.[15] In the absence of relaxation, the motion of the magnetization vector takes place on the Bloch sphere (for Bloch's theory,[16] see appendix A.3), in harsh contrast with the T_1 and T_2 relaxation behavior.

The characteristic time of Radiation damping is defined as τ_{rd}:

$$\tau_{rd}^{-1} = \frac{\mu_0 \gamma \eta Q M_z}{2}, \tag{5.2}$$

where η is the RF filling factor of the coil, which is defined as the ratio $\frac{E_{sample}}{E_{space}}$ where E_{space} is the total energy delivered by the coil,[17,18] whereas E_{sample} is the part of this RF energy delivered to the sample; Q is the quality factor of the coil; γ denotes the gyromagnetic ratio of the nucleus, and M_z represents the longitudinal component of the magnetization, equal to the Curie magnetization M_0 when the system is at thermal equilibrium. The time τ_{rd} determines the rate at which the magnetization precesses back to the equilibrium direction, and therefore the strength of the RF feedback field. Eqn. 5.1 predict a hyperbolic secant, rather than an exponentially decaying FID (see Fig. 5.1). However, in the case of small flip angles, where the FID is approximately exponential, a modified line width T_2' can be defined as:

$$\frac{1}{T_2'} = \frac{1}{T_2} + \frac{1}{\tau_{rd}} \tag{5.3}$$

It is worth noting that spin-spin relaxation induces a loss of coherence of the trans-

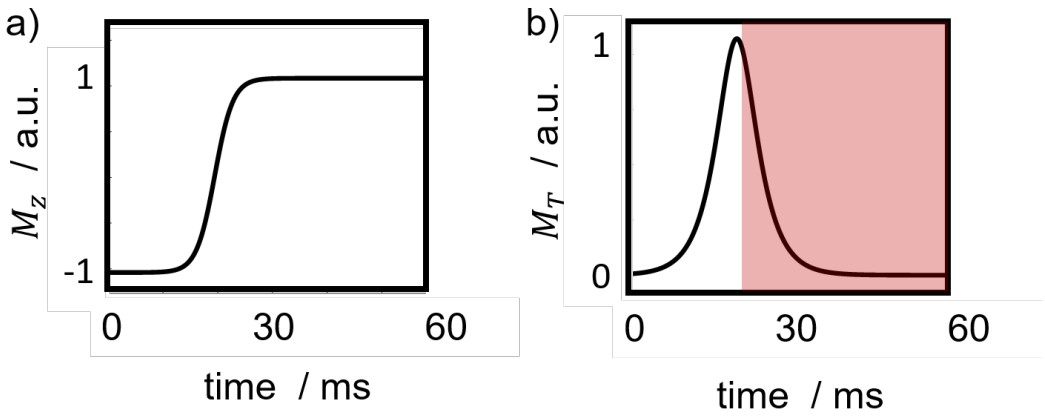

Figure 5.1: Time evolution of the normalized z (a) and transverse (b) magnetizations as a function of time in the case of strong coupling between the magnetization and the coil (RD). $\vec{M}$ is align to the -z axis at the beginning of the simulation. The relaxation mechanisms have been neglected. M_T evolution follows a hyperbolic secant as the RD forces $\vec{M}$ to turn back to its equilibrium value in the Bloch sphere and features a maximum when $\vec{M}$ crosses the xy plane. The exponential decay of M_T occurring in the case of small flip angle of the $\vec{M}$ with respect to the z axis is highlighted.

verse magnetization that tends to lower the efficiency of radiation damping. Thus, the RD can only be effective if the following condition is fulfilled:

$$T_2 > \tau_{rd} \tag{5.4}$$

The RD phenomenon depends on both the detection circuit and the sample properties. In brief, as seen from Eq.5.2, the larger the spin magnetization and the quality factor of the probe, the stronger the effect. For this reason, as the probes quality improves, radiation damping originating from the solvent (typically water proton spins in liquid state NMR) represents an increasing nuisance due to the unconventional dynamics of the water magnetization. Various approaches to suppress the impact of the RD in the NMR spectra have been developed. Hardware design such as special Q-switching probes,[19–22] suppression feedback field[23–25] or selective pulses[26,27] help to get rid of the spurious signals by preventing coupling of the spin system with the coil. Samples perdeuteration[28] and specific pulse sequences[29] also enable to quench the coupling between H_2O and the detection circuit.

5.2.2 RD in hyperpolarized solid samples: the Bloch-Maxwell-Provotorov (BMP) equations

Although RD is mainly observed in solution-state NMR, such spin-coil coupling effects have also been observed in the solid state for samples with a large magnetization, provided by DNP-hyperpolarized nuclear spins.[13] A qualitative description of the dynamics of the magnetization has been obtained by several authors by combining the set of equations 5.1 with the Provotorov equations describing the DNP process through thermal mixing.[13,14,30] As it has been previously developed in this thesis, in the thermal mixing regime, all interactions can be associated to thermodynamical reservoirs (see sections 1.2.7 and 3.3.3). The broad TEMPOL spectrum at low temperature (1.2 K) enables thermal mixing, which leads to proton hyperpolarization.[31] In a first round of investigations, we used the following equations 5.5 to describe the temporal evolution of the proton nuclear Zeeman and the electron dipolar reservoirs as in the TM model.

$$\begin{cases} \frac{d\beta_h}{dt} = -\frac{1}{\tau_{h,ee}}(\beta_h - \beta_{ee}) \\ \frac{d\beta_{ee}}{dt} = -\frac{C_n}{C_e}\frac{1}{\tau_{h,ee}}(\beta_{ee} - \beta_n) - \frac{1}{\tau_{ee,L}}(\beta_{ee} - \beta_L) \\ +\pi\omega_{1\,\mu w}^2 f(\omega_e - \omega_{\mu w})\frac{\omega_e - \omega_{\mu w}}{\delta\omega^2}\left[\omega_e\beta_e - (\omega_e - \omega_{\mu w})\beta_{ee}\right] \end{cases} \tag{5.5}$$

β_n, β_{ee} and β_L represent the inverse spin temperatures of the proton Zeeman and electron dipolar reservoirs and the lattice. $\tau_{n,ee}$ and $\tau_{ee,L}$ respectively are the characteristic time constants for the equilibration of the spin temperatures of the two connected reservoirs and the dissipation of the polarization of the electron spins in the dipolar reservoir into the lattice (phonons). The transfer of polarization from the electrons to the nuclei depends on the ratio between the nuclear and electronic heat capacities: $\frac{C_n}{C_e}$. The larger C_n, the faster the process. In other words, the efficiency of the DNP depends on the number of nuclei coupled to an electron. The third term of the second equation of Eqn. 5.5 describes the effect of the microwave pumping onto the spin temperature of the electron dipolar reservoir. Thus, the temperature varies as a function of the square of the microwave amplitude $\omega_{1\,\mu w}$ and the difference between the microave field $\omega_{\mu w}$ and the center of the EPR line ω_e. Both the shape $f(\omega)$ and the width $\delta\omega$ of the spectrum play important roles. Finally, the

microwave field couples the electron dipolar and Zeeman reservoirs. Therefore, the electron Zeeman inverse spin temperature explicitly appears as β_e.

In the thermal mixing picture, the thermodynamical reservoirs associated to the nuclear Zeeman and electron dipolar energies tend to equilibrate their spin temperatures. Thus, equations 5.5 predict a stationary nuclear magnetization M_z^{st} (see Eqn. 5.6) associated to a common inverse spin temperature of the two reservoirs $\beta_n = \beta_{ee}$ when the system is irradiated by a continuous microwave field.

$$M_z^{st} = \mathcal{N}_{\mathrm{H}} \frac{\gamma_n \hbar}{2} \tanh\left(\beta_{ee} \frac{\gamma_n \hbar B_0}{2k_B}\right) \tag{5.6}$$

where $\mathcal{N}_{\mathrm{H}}$ is the number of protons and γ_n the proton gyromagnetic ratio. Note that equation 5.6 can be reduced to $\frac{\gamma_n^2 \hbar^2 \mathcal{N}_{\mathrm{H}} B_0}{4\mathrm{k_B}} \beta_{ee}$ under the high temperature approximation, one of the assumptions of the Provotorov equations.

By combining Eqn. 5.1 and 5.5, the prediction of the nuclear magnetization under DNP conditions becomes possible (Eqn. 5.7). The large proton magnetization that is created through DNP induces an efficient coupling between the ^{1}H spin system and the detection circuit.

$$\begin{cases} \dot{M}_x = \delta M_y - \gamma G M_z M_x - \frac{M_x}{T_2} \\ \dot{M}_y = -\delta M_x - \omega_1 M_z - \gamma G M_z M_y - \frac{M_y}{T_2} \\ \dot{M}_z = \omega_1 M_y + \gamma G (M_x^2 + M_y^2) - \frac{\gamma_n^2 \hbar^2 \mathcal{N}_{\mathrm{H}} B_0}{4\mathrm{k_B} \tau_{n,ee}} (\beta_n - \beta_{ee}) \\ \frac{d\beta_{ee}}{dt} = -\frac{C_n}{C_e} \frac{1}{\tau_{n,ee}} (\beta_{ee} - \beta_n) - \frac{1}{\tau_{ee,L}} (\beta_{ee} - \beta_L) \\ + \pi \omega_{1\,\mu w}^2 f(\omega_{0e} - \omega_{\mu w}) \frac{\omega_e - \omega_{\mu w}}{\delta \omega^2} \left[\omega_e \beta_e - (\omega_e - \omega_{\mu w}) \beta_{ee}\right] \end{cases} \tag{5.7}$$

Given that the electron Zeeman reservoir heat capacity is much larger than the electron dipolar and nuclear ones (or that the energy involved in the electron Zeeman interaction is much higher than the nuclear Zeeman and electron dipolar ones), β_e is assumed to be constant and equal to the lattice temperature ($\beta_e = \beta_L$).[13] Since Eqn. 5.7 correspond to a combination of Provotorov and Bloch-Maxwell equations, we will refer to them as the Bloch-Maxwell-Provotorov equations (BMP). A summary sketch of the BMP theory in case of interacting electronic and proton baths under microwave irradiation is sketched in Fig. 5.2.

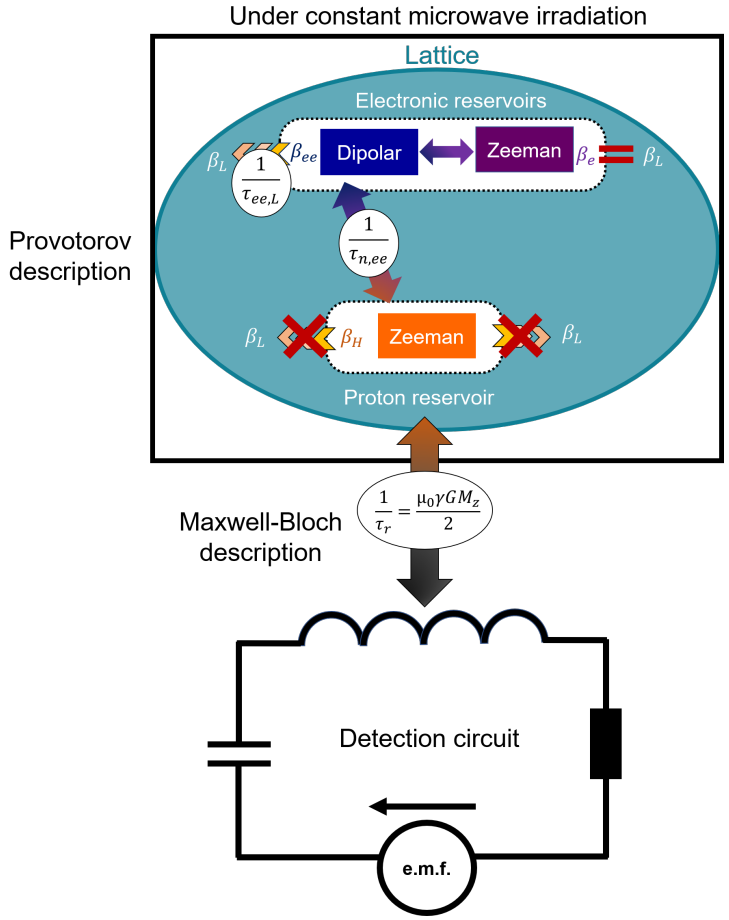

Figure 5.2: Schematic representation of the theory underlying the BMP equations (Eqn. 5.7). Provotorov's thermodynamical description is combined with the Maxwell-Bloch non-linear equations which describe a coupling between the spin system and the detection circuit. Under microwave irradiation, the electronic Zeeman and dipolar reservoirs are coupled. As the electron Zeeman temperature is constant and equal to the lattice temperature, the dipolar reservoir is continuously replenished. The ^{1}H spin-lattice relaxation time at cryogenic temperature ($\sim$ 5 min at 1.2 K) is much larger than the characteristic times of the RD and the reservoirs heat exchange. Its contribution can therefore be neglected. The electron dipolar reservoir dissipates its energy by spin-lattice relaxation with a rate $\frac{1}{\tau_{ee,L}}$ and also transfers its heat to the proton Zeeman reservoir with a rate $\frac{1}{\tau_{n,ee}}$.

In the absence of microwave irradiation, $\omega_{1\,\mu w} = 0$ and equations 5.7 reduce to:

$$\begin{cases} \dot{M}_x = \delta M_y - \gamma G M_z M_x - \frac{M_x}{T_2} \\ \dot{M}_y = -\delta M_x - \omega_1 M_z - \gamma G M_z M_y - \frac{M_y}{T_2} \\ \dot{M}_z = \omega_1 M_y + \gamma G (M_x^2 + M_y^2) - \frac{\gamma_n^2 \hbar^2 \mathcal{N}_{\mathrm{H}} B_0}{4 k_{\mathrm{B}} \tau_{n,ee}} (\beta_n - \beta_{ee}) \\ \frac{d\beta_{ee}}{dt} = -\frac{C_n}{C_e} \frac{1}{\tau_{n,ee}} (\beta_{ee} - \beta_n) - \frac{1}{\tau_{ee,L}} (\beta_{ee} - \beta_L) \end{cases} \tag{5.8}$$

We shall refer to these equations as Bloch-Maxwell-Provotorov (BMP) equations. Figure 5.3 illustrates the consequences of the switching off of the microwaves on the

spin system according to Provotorov's theory. Note that the coupling of the proton magnetization with the detection coil is not affected by the absence of microwave irradiation. In both cases (with and without microwave irradiation), the nuclear Zee-

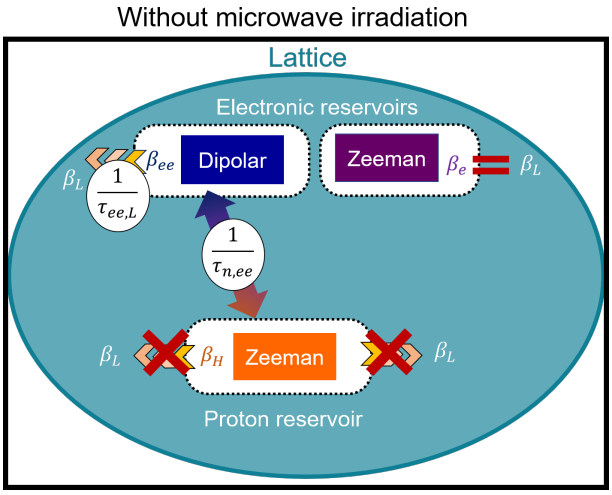

Figure 5.3: Schematic representation of Provotorov's theory in the absence of microvawe irradiation. The electron spin Zeeman and dipolar reservoirs are disconnected, and the electron dipolar and proton Zeeman reservoirs exchange polarization until they reach equal spin temperatures.

man and electron dipolar reservoirs are coupled and thus evolve towards a common spin temperature. However, without microwave irradiation, the electronic dipolar reservoir is not replenished by the electron Zeeman reservoir.

5.3 Experimental results

Figure 5.4 displays the hyperpolarized ^{1}H signals when the microwaves have been turned off after 15 minutes of irradiation at 188.380 GHz. This frequency leads to a negative nuclear polarization. The signal that stems from the negatively hyperpolarized protons of water is unusually long, since it lasts for more than 30 s. This leads to spectral widths that are narrower than 2 kHz after Fourier transform (see appendix D.1). In contrast, the typical duration of an FID at 1.2 K, either in the absence of DNP or in DNP experiments with positive polarization (irradiation at ca. 187.9 GHz) is on the order of tens of μs and leads to linewidth of ca. 25 kHz in reciprocal space. Hence, these unusual signals are observed only when the nuclear spins are polarized negatively.

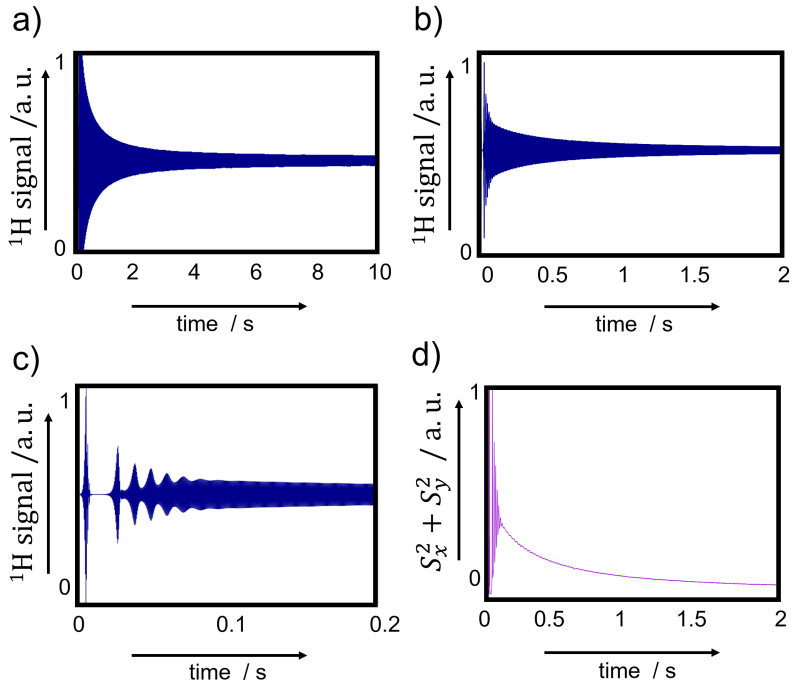

Figure 5.4: ^{1}H signal obtained at 1.2 K after ∼15 min of negative polarization (microwave frequency and power resp. 188.38 MHz and 12.6 mW). The microwave is turned off before the detection. a) b) and c) represent the real part of the signal in different time windows ([0,10], [0,2] and [0, 0.2] s); whereas d) is the squared norm of the signal as a function of time.

The behavior of the ^{1}H signal at short time scale (see figure 5.4 c) is highly evocative of manifestations of radiation damping, due to strong coupling between a large magnetization originating from a spin system located inside a cavity with a high quality factor Q. In 1979, P. Bösiger demonstrated that the magnetization of DNP-hyperpolarized aluminium nuclei in ruby cristals can lead to so-called MASER bursts upon microwave irradiation.[13] Here, we observed similar signal bursts of the ^{1}H signal in hyperpolarized (frozen) water, which is a very different sample. In order to verify this assumption, and to confirm that the sustained signal originates from the coupling between the detection circuit and the ^{1}H spins, simple complementary tests have been made. Detuning of the probe eliminates both the long term signal and the nonlinearities, and leads to signals that decay on a μs time scale. This observation validates the assumption that the long FIDs requires a strong coupling with a sensitive and properly tuned probe, typical of a RD contribution.

5.4 Simulating the dynamics of the DNP-hyperpolarized ^{1}H magnetization in the absence of microwave irradiation using the BMP equations

Using the BMP equations (Eqn. 5.8), the behavior of the ^{1}H NMR signal we observed in our DNP experiments in absence of microwave irradiation can be simulated. The resulting signals are strongly affected by different parameters and by the initial magnetization. Simulating the experimental signals, including the series of MASER bursts (Fig. 5.4), can provide information on the conditions that are required to achieve such a behavior, especially the time scale of the equilibration of the two reservoirs $\tau_{n,ee}$. As an illustration, the following set of model parameters: $\frac{1}{\tau_{ee,L}} = 10^{-4}$ s^{-1}, $\frac{C_n}{C_e} = 5$, $\frac{1}{\tau_{n,ee}} = 50$ s^{-1} , $\gamma G = 667$ m.s^{-1}.A^{-1} and $\frac{1}{T_2} = 25000$ s^{-1}, allowed us to qualitatively reproduce the experimental signal at short time scales using the BMP theory. Indeed, the comparison of the figures 5.5 c) and 5.4 c), shows that the simulated and experimental signals display comparable bursts at time $<$ 0.2 s.

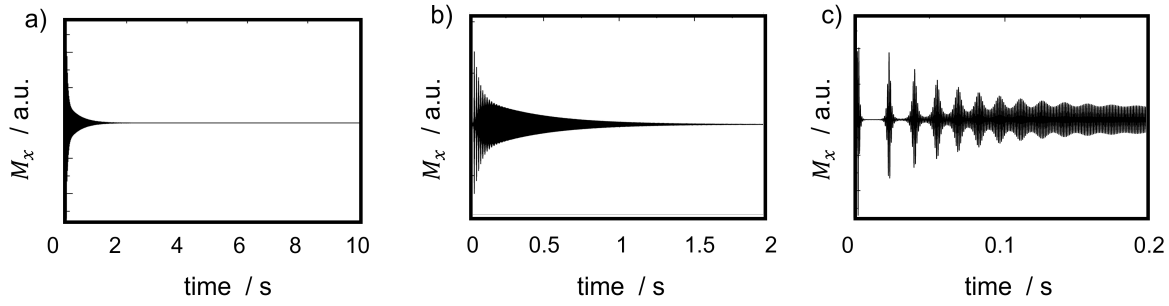

Figure 5.5: Simulation of the ^{1}H signal M_x with the BMP equations without microwave pumping (Eqn. 5.8). a), b) and c) show the evolution of M_x as a function of time in different observation time windows: [0,10], [0,2] and [0,0.2] s.

However, a comparison between the experimental behavior of the system (Fig. 5.4 a & Fig. 5.4 b) and the model (Fig. 5.5 a & Fig. 5.5 b) at longer times obviously shows that the model is unable to describe the long time behavior of the system. In particular, unlike the hyperpolarized ^{1}H signal that lasts more than 30 s, the transverse magnetization predicted by the simulations vanishes after 1 s.

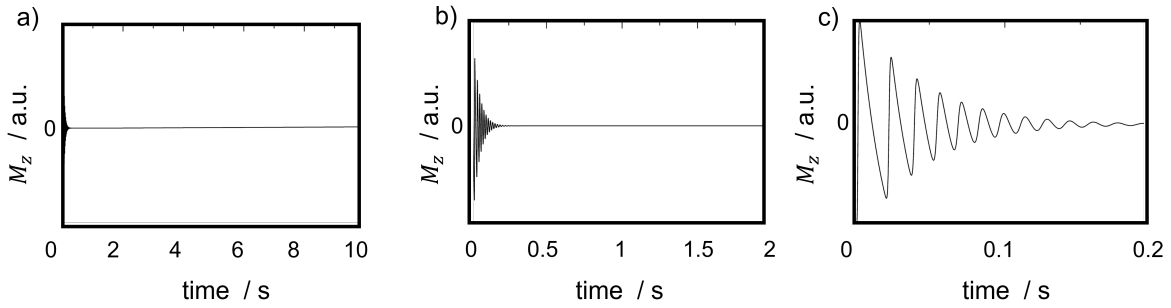

Figure 5.6: Simulations of the M_z component of the proton magnetization with the BMP equations without microwave pumping (Eqn. 5.8). a), b) and c) represent M_z as a function of time in different observation time windows: [0,10], [0,2] and [0,0.2] s.

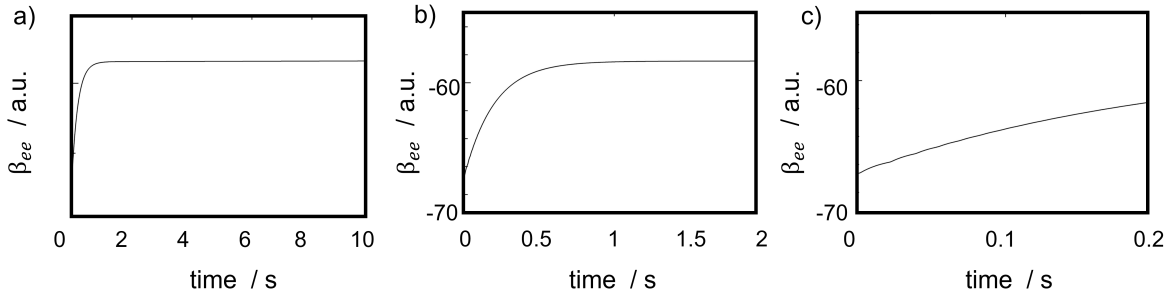

Figure 5.7: Simulation of the inverse electron dipolar spin temperature β_{ee} with the BMP equations (Eqn. 5.8). a), b) and c) represent β_{ee} as a function of time in different observation time windows: [0,10], [0,2] and [0,0.2] s.

5.5 Analysis of the experimental results

5.5.1 Evolution of the system without microwave irradiation

In the absence of microwave irradiation, the electron Zeeman reservoir is decoupled from the electron dipolar reservoir and the latter is not replenished any more. Both β_{ee} and β_n evolve toward β_L (see Eqn. 5.8 and Fig. 5.3). Two different contributions can clearly be identified: the short time scale MASER bursts on a time scale of tens of ms, and the long decay of the signal intensity on a time scale of s. The short time scale phenomenon strongly depends on the initial conditions of the experiment, whereas the decay on long time scales is independent from the initial conditions (see section 5.5.2). This is characteristic of the equilibration between the thermodynamical reservoirs in thermal contact.

As demonstrated in the previous section, Eqn. 5.8 qualitatively well account for the short time scale behavior of the observed signal, and reproduce similar MASER bursts. However, they are unable to explain the long term decay of the signal. The problem of the long time scale regime could partially be attributed to the fact that a third interacting reservoir was neglected: the deuterium Zeeman. The DNP samples possess an important deuterium bath (40% D_2O), that is also connected to the electron dipolar reservoir. The former may store a fraction of the energy of the system and affect the long term behavior of the proton Zeeman reservoir.

The consideration of a supplementary nuclear reservoir is in accordance with the Boesiger's experiments on ruby crystals (Al_2O_3:Cr^{3+})[13] where two different nuclear Zeeman reservoirs are taken into account: the ^{27}Al and ^{17}O Zeeman baths. The two nuclear reservoirs are indirectly connected with each other through the electron dipolar reservoir. The BMP equations 5.8 can therefore be modified to take into account this third reservoir (Eqn. 5.9).

$$\begin{cases} \dot{M}_x = \delta M_y - \gamma G M_z M_x - \frac{M_x}{T_2} \\ \dot{M}_y = -\delta M_x - \omega_1 M_z - \gamma G M_z M_y - \frac{M_y}{T_2} \\ \dot{M}_z = \omega_1 M_y + \gamma G (M_x^2 + M_y^2) - \frac{\gamma_n^2 \hbar^2 \mathcal{N}_{\mathrm{H}} B_0}{4 k_{\mathrm{B}} \tau_{n,ee}} (\beta_n - \beta_{ee}) \\ \dot{\beta}_{ee} = -\frac{C_n}{C_e} \frac{1}{\tau_{n,ee}} (\beta_{ee} - \beta_n) - \frac{C_d}{C_e} \frac{1}{\tau_{d,ee}} (\beta_{ee} - \beta_d) - \frac{1}{\tau_{ee,L}} (\beta_{ee} - \beta_L) \\ \dot{\beta}_d = -\frac{C_d}{C_e} \frac{1}{\tau_{d,ee}} (\beta_d - \beta_{ee}) \end{cases} \tag{5.9}$$

β_d, C_d and $\tau_{d,ee}$ correspond to the deuterium Zeeman inverse spin temperature, the deuterium heat capacity, and the characteristic time of the heat transfer between the electron dipolar and the deuterium Zeeman reservoirs. For the sake of simplicity, we define $\gamma_2 = \frac{1}{T_2}$, $\gamma_{d,ee} = \frac{1}{\tau_{d,ee}}$, $\gamma_{ee,d} = \frac{C_d}{C_e} \frac{1}{\tau_{d,ee}}$, $\gamma_{n,ee} = \frac{1}{\tau_{n,ee}}$, $\gamma_{ee,n} = \frac{C_n}{C_e} \frac{1}{\tau_{n,ee}}$ and $\gamma_{ee,\mathrm{L}} = \frac{1}{\tau_{ee,L}}$ so that Eqn. 5.9 become:

$$\begin{cases} \dot{M}_x = \delta M_y - \gamma G M_z M_x - \gamma_2 M_x \\ \dot{M}_y = -\delta M_x - \omega_1 M_z - \gamma G M_z M_y - \gamma_2 M_y \\ \dot{M}_z = \omega_1 M_y + \gamma G (M_x^2 + M_y^2) - \frac{\gamma_n^2 \hbar^2 \mathcal{N}_{\mathrm{H}} B_0}{4 k_{\mathrm{B}}} \gamma_{n,ee} (\beta_n - \beta_{ee}) \\ \dot{\beta}_{ee} = -\gamma_{ee,n} (\beta_{ee} - \beta_n) - \gamma_{ee,d} (\beta_{ee} - \beta_d) - \gamma_{ee,\mathrm{L}} (\beta_{ee} - \beta_L) \\ \dot{\beta}_d = -\gamma_{d,ee} (\beta_d - \beta_{ee}) \end{cases} \tag{5.10}$$

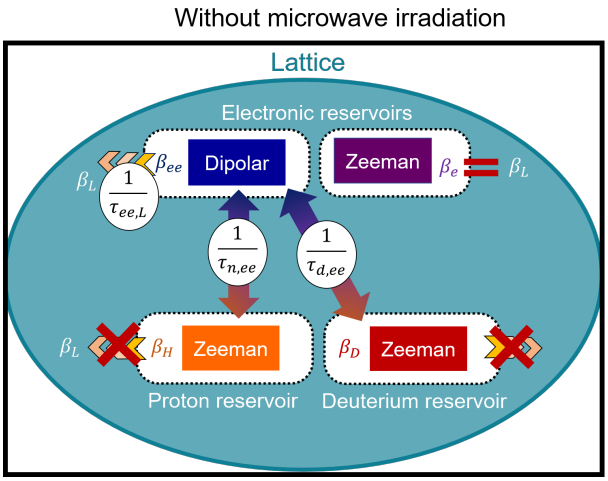

Figure 5.8: Modified model that takes into account a deuterium Zeeman reservoir. In the absence of microwave irradiation, the proton and deuterium Zeeman and electron dipolar reservoirs are interconnected. They tend to equilibrate their spin temperature.

We shall refer to this system as "extended BMP equations".

The model associated to Eqn. 5.9 has been used to fit the normalized intensity of the proton signals (see Fig. 5.9). The addition of further reservoir seems to better describe the long time scale behavior of the signals. The deuterium Zeeman reservoir may give a thermal "inertia" to the system, since its spin temperature slowly equilibrates with the electron dipolar and proton Zeeman spin temperatures (see Fig. 5.10 b and c). Under such circumstances, the long time scale proton signal mainly depends on the parameters $\gamma_{d,ee}$ and $\gamma_{ee,d}$ in the extended BMP equations 5.10. These three interacting reservoirs can explain a stabilization of the proton polarization to a negative value (see Fig. 5.10 a).

As far as the number of unknown parameters is concerned, the model is obviously underdetermined by the experimental data. The initial magnetization in the transverse plane that depends on the polarization of the system, its spin number, the nutation angle, the radiation damping characteristic time τ_{rd}, the filling factor η, the proton transverse relaxation time T_2, $\tau_{n,ee}$, $\frac{C_n}{C_e}$ and $\tau_{ee,L}$ all have to be determined. With an experimental access limited to the evolution of the magnetization in the transverse plane without normalization, signal fitting is rather challenging. Moreover, several model parameters: T_2, the initial steady-state spin temperature (or polarization) and $\mathcal{N}_{\mathrm{H}}$ are correlated.

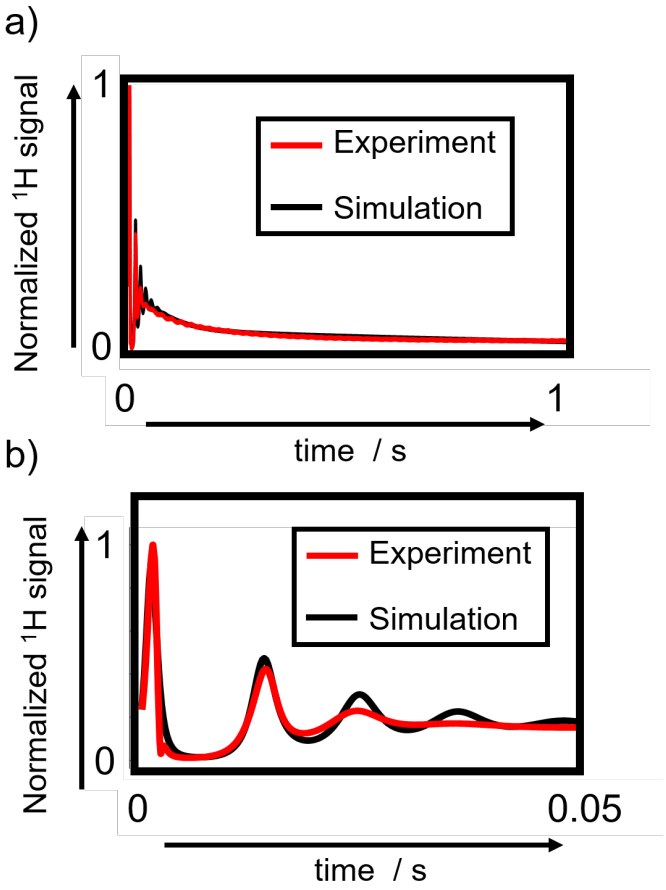

Figure 5.9: a) Comparison of simulated signals (black) obtained with the extended BMP equations (Eqn. 5.9) and the experimental proton signal intensities (red) at 1.2 K. b) Zoom on the early part of the signal.

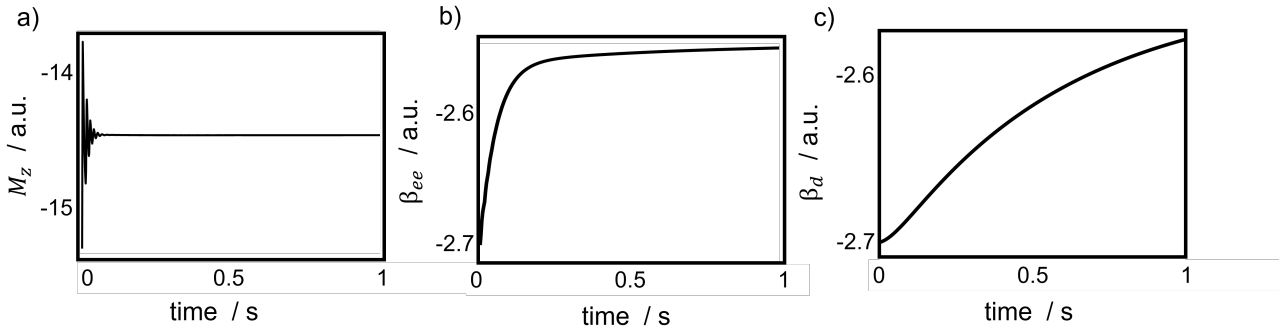

Figure 5.10: a) Simulated proton M_z magnetization component, b) dipolar reservoir and deuterium Zeeman inverse spin temperatures β_{ee} and β_d using the extended MBP equations.

The fit of the ^{1}H NMR signal can however give access to key information about the system. The characteristic times of exchange between the nuclear Zeeman reservoir and the electron dipolar reservoir ($\frac{1}{\tau_{n,ee}}$ and $\frac{1}{\tau_{d,ee}}$) and the heat capacity ratios $\frac{C_n}{C_e}$ and $\frac{C_d}{C_e}$ can indeed be evaluated. Thus, to obtain the fit displayed in Fig. 5.9, we

found: $\frac{1}{\tau_{n,ee}} \sim 150$ s^{-1} ($\tau_{n,ee} \sim 6.7 \cdot 10^{-3}$ s), $\frac{1}{\tau_{d,ee}} \sim 1.9 \cdot 10^{-1}$ s^{-1} ($\tau_{d,ee} \sim 5.2$ s), $\frac{C_n}{C_e} = 1.2 \cdot 10^{-1}$ and $\frac{C_d}{C_e} = 8.8 \cdot 10^{-1}$.

Considering the large number of parameters contained in the model, we used a Differential Evolution fitting algorithm,[32] a kind of genetic algorithm, for the fit. The main advantage of this strategy is to avoid trapping in local minima. But the main drawback is the absence of a proof of convergence.[33] Due to the large number of fitting parameters and to the fact that the model is underdetermined (only the transverse component of the magnetization is recorded), fitting was only achieved with difficulty. Therefore, quite a large number (several tens) of minimization cycles were performed, and only the one with the lowest target function was retained. In practice, a few runs lead to this lowest value. And since there is no way to ascertain convergence, this confers to the values retained for the different parameters a certain degree of uncertainty. However, the fit still provides useful insight into the timescales of the equilibration between the reservoirs and to the number of nuclei per electron in the sample that participate in the process.

Besides, it is interesting to note that all converging fits yield the value $\frac{1}{\tau_{ee,L}} \sim 0$. This result is surprising, and must be interpreted with caution, as remarked above. We could nonetheless assume that, even bearing in mind that the accuracy of the fit may be questionable, $\tau_{ee,L}$ is long enough so as to be neglected in our detection window (the fits were performed on a 1 s time window). In connection to this, the qualitative analysis of the extended BMP equations that takes into account the deuterium reservoir (Eqn. 5.9) is interesting. Indeed, it shows that in absence of microwave irradiation, two stable[34] steady-state solutions exist. The first one, which is trivial, corresponds to the Boltzmann equilibrium: the transverse magnetization is null and the magnetization is aligned along the +z axis. Moreover, a second stable steady-state with the magnetization aligned along the -z axis is possible only when $\gamma_{ee,\mathrm{L}} \to 0$ (see appendix D.3). This second stable fixed point with negative proton polarization (see Fig. 5.10 a) could explain the experimentally observed long-lived FID. The combination of the two competing processes (RD and the transfer of polarization from the electron dipolar bath to the proton Zeeman reservoir) transiently sustains a transverse component of the magnetization, which eventually decays to zero at

long times (long with respect to $\tau_{d,ee}$), when the ^{1}H magnetization has reached a value that is too low for RD to be effective.

5.5.2 Evolution of the system under constant microwave irradiation

As predicted by the BMP equations, the irradiation of the sample during the acquisition by microwaves affects the dynamics of the magnetization. Figure 5.11 compares the norm of the signal in the presence or absence of microwave irradiation. Both

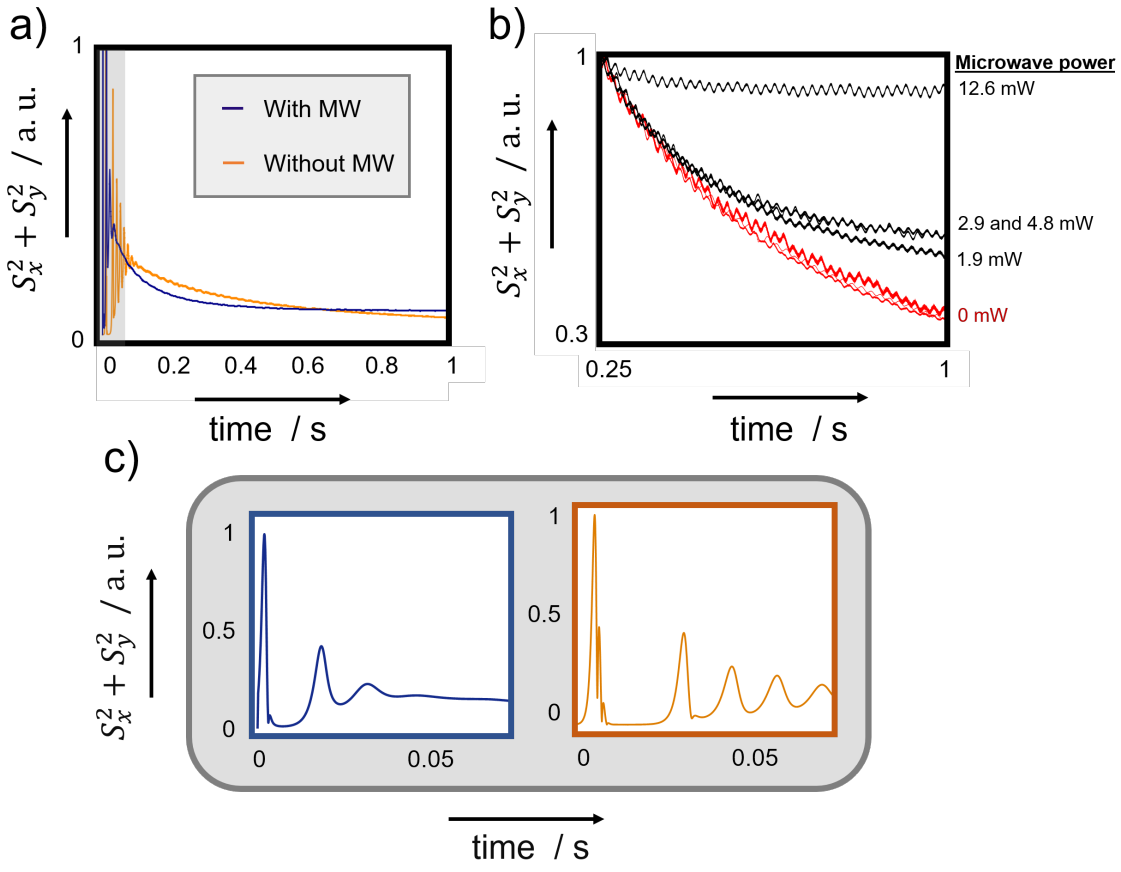

Figure 5.11: a) Comparison of the evolution of the normalized square of the amplitudes of the ^{1}H signal as function of time with (blue) and without (orange) microwave irradiation (MW). In the first case, the system is irradiated with a microwave power of 4.8 mW. The orange curve refers to the same experiment as the one depicted in figure 5.4. b) Normalized squared ^{1}H signal components for different microwave powers. The signal in the absence of microwave irradiation is represented in red. In black, the decreasing signal intensity is shown for microwave powers of 1.9, 2.9, 4.8 and 12.6 mW. c) At early times of the signal acquisition, MASER bursts are observed in both experiments: in the presence (blue) and absence (orange) of microwave irradiation.

signals in the presence or absence of microwave irradiation are sustained. However, when the system is continuously irradiated by low power microwaves (i.e. power $\leq$ 12.6 mW), the signal intensity ceases to decay after a time that depends on the microwave power, as illustrated in Fig. 5.11 b. These decays could not be fitted to a mono-exponential function and the corresponding rates are affected by the μw power, which illustrates the combined effects of $\gamma_{d,ee}$, $\gamma_{ee,d}$ and the microwaves on the time evolution of the system. The larger the latter, the faster the system reaches a steady-state, which is in accordance with the Bloch-Maxwell-Provotorov theory. In the extreme (and hypothetical) case where all terms that are not related to the microwave irradiation in equation 5.7 are neglected, we find that the time evolution of β_{ee} follows an exponential with a rate that depends on $\omega_{1\,\mu w}^2$.

$$\begin{aligned} \dot{\beta}_{ee} &\propto -\omega_{1\,\mu w}^2 \beta_{ee} + cste \\ \Rightarrow \beta_{ee} &\propto 1 - e^{-\omega_{1\,\mu w}^2 t} \end{aligned}$$

This suggests that a steady-state is reached faster when the microwave power is increased. Note that the decay rate in the absence of microwave irradiation at long times (red) is highly reproducible: the experiment has been repeated four times with different initial conditions. This has been achieved by changing the duration of the polarization or the pulse nutation angle. In the case of small pulse angles, the initial magnetization does not affect the behavior of the signal after 0.25 s.

5.5.3 Physical insights provided by this study

The choice of the microwave frequency is a key element to generate these long lived ^{1}H signals. When the spin system is negatively polarized (toward the -z axis in the laboratory frame), DNP competes with RD and both sustain the magnetization, keeping the spin system far from its equilibrium state. While RD tends to drive the ^{1}H magnetization to the +z on the Bloch sphere, the microwave pumping drives this magnetization toward the -z axis. When the time scales and the strengths of these two processes are comparable, the magnetization vector is kept in a steady-state with a non-vanishing transverse component. This effect can also happen in the

absence of microwave irradiation if the negative ^{1}H hyperpolarization is sufficient. Under TM conditions, a repolarization of the nuclear spin system after the switching the microwaves off occurs.[35] This means that the electron dipolar reservoir keeps fueling the proton Zeeman reservoir for a certain time. This could explain the MASER bursts followed by a long-lasting signal without a microwave pumping.

In case of positive polarization of the system (frequency of the microwave between 187.620 and 188 GHz), no resurrected nor sustained signals can be observed in our experiments. This corroborates our assumption as under these conditions, both RD and DNP processes tend to drive the magnetization from its non-equilibrium state to the Boltzmann equilibrium.

5.6 Material and Methods

5.6.1 Experimental details

The experiments were performed in the polarizer at 1.2 K. A continuous microwave irradiation at 188.380 MHz (negative polarization) was modulated by a 1 kHz saw-tooth wave over a bandwidth of 100 MHz. 150 μL of a DNP sample (50% glycerol-d_8, 40% D_2O, 10% H_2O and 50 mM TEMPOL) was inserted in a cylindrical TEFLON cup that does not contain any protons in order to avoid any spurious signals.

As different phenomena take place at different time scales, observing all of them in a single FID was rather challenging. MASER bursts occur on a time scale on the order of tens of ms, the frequency offset of the RF carrier is associated with oscillations at (or below) the ms time scale, whereas the decay of the amplitude of the signal can be observed on a time scale as long as several tens of seconds. Hence, signals were acquired with sampling times between 0.8 and 15 μs depending on the duration of the acquisition (from 1 to 30 s).

Nuclear spins were excited by a train of small nutation angles with low power pulses (0.1°) after presaturation (see section 2.2.4). Pulses are separated by a delay d_1 that is typically 5 s. To generate a long FID, low nutation angles $\alpha \ll 1°$ were required.

We therefore used low RF power for the detection. For instance, to generate a 0.1° nutation angle of the magnetization, the RF power was set at $5 \cdot 10^{-5}$ W during 5 μs.

5.6.2 Details on the fitting procedure

Time-dependent NMR signals have been manipulated using the free Python package Nmrglue[36] and the MATLAB DOSYToolbox.[37,38] Simulations and fits have been performed using a homemade Scilab[39] program which makes use of a differential evolution algorithm.[32]

Ten parameters are required to fit the experimental data with the equations 5.9.

System properties	
$\gamma_{n,ee} = \frac{1}{\tau_{n,ee}}$	
$\gamma_{ee,d} = \frac{1}{\tau_{ee,d}}$	Initial conditions
$\gamma_{ee,\mathrm{L}} = \frac{1}{\tau_{ee,L}}$	θ: angle $(\vec{M}, -\vec{z})$
$\frac{C_n}{C_e}$	T_S: spin temperature
$\frac{C_d}{C_e}$	
$\gamma_2 = \frac{1}{T_2(^1\mathrm{H})}$	
$\lambda = \eta Q$	
$\mathcal{N}_\mathrm{H}$	

The initial spin temperature and the number of spins together allow one to calculate the initial steady-state proton magnetization. 40000 iterations have been performed for each fit, each of them generating 33 individual populations. The signal was fitted over time windows of 1 s and a sampling interval of 7 μs.

5.7 Conclusions - Perspectives

The experiments that were performed under DNP conditions are qualitatively in accordance with the Boesiger's model. We were able to observe two distinct regimes:

a sustained MASER, with repeated RD burst at short times ($\leq$ 100 ms); and a regime of slow equilibration of the spin temperatures of the various reservoirs on a longer time scale. Importantly, the assumption that there are only two interacting reservoirs (proton Zeeman and electron dipolar) allows one to reproduce the system behavior at a short time scale, but not the long term evolution. The latter requires the additional assumption of a deuterium Zeeman reservoir coupled with the electron dipolar reservoir.

However, several aspects are not taken into account by this model. Firstly, it is important to bear in mind that the linear dependence of the inverse spin temperature on the magnetization relies on the high temperature approximation, which is constitutive of the Provotorov equations. This assumption, however, may not necessarily be true under our experimental DNP conditions, especially as far as the electrons are concerned. This may explain the discrepancies between our experimental observations and the model used for fitting, despite the clear qualitative agreement.

Secondly, the Maxwell-Bloch-Provotorov equations assume non-interacting spin systems, which is not valid under our experimental conditions. The dipolar width of the ^{1}H line in DNP samples is typically on the order of 25 kHz. It can be shown that the asymmetry of the MASER bursts is a direct consequence of this inhomogeneous linewidth. Further simulations could reproduce such effect by splitting the line into independent isochromats (not shown). Such simulations are very time consuming, therefore the asymmetry was reproduced for one isolated burst of the signal.

Finally, the microwave irradiation was not taken into account in our simulations. The prediction of the behavior of the ^{1}H signal sustained by microwaves would require the modeling of the electronic resonance properties of highly concentrated TEMPOL radicals at 1.2 K.

Bibliography

[1] G. Suryan. Nuclear magnetic resonance and the effect of the methods of observation. *Curr. Sci.*, 18:203, 1949.

[2] N. Bloembergen and R. V. Pound. Radiation damping in magnetic resonance experiments. *Phys. Rev.*, 95:8–12, 1954.

[3] C. R. Bruce, R. E. Norberg, and G. E. Pake. Radiation damping and resonance shapes in high resolution nuclear magnetic resonance. *Phys. Rev.*, 104:419–420, 1956.

[4] S. Bloom. Effects of radiation damping on spin dynamics. *J. Appl. Phys.*, 28(7):800–805, 1957.

[5] M. A. McCoy and W. S. Warren. Three-quantum nuclear magnetic resonance spectroscopy of liquid water: Intermolecular multiple-quantum coherence generated by spin-cavity coupling. *J. Chem. Phys.*, 93(1):858–860, 1990.

[6] Daniel Abergel, Marc A. Delsuc, and Jean-Yves Lallemand. Comment on: Is multiple quantum nuclear magnetic resonance spectroscopy of liquid water real? *J. Chem. Phys.*, 96(2):1657–1658, 1992.

[7] A. Vlassenbroek, J. Jeener, and P. Broekaert. Radiation damping in high resolution liquid nmr: A simulation study. *The Journal of Chemical Physics*, 103(14):5886–5897, 1995.

[8] D. Abergel and J.Y. Lallemand. Some microscopic aspects of radiation damping in nmr. *J. Magn. Reson. A*, 110(1):45 – 51, 1994.

[9] W. S. Warren, S. L. Hammes, and J. L. Bates. Dynamics of radiation damping in nuclear magnetic resonance. *J. Chem. Phys.*, 91(10):5895–5904, 1989.

[10] D. Abergel, A. Louis-Joeph, and J.-Y. Lallemand. Self-sustained maser oscillations of a large magnetization driven by a radiation damping-based electronic feedback. *J. Chem. Phys.*, 116(16):7073–7080, 2002.

[11] S. Datta, S. Y. Huang, and Y.-Y. Lin. Understanding spin turbulence in solution magnetic resonance through phase space dynamics and instability. *Concep. Magn. Reson. A*, 28A(6):410–421, 2006.

[12] J. Schlagnitweit, S. W. Morgan, M. Nausner, Müllern N., and H. Desvaux. Nonlinear signal detection improvement by radiation damping in single-pulse NMR spectra. *Chem. Phys. Chem*, 13(2):482–487, 2012.

[13] P. Bösiger, E. Brun, and D. Meier. Solid-state nuclear spin-flip maser pumped by dynamic nuclear polarization. *Phys. Rev. Lett.*, 38:602–605, 1977.

[14] Yu. F. Kiselev, A. F. Prudkoglyad, A. S. Shumovskii, and V. I. Yukalov. Detection of superradiant emission from a system of nuclear magnetic moments. *Sov. Phys. JETP*, 67:413–415, 1988.

[15] F. Arecchi and R. Bonifacio. Theory of optical maser amplifiers. *IEEE J. Quant. Elec.*, 1(4):169–178, 1965.

[16] F Bloch, W Hansen, and M Packard. Nuclear induction. *Phys. Rev.*, 69:127, 1946.

[17] D.I Hoult and R.E Richards. The signal-to-noise ratio of the nuclear magnetic resonance experiment. *J. Magn. Reson.*, 24(1):71 – 85, 1976.

[18] D.I. Hoult. The principle of reciprocity. *J. Magn. Reson.*, 213(2):344 – 346, 2011. Magnetic Moments.

[19] L. Picard, M. von Kienlin, and M. Décorps.

An overcoupled NMR probe for the reduction of radiation damping. *J. Magn. Reson., A*, 117(2):262 – 266, 1995.

[20] W. E. Maas, F. H. Laukien, and D. G. Cory. Suppression of radiation damping by q-switching during acquisition. *J. Magn. Reson. A*, 113:274–277, 1995.

[21] C. Anklin, M. Rindlisbacher, G. Otting, and F.-H. Laukien. A Probehead with Switchable Quality Factor. Suppression of Radiation Damping. *Journal of Magnetic Resonance*, 106:199–201, 1995.

[22] J.-H. Chen and X.-A. Mao. Simulation of the radiation damping artifacts in 2D COSY NMR experiments using the Q-switch technique. *Chemical Physics Letters*, 274(5):549 – 553, 1997.

[23] A. Louis-Joseph, D. Abergel, and J.-Y. Lallemand. Neutralization of radiation damping by selective feedback on a 400 MHz NMR spectrometer. *J. Biomol. NMR*, 5(2):212–216, 1995.

[24] D. Abergel, C. Carlotti, A. Louis-Joseph, and J.-Y. Lallemand. Improvements in Radiation-Damping Control in High-Resolution NMR. *J. Magn. Reson.*, 109:218–222, 1995.

[25] D. Abergel, , A. Louis-Joseph, and J.-Y. Lallemand. Amplification of radiation damping in a 600-MHz NMR spectrometer: Application to the study of water-protein interactions. *J. Biomol. NMR.*, 8:15–22, 1996.

[26] D. Abergel, A. Louis-Joseph, and J.-Y. Lallemand. A new concept for selective excitation in NMR. *Chemical Physics Letters*, 262(3):465 – 469, 1996.

[27] J.-H. Chen, A. Jerschow, and G. Bodenhausen. Compensation of radiation damping during selective pulses in NMR spectroscopy. *Chem. Phys. Lett.*, 308(5):397 – 402, 1999.

[28] B. Zengin, M. Z. Koylu, S. Korunur, and A. Yilmaz. Elimination of radiation damping effects from the NMR relaxation curves of H_2O/D_2O mixtures containing proteins and ions. *Chin. J. Phys.*, 51(4):692–699, 2013.

[29] P. R. Blake and M. F. Summers. Noesy-1-1-echo spectroscopy with eliminated radiation damping radiation damping. *J. Magn. Reson.*, 86(3):622 – 625, 1990.

[30] B. N. Provotorov. *Soviet Phys. JEPT*, 14:1126, 1962.

[31] A. Bornet, R. Melzi, S. Jannin, and G. Bodenhausen. Cross polarization for dissolution dynamic nuclear polarization experiments at readily accessible temperatures 1.2 K $<$ T $<$ 4.2 K. *App. Magn. Reson.*, 43:107–117, 2012.

[32] R. Storn and K. Price. Differential evolution – a simple and efficient heuristic for global optimization over continuous spaces. *J. Glob. Optim.*, 11(4):341–359, 1997.

[33] J. Socała and W. Kosiński. On convergence of a simple genetic algorithm. In Leszek Rutkowski, Ryszard Tadeusiewicz, Lotfi A. Zadeh, and Jacek M. Zurada, editors, *Artificial Intelligence and Soft Computing – ICAISC 2008*, pages 489–498, Berlin, Heidelberg, 2008. Springer Berlin Heidelberg.

[34] S. H. Strogatz. *Nonlinear Dynamics and Chaos: with Applications to Physics, Biology, Chemistry, and Engineering.* Westview Press, Boulder, 2015.

[35] S. F. J. Cox, V. Bouffard, and M. Goldman. The coupling of two nuclear zeeman reservoirs by the electronic spin-spin reservoir.

J. Phys. C: Sol. St. Phys., 6(5):L100, 1973.

[36] J. J. Helmus and C. P. Jaroniec. Nmrglue: An open source python package for the analysis of multidimensional NMR data. *J. Biomol. NMR.*, 55(4):355–367, 2013.

[37] MATLAB. *version 8.5.0 (R2018a)*. The MathWorks Inc., Natick, Massachusetts, 2018.

[38] M. Nilsson. The DOSY Toolbox: A new tool for processing PFG NMR diffusion data. *J. Magn. Reson.*, 200(2):296 – 302, 2009.

[39] Scilab Enterprises. *Scilab: Le logiciel open source gratuit de calcul numérique*. Scilab Enterprises, Orsay, France, 2012.

Chapter 6

Real-time monitoring pre-nucleation cluster formation of calcium phosphate by dissolution dynamic nuclear polarization

6.1 Introduction

NMR constitutes a powerful technique to study molecular dynamics. A prominent application is the study of protein-ligand or protein-protein interactions[1], which is particularly used in pharmaceutical industry for drug screening[2]. However, NMR spectroscopy suffers from an intrinsically low sensitivity, so that typical experiments require signal accumulation over long times. This impedes the real-time monitoring of fast reactions. Coupling NMR with dissolution DNP is therefore a promising strategy to overcome this limitation. It creates high signal intensities that open the way to real-time monitoring. Applications range from the real-time study of the enzymatic cascade of the pentophosphate pathway (PPP) using hyperpolarized glucose[3] to the study of the conversion of hyperpolarized pyruvate to lactate in cancerous cells[4]. Clearly, this approach constitutes a powerful method to study the kinetics of reactions for biomolecules. In small molecules, ^{13}C is the most commonly

used probe in DNP because of its low magnetic ratio and its long polarization lifetime. Carbon signals can be increased by a factor up to 10^4. Even though ^{13}C stays the most commonly used atomic probe for D-DNP experiments, its low natural abundance limits the sensitivity of the technique and in most of the cases forces one to use isotopic enrichment.

Unlike carbon, phosphorus has the advantage of having a spin-$\frac{1}{2}$ in 100% isotopic abundance:^{31}P. This nucleus constitutes an interesting probe as phosphate groups PO_4^- are involved in many biological events such as phosphorylation processes. The latter is defined as a post-translational modification (PTM) of a protein by covalent attachment of phosphate moieties and plays a key role in the activation or modification of the function of proteins by altering their 3D structure.[5] Phosphates are also present in the backbones of nucleic acids.[6] A large NMR community focuses on extracting structural and dynamical information about DNA and RNA using [^{1}H], [^{1}H-^{14}N] or [^{1}H-^{13}C] NMR spectroscopy.[7,8] In addition to their contribution to the structure and to the dynamics of biological molecules, phosphates play a very important role in mineral tissues such as bones and teeth. They contain crystalline structures composed of calcium and phosphate that are very similar to apatite.[9] Inorganic phosphates coupled with calcium ions may also cause diseases. Their high affinity can lead to an accumulation in inappropriate body parts such as joints. This phenomenon eventually causes osteoarthrisis. Moreover, calcium phosphates can form dihydrate dicalcium phosphates (or brushite minerals) that are involved in some cases of kidney stones.[10–12]

As far as we know, although biomineral calcium phosphates have been studied a lot in the past decades, none of the published papers provide quantitative informations on the dynamics of the pre-nucleation of these minerals. The structure has been intensively investigated, but the early stages of the reaction remains beyond the reach with conventional methods, due to the short time-scale on which the initial steps of calcification take place.

In this chapter, we propose to use the dissolution DNP (D-DNP) to boost the signals of inorganic phosphates. We extract information on the early stage of calcium phosphate precipitation and hence demonstrate that ^{31}P DNP is worth developing

as it can give access to fast biological processes.

6.2 DNP of phosphate

6.2.1 Phosphate samples for DNP

The buffer

Buffer based on (2-amino-2-hydroxymethyl-1,3-propanediol or TRIS) have proven not to interfere with the mineralization process and enable a pH window compatible with physiological conditions.[13,14] The goal was to end up after dissolution with a pH comparable with physiological conditions[15] (pH = 7.4). Using a 1 M concentrated TRIS-based buffer an adjusted pH around 7.8 using HCl, we demonstrated a sufficient ability to keep the pH of the sample after dissolution between 7.6 and 7.8 after dissolution.

Preparation of the DNP sample

The DNP samples are typically composed of a mixture of glycerol-d_8/D_2O/H_2O (5:4:1) where 1 M of inorganic phosphate (H_2KPO_4 powder) and 50 mM of TEMPOL have been dissolved. Since we needed high concentrations of phosphate for our experiments, and since H_2KPO_4 is not soluble in alcohols, we first dissolved the powder in the TRIS-based buffer to obtain a concentrated 2 M solution. Then, we added 50% of deuterated glycerol and the appropriate volume of a solution of 400 mM TEMPOL dissolved in D_2O. Finally, the sample was annealed until the precipitated H_2KPO_4 was entirely dissolved, inserted into a cylindrical Teflon® cup for a final volume of 250 μL that was subsequently vitrified in liquid helium.

Dissolution of the sample

The phosphate samples were dissolved using the set-up that has been described in section 2.1.1. The transfer from the polarizer at 1.2 K to the 10 mm tube in the 400 MHz spectrometer at room temperature typically takes 4 s. The hyperpolarized phosphate solution is injected in 500 μL of the buffer at pH 7.8. Under these circumstances, the final concentration of phosphate drops to ca. 100 mM upon mixing of the two solutions. The pH has been measured in the NMR tube after each dissolution. It varies between 7.8 and 6.5.

6.2.2 Build-up and enhancements

DNP has been performed at 1.2 K. The sample is hyperpolarized by direct irradiation with microwaves at a frequency of 2x93.950 MHz during approximately 1h30 with a power of 350 mW modulated in a saw-tooth mode over 100 MHz with modulation frequency of 1 kHz. In figure 6.1, the build up of the ^{31}P polarization is illustrated. The pulses affect only a small fraction of the ^{31}P magnetization if the flip angle is 1°.

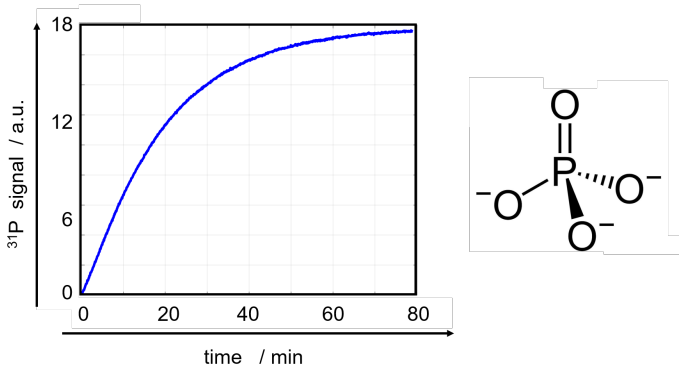

Figure 6.1: Build up of the ^{31}P signal as a function of time.

Although direct ^{31}P hyperpolarization is fast and efficient, asymmetric ^{31}P nuclei are typically characterized by a high CSA. This property induces rapid relaxation after dissolution at high magnetic field. As the time that is required to transfer hyperpolarized samples from the polarizer to the 9.4 T magnet is approximately 4 s, most ^{31}P nuclei would have completely lose their polarization almost completely.

Due to its symmetry however, inorganic phosphate possesses a vanishing CSA that enables the ^{31}P polarization to survive the transfer from the polarizer to the high field NMR spectrometer. The hyperpolarized signal sustained during approximately 30 s when applying 30° pulses every second. This results in a T_1 of approximately 10 s. With our setup we could achieve maximum signal enhancements $\epsilon = 10$ relatively to the thermal equilibrium signal. an earlier study presents an enhancement $\epsilon = 11000$ for phosphate DNP after dissolution with a transfer time of 15 to 16 s and a relaxation time $T_1 = 29$ s.[16] Contrary to our set-up, they used low fields (3 T polarizer and 5.4 T spectrometer), the phosphate concentrations involved were much lower (on the order of a few mM), and the signals detected at a basic pH. Moreover, the solvent that was used in this study contained only 10 % of protonated water.

Our study proves that even at high magnetic field and with high concentration of protons and phosphates, DNP can give access to kinetic parameters that remain inaccessible for other techniques.

6.3 Phosphate calcification

The precipitation of calcium phosphate (CaP) is a most important process in industrial, biological and geological contexts.[17] Its understanding is of great interest for many fields of research with major applications ranging from bone formation to mineralogy and dentistry.[18] However, despite its importance, the onset of CaP precipitation remains to a large extent elusive and subject to many speculations. The current state-of-the-art assumes a multi-stage process via the formation of amorphous pre-nucleation clusters and precipitation seeds to the formation of macroscopic precipitates accompanied by a disorder-to-order transition concerning the crystalline architecture.[19–22] To this debate, we can contribute a temporal dimension on short time scales. We demonstrate real-time monitoring of the initial phase of pre-nucleation cluster formation, which was - for the first time - made possible by D-DNP[23–26], embedded into a methodologically integrative[27] structural and kinetic characterization of CaP bio-mineralization. D-DNP allowed us to follow the out-of-equilibrium Ca^{2+} phosphate (P_i) interaction kinetics in calcium phosphate

solutions with a 1 s temporal resolution. In combination with electron microscopy (EM) and solid-state nuclear magnetic resonance (ssNMR) spectroscopy, we show that during the first 5 s after rapid mixing of a P_i solution with a Ca^{2+} solution nanoscopic pre-nucleation clusters (PNCs)[21] form with a rate constant on the order of 1.5 s^{-1} comprising 2-3 P_i units with a diameter of ca. 0.4 nm, before growing into larger nucleation seeds of ca. 10-40 nm after 30 s that lead to the eventual formation of macroscopic crystalline precipitates. These findings are important as they enlighten the kinetics of PNC formation at the onset of CaP bio-mineralization, which constitutes the limiting factor for the kinetics.

6.3.1 Experimental strategy

D-DNP produces substrates with enhanced NMR signals (often called "hyperpolrized") by first applying microwave irradiation to a sample containing paramagnetic polarization agents (PAs) at cryogenic temperatures and a subsequent rapid heating, dissolution and transfer of the hyperpolarized solution to a liquid-state NMR spectrometer. Our experimental strategy for real-time monitoring of pre-nucleation cluster formation is thus based on (i) the production of a hyperpolarized, P_i solution, i.e., with enhanced NMR signals and subsequent dissolution and rapid mixing "in-situ", i.e., within an NMR spectrometer, with a buffered Ca^{2+} solution at pH 7.8 and (ii) time-resolved detection of ^{31}P NMR spectra of hyperpolarized P_i exploiting the central phosphorous nucleus as a probe that reports with a 1 Hz sampling rate on the local nuclear environment of the phosphates involved (see Fig. 6.2 for a sketch).[16] (For details on the experimental parameters, see the Materials and Methods). This approach allows one to monitor the P_i interaction with Ca^{2+} on a time scale of a few seconds after mixing of the two reaction partners.

6.3.2 Results and discussion

We embedded the approach for fast time-resolved monitoring of bio-mineralization into an integrative strategy employing cryo-electron microscopy (EM) for the char-

acterization of the sample morphology 30 s after the initial mixing of the P_i and Ca^{2+} solutions as well as solid-state NMR to characterize the molecular architecture of stable macroscopic precipitates formed 10 min. after mixing. Thus, we characterized the different phases of the CaP precipitation event: PNC formation, growth of precipitation nuclei and macroscopic precipitation.

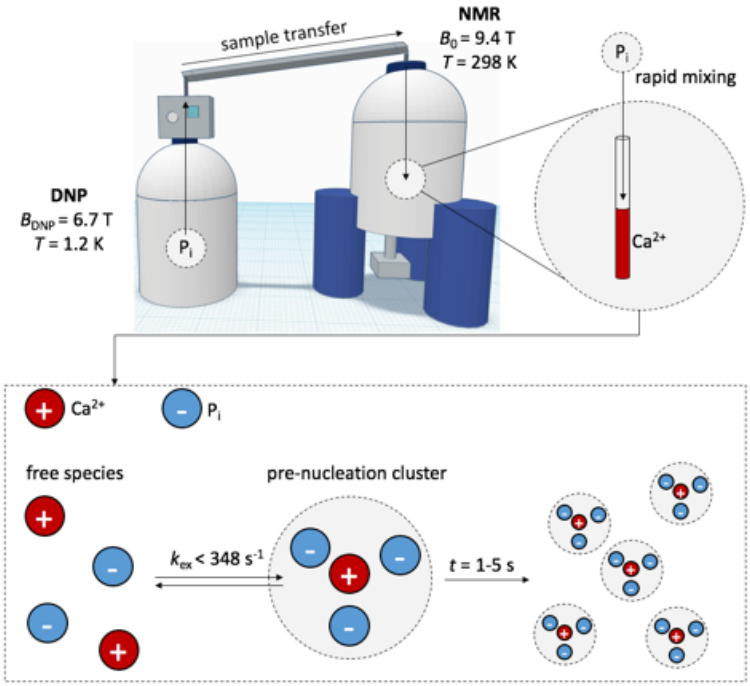

Figure 6.2: Sketch of the D-DNP experiment for real-time monitoring of CaP PNC formation. P_i is DNP hyperpolarized at 1.2 K to boost ^{31}P NMR signals. The hyperpolarized sample is subsequently dissolved and transferred to a NMR spectrometer where it is mixed with a Ca^{2+} solution that is waiting in an NMR tube. After mixing the PNC formation takes place on a timescale of 1-5 s observed at 25°C and pH 7.8.

6.3.3 Dissolution DNP- Real-time monitoring of PNC formation

After completion of the hyperpolarization step, i.e., of the ^{31}P signal enhancement procedure at low temperatures, the hyperpolarized P_i was dissolved, rapidly transferred and mixed in-situ, i.e. in a 9.4 T NMR spectrometer with a $CaCl_2$ solution at pH 7.8 and 25°C. NMR detection was than achieved with a train of 30° radio frequency (RF) pulses for ^{31}P signal detection applied at a repetition rate of 1 Hz. (For details see the section 6.3.5: Materials and methods.) Our first observation was

a dependence of the resulting phosphate spectra on the Ca^{2+} concentration. Fig. 6.3 a displays the appearance of spectra 3 s after mixing of 0.2 M P_i with the $CaCl_2$ solution. At a lower Ca^{2+} concentrations of 7 mM we observed only a single resonance corresponding to free dissolved P_i. In stark contrast, at a Ca^{2+} concentration of 13 mM, we found two signals, one sharp signal (with a linewidth $\lambda(P_i) \sim 45$ Hz) corresponding again to free P_i and a second, much broader signal with a chemical shift $\delta(^{31}P)$ significantly shifted from free P_i with a linewidth $\lambda(P_{PNC}) \sim 130$ Hz. At even higher Ca^{2+} concentrations of 25 mM, we again observe only one signal with a resonance frequency averaged between the two peaks observed at $c(Ca^{2+}) = 13$ mM.

These results can be interpreted in two ways: (i) The dependence of linewidth on the molecular mass of a molecule, and (ii) the dependence of the number of signals on the Ca^{2+} concentration.

Ad i), in NMR spectroscopy, the linewidth of a signal is directly proportional to the transverse relaxation rate R_2 of a nuclear spin. This relation gives rise to information about the dynamic behavior of the underlying species as R_2 depends on the rotational diffusion (more precisely on the rotational correlation time τ_c) of the molecule, which in return depends on its size (see the section 6.3.5 for details). From the linewidth of the second, broad peak at $c(Ca^{2+}) = 13$ mM, we can hence conclude that the P_i moieties giving rise to this signal are embedded in a complex that is several times heavier and has a rotational diffusion that must be more constrained than free P_i. Assuming that $R_2 \propto \tau_c$ (which might be an oversimplification[28], but serves here only for a first estimation of the size of the complex), a three-fold broader linewidth indicates a ca. three-fold slower rotational diffusion. This is in excellent agreement with results published by Habrakan et al.,[20] who found that pre-nucleation clusters of CaP are formed of three P_i units. We therefore conclude that we directly observed nanoscopic objects, which are PNCs of CaP that precede the precipitation of calcium phosphate.

The observation of the broad PNC signal by NMR is only possible with D-DNP. Such signals normally remain below the detection threshold of conventional techniques.

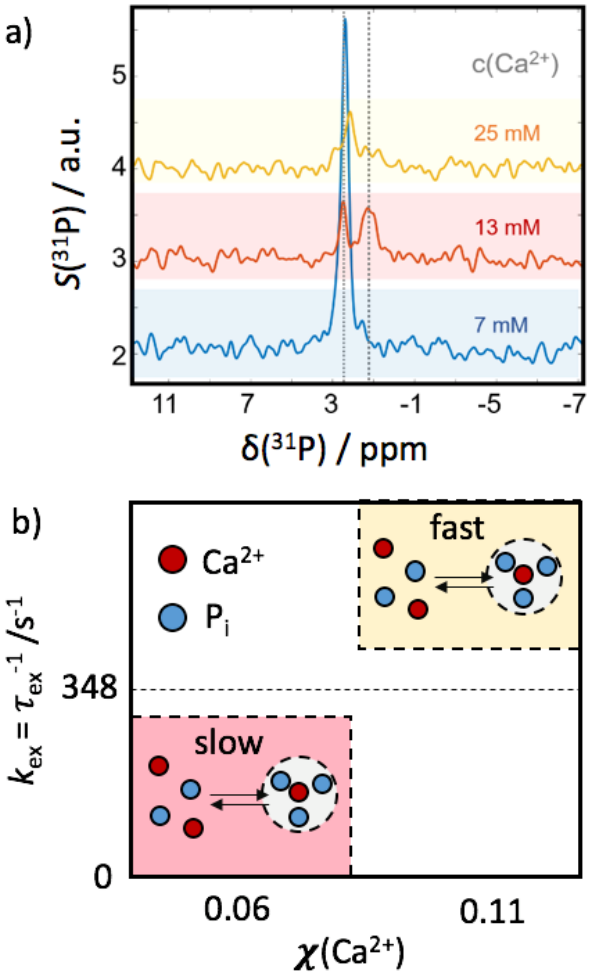

Figure 6.3: Dependence of the phosphate residence time in PNCs on the Ca^{2+} concentration. a) ^{31}P NMR spectra obtained 3 s after mixing of the hyperpolarized P_i solution with the Ca^{2+} solution at different concentrations (indicated in the figure). At c(Ca^{2+}) = 7 mM, only the signal of unbound P_i is observed at $\delta(^{31}P) = 2.8$ ppm. At c(Ca^{2+}) = 13 mM free P_i and P_{PNC} at $\delta(^{31}P) = 1.4$ ppm are simultaneously observed. At c(Ca^{2+}) = 25 mM a single signal at an averaged peak position at $\delta(^{31}P) = 2.2$ ppm is detected. b) Sketch of the dependence of the phosphate exchange constant k_{ex} on the Ca^{2+} mole fraction $\chi(Ca^{2+}) = c(Ca^{2+})/(c(Ca^{2+}) + c(P_i))$. With increasing Ca^{2+} concentrations, the exchange of phosphate between PNCs and free species accelerates.

Ad ii) At an intermediate Ca^{2+} concentration of 13 mM, the appearance of the second PNC signal indicates that the binding of P_i to Ca^{2+} takes place on a timescale that is accessible by our D-DNP approach. The simultaneous presence of two separate signals allows us to conclude that the exchange of P_i between its free and bound forms is slow on the NMR timescale, i.e., $k_{ex} < \Delta\omega$, where $\Delta\omega$ denotes the difference in resonance frequency of the two signals. $\Delta\omega$ was 1.4 ppm (348 Hz) so that the exchange constant can be estimated to < 348 s^{-1}. At a higher Ca^{2+} concentration of 25 mM, the signal averaged between the resonances of the free and

bound phosphates indicates a fast exchange regime, i.e., $k_{ex} \geq 384$ Hz. In other words, depending on the calcium concentrations, the system undergoes a transition between long residence times of P_i in the PNCs to shorter residence times. At lower Ca^{2+} concentrations, no PNC formation could be detected under our experimental conditions. This dependence is displayed in Fig. 6.4 b.

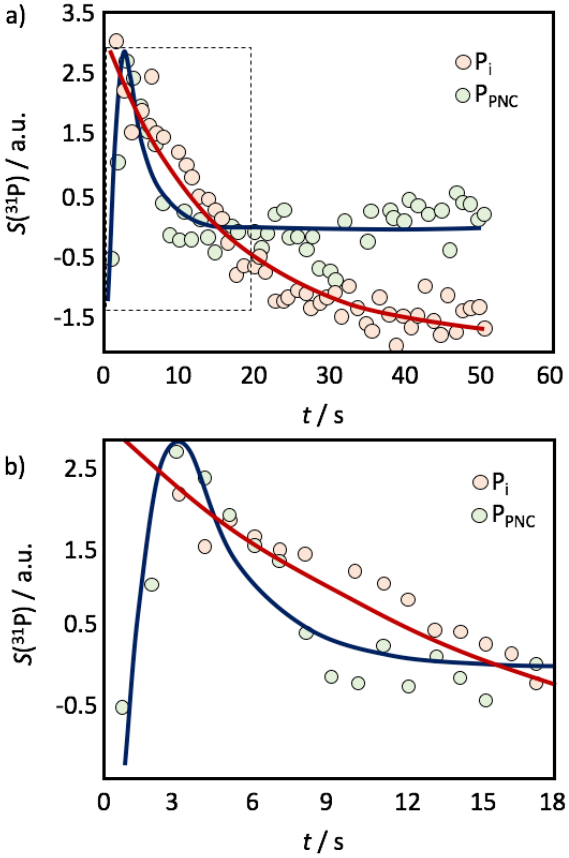

Figure 6.4: Temporal evolution of the ^{31}P signal intensity of free P_i and P_{PNC} after mixing. a) Evolution at t = 0 after mixing at a calcium concentration of c(Ca^{2+}) = 13 mM, pH 7.8 and T = 298 K. b) Zoom onto the region marked with a dashed square in panel a).

Interestingly, we observe only one signal next to that of free P_i indicating that the pre-nucleation process leads to the formation of a well-defined species with a defined molecular architecture, since the presence of other morphologies would lead to the appearance of further signals.

In a next step, we analyzed the kinetics of the pre-nucleation event. Fig. 6.3 shows the NMR signal intensity as a function of time of free P_i as well as P_i in pre-nucleation clusters (denoted P_{PNC} from here on). As P_i is in large excess with respect to Ca^{2+} in our experiments, the signal intensity of free P_i after injection primarily

decreases due to the decay of the hyperpolarization towards thermal equilibrium, which causes an exponential signal decay. The formation of pre-nucleation clusters might also cause a transfer of signal intensity from free P_i to the PNC signals, but this effect is here considered to be negligible. We observed a build-up of the intensity of the signal of P_{PNC} during the first 4 s after mixing before a decaying to naught. The build-up starts immediately up-on mixing of the two components, so that we already detect a significant signal 1 s after initiation of the PNC formation. The subsequent decrease of the P_{PNC} signal has two causes. Firstly, the above-mentioned decay of the hyperpolarization and secondly, a possible rapid growth or aggregation of the CaP PNCs beyond a molecular mass that is detectable by NMR. The time-dependence of P_i and P_{PNC} can be fitted to mono- and bi-exponential functions, respectively, revealing a characteristic decay rate of $R_1(\mathrm{Pi}) = 0.12 \pm 0.02\ \mathrm{s}^{-1}$ for the free P_i and apparent decay rate of $R_1(P_{PNC}) = 0.4 \pm 0.05\ \mathrm{s}^{-1}$ for P_i in pre-nucleation clusters (P_{PNC}). Assuming that the growth of PNCs is too slow to significantly affect their relaxation behavior, and assuming a ^{31}P chemical shift anisotropy (CSA) of P_{PNC} of 68 ppm,[29,30] we can determine the effective hydrodynamic radius R_h of the PNC, via the dependence of the relaxation rates of a molecule on its mass. Thus, we find a R_h of the PNC of ca. 0.4 nm (see section 6.3.5 for the calculations), which is again in excellent agreement with published estimates of the size of CaP PNCs.

The build-up rate constant of the signal of P_{PNC} can be determined to be $R_{UP}(P_{PNC}) = 1.5 \pm 0.5\ \mathrm{s}^{-1}$. Under the assumption that no other processes influence the build-up of the PNC signal, this rate constant corresponds to the kinetic constant k_{PNC} of PNC formation. In other words, within only 1.5 s ca. 2/3 (more precisely a fraction of 2/e) of the maximal PNC concentration is formed to initiate the growth of CaP precipitation seeds.

This process is here monitored in real-time, to the best of our knowledge for the first time. D-DNP not only yields the rate of PNC formation, but also an estimate for the residence time of P_{PNC} within the clusters, which, as we have shown here is dependent on the Ca^{2+} concentration.

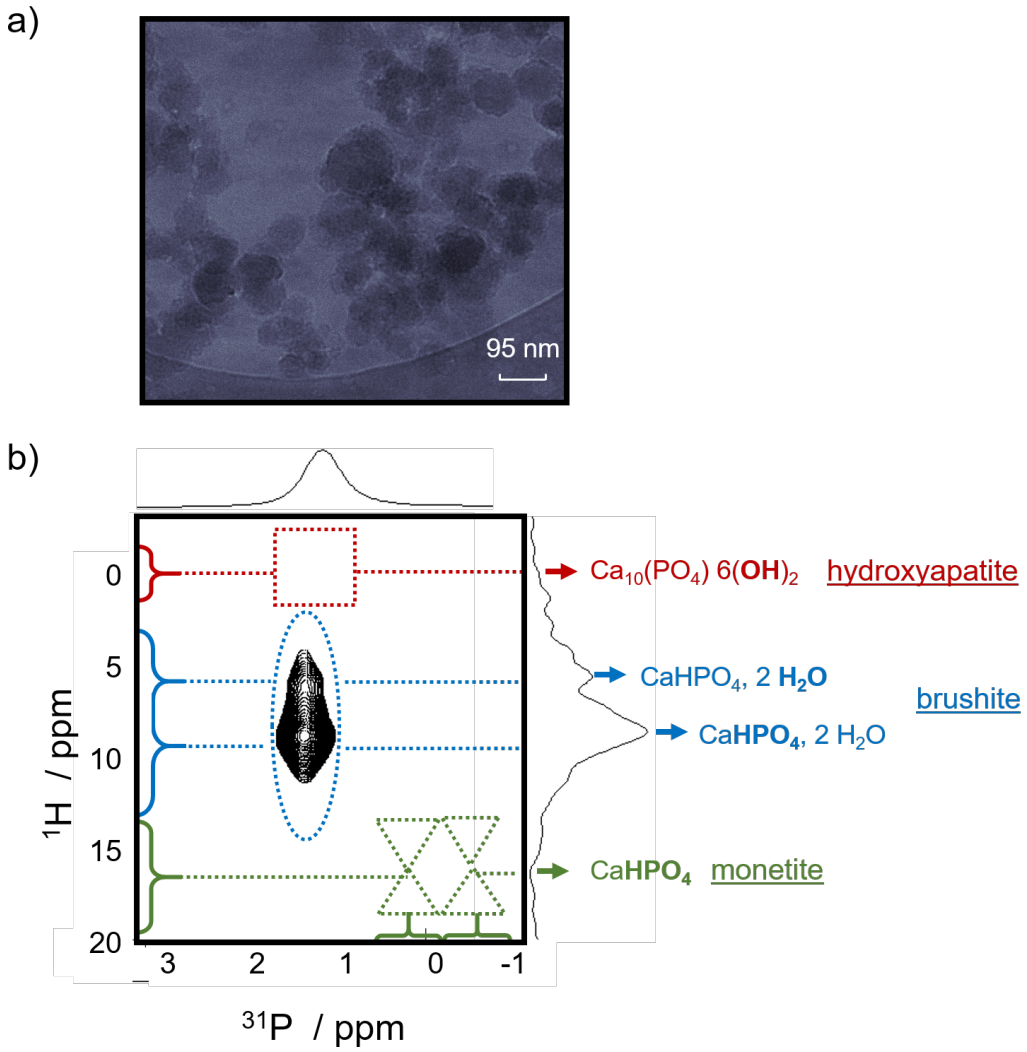

Figure 6.5: Evolution of the sample on a longer timescale. a) Representative cryo-electromicrograph of a CaP solution mimicking the D-DNP conditions for c(Ca^{2+}) = 13 mM. The sample was vitrified 30 s after mixing. Nanoscopic aggregates are observable with diameters varying between ca. 10 and 100 nm. b) ^{1}H-^{31}P heteronuclear correlation spectrum (HETCOR) of the precipitate formed of a D-DNP sample at c(Ca^{2+}) = 13 mM, 10 min. after mixing. A single peak in ^{31}P dimension characteristic for brushite, $CaHPO_4 \cdot 2H_2O$, can be observed indicating a homogeneous molecular architecture of the samples.

6.3.4 Cryo-EM and ssNMR - Characterization of precipitates

To further characterize the evolution of the morphology of the sample subsequent to PNC formation, we performed cryo-EM experiments on a similar sample, but vitrified 30 s after mixing by plunging it into liquid ethane. A representative micrograph is shown in Fig. 6.3. We find that the initially 0.4 nm large clusters grow

to CaP agglomerates to form nanoparticles with a heterogeneous size distribution ranging from 10-100 nm. These particles nicely correspond with CaP nucleation seeds, reported in the literature, that are formed from aggregation of PNCs.

Finally, we determined the internal architecture of the crystallites formed 10 min. after mixing by means of ssNMR following the approach published in references([31–33]), relying on heteronuclear correlation (HETCOR) spectroscopy. The spectrum in Fig. 6.5 features a peak characteristic for $CaHPO_4{\cdot}H_2O$, i.e., brushite. Such spectra remained unchanged for 2 days after sample preparation.

Notably, the spectrum in Fig. 6.5 displays a brushite-like internal architecture with two well defined peaks stemming from the two types of protons within the complex. Hence, starting from rather mobile PNCs that form on a time scale of a few seconds, macroscopic brushite crystallites form via the formation of nucleation seeds of 10-40 nm diameter and their subsequent growth, thereby undergoing a disorder-to-order transition from PNC to macroscopic brushite on a timescale from seconds to minutes.

6.3.5 Materials and methods

D-DNP 250 μL of a 1 M P_i (TRIS buffer at pH 7.8) supplemented with 50 mM of the PA TEMPOL and mixed 1:1 v/v with glycerol-d_8 as cryo-protectant was hyperpolarized at a temperature of 1.2 K and a magnetic field of 6.7 T for 1.5 h in a Bruker prototype polarizer.[34] The microwave frequency was set to 188.38 GHz and modulated with a saw-tooth function at with a modulation frequency of 1 kHz and an amplitude of 100 MHz.[35] The hyperpolarized sample was dissolved by a burst of 5 mL superheated D_2O at 180°C and 10.5 bar and propelled via a 0.9 T "magnetic tunnel"[36] with pressurized helium at 7 bar within 4 s to a Bruker Avance II 9.4 T NMR spectrometer operating at 298 K. There, the hyperpolarized sample was mixed with a 500 μL TRIS buffer containing 7, 13 or 25 mM $CaCl_2$. Detection was achieved once a second by a 30° pulse with a ^{31}P carrier frequency set to 0 ppm.

Cryo-EM The specimens were rapidly frozen by plunging them into liquid ethane, itself cooled by liquid nitrogen (LEICA EM CPC, Vienna, Austria). The cryofixed

specimens were mounted into a Gatan cryoholder (Gatan inc., Warrendale, PA) for direct observation at 93 K (-180 °C) in a JEOL 2100HC cryo-TEM system operating at 200 kV with a LaB6 filament. Images were recorded in zero-loss mode with a Gif Tridiem energy-filtered-CCD camera equipped with a 2k x 2k pixel-sized chip (Gatan Inc., Warrendale, PA). Acquisition was accomplished with Digital Micrograph software (versions 2.31.734.D, Gatan Inc., Warrendale, PA).

Solid-state NMR Under the assumption of a simple spherical rotation of the PNCs, the longitudinal relaxation rate of a single ^{31}P spin depends on the CSA of the ^{31}P spins according to

$$R_1 = \frac{2}{15} \left(\gamma B_0 \Delta\sigma\right)^2 \frac{\tau_c}{1 + (\omega\tau_c)^2} \tag{6.1}$$

where all symbols have their usual meaning.[28] Assuming a CSA of $\Delta\sigma = 68$ ppm, this results in $\tau_c = 0.9 \cdot 10^{-10}$ s. The effective hydrodynamic radius R_h is then calculated according to the Stokes-Einstein relation:

$$R_h = \sqrt[3]{\frac{3\mathrm{k_B}T\tau_c}{4\pi\eta}} \tag{6.2}$$

Where again all symbols have their usual meaning.

6.4 Conclusions

Summarizing, we demonstrate that real-time monitoring of PNC formation is possible with D-DNP. The method should be generally applicable,as shown by our example of CaP biomineralization. Wide ranges of concentration, pH and temperature regimes are in principle accessible. As for the temporal resolution, the signal intensity is not a limiting factor over time scales of seconds to minutes. In our example, we find that the residence time of P_i in a PNC depends on the Ca^{2+} concentration and that the time scales of the CaP formation are on the order of seconds. As PNCs are currently assumed to constitute the first step in nucleation and growth mecha-

nisms, their rate of formation can be considered to be important, possibly a limiting factor of the growth rate that determines the kinetics of CaP biomineralization.

Bibliography

[1] O. Cala, F. Guillère, and I. Krimm. NMR-based analysis of protein-ligand interactions. *Anal. Bioanal. Chem.*, 406(4):943—956, 2014.

[2] M. Pellechia, I. Bertini, D. Cowburn, C. Dalvit, E. Giralt, W. Jahnke, T. L. James, S. W. Homans, H. Kressler, C. Luchinat, B. Meyer, H. Osckinat, J. Peng, H. Schwalbe, and G. Siegal. Perspectives on NMR in drug discovery: a technique comes of age. *Nat. Rev. Drug Disc.*, 7:739–745, 2008.

[3] Sadet A., Weber E. M. M., Jhajharia A., Kurzbach D., Bodenhausen G., Miclet E., and Abergel D. Rates of chemical reactions embedded in a metabolic network by dissolution dynamic nuclear polarisation NMR. *Chem. – Europ. J.*, 24(21):5456–5461, 2017.

[4] R. Balzan, L. Fernandes, L. Pidial, A. Comment, B. Tavitian, and P. R. Vasos. Pyruvate cellular uptake and enzymatic conversion probed by dissolution DNP-NMR: the impact of overexpressed membrane transporters. *Magn. Reson. Chem.*, 55(6):579–593, 2017.

[5] F.-X. Theillet, H. M. Rose, S. Liokatis, A. Binolfi, R. Thongwichian, M. Stuiver, and P. Selenko. Site-specific NMR mapping and time-resolved monitoring of serine and threonine phosphorylation in reconstituted kinase rezctions and mammalian cell extracts. *Nat. Prot.*, 8(7):1416–1432, 2013.

[6] P. A. Levene. The structure of yeast nucleic acid. iv. ammonia hydrolysis. *J. Biol. Chem.*, 40:415–424, 1919.

[7] T. A. Early, D. R. Kearns, W. Hillen, and R. D. Wells. A 300 MHz and 600 MHz proton NMR study of a 12 base pair restriction fragment: investigation of structure by relaxation measurements. *Nuc. Ac. Res.*, 8(23):5795–5812, 1980.

[8] J. Feigon, V. Skelenář, E. Wang, D. E. Gilbert, R. F. Macaya, and Peter Schultze. ^{1}H NMR spectroscopy of DNA. In *DNA Structures Part A: Synthesis and Physical Analysis of DNA*, volume 211 of *Methods in Enzymology*, pages 235 – 253. Academic Press, 1992.

[9] B. Wopenka and J. D. Pasteris. A mineralogical perspective on the apatite in bone. *Mat. Sc. and Eng. C*, 25(2):131 – 143, 2005.

[10] C. Y. C. Pak. Physicochemical basis for formation of renal stones of calcium phosphate origin: calculation of the degree of saturation of urine with respect to brushite. *J. Clin. Invest.*, 48(10):1914–1922, 1969.

[11] C. Y. C. Pak, E. D. Eanes, and B. Ruskin. Spontaneous precipitation of brushite in urine: Evidence that brushite is the nidus of renal stones originating as calcium phosphate. *PNAS*, 68(7):1456–1460, 1971.

[12] M. Ohata and C. Y. C. Pak. The effect of diphosphonate on calcium phosphate crystallization in urine in vitro. *Kidney Intern.*, 4:401–406, 1973.

[13] T. Yokoi, M. Kawashita, and C. Ohtsuki. Biomimetic mineralization of calcium phosphates in polymeric hydrogels containing carboxyl groups. *J. Asian Cer. Soc.*,

1(2):155 – 162, 2013.

[14] B. Hoac, T. Kiffer-Moreira, J. L. Millan, and M. D. McKee. Polyphosphates inhibit extracellular matrix mineralization in mc3t3-e1 osteoblast cultures. *Bone*, 53(2):478–486, 2013.

[15] M. B. Tomson and G. H. Nancollas. Mineralization kinetics: A constant composition approach. *Nature*, 200:1059–1060, 1978.

[16] Nardi-Schreiber A., A. Gamliel, T. Harris, G. Sapir, J. M. Gmori, and R. Katz-Brull. Biochemical phosphates observed using hyperpolarized ^{31}P in physiological solutions. *Nat. Comm.*, 8:341–, 2017.

[17] R. Z. LeGeros. Calcium phosphate-based osteoinductive materials. *Chem. Rev.*, 108(11):4742–4753, 2008.

[18] W. Habraken, P. Habibovic, M. Epple, and M. Bohner. Calcium phosphates in biomedical applications: materials for the future? *Mat. Tod.*, 19(2):69 – 87, 2016.

[19] A. Dey, P. H. H. Bomans, and M˙ The role of prenucleation clusters in surface-induced calcium phosphate crystallization. *Nat. Mat.*, 9:1010–1014, 2015.

[20] W. J. E. M. Habraken, J. Tao, L. J. Brylka, H. Friedrich, L. Bertinetti, A. S. Schenk, A. Verch, V. Dmitrovic, P. H. H. Bomans, P. M. Frederik, J. Laven, P. van der Schoot, B. Aichmayer, G. de With, J. J. DeYoreo, and N. A. J. M. Sommerdijk. Ion-association complexes unite classical and non-classical theories for the biomimetic nucleation of calcium phosphate. *Nat. Comm.*, 4(1507), 2013.

[21] G. Mancardi, U. Terranova, and N. H. de Leeuw. Calcium phosphate prenucleation complexes in water by means of ab initio molecular dynamics simulations. *Cryst. Growth Design*, 16(6):3353–3358, 2016.

[22] A. Carino, C. Ludwig, A. Cervellino, and M˙ Formation and transformation of calcium phosphate phases under biologically relevant conditions: Experiments and modelling. *Acta Biomater.*, 74:478 – 488, 2018.

[23] J. H. Ardenkjær-Larsen, B. Fridlund, A. Gram, G. Hansson, L. Hansson, M. H. Lerche, R. Servin, M. Thaning, and K. Golman. Increase in signal-to-noise ratio of > 10,000 times in liquid-state NMR. *Proceed. Nat. Acad. Sc.*, 100(18):10158–10163, 2003.

[24] M. Karlsson, P. R. Jensen, J. O. Duus, S. Meier, and M. Lerche. Development of dissolution DNP-MR substrates for metabolic research. *App. Magn. Reson.*, 43:223–236, 2012.

[25] A. Bornet and S. Jannin. Optimizing dissolution dynamic nuclear polarization. *J. Magn. Res.*, 264:13–21, 2016.

[26] X. JI, A. Bornet, B. Vuichoud, J. Milani, D. Gajan, A. J. Rossini, L. Emsley, G. Bodenhausen, and S. Jannin. Transportable hyperpolarized metabolites. *Nat. Comm.*, 8:13975, 2017.

[27] E. M. M. Weber, G. Sicoli, H. Vezin, G. Frébourg, D. Abergel, G. Bodenhausen, and D. Kurzbach. Sample ripening through nanophase separation influences the performance of dynamic nuclear polarization. *Angew. Chem. Intern. Ed.*, 57(18):5171–5175.

[28] J. Kowalewski and L. Maler. *Nuclear Spin Relaxation in Liquids: Theory, Experiments and Applications.* Series in Chemical Physics (CRC PRess), US, 2006.

[29] A. S. Goryan. Nuclear magnetic resonance studies on bentonite in complex mixed sys-

tems, 2012.

[30] W. P. Rothwell, J. S. Waugh, and J. P. Yesinowski. High-resolution variable-temperature phosphorus-31 nmr of solid calcium phosphates. *J. Am. Chem. Soc.*, 102(8):2637–2643, 1980.

[31] E. R. Wise, S. Maltsev, M. E. Davies, M. J. Duer, C. Jaeger, N. Loveridge, R. C. Murray, and D. G. Reid. The organic mineral interface in bone is predominantly polysaccharide. *Chem. Mat.*, 19(21):5055–5057, 2007.

[32] Y.-H. Tseng, Y.-L. Tsai, T. W. T. Tsai, J. C. H. Chao, C.-P. Lin, S.-H. Huang, C.-Y. Mou, and J. C. C. Chan. Characterization of the phosphate units in rat dentin by solid-state NMR spectroscopy. *Chem. Mat.*, 19(25):6088–6094, 2007.

[33] G. Cho, Y. Wu, and J. L. Ackerman. Detection of hydroxyl ions in bone mineral by solid-state NMR spectroscopy. *Science*, 300:1123–1127, 2003.

[34] D. Guarin, S. Marhabaie, A. Rosso, D. Abergel, G. Bodenhausen, K. L. Ivanov, and D. Kurzbach. Characterizing thermal mixing dynamic nuclear polarization via cross-talk between spin reservoirs. *J. Phys. Chem. Lett.*, 8(22):5531–5536, 2017.

[35] A. Bornet, J. Milani, B. Vuichoud, A. J. P. Linde, G. Bodenhausen, and S. Jannin. Microwave frequency modulation to enhance dissolution dynamic nuclear polarization. *Chem. Phys. Lett.*, 602:63–67, 2014.

[36] J. Milani, A. Bornet, P. Miéville, R. Mottier, S. Jannin, and G. Bodenhausen. A magnetic tunnel to shelter hyperpolaryzed fluids. *Rev. Sc. Inst.*, 86:024101–1–8, 2015.

Conclusions

Dissolution dynamic nuclear polarization is a powerful technique that offers great perspectives in NMR for fast reaction real-time study or for the study of nuclei with low gyromagnetic ratios in natural abundance. The mechanisms enabling to transfer the polarization from electrons to surrounding nuclei strongly depend on the experimental conditions. The EPR linewidth of the paramagnetic agents and the spectral diffusion are key criteria to allow one of the three solid state DNP mechanisms to play a dominant role. At 4 K and in a static magnetic field of 6.7 T, typical samples for D-DNP experiments contain high concentration of TEMPOL. Both the inhomogeneous and the homogeneous linewidths are consequently very broad. Under such circumstances, the electron spectral diffusion (eSD) is not sufficiently fast to lead to a homogeneous spin-lattice relaxation across the entire spectrum. Experiments show that different $T_{1e}(\omega)$ can be measured at different frequencies ω in the spectrum, demonstrating only a "local" homogenization $T_{1e}(\Delta_i)$. Even though the DNP process involves contributions of several mechanisms under the conditions required for D-DNP, an in-depth study of the anisotropic $T_{1e}(\Delta_i)$ in Borghini's thermal mixing (TM) model lead to an improvement of the predictions of proton polarization as a function of the microwave frequency ("profile").

Moreover, it is well known that liquid mixtures of glycerol and water experience a time-dependent nanophase separation. In our experiments, this phenomenon generates variations of the efficiency of the DNP process as radicals such as TEMPOL or AMUPol have better affinity for water than glycerol and therefore tend to agglomerate in water-rich vesicles. The resulting high local concentrations of radicals in water (H_2O/D_2O) can boost the proton signal as much as 20 % compared to

homogeneous samples.

In addition to these effects, we could observe non-linear behavior of the signals of negatively hyperpolarized H_2O protons of DNP samples at 1.2 K. MASER bursts that are characteristic of radiation damping (RD), a phenomenon that is commonly encountered in liquid state NMR, have also been generated in our glassy "DNP-Juice". Moreover by using equations previously developed for pumped ^{27}Al nuclei in ruby crystals, we were able to reproduce these bursts qualitatively by simulations. They can provide access to key parameters that are relevant for DNP, such as the rate constant of the equilibration between the electron dipolar and the Zeeman nuclear reservoirs in the TM regime. Our DNP setup creates such a strong ^{1}H polarization of water that noise suffices to give rise to signals that survive for more than 30 s. We showed that an interaction of the deuterium bath with the electron dipolar reservoir could explain this long lived ^{1}H signal. as the the transverse component of the magnetization is sustained by two competing phenomena: radiation damping and the pumping of ^{1}H polarization by microwave irradiation toward a negative spin temperature.

Although ^{13}C is often used in D-DNP, other nuclei such as ^{31}P that are highly relevant for studying biological mechanisms, are still a challenge for this technique. ^{31}P nuclei typically exhibit a large CSA that leads to short-lived signals. The CSA relaxation rates increase with the square of the external field. We show nonetheless that, despite small enhancements, high field ^{31}P D-DNP can give access to very fast processes such as the early stage of the clustering that occurs prior to the bio-mineralization of the calcium ions with inorganic phosphates.

Appendices

Appendix A

Theory of NMR

A.1 Relevant interactions

Interactions are the key to get information on a system. They enable the differentiation of nuclei, give access to dynamical properties on different time scales, depending on their magnitude, or help to describe the structure of molecules. In a more fundamental way, we could not detect any NMR signal without them. In this thesis, the Zeeman, dipolar and chemical shift interactions are described, but this list is not exhaustive. We propose here to complete the description of the interactions that are important in NMR.

A.1.1 Scalar couplings

Also called 'J-couplings', scalar couplings are a magnetically independent weak interactions between nuclei (on the order of tens of Hz for protons). This interaction mostly occurs between nuclei that are linked by covalent bonds in a molecule. The overlapping of the electronic wave functions and the nuclei modifies the local magnetic field experienced by each nucleus, such that the state of one nucleus will impact the state of the second through propagation of the information of the spin state through the electronic wave function. This interaction between nuclear and

electronic magnetic moments implies a non-zero probability for an electron to be localized at the site of the nuclei and is called Fermi contact interaction. Only the s-orbitals have a non-zero probability at the location of a nucleus. When the system verifies $\omega_i - \omega_j \gg J_{ij}$ with ω_i and ω_j, the resonance frequencies of nuclei i and j coupled with a scalar coupling J_{ij}, the latter can be expressed using only products of $\hat{I}_z$.[1] The J-coupling Hamiltonian $\hat{H}_J$ experienced by one nucleus i corresponds then to the sum of all the different couplings coming from the interconnected nuclei j in the molecule (Eqn. A.1).

$$\hat{H}_J = \sum_i J_{ij} \hat{\mathbf{I}}_i \cdot \hat{\mathbf{I}}_j \approx J_{ij} \hat{I}_{iz} \cdot \hat{I}_{jz} \tag{A.1}$$

Taking into account the nature of the interaction, a nucleus is usually primarily affected by atoms connected by less than three successive bonds in the molecule. The further the nuclei are from one another, the weaker is the J-coupling. Hence, nuclei separated by two bonds have a stronger coupling than the ones separated by three. One important characteristic of this scalar coupling is its reciprocity. Indeed, if two nuclei i and j interact, they will experience the same J_{ij}. In the spectra, internuclear scalar couplings split the lines if the interacting nuclei are magnetically inequivalent. It depends, of course, on the nature of the nuclei but also on their environment. For example, we can consider two magnetically inequivalent protons A and B which are coupled by ${}^2J_{AB}$. This notation means that A and B are separated from each other by two bonds. The resonance frequency of spin A will be affected by the state of spin B according to the strength of their coupling. This leads to two different resonances separated by J_{AB}. Hence, the J coupling can be directly measured in the spectra because each peak is shifted from the chemical shift frequency by $\frac{J}{2}$. The number of peaks resulting from scalar couplings depends on the number of energy levels of the coupled spins (i.e. their spin quantum number). A spin-$\frac{1}{2}$ has two energy levels, each resonance is thus split in two. Nuclei with spin 1 have three energy states: $m = -1, 0, 1$ where m is the magnetic quantum number. Such spins therefore induce a splitting of each resonance into three equal peaks. As each line is displaced from its chemical shift frequency by the same factor, degeneracies may occur, which impact on the intensity of each peak. Three J-coupled spin 1 nuclei

generate a septuplet with intensities of each peak given by a binomial distribution. In addition to giving information on the nuclei that are coupled, J-couplings are also sensible to the number of nuclei coupled to one spin. The more a nucleus is subjected to couplings, the more its resonance is split. Hence, one can extract structural information from scalar couplings as they give access to the through-bond connectivities between spins.[2]

A.1.2 Quadrupolar coupling

The quadrupolar coupling is a strong interaction (up to tens of MHz), that occurs in nuclei which have a spin quantum number greater than $\frac{1}{2}$.[3–8] Indeed, unlike spin-$\frac{1}{2}$ nuclei, nuclei with $I > \frac{1}{2}$ do not have a spherical distribution of their electric charges. They can be represented in classical terms as prolate or oblate spheroids. Hence, even if the electric field at the nucleus position is zero, the spatial derivative of that field (electric field gradient) does not necessarily vanish. This leads to an interaction between the nuclear quadrupole and the electric field gradient (EFG) generated by the surrounding electrons. The semi-classical quadrupolar Hamiltonian can be expressed as:

$$\hat{H}_Q = \frac{eQ}{2I(2I-1)\hbar}\hat{\mathbf{I}} \cdot \mathbf{V} \cdot \hat{\mathbf{I}} \tag{A.2}$$

with e, the electronic charge, Q, the quadrupolar constant, I, the spin quantum number associated with the spin angular momentum operator $\hat{\mathbf{I}}$ and $\mathbf{V}$, the matrix representing the EFG. The different components of $\mathbf{V}$ are evaluated using second derivatives of the potential at the location of the nucleus.

$$V_{\alpha\beta} = \left.\frac{\partial^2 \mathbf{V}}{\partial\alpha\partial\beta}\right|_0 \tag{A.3}$$

One can also express the quadrupolar Hamiltonian in a frame where $\mathbf{V}$ is diagonal. This frame is known as the 'principal axis system' (PAS).

$$\begin{pmatrix} V_{xx} & V_{xy} & V_{xz} \\ V_{yx} & V_{yy} & V_{yz} \\ V_{zx} & V_{zy} & V_{zz} \end{pmatrix} \rightarrow \begin{pmatrix} V_{XX} & 0 & 0 \\ 0 & V_{YY} & 0 \\ 0 & 0 & V_{ZZ} \end{pmatrix} \tag{A.4}$$

In the principal axis frame (PAS), $\mathbf{V}$ is traceless ($Tr(\mathbf{V}) = V_{XX} + V_{YY} + V_{ZZ} = 0$). We can thus introduce an asymmetry parameter η_Q which is defined in the equation A.5.

$$\eta_Q = \frac{V_{XX} - V_{YY}}{V_{ZZ}} \tag{A.5}$$

Considering that the magnitude of the EFG at the position of the nucleus corresponds to $V_{ZZ} = eq$, the quadrupolar Hamiltonian in the principal axis system (PAS) of the EFG tensor can be expressed as:

$$\hat{H}_Q^{PAS} = \frac{\chi}{4I(2I-1)} \left(3\hat{I}_Z^2 - \hat{\mathbf{I}}^2 + \eta_Q \left(\hat{I}_X^2 - \hat{I}_Y^2 \right) \right) \tag{A.6}$$

In the literature, χ is called the quadrupolar constant. It corresponds to the magnitude of V_{ZZ}. It determines the strength of the quadrupolar interaction for a nucleus.

$$\chi = \frac{e^2 Q q}{\hbar} \tag{A.7}$$

The splitting of the nuclear levels due to quadrupolar couplings depends on χ, its spin quantum number and the geometry of the system.

A.2 The matrix representation

In quantum mechanics, an operator $\hat{Q}$ can be represented as a matrix that acts on a superposition state $|\psi\rangle$ leading to the transformation of $|\psi\rangle$ into $|\psi'\rangle$:

$$\hat{Q} |\psi\rangle = |\psi'\rangle = \sum_i \eta_i c_i |\psi_i\rangle \tag{A.8}$$

where c_i are coefficients associated with the eigenvectors $|\psi_i\rangle$ and with the eigenvalues (or observable) η_i verifying:

$$\langle\psi_i| \hat{Q} |\psi_i\rangle = \eta_i c_i^* c_i \tag{A.9}$$

$c_i^* c_i$ corresponds to the probability of finding the system in the $|\psi_i\rangle$ state when a large number of measurement are performed. The projection of $|\psi\rangle$ onto $\hat{Q}$ corresponds

to a multiplication of a matrix and a vector. The resulting vector $|\psi'\rangle$ is a linear combination of eigenvectors $\hat{Q}$ also called basis functions. The basis functions are orthogonal and can entirely describe the space (see equation A.10).

$$\forall i, j, \langle \psi_i | \psi_j] \rangle = 0 \text{ and } \langle \psi_i | \psi_i \rangle = 1 \tag{A.10}$$

Each element Q_{ij} of the matrix can be calculated by equation A.11.

$$Q_{ij} = \langle i | \hat{Q} | j \rangle = \int \psi_i^* \hat{Q} \psi_j dt \tag{A.11}$$

In the case of a spin system with $\frac{1}{2}$, each component of the spin angular momentum can be associated with a matrix. For $\hat{Q} = \hat{I}_z$, the operator has two basis functions $|\alpha\rangle$ and $|\beta\rangle$ respectively associated to its eigenvalues $\frac{\hbar}{2}$ and $-\frac{\hbar}{2}$. $\hat{I}_z$ can thus be built following the equation A.12.

$$\hat{I}_z = \begin{pmatrix} \langle \alpha | \hat{I}_z | \alpha \rangle & \langle \alpha | \hat{I}_z | \beta \rangle \\ \langle \beta | \hat{I}_z | \alpha \rangle & \langle \beta | \hat{I}_z | \beta \rangle \end{pmatrix} = \frac{\hbar}{2} \begin{pmatrix} 1 & 0 \\ 0 & -1 \end{pmatrix} \tag{A.12}$$

In a same way, we can obtain the matrix representations of the other $\hat{I}$ components $\hat{I}_x$ and $\hat{I}_y$ (see Eqn. A.13).

$$\hat{I}_x = \frac{\hbar}{2} \begin{pmatrix} 0 & 1 \\ 1 & 0 \end{pmatrix} \text{ and } \hat{I}_y = \frac{\hbar}{2} \begin{pmatrix} 0 & -i \\ i & 0 \end{pmatrix} \tag{A.13}$$

To express some interaction, the raising and lowering (shift) operators $\hat{I}_+$ and $\hat{I}_-$ can be quite useful. They represent a linear combination of the $\hat{I}_x$ and $\hat{I}_y$ operators (see Eqn. A.14).

$$\hat{I}_\pm = \hat{I}_x \pm i \hat{I}_y \tag{A.14}$$

For a spin system with two energy levels, the matrix representations of these operators are:

$$\hat{I}_+ = \hbar \begin{pmatrix} 0 & 1 \\ 0 & 0 \end{pmatrix} \text{ and } \hat{I}_- = \hbar \begin{pmatrix} 0 & 0 \\ 1 & 0 \end{pmatrix} \tag{A.15}$$

These operators have a very important role in quantum mechanics. Indeed, the raising operator $\hat{I}_+$ increases the eigenvalue of an operator whereas the lowering

operator decreases it. Hence, we can summarize the impact of the shift operator in the equation A.16 using Eqn. 1.3.

$$\hat{I}_z\hat{I}_\pm \left|s,m\right\rangle = \hbar(m \pm 1)\left|s,m \pm 1\right\rangle \tag{A.16}$$

with s and m, respectively corresponding to the eigenvalues of the operators $\hat{\mathbf{I}}^2$ and $\hat{I}_z$. Moreover, let's consider a system with $\frac{1}{2}$-spin with two energy levels corresponding to the up and down spin states, or to the eigenvalues $\frac{\hbar}{2}$ and $-\frac{\hbar}{2}$ of $\hat{I}_z$. If the spin is in one of the two states ($\left|\alpha\right\rangle, \left|\beta\right\rangle$), applying the raising operator on the $\left|\beta\right\rangle$ state will transform it into $\left|\alpha\right\rangle$ and vice versa for the lowering operator. However, projecting α onto the lowering operator (or β onto the raising operator) won't change the spin state.

A.3 The Bloch model

The Bloch model[9] constitutes a semi-classical vectorial description of the behavior of systems with non-interacting spin-$\frac{1}{2}$ nuclei.[10] In classical mechanics, applying a magnetic field $\vec{B}$ to a magnetic dipole $\vec{\mu}$ generates a torque Γ whose amplitude is described by Eqn. A.17.

$$\Gamma = \frac{d}{dt}\hat{\mathbf{I}} = \vec{\mu} \times \vec{B}(t) \tag{A.17}$$

This torque affects the spin-angular momentum $\hat{\mathbf{I}}$ leading to its precession around the applied magnetic field at a frequency that depends on the particularities of the system. In a system with several spins, we can extract a statistically averaged magnetic moment of an ensemble of spins. Hence, each nucleus i with its intrinsic magnetic moment $\vec{\mu}_i$ contributes to a macroscopic average of the spin ensemble. The corresponding bulk magnetic moment $\vec{M}(t)$, the magnetization, corresponds to the sum of all nuclear magnetic moments.

$$\vec{M}(t) = \sum_i \vec{\mu}_i \tag{A.18}$$

In the laboratory frame, the magnetization experiences a torque similar as the one described in Eqn. A.17 due to the interaction of each magnetic moment with an applied magnetic field $\vec{B}(t)$. Considering the relation between the spin angular momentum $\hat{\mathbf{I}}$ and $\vec{\mu}$, $\vec{\mu} = \gamma\hat{I}$ where γ is the gyromagnetic ratio, we can derive the equation A.19.

$$\frac{d\vec{M}(t)}{dt} = \vec{M}(t) \times \gamma\vec{B}(t) \tag{A.19}$$

For the sake of simplicity, one can change the reference laboratory frame ($\vec{i}$, $\vec{j}$, $\vec{k}$) to a rotating frame ($\vec{i'}$, $\vec{j'}$, $\vec{k'}$) which experiences a rotation at a constant $\vec{\Omega}$ frequency around the $\vec{z}$ (cf Fig. A.1). In other words, $\vec{k}$ is not affected by the change of frame:

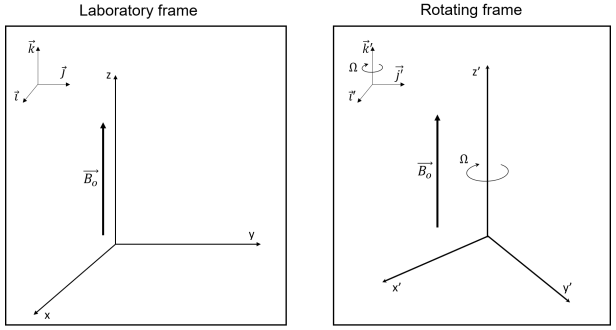

Figure A.1: Scheme of the two frames: the laboratory one defined by the basis ($\vec{i}$,$\vec{j}$,$\vec{k}$) is static whereas the other ($\vec{i'}$,$\vec{j'}$,$\vec{k'}$) is rotating with the frequency Ω around $\vec{k}$. A vector in the static (resp. rotating) frame can be expressed by its (x,y,z) (resp. (x',y',z')) coordinates.

$\vec{k} = \vec{k'}$. On the other hand, $\vec{k'}$, $\vec{i'}$ and $\vec{j'}$ are time-dependent in the laboratory frame. This must be taken into account when we want to express equation A.19 in the laboratory frame.

$$\vec{u'} = \vec{i'} + \vec{j'} + \vec{k'} \tag{A.20}$$

$$\frac{d\vec{u}}{dt} = \vec{\Omega} \times \vec{u} \tag{A.21}$$

Equation A.21 represents the definition of the rotating frame $\vec{u'}$ with respect to the laboratory frame. A rotation $\vec{\Omega}$ explicitly appears and its contribution must be added to all derivatives in the rotating frame.

$$\left[\frac{d\vec{M}(t)}{dt}\right]_{rot} = \left[\frac{d\vec{M}(t)}{dt}\right]_{lab} + \vec{M}(t) \times \vec{\Omega} \tag{A.22}$$

$$= \vec{M}(t) \times \gamma \vec{B}_{eff} \tag{A.23}$$

By manipulating Eqn. A.22 and considering an effective field $\vec{B}_{eff} = \vec{B}(t) + \frac{\vec{\Omega}}{\gamma}$ we can can derive equation A.23 which has the same form as the Bloch equation in the laboratory frame. It is important to properly chose the characteristics of the rotating frame. If we consider a frame that fulfills:

$$\vec{\Omega} = -\gamma \vec{B}(t) \tag{A.24}$$

$$\Rightarrow \vec{B}_{eff} = \vec{0} \tag{A.25}$$

The magnetization thus becomes a stationary vector in this frame. In the presence of an external static magnetic field $\vec{B_0}$ and without any external excitation of the system, the z components (μ_z) of the nuclear moments $\vec{\mu} = (\mu_x, \mu_y, \mu_z)$ are preferably aligned with $\vec{B_0}$. They follow the Boltzmann distribution, leading to

$$M_z(0) = M_0 = \frac{\gamma\hbar}{2}\left(N_\alpha^0 - N_\beta^0\right) \tag{A.26}$$

$$= \frac{\gamma\hbar}{2} N_\alpha^0 \left(1 - \exp\left(-\frac{\Delta E}{k_B T}\right)\right) \tag{A.27}$$

By combining Eqn. A.26 with Eqn. 1.25 and 1.26 we can also express the magnetization as a function of the polarization:

$$M_0 = \frac{\gamma N\hbar}{2}(p_\alpha - p_\beta) \tag{A.28}$$

$$= \frac{\gamma N\hbar}{2} P_I^0 \tag{A.29}$$

with P_I^0, the polarization at Boltzmann equilibrium as it has been defined in Eqn. 1.30. It is possible to extend equation A.29 to systems that are not at equilibrium by introducing populations of the energy levels N_α and N_β. A more general definition of the nuclear polarization P_n is analogous to Eqn. 1.23 that has been originally

used for electrons.

$$M_z(t) = \frac{\gamma\hbar}{2}(N_\alpha - N_\beta) \tag{A.30}$$

$$= \frac{\gamma N\hbar}{2}P_n \tag{A.31}$$

Unlike M_z, the transverse components of the nuclear magnetic moments are randomly distributed in the sample which leads to the cancellation of these components which vanish in equilibrium: $M_x(0)$ and $M_y(0)$.

$$M_x(0) = M_y(0) = 0 \tag{A.32}$$

The nuclear magnetization must be excited to enable its detection. Detection coils are perpendicular to the (x,y) plane and are sensitive to variations of the magnetic field at their location. Because of their geometry, only projections of the magnetization onto the (x',y') plane can generate a current in the coils and may thus generate a signal. Driving the magnetization away from its equilibrium position and towards the transverse plane is feasible by applying a linearly polarized radiofrequency field, or "pulse", $\vec{B_1} = B_1\cos(\omega_{rf}t + \phi)\cdot\vec{y}$. The resulting effective field in the rotating frame $\vec{B_{rot}}$ can be expressed as:

$$\vec{B}_{rot} = B_1\cos\phi\cdot\vec{i'} + B_1\sin\phi\cdot\vec{j'} + \Delta B_o\cdot\vec{k'} \tag{A.33}$$

By combining equations A.23 and A.33, we can illustrate the impact of the field $\vec{B_1}$ onto the magnetization (Eqn. A.34) in the rotating frame ($\vec{i'}$, $\vec{j'}$, $\vec{k'}$).

$$\frac{d\vec{M}(t)}{dt} = \vec{M}(t)\times\gamma\left[\left(\Delta B_0 + \frac{\vec{\Omega}}{\gamma}\right)\cdot\vec{k'} + B_1\cdot\vec{j'}\right] \tag{A.34}$$

$$= \vec{M}(t)\times\gamma\left[\left(\frac{\omega_n - \omega_{rf}}{\gamma}\right)\cdot\vec{k'} + \omega_1\cdot\vec{j'}\right] \tag{A.35}$$

where ω_n is the nuclear frequency (including the effect of shielding), ω_{rf}, the nutation frequency induced by the field $\vec{B_1}$ and ω_1, which is proportional to the $\vec{B_1}$ amplitude. For spins with high gyromagnetic ratios, if their frequency of resonance is equal to

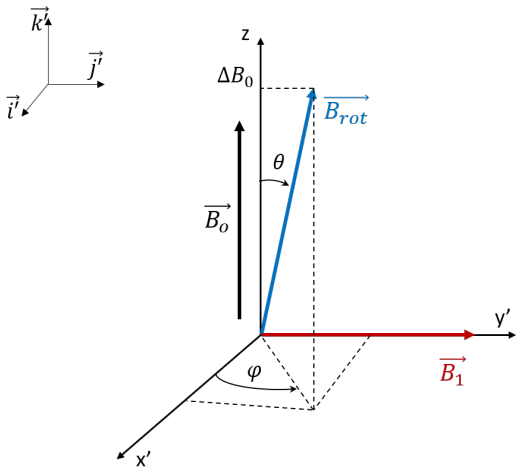

Figure A.2: Effective local field $\vec{B}_{rot}$ and applied $\vec{B}_1$ field in the orthonormal rotating frame ($\vec{i'}$, $\vec{j'}$, $\vec{k'}$).

the rotation frequency of $\vec{B}_1$, the z' component of the effective magnetic field is canceled out, only the component due to the pulse remains which corresponds to a torque on each nuclear spin. Thus, $\vec{B}_1$ tilts the effective field from the z direction at a rate of ω_1 driving the magnetization away from its equilibrium value.

$$\frac{d\vec{M}(t)}{dt} = -\omega_1 \cdot \vec{i'} \tag{A.36}$$

The system is thus excited by a linearly polarized field $\vec{B}_1$ and a signal can finally be detected. The angle of the magnetization after the pulse θ_M linearly depends on its duration τ_p (cf Eqn. A.37).

$$\theta_M = \omega_1 \tau_p \tag{A.37}$$

The amplitude of the RF field also plays an important role in this process. In an ideal case, the RF field is coupled to all magnetic moments in the sample and drives them all toward the (x,y) plane leading to a linear dependency of the angle on the amplitude B_1 (cf Eqn. A.37). However, in real cases, the coupling between the magnetic field and the nuclei depends on their gyromagnetic ratio: nuclei with low magnetic ratios are more difficult to drive away from their equilibrium value. Eqn. A.37 must consequently be modified by replacing the unique contribution of the amplitude of the applied RF ω_1 by the nutation frequency ω_{rf}[11] that takes into account both parameters: the field strength and its coupling with nuclei (cf. Eqn.

A.38).

$$\theta_M = \omega_{rf}\tau_p \tag{A.38}$$

Introduction of relaxation into the Bloch model

If we only consider the equation A.23, the magnetization would precess indefinitely in the transverse plane once the rf field has been switched off. This means that the system would remain excited indefinitely. However, relaxation mechanisms tend to drive back $\vec{M}(t)$ towards its equilibrium value $M_0 \cdot \vec{k}$. Thus, $\mathbf{R}$, which stands for the relaxation matrix, must be introduced into Eqn. A.23 to obtain an accurate description of the evolution of the system.

$$\frac{d\vec{M}}{dt} = \vec{M}(t) \times \gamma\vec{B}_{eff} + \mathbf{R} \cdot \left(\vec{M} - \vec{M}_0\right) \tag{A.39}$$

$$= \gamma \begin{pmatrix} B_y M_z - B_z M_y \\ B_z M_x - B_x M_z \\ B_x M_y - B_y M_z \end{pmatrix} + \begin{pmatrix} -R_2 & 0 & 0 \\ 0 & -R_2 & 0 \\ 0 & 0 & -R_1 \end{pmatrix} \begin{pmatrix} M_x \\ M_y \\ M_z - M_0 \end{pmatrix} \tag{A.40}$$

The R matrix that has been represented in the equation A.40 only described isolated spins, which explains the fact that it is diagonal. In real cases, all spins are constantly interacting, which complexifies the representation by the appearance of cross-relaxation effects.

Bibliography

[1] S. Appelt, F. W. Häsing, U. Sieling, A. Gordji-Nejad, S. Glöggler, and B. Blümich. Paths from weak to strong coupling in nmr. *Phys. Rev. A*, 81:023420, 2010.

[2] J. Keeler. *Understanding NMR Spectroscopy - Second Edition*. 2010.

[3] P. J. Hore. *Nuclear Magneric Resonance*. Oxford University Press, New York, 1995.

[4] J. A. S. Smith. Nuclear quadrupole resonance spectroscopy: General principles. 48(1):39, 1971.

[5] P. P. Man. *NMR of Quadrupolar Nuclei in Solid Materials*. Wiley and Sons Ltd, Chichester, UK, 2012.

[6] C. P. Slichter. *Principles of Magnetic Resonance*. Springer-Verlag, New York, 3 edition, 1990.

[7] M. H. Cohen and F. Reif. Solid state physics. 5:327, 1957.

[8] A. Abragam. *The Principles of Nuclear Magnetism*. Oxford University Press, Oxford, 1961.

[9] F. Bloch. Nuclear induction. *Phys. Rev.*, 70:460–474, Oct 1946.

[10] J. Cavanagh, W. J. Fairbrother, A. G. III Palmer, Mark Rance, and N. J. Skelton. *Protein NMR Spectroscopy*. Elsevier, 2007.

[11] M. H. Levitt. *Spin dynamics: Basics of Nuclear Magnetic resonance.* John Wiley & Sons, Paris, 1973.

Appendix B

Complementary informations about OE and SE mechanisms

B.1 The Overhauser Effect

As introduced in section 1.2.3, the enhancement ϵ that can be reached using OE depends on three different parameters: f, s and ξ (see Eqn. 1.47). Paramagnetic species in the vicinity of nuclei induce paramagnetic relaxation and thus decrease the final enhancement. This effect is described by the leakage factor f that is defined as:

$$f = \frac{R_{1p}}{R_{1I}} \tag{B.1}$$

The equation B.1 quantifies the contribution of the paramagnetic relaxation rate R_{1p} to the total relaxation rate of the nuclei R_{1I}. The power of the microwave and its efficiency must also be taken into account to determine the final enhancement. In the case of a single homogeneous EPR line, the saturation factor enables to quantify it:[1]

$$s = \frac{\gamma_e^2 B_{1\,\mu w}^2 T_{1e} T_{2e}}{1 + \gamma_e^2 B_{1\,\mu w}^2 T_{1e} T_{2e}} \tag{B.2}$$

s depends on the microwave irradiation power $B_{1\,\mu w}$, the electron spin-lattice relaxation T_{1e} and the electron spin-spin relaxation T_{2e}. When strong microwave power is applied, $s \sim 1$, all electrons are fully saturated whereas for too weak powers, the

saturation factor approaches 0: the nuclear signal intensity is not enhanced and can even be reduced by the paramagnetic species induced relaxation.

Finally, a coupling constant ξ takes into account the contribution of the cross-relaxation between electrons and nuclei and compares it to the paramagnetic relaxation.[2] This experimental constant depends on the DQ and ZQ transition rates (cf fig. 1.4) and constitutes a direct link to the rotational-diffusion time of the paramagnetic impurities and their interaction with surrounding molecules.[3,4] In liquid state, the electron-nucleus cross-relaxation dominantly occurs through the DQ transition, which causes negative enhancements. However, OE can also be present in insulating solids where the ZQ pathway dominates. This results in positive enhancements as it has been observed with the use of BDPA as paramagnetic agent.[5]

The Overhauser mechanism efficiency decreases as the external magnetic field increases. In addition to strong hyperfine coupling, OE requires a smaller homogeneous line width of electron resonance than the Larmor frequency of nuclei. The larger the field is, the broader becomes the electron line. Unfortunately, one major limitation of OE DNP in solution is the dielectric heat up of the sample generated by the strong microwave irradiation. A higher temperature affects the transition probabilities, relaxation rates and molecular diffusion leading to a smaller final nuclear polarization, which strongly influence the Overhauser factors (f, s, ξ) in equation 1.47. However, high field solution DNP is still possible. Small radicals such as TEMPOL, TEMPONE or Fremy's salts are chosen as paramagnetic agents in Overhauser DNP experiments because of their small electron line width, their fast rotation and fast diffusion.[6] In addition, reduced volumes of solution down to tens of nL are commonly used in order to assure a stable temperature.[7] Finally, some programs are looking for a technical solution to reduce the sample heating issues. A special magnet enables to hyperpolarize samples at low field (0.35 T) via the OE and then transfer the sample using a shuttle for the detection at high field (14 T).[8–10]

B.2 The Solid Effect: mixing of the spin states monitored by the hyperfine interaction

The Hamiltonian $\hat{H}$ of a system composed of an electron (**S**) coupled to a nucleus (**I**) by hyperfine interaction in $\hbar$ unit can be expressed as following:

$$\begin{aligned} \hat{H} &= \hat{H}^I_{Zeeman} + \hat{H}^S_{Zeeman} + \hat{H}_{SI} \\ &= \omega_n I_z + \omega_e S_z + \mathbf{S}\cdot\mathbf{A}\cdot\mathbf{I} \end{aligned} \tag{B.3}$$

H^I_{Zeeman} and H^S_{Zeeman} respectively refer to the Zeeman interactions of the nucleus and the electron, H_{SI} is the Hamiltonian representing the hyperfine interaction whose strength is given by the hyperfine constant A and ω_n and ω_e are the Larmor frequency of the nucleus and the electron. Under the high-field approximation, only the terms that commute with the Zeeman Hamiltonians (i.e. that commute with I_z or S_z operators) are considered. According to perturbation theory, we can then distinguish two contributions in the Hamiltonian that has been defined in equation B.3: the unperturbed Hamiltonian H_0, which is only constituted by secular operators and the perturbation H_1 in which the pseudo-secular terms are summed. (cf eqn. B.4). Unlike $\hat{H}_1$, $\hat{H}_0$ is diagonal in the chosen basis. The equation B.3 can thus be written as:[11]

$$\hat{H} = \hat{H}_0 + \hat{H}_1 \tag{B.4}$$

$$= \omega_S S_z - \omega_I I_z + A_1 \cdot S_z I_z + C \cdot S_z I_+ + C^* I_- S_z \tag{B.5}$$

In this equation, $A_1 \cdot S_z I_z$ and $C \cdot S_z I_+ + C^* I_- S_z$ respectively correspond to the secular and the pseudo-secular terms of the hyperfine interaction. A_1 and C are the coefficients that are involved in the dipolar interaction between two spins according to the Van Vleck notation (cf dipolar interaction in part 1.1.3):

$$A_1 = 3\frac{\mu_0 \gamma_I \gamma_S}{4\pi r^3}\left(\cos^2 - 1\right) \tag{B.6}$$

$$C = \frac{-3}{2}\frac{\mu_0 \gamma_I \gamma_S}{4\pi r^3}\sin\theta\cos\theta e^{-i\phi} \tag{B.7}$$

This pseudo-secular hyperfine interaction plays a very important role in the SE as it can lead to a small mixing up of the nuclear Zeeman spin states, which can be quantified by a factor q. q depends on the strength of the pseudo-secular hyperfine coupling C compared to the nuclear Larmor frequency ω_n.

$$q \approx \frac{C}{2\omega_n} \tag{B.8}$$

The mixing of the nuclear states increases the probability of the ZQ and DQ transitions that are necessary for SE DNP.

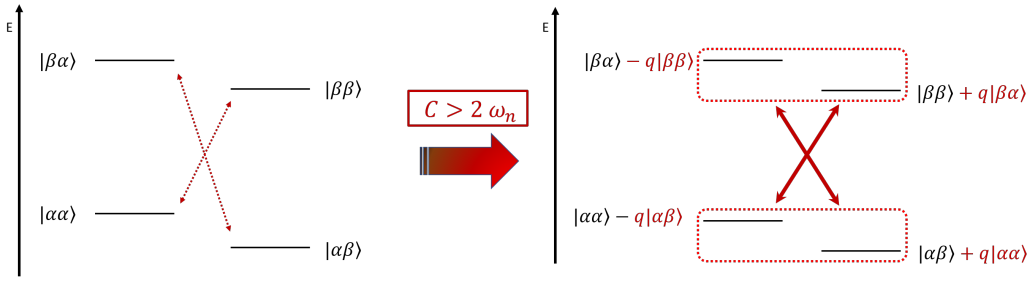

Figure B.1: Mixing up of the nuclear Zeeman energy levels due to the pseudo-secular hyperfine interaction. The forbidden transitions DQ and ZQ consequently become allowed.

Bibliography

[1] A. Abragam. *The Principles of Nuclear Magnetism*. Oxford University Press, Oxford, 1961.

[2] K. H. Hausser and D. Stehlik. Dynamic nuclear polarization in liquids. *Adv. Magn. Res.*, 3:79–139, 1968.

[3] J. H. Ortony, C.-H. Cheng, J. M. Franck, R. Kausik, A. Pavlova, J. Hunt, and S. Han. Probing the hydration water diffusion of macromolecular surfaces and interfaces. *New Journal of Physics*, 13(1):015006, 2011.

[4] J. M. Franck, A. Pavlova, J. A. Scott, and S. Han. Quantitative cw Overhauser effect dynamic nuclear polarization for the analysis of local water dynamics. *Prog. in Nuc. Magn. Res. Spec.*, 74:33 – 56, 2013.

[5] T. V. Can, M. A. Caporini, F. Mentink-Vigier, B. Corzilius, J. J. Walish, M. Rosay, W. E. Maas, M. Baldus, S. Vega, T. M. Swager, and R. G. Griffin. Overhauser effects in insulating solids. *J. Chem. Phys.*, 141(6):064202, 2014.

[6] N. Enkin, G. Liu, M. C. Gimenez-Lopez, K. Porfyrakis, I. Tkach, and M. Bennati. A high saturation factor in Overhauser DNP with nitroxide derivatives: the role of ^{14}N nuclear spin relaxation. *Phys. Chem. Chem. Phys.*, 17:11144–11149, 2015.

[7] E. Ravera, C. Luchinat, and G. Parigi. Basic facts and perspectives of Overhauser DNP NMR. *J. Magn. Res.*, 264:78–87, 2016.

[8] M.-T., Reese, D. Lennartz, T. Marquardsen, P. Höfer, A. Tavernier, P. Carl, M. Bennati, T. Carlomagno, F. Engelke, and C. Griesinger. Construction of a liquid-state NMR DNP shuttle spectrometer: First experimental results ad evaluation of optimal performance characteristics. *App. Magn. Res.*, 34:301–311, 2008.

[9] M. Reese, M.-T. Türke, I. Tkach, G. Parigi, C. Luchinat, T. Marquardsen, A. Tavernier, P. Höfer, F. Engelke, C. Griesinger, and M. Bennati. ^{1}H and ^{13}C dynamic nuclear polarization in aqueous solution with a two-field (0.35 T/14 T) shuttle DNP spectrometer. *J. Am. Chem. Soc.*, 131:15086–15087, 2009.

[10] A. Krahn, P. Lottmann, T. Marquardsen, A. Tavernier, M.-T. Türke, M. Reese, A. Leonov, M. Bennati, P. Hoefer, F. Engelke, and C. Griesinger. Shuttle DNP spectrometer with a two-center magnet. *Phys. Chem. Chem. Phys.*, 12:5830–5840, 2010.

[11] T. V. Can, Q. Z. Ni, and R. G. Griffin. Mechanisms of dynamic nuclear polarization in insulating solids. *J. Magn. Res.*, 253:23–35, 2015.

Appendix C

Sample Ripening through Nanophase Separation Influences the Performance of Dynamic Nuclear Polarization

C.1 Experimental

DNP was performed on a Bruker BioSpin prototype operating at 4.2 K with a static magnetic field of 6.7 T, as described earlier,[1,2] after immersing the sample in liquid helium. Microwaves were generated by an ELVA1 microwave source coupled to a VDI frequency doubler, yielding a central frequency in the vicinity of 188.2 GHz. A maximal absolute nuclear polarization was achieved at 187.90 GHz for TEMPOL and AMUPol and at 188.22 GHz for Trityl. To increase the efficiency, a 2 kHz saw-tooth frequency modulation over a range of 100 MHz was used. The microwave power at the location of the sample was ca. 12 mW.

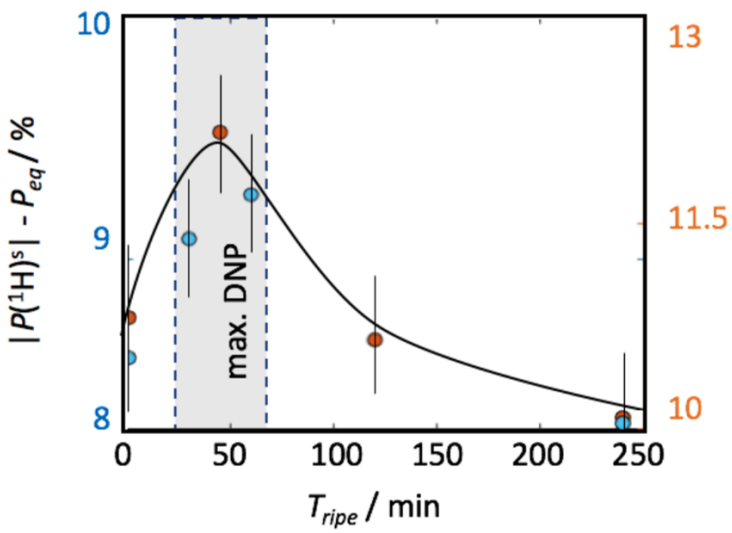

Figure C.1: Reproducibility of the ripening process for 50 mM TEMPOL (sample **I**). Two different runs are indicated by red and blue colors. The black line serves as guide to the eye. The results are similar to those in the main text (Fig. 4.1).

For cryo-TEM, the specimens were rapidly frozen by immersing them into liquid ethane, cooled by liquid nitrogen (LEICA EM CPC, Vienna, Austria). The cryofixed specimens were mounted into a Gatan cryoholder (Gatan inc., Warrendale, PA) for direct observation at 90 K in a JEOL 2100HC cryo-TEM operating at 200 kV with a LaB6 filament. Images were recorded in zeroloss mode with a Gif Tridiem energy-filtered-CCD camera equipped with a 2k x 2k pixel-sized chip (Gatan Inc., Warrendale, PA). Acquisition was accomplished with Digital Micrograph software (versions 2.31.734.D, Gatan inc., Warrendale, PA).

Field-swept continuous-wave (CW) spectra of the entire set of H_2O/glycerol mixtures containing 5 mM TEMPOL were recorded at X-band (9.4 GHz) on a Bruker ELEXSYS E500 spectrometer at 120 K with a microwave power of 0.1 mW. The modulation amplitude was set to 0.2 mT. CW experiments were recorded with an average of four scans. Contributions of line broadening effects to the apparent value of A_{zz} were carefully excluded. Relaxation time measurements were performed at 77 K as indicated in reference[3]. DEER experiments were performed using a four-pulses sequence (see section 2.3.3):

$$\pi/2(\nu_1) - \tau_1 - \pi(\nu_1) - \tau_0 - \pi(\nu_2) - (\tau_1 + \tau_2 - \tau_0) - \pi(\nu_1) - \tau_2 - echo$$

The 32 ns pump pulse with a microwave frequency ν_2 was applied to the maximum of the nitroxide spectrum. The detection pulses are applied at a microwave frequency ν_1 with an offset $\Delta\nu = \nu_2 - \nu_1 = 55$ MHz. Pulse sequences were generated by an arbitrary wave generator (AWG). The dipolar evolution time was chosen to be 2.2 μs. The separation τ_1 was set to 344 ns. Primary experimental data were background-corrected by fitting a decay function $V(t)$ for the intermolecular contribution, followed by normalization of the function.

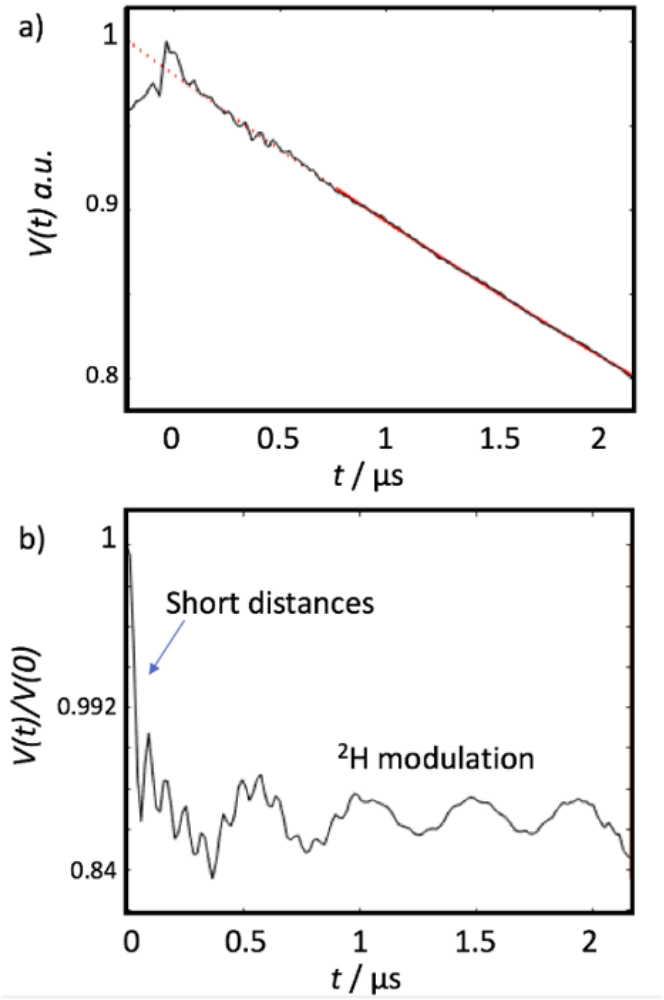

Figure C.2: a) Raw DEER intensities $V(t)$ for 1 mM TEMPOL in a mixture of glycerol-d8/D2O/H2O 5:4:1 v/v, recorded after the sample was allowed to ripen for $T_{ripe} = 45$ min. The red line indicates the homogeneous background contribution from long-distance dipolar couplings. At $t = 0$ - 0.5 μs, non-exponential contributions indicate deviations from a homogeneous distribution of radicals in the sample. This is not the case for $T_{ripe} = 0$. b) Normalized DEER ratio ($V(t)/V(0)$) after background subtraction in a similar solvent mixture measured at 1 mM TEMPOL. The fast initial decay indicates the presence of short distances between radicals after sample ripening and a inhomogeneous local packing of radicals. The modulations stem from hyperfine couplings to ^{2}H nuclei.

C.2 Impact of NPS at low PA concentrations

In a heterogeneous sample, an increase of the local concentration of paramagnetic species increases the number of nuclei that experience paramagnetic shifts. This phenomenon directly impacts the signal intensity and apparent polarization by decreasing the number of observable nuclei. In order to exclude contributions of this effect, each polarization has been calculated with respect to the NMR signal in thermal equilibrium (Fig. C.3). The local concentration of radicals and the fraction of invisible nuclei can be considered to be similar for the hyperpolarized and reference spectra. Moreover, polarization profiles of samples which are less concentrated in paramagnetic species, and less subject to bleaching effects, also display a strong dependence on the ripening time (Fig. C.4).

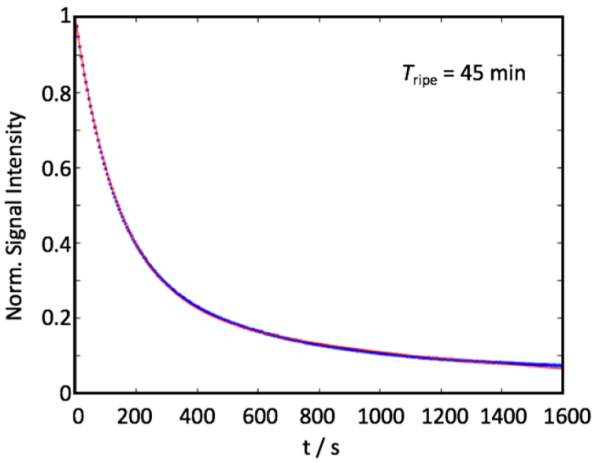

Figure C.3: Decay of the normalized signal intensity for 50 mM TEMPOL (sample **I**) after T_{ripe} = 45 min. The system has been polarized until it reached its steady-state prior to turning off the microwave irradiation and observing the decay, which has been fitted to a bi-exponential equation: $a \cdot \exp(R_1 t) + (1-a) \cdot \exp(R_1^* t) + c$ with $R_1 = 0.0071$ s^{-1} and $R_1^* = 0.00084$ s^{-1} ; $a = 0.26$.

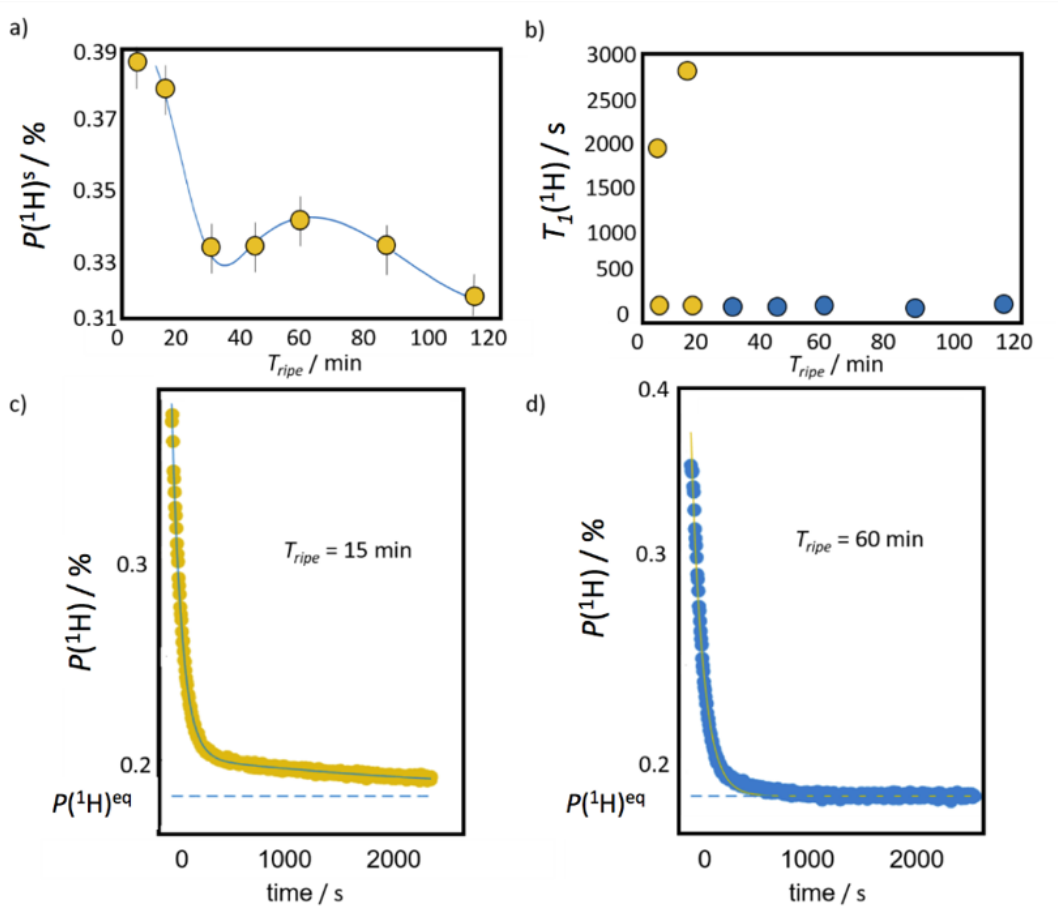

Figure C.4: a) Dependence of steady-state proton polarization $P(^1H)$ on the ripening interval for a sample containing only ca. 5 mM AMUPol at 4 K and 6.7 T in a mixture of glycerol-d8/D2O/H2O 5:4:1 v/v. Even at these low concentrations ripening effects can be observed. The difference of the profile as compared to high concentrations (see main text) indicates that thermal mixing is a dominant DNP mechanism at higher concentrations, while at lower concentrations the cross-effect dominates, which features a different concentration dependence. b) Longitudinal relaxation times $T_1(^1H)$ of the protons as a function of the sample ripening time T_{ripe} for the same of ca. 5 mM AMUPol. Decays observed when for $T_{ripe} < 35$ min show clear bi-exponential decays (fitted with two time constants yellow) whereas decays obtained for $T_{ripe} > 35$ min are mono-exponential (blue). c) Decay of the polarization $P(^1H)$ for 10 mM AMUPol after $T_{ripe} = 15$ min. The system has been polarized until it reached its steady-state prior to turning off the microwave irradiation and observing the decay, which has been fitted to a bi-exponential equation. The thermal equilibrium polarization $P(^1H)_{eq}$ corresponds to the asymptotic limit determined by fitting the decay function. d) Mono-exponential decay of the polarization $P(^1H)$ for 10 mM AMUPol after $T_{ripe} = 60$ min.

C.3 CW EPR as a function of the water-glycerol ratio

To shed further light on the distribution of the PAs during nanophase separation, we performed solid-state EPR studies of DNP samples vitrified at 120 K for different glycerol/water ratios at $T_{ripe} = 45$ min, for which NPS was observed by cryo-TEM. For samples **I** and **II**, the splitting $\Delta\omega$ of the EPR line gives a measure of the hydrophobicity of the local environment of the radicals. For TEMPOL and AMUPol, $\Delta\omega$ is in part determined by the hyperfine coupling between the ^{14}N nucleus and the unpaired electron of the nitroxide moiety. The larger the hyperfine coupling (i.e., the larger the z-component A_{zz} of the hyperfine tensor that determines the splitting in the spectrum), the wider the EPR line, the less hydrophilic the environment.[4] (We consider water to be more hydrophilic and less hydrophobic than glycerol despite the dipolar moments of 4.21 D for glycerol and 1.85 D for water, for the polarity of glycerol relative to water is ca. 0.8.)[5] This effect is shown in Fig. C.4 a and b for TEMPOL. The origin of this effect is visualized qualitatively in Fig. C.4 c. The hydrophobicity of the local environment influences the electronic configuration of TEMPOL leading to a resonance structure in which the unpaired electron is localized at the ^{14}N nucleus in less hydrophobic surroundings. This increases the hyperfine coupling A_{zz}.[4,6] (More elaborate models exist that take into consideration the molecular orbital structure of nitroxides).[7] The modification of the nitroxide resonance structure only causes minor changes in the EPR spectra and effects on DNP are considered negligible. For Trityl, a qualitatively similar dependence of the peak-to-peak separation Γ (as indicated in Fig. C.4 f) on the environmental hydrophobicity can be expected, due to solvent interactions and unresolved heterogeneous couplings, rather than to changes in intramolecular hyperfine couplings.[8] However, the unpaired electron is located on a well-shielded carbon nucleus, so that the EPR linewidth is expected to be less sensitive to the environment than the hyperfine splitting for nitroxides.[9] Studying the dependence of the EPR spectrum on the water-glycerol ratio (the samples were vitrified $T_{ripe} = 45$ min after preparation) we find a non-monotonic behavior for TEMPOL (sample **I**) (see Fig. C.4 d). Indeed, at 40-50% glycerol content typical for DNP, we find that the splitting $\Delta\omega$ is close to the value found in pure water, and not to the value expected for a homogeneous water/glycerol mixture. (The experimental spectra stem from a weighted superposition of all species present in the heterogeneous sample.) This observa-

tion corroborates the hypothesis that during the NPS process, TEMPOL radicals are concentrated in the water- rich nanophase, where they get trapped upon rapid vitrification. The depletion of the PAs in the glycerol-rich nanophase and the concomitant increase of their local concentration in the water-rich nanophase does not entail any macroscopic phase separation or crystallization, which is known to impede DNP by slowing down spin diffusion and hence the polarization build-up process. A similar behavior is observed for AMUPol (sample **II**), where the local concentration of the PA increases in the hydrophilic phase (Fig. C.4 g). For Trityl (sample **III**), we find a decrease of the linewidth for 50% v/v water, indicating increased glycerol content in the direct vicinity of the PAs after vitrification, which is in agreement with our above deduction that Trityl radicals tend to cluster in glycerol-rich phases during NPS, in contrast to nitroxide-based radicals.

The EPR data in Fig. C.4 is corroborated by the finding of locally elevated PA and proton concentrations in water-rich nanophases (cf. Figs. 4.2 and 4.3 of the main text) as well as by the dependence of the proton polarization on the ripening interval. Note that the separation of PA-rich and -depleted phases can not only lead to a bi-exponential build-up (cf. Fig. 4.1 a), but also to bi-exponential relaxation of hyperpolarization under certain circumstances (see Fig. C.4).

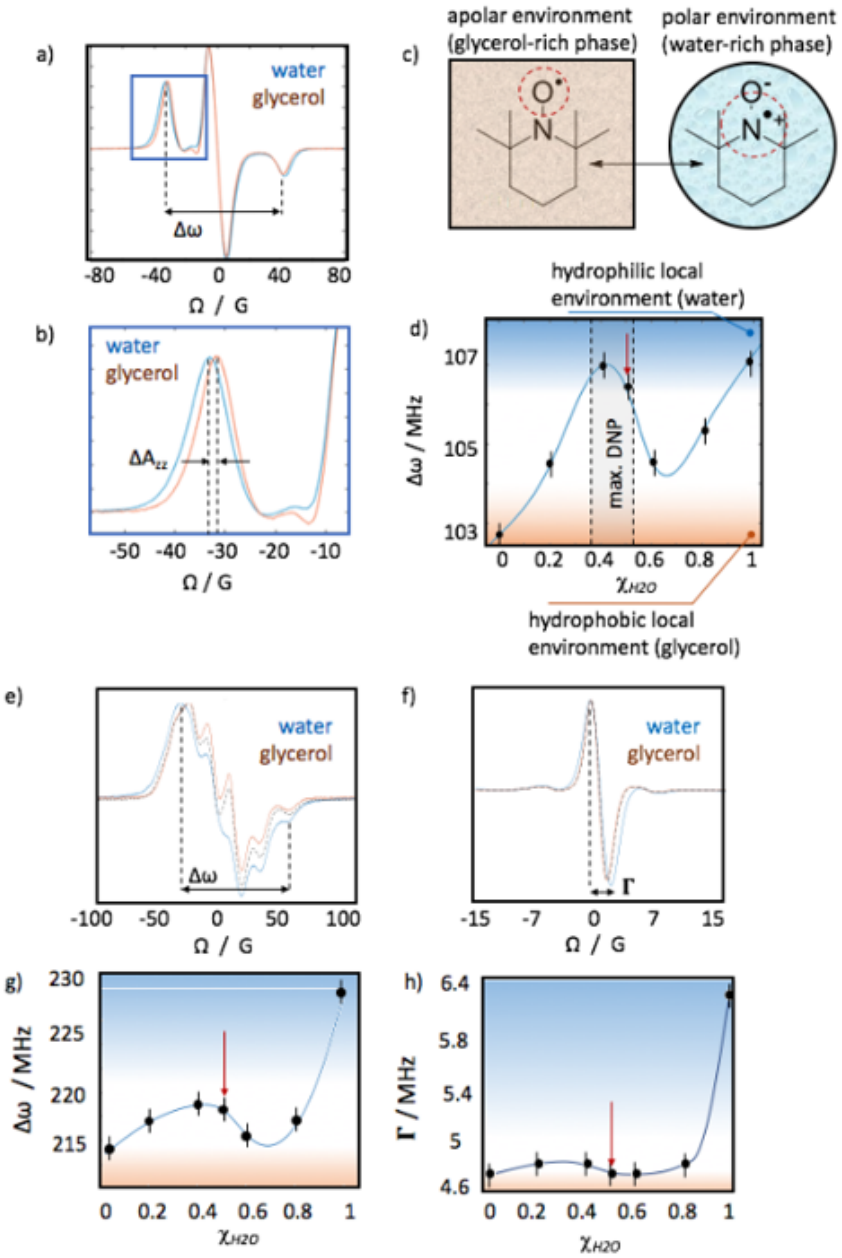
a)
water
glycerol
Δω
-80 -40 0 40 80
Ω / G
b)
water
glycerol
ΔA_zz
-50 -40 -30 -20 -10
Ω / G
c)
apolar environment
(glycerol-rich phase)
polar environment
(water-rich phase)
d)
hydrophilic local
environment (water)
Δω / MHz
107
105
103
max. DNP
0 0.2 0.4 0.6 0.8 1
χH2O
hydrophobic local
environment (glycerol)
e)
water
glycerol
Δω
-100 -50 0 50 100
Ω / G
f)
water
glycerol
Γ
-15 -7 0 7 15
Ω / G
g)
Δω / MHz
230
225
220
215
0 0.2 0.4 0.6 0.8 1
χH2O
h)
Γ / MHz
6.4
5.8
5.4
5
4.6
0 0.2 0.4 0.6 0.8 1
χH2O

Figure C.4 *(previous page)*: EPR studies of TEMPOL, AMUPol and Trityl during nanophase separation. a) Solid-state CW EPR spectra of TEMPOL observed at 120 K in a 20/80% v/v glycerol/water mixture (blue) and in pure glycerol (orange) at X-band (9.4 GHz). The samples were vitrified rapidly in liquid nitrogen after ripening at room temperature for $T_{ripe} = 45$ min after preparation. The splitting $\Delta\omega$ between the satellite transitions is indicated. b) Zoom of the low-field region of the spectra in a). The hyperfine coupling constant in the z-direction of the molecular frame A_{zz} is smaller in more hydrophobic environments, leading to a shift ΔA_{zz} of the satellite lines that depends on the solvent hydrophobicity, which in turn impacts the splitting $\Delta\omega$. c) Origin of the solvent-dependent changes in hyperfine coupling constants. In more hydrophilic environments the zwitterionic resonance structure is preferred, leading to a closer proximity of the unpaired electron to the ^{14}N nitrogen nucleus, thus increasing their mutual hyperfine coupling. d) Splitting $\Delta\omega$ vs. the H_2O volume fraction χ_{H2O} in binary water/glycerol mixtures for $T_{ripe} = 45$ min. In the range $40\% < \chi_{H2O} < 50\%$, the splitting resembles that in pure water, indicating the accumulation of the TEMPOL radicals in the water-rich phase (cf. Fig. 4.2). The blue line serves to guide the eye. e) Solid-state CW EPR spectra at X-band of AMUPol in a 2% v/v glycerol/water mixture (blue), in 97% v/v glycerol/water mixture (orange) and in 80% v/v glycerol/water solution (dashed line). The samples were vitrified in liquid nitrogen $T_{ripe} = 45$ min after preparation. f) Solid-state CW EPR spectra at X-band of Trityl in a 2% v/v glycerol/water mixture (blue), in a 20% v/v glycerol/water mixture (dashed line) and in pure glycerol. g) The splitting $\Delta\omega$ in AMUPol vs. the H_2O volume fraction χ_{H2O} in binary water/glycerol mixtures for $T_{ripe} = 45$ min. The blue line is to guide the eye. The response of the AMUPol spectra to a change from a hydrophobic to a hydrophilic environment is similar to but less pronounced than changes observed for TEMPOL. h) EPR linewidth Γ of Trityl vs. the H_2O volume fraction χ_{H2O} in binary water/glycerol mixtures at $T_{ripe} = 45$ min. The blue line is to guide the eye. In contrast to TEMPOL and AMUPol, Trityl features a local minimum at 50% v/v glycerol content (highlighted by red dashes). This indicates a more hydrophobic environment upon NPS due to the accumulation of the PA in the glycerol-rich phase.

Bibliography

[1] D. Kurzbach, E. Canet, A. G. Flamm, A. Jhajharia, E. M. M. Weber, R. Konrat, and G. Bodenhausen. Investigation of intrinsically disordered proteins through exchange with hyperpolarized water. *Ang. Chem. Inter. Ed.*, 56(1):389–392, 2017.

[2] D. Kurzbach, E. M. M. Weber, A. Jhajharia, S. F. Cousin, A. Sadet, S. Marhabaie, E. Canet, N. Birlirakis, J. Milani, S. Jannin, D. Eshchenko, A. Hassan, R. Melzi, S. Luetolf, M. Sacher, M. Rossire, J. Kempf, J. A. B. Lohman, M. Weller, G. Bodenhausen, and D. Abergel. Dissolution dynamic nuclear polarization of deuterated molecules enhanced by cross-polarization. *J. Chem. Phys.*, 145(19):194203, 2016.

[3] F. Mentink-Vigier, A. Collauto, A. Feintuch, I. Kaminker, V. Tarle, and D. Goldfarb. Increasing sensitivity of pulse EPR experiments using echo train detection schemes. *J. Magn. Res.*, 236:117 – 125, 2013.

[4] D. Kurzbach, M. J. N. Junk, and D. Hinderberger. Nanoscale inhomogeneities in thermoresponsive polymers. *Macromol. Rap. Comm.*, 34(2):119–134, 2013.

[5] C. Reichardt. *Solvents and Solvent Effects in Organic Chemistry.* Wiley VCH, Weinheim/Germany, 2003.

[6] D. Kurzbach, W. Hassouneh, J. R. McDaniel, E. A. Jaumann, A. Chilkoti, and D. Hinderberger. Hydration layer coupling and cooperativity in phase behavior of stimulus responsive peptide polymers. *J. Am. Chem. Soc.*, 135(30):11299–11308, 2013.

[7] P. G. I. Likhtenshtein, J. Yamauchi, S; I. Nakatsuji, A. I. Smirnov, and R. Tamura. *Nitroxides: Applications in Chemistry, Biomedicine, and Materials Science.* Wiley VCH, 2008.

[8] L. Yong, J. Harbridge, R. W. Quine, G. A. Rinard, S. S. Eaton, G. R. Eaton, C. Mailer, E. Barth, and H. J. Halpern. Electron spin relaxation of triarylmethyl radicals in fluid solution. *J. Magn. Res.*, 152(1):156 – 161, 2001.

[9] S.N. Trukhan, V.F. Yudanov, V.M. Tormyshev, O.Yu. Rogozhnikova, D.V. Trukhin, M.K. Bowman, M.D. Krzyaniak, H. Chen, and O.N. Martyanov. Hyperfine interactions of narrow-line trityl radical with solvent molecules. *J. Magn. Res.*, 233:29 – 36, 2013.

Appendix D

Observation of a DNP-hyperpolarized solid-state water NMR MASER phenomenon

D.1 Narrowing of the line and long lived signal

The first observations we made in the polarizer was a shrinking of the ^{1}H line when the system is negatively polarized at 1.2 K. When the system is sufficiently polarized, the linewidth diminishes as the temporal signal becomes longer due to a continuous repolarization of the system by the microwave irradiation. Figure D.1 is an example of such experiments where the angle of detection has be chosen to be very small (0.1 °). This increased resolution can be explained by long-lived ^{1}H signals. Even in absence of microwave irradiation, the negatively polarized signal is sustained for tens of seconds (see Fig. D.2). Note that the truncation of the FID makes difficult the extraction of informations in the reciprocal space.

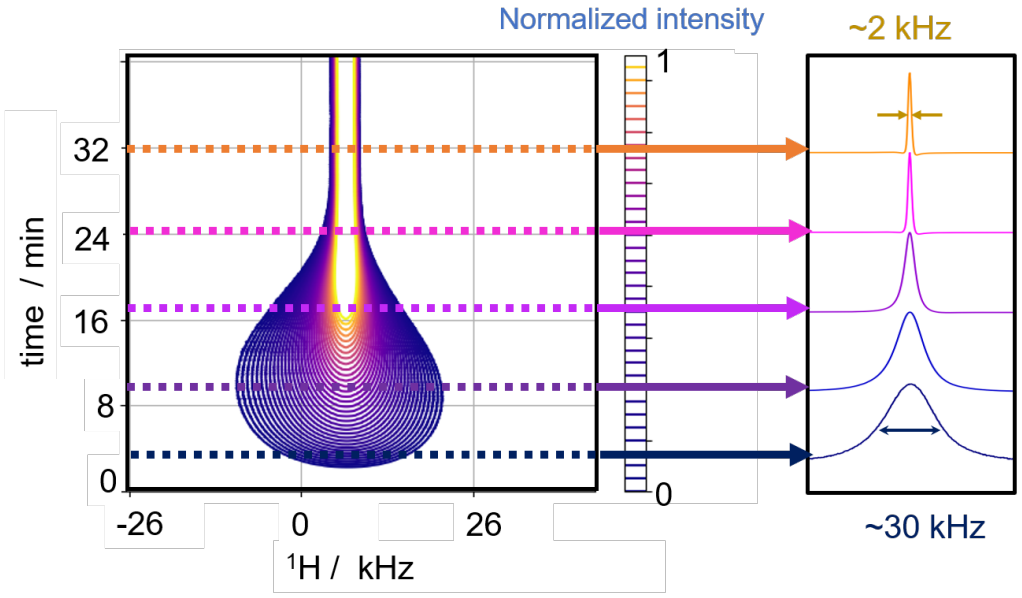

Figure D.1: Evolution of the ^{1}H signal in the frequency domain versus time at 1.2 K. The signal is detected each 5 s using small low power pulses (angle= 0.1°, power = $5 \cdot 10^{-5}$ W and duration = 5 μs). The microwave continuously irradiates the system at 188.380 GHz with a power of 34 mW.

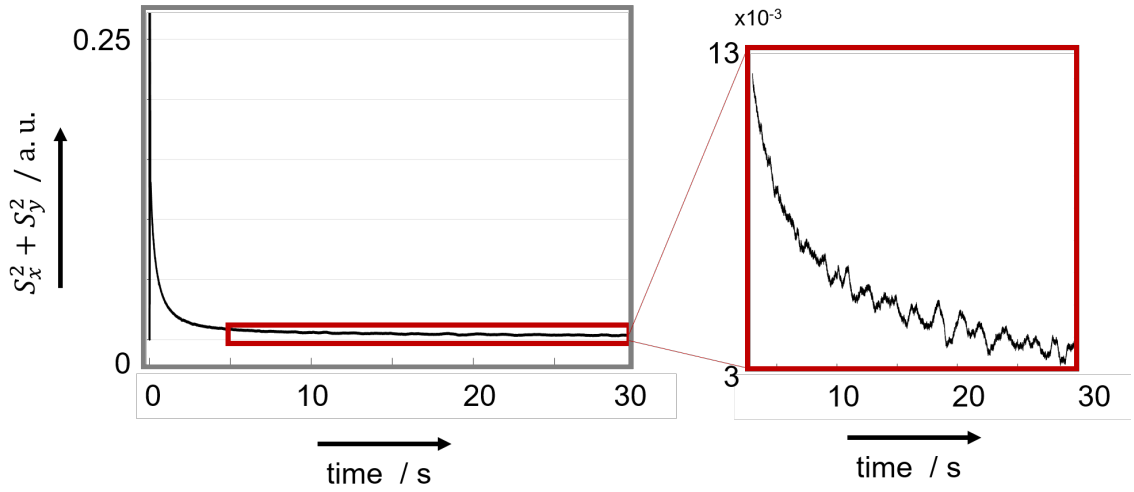

Figure D.2: Evolution of the normalized square of the ^{1}H signal intensity in absence of microwave irradiation during 30 s of acquisition. The experiment is the same as the one analyzed in the section 5.6 and displayed in figure 5.4. Note that the maximum of the signal has been cut and that magnetization in the transverse plane persists in our detection period.

D.2 Signal triggered by noise such as receiver opening

Only a small perturbation of the system suffices to trigger a signal under microwave irradiation. In the following experiments, the samples have been irradiated (frequency: 188.38 GHz, power: 34 mW at sample location) for approximately 20 minutes prior the acquisition and microwave is kept on during the detection. Considering the long $T_1(^1\mathrm{H})$ at 1.2 K ($\sim$ 5 min), a train of 90° hard pulses (presaturation) have been applied to the system before each polarization build up. Hence, signals after different acquisitions on a sample can be compared as the system has been prepared in the same way. All pulses have been removed from the sequences. Nonetheless, a signal is triggered 12 s after the beginning of the detection (see Fig. D.3). Its amplitude does not decay neither is constant with time. A burst at the beginning of the signal can be clearly identified.

This created signal tens of seconds after the beginning of the detection is not easily reproducible. The delay between the opening of the receiver and the signal vary between 2 s and several minutes. This effect strongly depends on initial conditions such as the polarizing time, the tuning of the probe and/or the sample preparation. This resurrection of NMR signal and this dependency to initial conditions is characteristic to chaotic behaviors and has been previously observed in liquid state NMR.

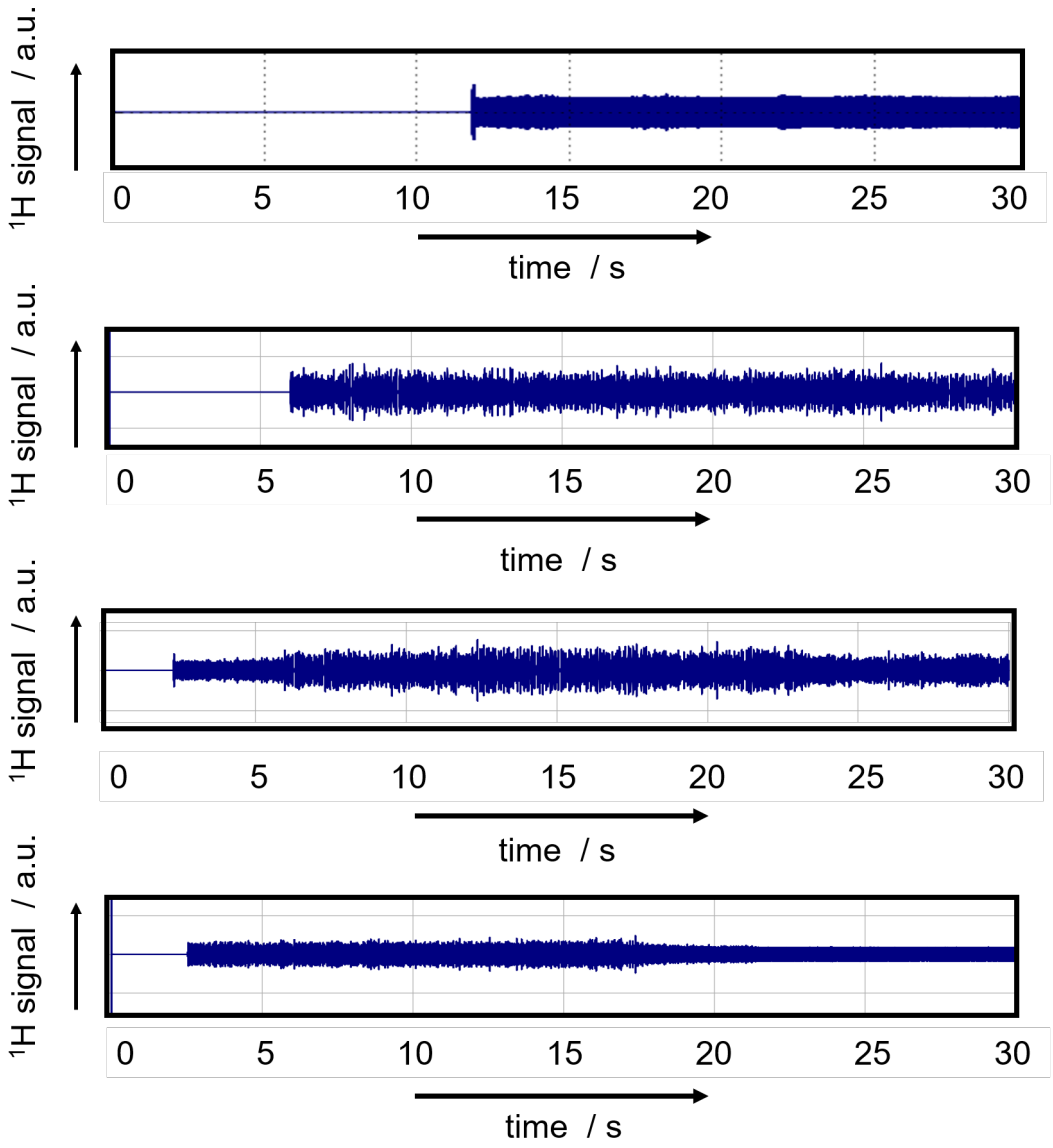

Figure D.3: ^{1}H signal versus time. The system is under constant microwave irradiation (frequency: 188.380 GHz, power at the sample location: 34 mW). All pulses have been removed from the acquisition sequence. A signal appears between ca. 2 and 12 s of acquisition.

D.3 Qualitative analysis of the BMP equations

It is in general difficult to find explicit solutions of nonlinear differential systems, and no general rules or criteria, other than numerical, allow one to predict the time evolution. Here, we perform a qualitative analysis of the extended BMP equations (Eqn. 5.9) that considers two interacting nuclear Zeeman reservoirs (proton and deuterium) and one electron dipolar reservoir to obtain some insight into the behavior of the system. The stationary solutions of this differential system are deter-

mined, and the evolution of the magnetization and the nuclear and electron dipole spin temperatures can be studied near their stationary solutions, the fixed points in the dynamical system theory parlance. In order to do so, we introduce the variables: $u(t) = M_x^2 + M_y^2$, $z(t) = \frac{\gamma_{\mathrm{H}}^2\hbar^2\mathcal{N}_{\mathrm{H}}B_0}{4k_B}\beta_n = B_h\beta_n$, $w(t) = B_h\beta_{ee}$, $\lambda = \frac{\mu_0}{2}\gamma\eta Q$ and $w_{\mathrm{L}}^0 = \mathcal{N}_{\mathrm{H}}\frac{\gamma_n\hbar}{2}\tanh\left(\beta_{\mathrm{L}}\frac{\gamma_n\hbar B_0}{2\mathrm{k_B}}\right) \approx \frac{\gamma_{\mathrm{H}}^2\hbar^2\mathcal{N}_{\mathrm{H}}B_0}{4k_B}\beta_{\mathrm{L}} = B_h\beta_{\mathrm{L}}$, the latter being the nuclear thermal magnetization under the high temperature approximation. Therefore, the BMP equations (Eqn. 5.9) in presence of microwave irradiation become:

$$\begin{aligned}
\dot{u}(t) &= -2(\lambda z(t) + \gamma_2)u(t) \\
\dot{z}(t) &= \lambda u(t) - \gamma_{n,ee}(z(t) - w(t)) \\
\dot{\phi}(t) &= -\delta \\
\dot{w}(t) &= -\gamma_{ee,n}(w(t) - z(t)) - \gamma_{ee,d}w(t) + \gamma_{ee,d}B_h\beta_d(t) - \gamma_{ee,\mathrm{L}}(w(t) - w_{\mathrm{L}}^0) - \delta_1 w(t) \\
\dot{\beta}_d(t) &= -\gamma_{d,ee}(\beta_d(t) - \frac{1}{B_h}w(t)),
\end{aligned} \tag{D.1}$$

The rates $\gamma_{ee,n}$ and $\gamma_{ee,d}$ are defined as: $\gamma_{ee,n} = \frac{c_{\mathrm{H}}}{c_{\mathrm{E}}}\gamma_{n,ee}$ and $\gamma_{ee,d} = \frac{c_{\mathrm{D}}}{c_{\mathrm{E}}}\gamma_{d,ee}$. The equation for $\dot{w}(t)$ can be rewritten as: $\dot{w}(t) = bz(t) + aw(t) + d\beta_d(t) + c$, where the coefficients a, b, c are defined as:

$$\begin{aligned}
a &= -\gamma_{ee,n} - \gamma_{ee,\mathrm{L}} - \gamma_{ee,d} - \delta_1 \\
b &= \gamma_{ee,n} \\
c &= (\gamma_{ee,\mathrm{L}} + \Omega)w_{\mathrm{L}}^0 \\
d &= B_h\gamma_{ee,d}
\end{aligned} \tag{D.2}$$

In these equations, δ_1 and Ω are defined as:

$$\begin{aligned}
\Omega &= \pi\omega_{1\,\mu w}^2 f(\Delta_0)\frac{\Delta_0}{\delta\omega^2}\omega_e \\
\delta_1 &= -\pi\omega_{1\,\mu w}^2 f(\Delta_0)\frac{\Delta_0^2}{\delta\omega^2}
\end{aligned}$$

where $\Delta_0 = \omega_e - \omega_{\mu w}$, the offset of the microwave frequency $\omega_{\mu w}$ from the electron resonance frequency. The other terms are defined in the main text (section 5.2.2)

This system of differential equation admits two fixed points:

$$F1: \quad \left(0, \frac{w_{\mathrm{L}}^0(\gamma_{ee,\mathrm{L}}+\Omega)}{\gamma_{ee,\mathrm{L}}+\delta_1}, w^{st}=z^{st}, \beta_d^{st}=\frac{1}{B_h}w^{st}\right) \tag{D.3}$$

$$F2: \quad \left(-\frac{\gamma_{n,ee}}{\lambda^2}\left[\frac{\gamma_2(\gamma_{ee,\mathrm{L}}+\delta_1)+\lambda w_{\mathrm{L}}^0(\gamma_{ee,\mathrm{L}}+\Omega)}{\gamma_{ee,n}+\gamma_{ee,\mathrm{L}}+\delta_1}\right], \ ... \right. \tag{D.4}$$
$$\left. -\frac{\gamma_2}{\lambda}, \frac{\lambda w_{\mathrm{L}}^0(\gamma_{ee,\mathrm{L}}+\Omega)-\gamma_{ee,n}\gamma_2}{\lambda(\gamma_{ee,n}+\gamma_{ee,\mathrm{L}}+\delta_1)}, \frac{1}{B_h}w^{st}\right)$$

In order to study the linearized system in the vicinity of the fixed points, the following change of variables is used: $u(t)=U(t)+u^{st}$, $z(t)=Z(t)+z^{st}$, $w(t)=W(t)+w^{st}$, and $\beta_d(t)=R(t)+\beta_d^{st}$, so that Eqn. D.1 becomes:

$$\begin{pmatrix}\dot{U}\\ \dot{Z}\\ \dot{W}\\ \dot{R}\end{pmatrix} = \begin{pmatrix}-2(\lambda z^{st}+\gamma_2) & -2\lambda u^{st} & 0 & 0\\ \lambda & -\gamma_{n,ee} & \gamma_{n,ee} & 0\\ 0 & b & a & d\\ 0 & 0 & \gamma_{d,ee}/B_h & -\gamma_{d,ee}\end{pmatrix}\begin{pmatrix}U\\ Z\\ W\\ R\end{pmatrix}+\begin{pmatrix}-2\lambda ZU\\ 0\\ 0\\ 0\end{pmatrix}, \tag{D.5}$$

The behavior of the system is given by the analysis of the linearized system in the vicinity of the fixed points. When microwave is turned off, $\Omega=\delta_1=0$, equations D.3 and D.4 become:

$$F1: \quad \left(0, \ w_{\mathrm{L}}^0, w^{st}=z^{st}, \beta_d^{st}=\frac{1}{B_h}w^{st}\right) \tag{D.6}$$

$$F2: \quad \left(-\frac{\gamma_{n,ee}}{\lambda^2}\left[\frac{\gamma_2\gamma_{ee,\mathrm{L}}+\lambda w_{\mathrm{L}}^0\gamma_{ee,\mathrm{L}}}{\gamma_{ee,n}+\gamma_{ee,\mathrm{L}}}\right], \ ... \right. \tag{D.7}$$
$$\left. -\frac{\gamma_2}{\lambda}, \frac{\lambda w_{\mathrm{L}}^0\gamma_{ee,\mathrm{L}}-\gamma_{ee,n}\gamma_2}{\lambda(\gamma_{ee,n}+\gamma_{ee,\mathrm{L}})}, \frac{1}{B_h}w^{st}\right)$$

Only $F1$ is an acceptable stationary solution when microwave irradiation is turned off because $F2$ admits a negative u^{st}, which is incompatible with the definition of $u(t)$. There exists, however, an interesting particular limiting case where the electron dipole relaxation rate is vanishingly small $\gamma_{ee,\mathrm{L}}\to 0$. Indeed, the value of u^{st} then tends to zero, and $F2$ is an acceptable solution, with $F2: \ (0, -\frac{\gamma_2}{\lambda}, -\frac{\gamma_2}{\lambda}, -\frac{\gamma_2}{\lambda B_h})$.

Thus, when $\gamma_{ee,\mathrm{L}}=0$, the eigenmodes of the linearized system of Eqn. D.5 are given

by the roots of the determinant (since $\lambda z^{st} + \gamma_2 = 0$):

$$\begin{vmatrix} x + \gamma_{n,ee} & -\gamma_{n,ee} & 0 \\ -\gamma_{ee,n} & x + \gamma_{ee,n} + \gamma_{ee,d} & -B_h\gamma_{ee,d} \\ 0 & -\gamma_{d,ee}/B_h & x + \gamma_{d,ee} \end{vmatrix} \tag{D.8}$$

which are:

$$\begin{aligned} x_0 &= 0 \\ x_\pm &= \frac{-(\gamma_{n,ee} + \gamma_{ee,n} + \gamma_{ee,d} + \gamma_{d,ee}) \pm \sqrt{\Delta}}{2}, \end{aligned} \tag{D.9}$$

and:

$$\Delta = (\gamma_{n,ee}+\gamma_{ee,n})^2 - 2\gamma_{ee,d}(\gamma_{n,ee}-\gamma_{ee,n}) - 2\gamma_{d,ee}(\gamma_{n,ee}+\gamma_{ee,n}) + (\gamma_{ee,d}+\gamma_{d,ee})^2. \tag{D.10}$$

Since $-2\gamma_{ee,d}(\gamma_{n,ee} - \gamma_{ee,n}) < 2\gamma_{ee,d}(\gamma_{n,ee} + \gamma_{ee,n})$, one has $\Delta \leq (\gamma_{n,ee} + \gamma_{ee,n})^2 + 2(\gamma_{n,ee} + \gamma_{ee,n})(\gamma_{d,ee} + \gamma_{ee,d}) + (\gamma_{ee,d} + \gamma_{d,ee})^2 = (\gamma_{n,ee} + \gamma_{ee,n} + \gamma_{ee,d} + \gamma_{d,ee})^2$, so that both eigenvalues of the linear part of the differential system in Eqn. D.5 are negative, $x_\pm \leq 0$, so that $F2$ is stable.

Résumé

La polarisation dynamique nucléaire (PDN) peut aider à s'affranchir de la faible sensibilité des expériences de résonance magnétique. Afin d'obtenir d'importantes polarisations dans les expériences de PDN suivies par une dissolution (d-PDN), un mélange d'eau et de glycérol contenant une forte concentration d'agents paramagnétiques est nécessaire. TEMPOL est un des agents polarisants les plus utilisés en PDN. A des températures cryogéniques, son spectre RPE est très large ce qui complique considérablement la description des mécanismes responsables du transfert de polarisation des électrons aux protons. La lente diffusion spectrale n'est pas assez efficace pour homogénéiser le temps de relaxation électron-réseau sur l'ensemble du spectre. Dans cette thèse, l'anisotropie de T_{1e} a été intégrée dans le modèle du mélange thermique (TM) établi par Abragam et Borghini. La comparaison de la polarisation des ^{1}H prédite par le TM avec les données expérimentales montre que l'établissement d'un modèle complet nécessite la prise en compte de l'anisotropie de T_{1e}. D'autre part, les mélanges liquides eau/glycérol présentent un phénomène de séparation de phase qui dépend du temps. Ce processus peut engendrer une variation approximative de 20% de la polarisation à 4 K dans un champ magnétique statique de 6.7 T. La combinaison d'expériences de RPE et de cryo-MET, nous a permis de comprendre l'impact de la maturation du « jus PDN » sur la polarisation des protons que l'on peut atteindre par PDN. En plus de ces phénomènes, le couplage fort entre une sonde ayant un Q élevé et la forte aimantation des spins ^{1}H contenus dans le « jus PDN » mène à des comportements non-linéaires de l'aimantation nucléaire sous forme d'impulsions RMN MASER aux temps courts, et engendre des signaux RMN qui peuvent durer plusieurs dizaines de secondes ou plus. Enfin, la d-PDN est utilisée pour hyperpolariser le ^{31}P des phosphates inorganiques dans le but de mieux comprendre la formation de clusters de calcium et de phosphate qui intervient au début de la calcification.

Mots Clés

Polarisation dynamique nucléaire, RMN, mélange thermique, effet MASER, bio-minéralisation

Abstract

Dynamic Nuclear Polarization (DNP) can help to overcome the intrinsically low sensitivity of magnetic resonance experiments. To reach high nuclear polarization in dissolution DNP (d-DNP), a mixture of water and glycerol containing a high concentration of paramagnetic polarizing agents is required. TEMPOL is one of the most commonly used polarizing agent in DNP. At cryogenic temperatures, the EPR spectrum of TEMPOL is very broad. This considerably complicates the description of the mechanisms that are responsible for the transfer of polarization from electrons to protons. The slow electronic spectral diffusion is not sufficient to average the electron spin-lattice relaxation time over the entire spectrum. In this thesis, the anisotropy of T_{1e} has been included in Abragam's and Borghini's thermal mixing (TM) model. Comparisons of experimental ^{1}H polarizations with predictions of the TM model demonstrate that an accurate DNP model requires the consideration of the anisotropy of T_{1e}. On the other hand, it is known that water/glycerol mixtures can undergo a time-dependent phase separation in liquid phase. Such a process can generate variations of ca. 20% of the proton polarization in our DNP samples at 4 K in a static magnetic field of 6.7 T. Combining EPR and cryo-TEM experiments helped us to understand the impact of the ripening of "DNP-juice" on the proton polarization that can be achieved by DNP. In addition to these phenomena, the strong coupling between a high-Q probe and the large magnetization of the ^{1}H spins contained in the "DNP-juice" leads to nonlinear behavior of the nuclear magnetization at short times in the form of NMR MASER bursts, and gives rise to NMR signals that can last more than several tens of seconds. Finally, d-DNP is used to hyperpolarize ^{31}P in inorganic phosphates to get a better understanding of the calcium phosphate clustering that occurs at the early stages of calcification.

Keywords

Dynamic Nuclear Polarization, NMR, Thermal Mixing, MASER effect, bio-mineralization